Modelling neodymium isotopes to investigate the marine neodymium cycle

Suzanne Robinson

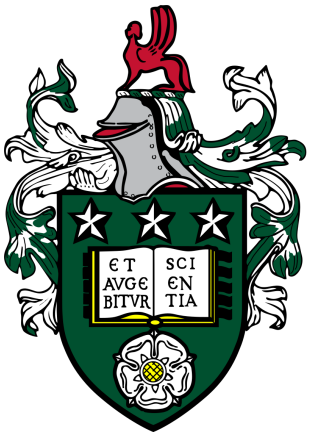

Submitted in accordance with the requirements for the degree of Doctor of Philosophy

The University of Leeds
School of Earth and Environment
September 2022

Declaration

The candidate confirms that the work submitted within the thesis is her own, except where work which has formed part of jointly authored publications has been included. The contribution of the candidate and the other authors to this work has been explicitly indicated below. The candidate confirms that appropriate credit has been given within the thesis where reference has been made to the work of others.

The work in **Chapter 2** of this thesis has been published in *Chemical Geology* as follows: Suzanne M. Robinson, Ruza F. Ivanovic, Tina van de Flierdt, Cécile L. Blanchet, Kazuyo Tachikawa, Ellen E. Martin, Carys P. Cook, Trevor Williams, Lauren J. Gregoire, Yves Plancherel, Catherine Jeandel, and Thomas Arsouze. Global continental and marine detrital ε_{Nd}: An updated compilation for use in understanding marine Nd cycling, *Chemical Geology*, 567, 120119, `https://doi.org/10.1016/j.chemgeo.2021.120119`, 2021. SMR designed and executed the main project, including conducting background research, coordinating the integration of the database, developing, and applying methods to interpolate the observations into gridded global maps, analysing the results and preparing the manuscript. All with core guidance from RFI and TF, and further input from all co-authors. Additionally, CLB curated the ε_{Nd} database, KT provided a compilation of detrital Nd data, CPC and EEM contributed new Southern Ocean Nd data, and TW compiled the large Southern Ocean published Nd dataset. CJ and TA provided support concerning their previous methodology, including input files.

The work in **Chapter 3** of this thesis has been submitted to *Geoscientific Model Development*, with the authorship of Suzanne M. Robinson, Ruza F. Ivanovic, Lauren J. Gregoire, Julia C. Tindall, Tina van de Flierdt, Yves Plancherel, Frerk Pöppelmeier, Kazuyo Tachikawa, and Paul Valdes. SMR conducted the background research, implementation of the code, updating model boundary conditions, designing, and running the simulations, analysing the results and preparing the manuscript. RFI, LJG, and JCT provided technical support in the implementation of the new isotopic equations. All co-authors contributed scientific expertise during the implementation and to help analyse results and suggested improvements to the manuscript. PV designed and ran the pre-industrial FAMOUS GCM ensemble. FP shared an updated dust source ε_{Nd} boundary condition. YP provided the seawater REE compilation, which SMR updated with recent GEOTRACES publications. We acknowledge the contribution of Jamie D Wilson (University of Bristol) and Andy Ridgwell (University of California, Riverside) for valuable discussions early in the Nd isotope scheme design.

The work in **Chapter 4** of this thesis has been submitted to *Biogeosciences*, with the authorship of Suzanne M. Robinson, Ruza F. Ivanovic, Lauren J. Gregoire, Lachlan Astfalck, Tina van de Flierdt, Yves Plancherel, Frerk Pöppelmeier and Kazuyo Tachikawa. SMR conducted the background research, designed, and ran the simulations, analysing the results and preparing the manuscript. SMR, RFI and LJG conceived the study and the overall approach to each component of it. SMR designed and ran the optimisation and sensitivity simulations, with technical input from RFI and LJG. LA constructed the Gaussian Process emulator utilised to optimise the scheme in collaboration with SMR. SMR produced the manuscript with input from all co-authors. All co-authors contributed

scientific expertise throughout.

Acknowledgements

I would like to express my deepest gratitude to my supervisors: Ruza Ivanovic, Lauren Gregoire, and Tina van de Flierdt for all their invaluable support, time, inspiration, and feedback throughout. In particular, I am so grateful to Ruza for the endless hours of encouragement and passion which allowed me to gain ever-increasing confidence and drive; to Lauren for all the technical assistance and unwavering belief; and to Tina for sharing her wide expertise and for her limitless curiosity which always kept me inspired.

I could not have undertaken this journey without my amazing team of collaborators I have been fortunate to work with: Julia Tindall, Cécile Blanchet, Kazuyo Tachikawa, Yves Plancherel, Frerk Pöppelmeier, Lachlan Astfalck, Paul Valdes, Ellen Martin, Carys Cook, Trevor Williams, Catherine Jeandel and Thomas Arsouze. I would like to especially thank Julia Tindall for dedicating so many hours to the code development, and always being so patient and kind. I am also grateful to Jamie Wilson and Andy Ridgwell for helpful conversations about biogeochemical modelling.

I am thankful to all my friends and especially fellow PhD students within ICAS and the Climate-Ice and Physical Climate Change research groups. I am so lucky to have been around such an amazing and positive group for all the coffee and ice-cream breaks, cake Wednesdays, pub trips, days out, summer schools, and especially for all the support and games throughout the COVID pandemic.

A special thank you to my Mum, Dad, Caroline, and Auntie Margaret for all their immense support, love, and guidance throughout. Lastly, thank you Rohan Patel for being so incredibly encouraging and reassuring every single step of the way.

This project was funded by the Natural Environment Research Council (NERC) SPHERES Doctoral Training Partnership (DTP), #NE/L002574/1.

Abstract

The neodymium (Nd) isotope composition (ε_{Nd}) of seawater is used to trace ocean circulation. However, there remains uncertainty in quantifying oceanic budgets of Nd. For example, a recently proposed benthic Nd flux complicates traditional interpretations of the seawater ε_{Nd} signal by introducing a major non-conservative process.

This thesis implements marine Nd isotopes into a fast General Circulation Model (FAMOUS); revisiting the sources, sinks and transformation of Nd within the ocean. A statistical emulator is applied to explore three key parameters, and to optimise the scheme's ability to represent modern seawater measurements. Altogether, the calibrated simulation captures the influence of the physical/biogeochemical processes to which global ε_{Nd} distributions are known to be sensitive (i.e., inputs/sinks, internal cycling, and water mass structure and mixing). Of the total Nd sourced to the ocean, 64% comes from the seafloor sediment flux, 30% from rivers, and 6% from dust, and simulated Nd has an estimated residence time of 727 years. Sensitivity tests reveal that vertical Nd transport via reversible scavenging maintains water provenance signals by enhancing basinal ε_{Nd} signatures. Model-data inconsistencies in the North Pacific and northern North Atlantic imply that a spatially uniform seafloor-wide bulk sediment benthic Nd flux does not capture the mobile particle-seawater exchange in all instances. Furthermore, simulations exploring the mobilisation of 'reactive' sediment Nd demonstrate sluggish Pacific waters are sensitive to benthic flux alterations, whereas the well-ventilated North Atlantic displays a much weaker response.

In closing, there are distinct regional differences in how seawater acquires its ε_{Nd} signal. More careful interpretations to set apart the interlinked roles of major Nd sources (ε_{Nd} composition, spatial extent, and reactivity), from ocean structure (water mass presence, convection, and ventilation), and regional environmental conditions (biological productivity, pH, redox conditions) are required for the robust applications of ε_{Nd} as an ocean circulation tracer.

Contents

List of Figures

List of Tables

List of Abbreviations

$\delta^{13}C$ $^{13}C/^{12}C$ ratio of a sample relative to a standard (‰)

$\Delta^{14}C$ $^{14}C/^{12}C$ ratio of a sample relative to a standard, corrected for isotopic fractionation effects and normalised to the mean value for terrestrial wood (‰)

$\delta^{18}O$ $^{18}O/^{16}O$ ratio of a sample relative to a standard (‰)

ε_{Nd} $^{143}Nd/^{144}Nd$ ratio of a sample relative to the Chondritic Uniform Reservoir

K_d equilibrium scavenging coefficient

AABW Antarctic Bottom Water

AAIW Antarctic Intermediate Water

ACC Antarctic Circumpolar Current

AMOC Atlantic Meridional Overturning Circulation

AOGCM Atmosphere-Ocean General Circulation Model

Bern3D Bern 3-dimensional Earth system Model of Intermediate Complexity

CCSM3 Community Climate System Model

CDW Circumpolar Deep Water

CESM Community Earth System Model

CHUR Chondritic Uniform Reservoir

CMIP Coupled Model Intercomparison Project

CMS Computational Modelling Services

CSIRO Mk3L Commonwealth Scientific and Industrial Research Organisation climate system model

EEP Eastern Equatorial Pacific

EMIC Earth system Model of Intermediate Complexity

ESM Earth System Model

FAMOUS Fast Met Office/U.K Universities Simulator

FGOALS Flexible Global Ocean-Atmosphere-Land system model

GCM General Circulation Model

GEOTRACES An International Study of the Marine Biogeochemical Cycles of Trace Elements and Isotopes

GEUS Geological Survey of Denmark and Greenland

GFDL Geophysical Fluid Dynamics Laboratory coupled climate model

GIS Geographic Information System

GMOC Global Meridional Overturning Circulation

GP Gaussian Process

HadCM3 Hadley Centre Coupled atmosphere-ocean General Circulation Model (version 3)

HadGEM2 Hadley Centre Global Environmental Model (version 2)

HadOCC Hadley Centre Ocean Carbon Cycle model

IR isotopic ratio

IRD ice rafted debris

ka thousand years

LGM Last Glacial Maximum

Ma million years

MAE mean absolute error

MIS Marine Isotope Stage

MOC Meridional Overturning Circulation

MOSES Met Office Surface Exchange Scheme

NADW North Atlantic Deep Water

NCAS National Centre for Atmospheric Science

NERC Natural Environmental Research Council

NN nearest neighbour

NOAA National Oceanic and Atmospheric Administration

NPZD nutrient-phytoplankton-zooplankton-detritus

NROY not-ruled-out-yet

OCMIP Ocean Carbon-Cycle Model Intercomparison Project

pCO_2 partial pressure of CO_2

PDW Pacific Deep Water

PETM Palaeocene-Eocene Thermal Maximum

PMOC Pacific Meridional Overturning Circulation

POC particulate organic carbon

PSU practical salinity units

PUMA Providing Unified Model Access

RAPID-AMOC Rapid Meridional Overturning Circulation Array

REE Rare Earth Element

SedDB Online data management and information system for sediment geochemistry

SGD submarine groundwater discharge

Sv Sverdrup

THC thermohaline circulation

UM Unified Model

xxx

Chapter 1

Introduction

1.1 Context to thesis

1.1.1 Ocean circulation and climate

The global climate system is formed of five major components: the atmosphere, hydrosphere, cryosphere, lithosphere and biosphere, and the intricate interactions amongst them (Baede et al., 2001). Climate evolves over time when forced by its own internal dynamics and in response to external forcings (e.g., solar variations, orbital cycles, volcanic eruptions and anthropogenic forcings). Covering 71% of Earth's surface, the ocean forms a key component, driving force and essential regulator of the global climate system. The ocean continuously exchanges with the atmosphere and redistributes mass, heat, carbon, freshwater, nutrients, and other substances away from their sources and between hemispheres (Luo et al., 2018; Macdonald and Wunsch, 1996; Ganachaud and Wunsch, 2000; Schmittner et al., 2013; Buckley and Marshall, 2016; Rahmstorf, 2002; McCarthy et al., 2015).

Ocean circulation is a highly complex and turbulent system, yet if the mass and corresponding property fluxes (e.g. temperature and salinity) are integrated across ocean basins, a somewhat simpler (but still very complicated) circulation pattern emerges (Macdonald and Wunsch, 1996). The Global Meridional Overturning Circulation (GMOC; Fig. 1.1) describes a system of surface and deep ocean currents which transpose across all ocean basins, connecting the surface ocean and atmosphere with the large deep ocean reservoir (Rahmstorf, 2002). The overturning system is governed by a combination of wind driven surface currents and tides (mostly confined to the upper hundred meters), alongside density driven thermohaline circulation (THC), whereby the density of water is related to its temperature and salinity properties (where colder and saline waters have the highest density).

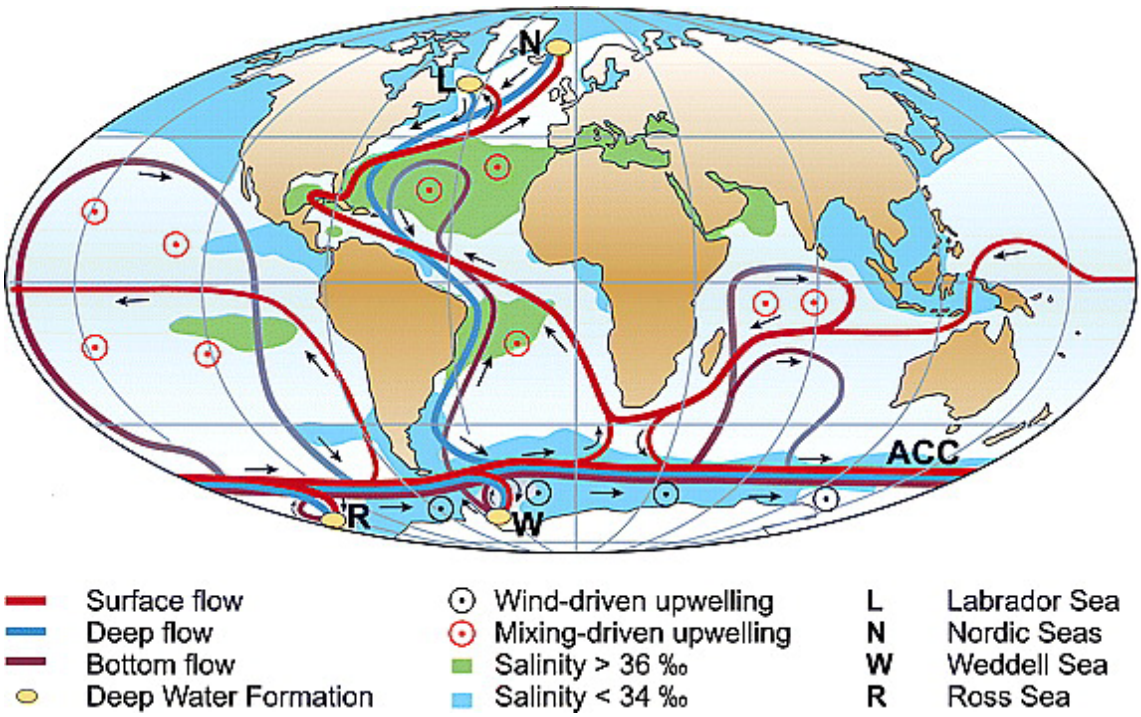

Figure 1.1: Schematic of the modern global overturning circulation from Kuhlbrodt et al. (2007), following Broecker (1997); Rahmstorf (2002). Surface flows mostly constrained to the upper hundred meters of the ocean (red) flow towards high latitude deep water formation regions (yellow ovals) in the North Atlantic and Southern Ocean and circulate through the ocean interior as deep and bottom water currents (blue and purple). Wind-driven upwelling occurs across the Antarctic Circumpolar Current.

In the modern ocean, northward flowing saline surface waters originating from the Gulf of Mexico release substantial heat to the atmosphere in the northern North Atlantic, attaining critical density at sites in the marginal Labrador and Greenland Seas. These waters then sink to form North Atlantic Deep Water (NADW), which returns southwards as a deep western boundary current, reaching the Antarctic Circumpolar Current (ACC) of the Southern Ocean (Schmittner et al., 2013). This deep water then mixes with other deep-water masses such as Pacific Deep Water (PDW) to form Circumpolar Deep Water (CDW), of which some penetrates northwards filling deep waters into the Pacific and Indian Oceans. Along the Antarctic coast, in the Ross and particularly the Weddell Seas, the second key regions of modern deep and bottom water formation occur. Here processes associated with sea ice formation (brine water rejection) create Antarctic Bottom Water (AABW). These waters are characterised as the densest on Earth, distinctly colder and fresher than NADW and flow northward at abyssal depths in the Atlantic (Talley, 2013; Orsi et al., 1999).

Moreover, distributions of nutrients and patterns of biological production in the ocean are determined by the complex interplay of biogeochemical and physical processes, and external sources. The observed spatial characteristics of macro-nutrients (e.g., nitrate, phosphate, and silicate) broadly reflect those of classical water masses (e.g., NADW, AABW), demonstrating physical transport and large-scale overturning circulation as the principal mechanism determining their inter-basinal distributions (Baede et al., 2001).

Despite its importance on multiple aspects of the Earth system (e.g., Bigg et al., 2003; Ferreira et al., 2018; Frierson et al., 2013; Johns et al., 2011; Marshall et al., 2014; Pérez et al., 2013; Takahashi et al., 2009; Vellinga and Wood, 2002), a mechanistic understanding of large-scale physical ocean overturning, its internal variability, response to external

forcings and resultant implications upon the climate system remains incomplete, and historically observations of large-scale ocean dynamics have been challenging (Buckley and Marshall, 2016; McCarthy et al., 2015). Moreover, due to the millennial timescales that deep ocean circulation operates upon (Broecker and Peng, 1982), the decadal timescales of the observational record remain far too short to attribute the relative contribution of internal variability, natural forcing and anthropogenic forcings to any observed changes (Stocker et al., 2013).

The geological record can provide insights into the internal and external mechanisms that drive multi-decadal to multi-millennial variability of the ocean and climate system. These records are useful for understanding long-term changes in ocean and atmospheric chemistry, heat and freshwater fluxes, and global wind patterns (as inferred from mineralogical, geochemical, and isotopic composition of dust deposited in the oceans and ice sheets) (Lynch-Stieglitz, 2017; McManus et al., 2004; Lynch-Stieglitz and Marchitto, 2003). In particular, the application of geochemical ocean circulation tracers can overcome the severe spatiotemporal limitations of direct ocean circulation measurements, and improve our conceptual understanding of the background state of the deep ocean, and its response to perturbations (von Blanckenburg, 1999; Lynch-Stieglitz, 2003, 2017).

1.1.2 Tracers of ocean circulation

Our knowledge of past ocean-climate dynamics has been widely informed by multiple palaeocirculation proxies. Traditional hydrographic parameters (temperature and salinity) are intrinsic to any water mass definition; however they provide only limited information on water mass formation processes and are not preserved back in time (England and Maier-Reimer, 2001). Crucial information can be gained instead from geochemical tracers (Table 1.1), providing a novel means for understanding imperative ocean ventilation processes that cannot be obtained by temperature and salinity alone (see Lynch-Stieglitz and Marchitto, 2003, for review).

Table 1.1: Summary of ocean circulation tracers, their main proxy application and associated key studies

Tracer	Ocean circulation proxy application	References
$\delta^{13}C$	Air sea gas exchange, nutrients, productivity	(McManus et al., 2004; Henry et al., 2016; Oliver et al., 2010; Menviel et al., 2017)
Cd/Ca	Nutrient concentrations and properties	(Boyle and Keigwin, 1982; Bertram et al., 1995; Rosenthal et al., 1997)
$\delta^{18}O$	Density, temperature, salinity	(Lynch-Stieglitz et al., 1999a,b)
$\Delta^{14}C$	Ventilation rates, air-sea exchange	(Broecker et al., 2004, 1960; Sweeney et al., 2007)
$^{231}Pa/^{230}Th$	Circulation kinematics, particle processes and scavenging	(McManus et al., 2004; Bohm et al., 2015; Lippold et al., 2009; Gherardi et al., 2005; Yu et al., 1996)
ε_{Nd}	Water mass provenance and mixing, large-scale weathering regimes	(Scher and Martin, 2006; Gutjahr et al., 2008; Howe et al., 2016; Hu and Piotrowski, 2018; Rutberg et al., 2000; Blaser et al., 2019b)

Stable carbon isotopes ($\delta^{13}C$) and the cadmium/calcium ratios (Cd/Ca) recorded and preserved in benthic foraminifera were historically the most frequently applied geochemical tracer to reconstruct deep ocean circulation (Frank, 2002). The $\delta^{13}C$ of deep waters generally is negatively correlated with nutrient (phosphate) concentrations due to preferential

incorporation of ^{12}C onto organic matter in the surface ocean, and corresponding release during remineralisation at depth. However, $\delta^{13}C$ is also sensitive to temperature, nutrient availability, and carbonate ion concentration (Broecker and Peng, 1982). Cd/Ca positively correlates with nutrient concentration (phosphate, nitrate), but thermodynamic processes can cause problems with their interpretation (Lynch-Stieglitz, 2003). Combining these tracers allows the distinction between low nutrient (e.g., NADW) and high nutrient (e.g., North Pacific) deep waters, providing useful proxies for past water mass distributions controlled by processes in the surface ocean. Yet, it remains difficult to make quantitative estimates of water mass mixing on the basis of $\delta^{13}C$ and Cd/Ca because neither proxy exclusively mirrors nutrient concentrations of ambient deep water (Frank, 2002; Lynch-Stieglitz, 2003).

Stable oxygen isotopes ($\delta^{18}O$) in seawater are determined by fractionation during evaporation and sea ice formation, alongside the $\delta^{18}O$ content of precipitation and continental run-off (Lynch-Stieglitz, 2003). As such seawater $\delta^{18}O$ changes recorded in foraminifera can be applied as a conservative density tracer due to its relation to seawater temperature and ocean conditions (e.g. salinity) upon calcification (Lynch-Stieglitz et al., 1999a,b). The counteracting temperature and salinity effects (which are further hard to separate) on $\delta^{18}O$ can however lead to small gradients amongst key water masses (NADW and AABW), and there are known issues with interspecies calibration (Lynch-Stieglitz, 2003).

Circulation rate and volume transport tracers of ocean circulation include the use of natural and anthropogenic radiocarbon ($\Delta^{14}C$) and protactinium/thorium ratios (^{231}Pa /^{230}Th). Radiocarbon (^{14}C) is produced by cosmic rays in the atmosphere and is subsequently dissolved into the surface mixed layer in partial equilibrium, ^{14}C decays with a half-life of 5,730 years (Godwin, 1962). As such, the more negative the $\Delta^{14}C$ the more time has elapsed since the water mass was in contact with the atmosphere, enabling the tracing of deep-ocean ventilation rates (Lynch-Stieglitz, 2003). Radiocarbon content in the atmosphere does change with time, complicating the use of this tracer, which is further restricted by its short half-life limiting its palaeo-proxy use to the last 30-50 thousand years (ka) (von Blanckenburg, 1999; England and Maier-Reimer, 2001; Reimer et al., 2009). Conversely, protactinium (^{231}Pa) and thorium (^{230}Th) are produced in the water column and scavenged by marine particles onto the seafloor. Thorium (^{230}Th) is scavenged more efficiently than ^{231}Pa, leading to contrasting residence times in seawater, and resulting in differing lateral transport. As such, measurable shifts in the $^{231}Pa/^{230}Th$ of marine sediments can be used to estimate ventilation rates (Yu et al., 1996; McManus et al., 2004). However, robust palaeocirculation reconstructions using $^{231}Pa/^{230}Th$ require detailed information of past particle fluxes and composition due to the complex interplay between deep water ventilation rates and the particle scavenging of the elements (Lynch-Stieglitz, 2003).

The application of inorganic trace elements, such as neodymium isotopes (ε_{Nd}) as valuable tracers of both modern and past ocean circulation has led to their increased exploitation over the past four decades (Goldstein and Hemming, 2003; Tachikawa et al., 2017; van de Flierdt et al., 2010). The estimated mean oceanic residence time of Nd in seawater of 360 to 785 years (Arsouze et al., 2009; Gu et al., 2019; Pöppelmeier et al., 2020a; Rempfer et al., 2011), is shorter than the global ocean overturning time ($\approx$ 1500 years; Broecker and Peng, 1982), and explains the heterogenous ε_{Nd} distributions in deep water (Fig. 1.2). Moreover, in pelagic seawater, ε_{Nd} can exhibit conservative behaviour, corresponding to water mass advection and mixing (Goldstein and Hemming, 2003; Piotrowski et al., 2008; Tachikawa et al., 2017; Hu et al., 2016; Piepgras et al., 1979; van de Flierdt et al., 2016). It is these characteristics of ε_{Nd} that has led to the use of ε_{Nd} to trace water mass provenance, structure and mixing; providing important insights into both modern and palaeo-ocean circulation (see reviews by Frank, 2002; Goldstein and Hemming, 2003; van de Flierdt et al., 2010). An advantage of dissolved ε_{Nd} in

seawater compared to carbon isotopes, is that the former experiences negligible biological fractionation, and is not influenced by air-sea exchange processes (Blaser et al., 2019a).

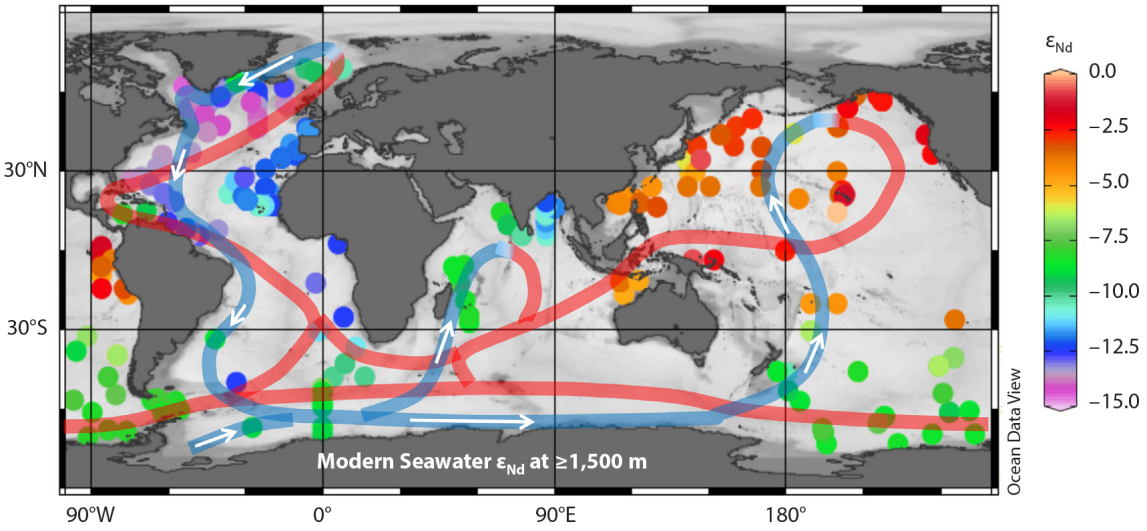

Figure 1.2: Distribution of deep-water Nd isotopic composition in the modern ocean taken from Tachikawa et al. (2017) and the schematised global thermohaline circulation from Broecker (1991). The coloured dots indicate ε_{Nd} measurements at 1,500 m depth in the water column or at a water depth closest to 1,500 m. Figure demonstrates the water mass provenance and circulation properties of ε_{Nd} in seawater. Figure reprinted from Tachikawa et al. (2020).

The Nd isotope composition is imprinted on waters via exchange with terrigenous sediments and is recorded and preserved in multiple authigenic (seawater) archives (e.g., sediment leaches, fish teeth/debris and foraminifera). The ε_{Nd} signature of authigenic sediment phases are considered robust ocean circulation proxies, applicable across long timescales, including the Palaeocene-Eocene Thermal Maximum (PETM) $\approx$ 55 million years ago (Ma) (Abbott et al., 2016b). Furthermore due to ε_{Nd} not being actively involved in marine biogeochemical cycling (Blaser et al., 2019a), palaeo-reconstructions of ocean circulation during periods of rapid, climatically induced biological and chemical change are possible, providing unique insights into large-scale ocean circulation dynamics (von Blanckenburg, 2001).

However, a lack of constraints regarding the major global marine Nd budgets, including absence of a full description and quantification of the major sources, sinks and internal processes governing seawater Nd isotope distributions complicates the use of this tracer, leading to hotly debated interpretations regarding their oceanic cycling (Haley et al., 2017; Abbott et al., 2015b; Du et al., 2016; Abbott et al., 2015a; Abbott, 2019; Abbott et al., 2016b; Wang et al., 2021; Rousseau et al., 2015; Haley et al., 2021; Jeandel, 2016; Johannesson and Burdige, 2007; Lacan and Jeandel, 2005a). Thus, it is important to constrain the processes governing global marine Nd cycling and distributions, unlocking the full potential of Nd isotopes as a palaeoceanographic tracer, and forms the main motivation and focus of this study.

1.1.3 Neodymium isotopes in seawater

There are seven naturally occurring isotopes of Nd (^{142}Nd, ^{143}Nd, ^{144}Nd, ^{145}Nd, ^{146}Nd, ^{147}Nd, ^{148}Nd, ^{149}Nd and ^{150}Nd). The samarium (Sm)-Nd system is a long-lived radiogenic isotope system, characterised by the slow decay of the parent isotope compared with the age of the Solar System. Here ^{147}Sm decays to produce its radiogenic daughter ^{143}Nd,

with a half-life of 160 billion years. During melting of the Earth's mantle, ^{143}Nd (which is more incompatible during melting than ^{147}Sm) is preferentially partitioned into magmas which form continental crust, together with ingrowth of ^{143}Nd, this results in characteristic ^{143}Nd/^{144}Nd fingerprints in rocks, which generally vary as a function of age and geological composition. The ratio of Nd isotopes relative to the bulk earth standard is denoted:

$$\varepsilon_{Nd} = \left(\frac{(^{143}\mathrm{Nd}/^{144}\mathrm{Nd})_{\mathrm{sample}}}{(^{143}\mathrm{Nd}/^{144}\mathrm{Nd})_{\mathrm{CHUR}}} - 1 \right) \times 10^4, \tag{1.1}$$

where $(^{143}\mathrm{Nd}/^{144}\mathrm{Nd})_{\mathrm{CHUR}}$ relates to the Chondritic Unform Reservoir (CHUR; 0.512638: Jacobsen and Wasserburg 1980), and one ε_{Nd}-unit represents one part per 10,000 deviation from CHUR.

The Nd isotope distributions of continental rock display spatial heterogeneity (Fig. 1.3). Generally, older continental crust has lower ^{147}Sm/^{143}Nd and low ε_{Nd} values (e.g., old exposed Archean rocks composing the North Atlantic Craton, $\varepsilon_{Nd} \approx -25$), compared with younger mantle-derived rocks, which have higher ^{147}Sm/^{143}Nd and high ε_{Nd} values (e.g., Hawaiian island chain, $\varepsilon_{Nd} \approx +7$) (Robinson et al., 2021). Seawater acquires its ε_{Nd} signal externally from weathering of lithogenic material (which is then further redistributed internally via mixing and particle cycling), and water masses become 'tagged' with a distinct ε_{Nd} related to provenance (e.g. Tachikawa et al., 2017; van de Flierdt et al., 2016, for reviews).

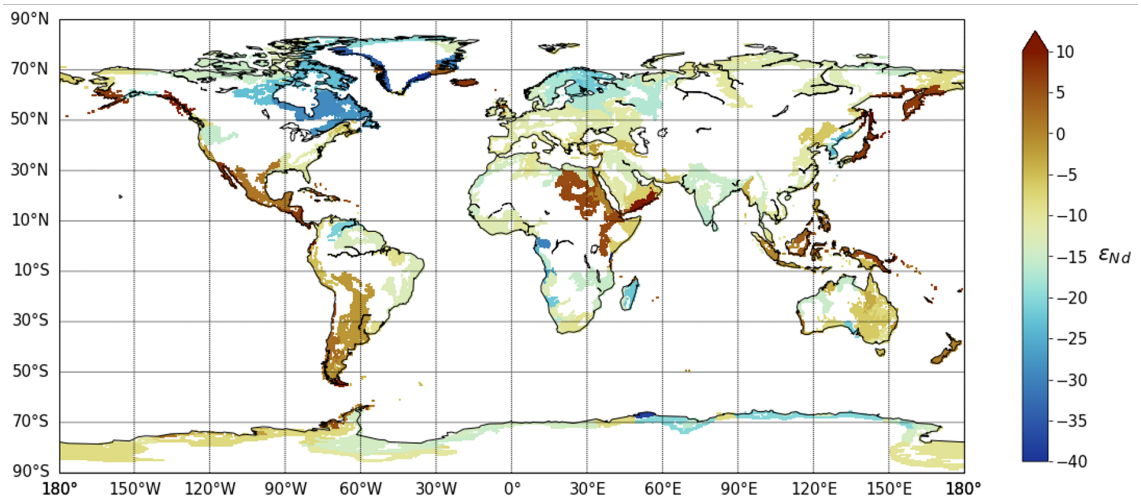

Figure 1.3: Neodymium isotope distributions of continental rock proximal to oceanic margins, demonstrating the spatial heterogeneity in crustal ε_{Nd} related to its age and composition. Figure reprinted from Robinson et al. (2021).

Of the major deep-water masses, northern sourced NADW displays an ε_{Nd} value of -13.2 ± 0.5 (Lambelet et al., 2016), while southern sourced AABW displays an ε_{Nd} value of -9.1 ± 0.5 (Stichel et al., 2012; Lambelet et al., 2018). North Pacific waters in contrast possess much more radiogenic ε_{Nd} values ranging between -4 to -2 (Amakawa et al., 2009; Fuhr et al., 2021; Behrens et al., 2018; Fröllje et al., 2016). It is the difference in ε_{Nd} carried by northern sourced, and more unradiogenic NADW, compared with southern sourced, and comparably less radiogenic AABW (and their corresponding glacial counterparts), in particular that has been key for many palaeoceanographic reconstructions (Frank, 2002; Piotrowski et al., 2004; Gutjahr et al., 2008; Piotrowski et al., 2008; Roberts et al., 2010; Lippold et al., 2016; Piotrowski et al., 2012; van de Flierdt et al., 2010; Howe et al., 2017; Dausmann et al., 2017; Hu and Piotrowski, 2018; Jonkers et al., 2015; Wilson et al., 2015; Xie et al., 2014; Pöppelmeier et al., 2020b; Blaser et al., 2019a).

The first direct seawater ε_{Nd} measurements were obtained in the late 1970s (Piepgras and Wasserburg, 1980; Piepgras et al., 1979), since then, and upon the launch of the GEOTRACES international programme in 2010 (Measures et al., 2007), which identifies ε_{Nd} as a key parameter measured on every cruise, the amount and distribution of high-quality seawater ε_{Nd} and Nd concentration ([Nd]) measurements have increased substantially from only 54 measurements in the late 1970s to over 3,200 in 2022 (e.g., see GEOTRACES cruise sections in Fig. 1.4 and seawater compilations by GEOTRACES Intermediate Data Product Group, 2021; Lacan et al., 2012; Osborne et al., 2015; Tachikawa et al., 2017; van de Flierdt et al., 2016).

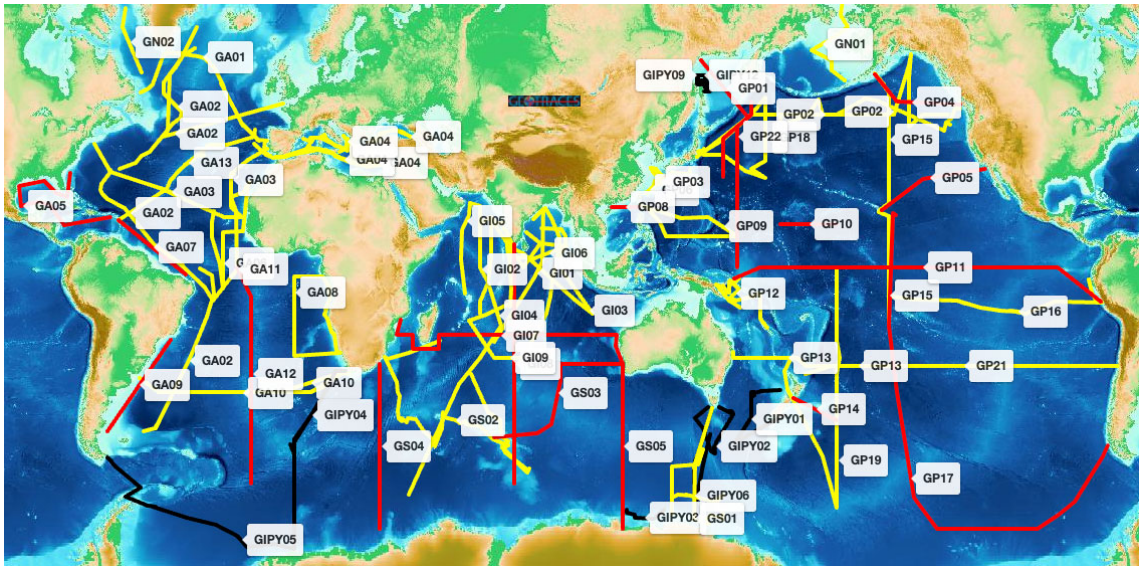

Figure 1.4: GEOTRACES section cruises, where coloured lines show the sections that are either completed (yellow), planned (red), or cruises from the International Polar Year 2007-2008 (black). Demonstrating the recent effort to map the global distribution of trace elements and isotopes; including Nd concentration and isotopes which are measured on every cruise. Figure reprinted from `https://www.geotraces.org/`.

The expanded seawater ε_{Nd} database has provided novel insights into the oceanic Nd cycle. First of all, the observed features are consistent with the conventional view that Nd isotopes generally follow the patterns of advection, increasing along the global circulation pathway with low ε_{Nd} values in young waters of the North Atlantic and high ε_{Nd} values in old waters of the North Pacific (Fig. 1.5a); confirming the capability of marine Nd isotopes to trace modern large-scale ocean circulation pattens.

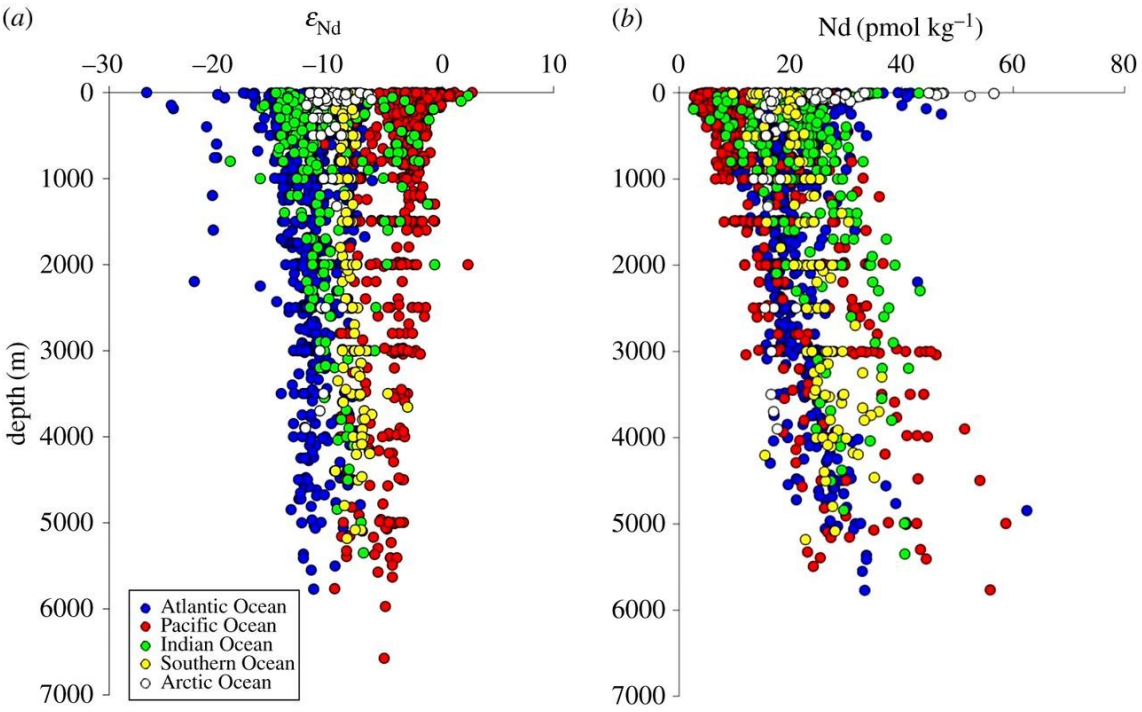

Figure 1.5: Global depth profiles for measured (a) Nd isotope compositions and (b) Nd concentrations in seawater. Colour of filled circles corresponds to different geographical regions. Figure reprinted from van de Flierdt et al. (2016).

Comparing seawater ε_{Nd} measurements with hydrography parameters (e.g., temperature, salinity, nutrients, and oxygen) demonstrates a close correspondence of pelagic seawater ε_{Nd} (at depths $> 1,500$ m) to water mass advection and mixing; suggesting these processes are a primary control on deep-water ε_{Nd} distributions (see Fig. 1.6 for correlation of seawater ε_{Nd} with nutrient parameters) (Goldstein and Hemming, 2003; Piotrowski et al., 2008; Tachikawa et al., 2017; Hu et al., 2016; Piepgras et al., 1979; van de Flierdt et al., 2016). However, instances where seawater ε_{Nd} deviates from expected water mass mixing do occur (highlighted by black circles in Fig. 1.6), whereby ε_{Nd} evolves through non-mixing (i.e., non-conservative) processes, eluding towards instances of local/regional detrital influence (Wilson et al., 2012; Pearce et al., 2013; Abbott et al., 2015a; Roberts and Piotrowski, 2015; Abbott et al., 2016b; Du et al., 2016; Howe et al., 2017; Jeandel, 2016; Haley et al., 2017; Abbott et al., 2019; Grenier et al., 2013; Lacan and Jeandel, 2005a; Grasse et al., 2012; Tachikawa et al., 2017).

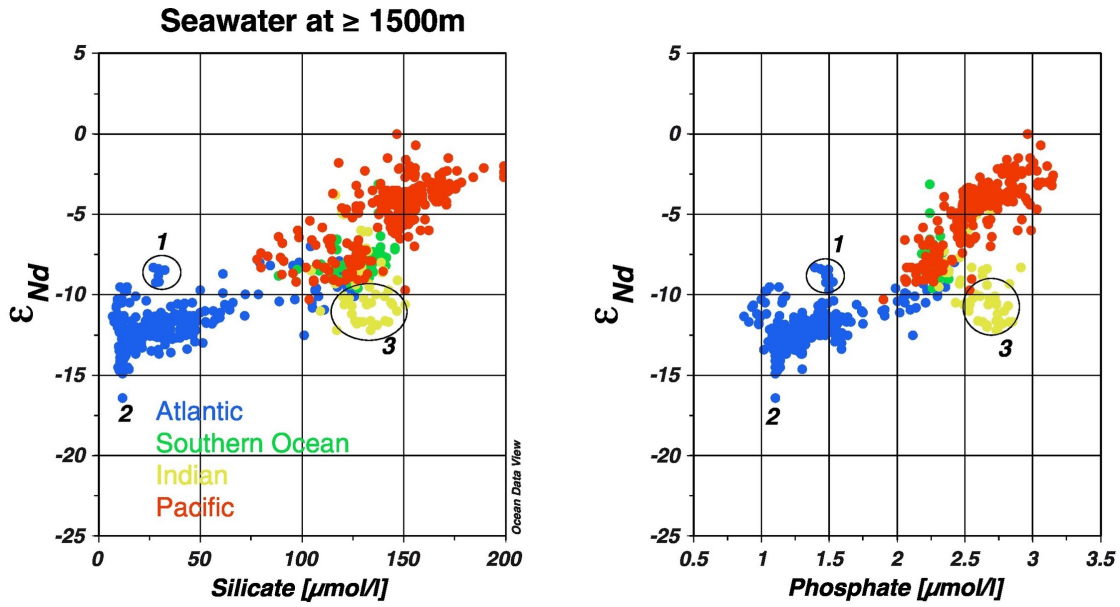

Figure 1.6: Seawater multi-scatter plots showing the relationship between measurements of ε_{Nd} below 1,500 m and hydrography parameters (silicate and phosphate). Colour of filled circles corresponds to different geographical regions. The almost linear relationship of pelagic seawater ε_{Nd} with nutrient hydrography parameters demonstrate the water mass tracer properties of marine Nd isotopes. The numbered black circles show localised areas where seawater ε_{Nd} values are offset from the general trend, here (1) encompasses measurements from the Caribbean Sea, (2) are measurements from Baffin Bay and (3) are measurements from the Bay of Bengal. Figure reprinted from Tachikawa et al. (2017).

The 'Nd paradox' (Goldstein and Hemming, 2003), describes the general decoupling between the apparently conservative behaviour of ε_{Nd} and the non-conservative behaviour of [Nd] (Fig. 1.5), which become more concentrated with increasing depth in the water column and broadly increase along the circulation pathway, suggesting the influence of vertical cycling of Nd via reversible scavenging processes (Bertram and Elderfield, 1993). There is also evidence of intense non-conservative ε_{Nd} processes, concentrated around continental margins, that modify ε_{Nd} without significantly affecting [Nd], acting on local to regional scales, termed 'boundary exchange' (Lacan and Jeandel, 2005a; Arsouze et al., 2009; Grasse et al., 2012; Wilson et al., 2013; Pearce et al., 2013).

More recently, there have been measurements of Nd mobilisation from sediment pore water during early sediment diagenesis (which describes the sum of all processes and transformations that bring about changes in sediment or sedimentary rock subsequent to deposition in water), and suggestions this flux may act to overprint deep water mass end member ε_{Nd} signals (Abbott et al., 2015b; Abbott, 2019; Abbott et al., 2015a; Haley et al., 2017; Du et al., 2016). A benthic flux of Nd to seawater from sediment porewater therefore has the potential to complicate interpretations of water mass mixing from seawater ε_{Nd}, particularly if this flux is not limited by proximity to shallow continental margins (Abbott et al., 2015b; Abbott, 2019; Abbott et al., 2015a; Haley et al., 2017; Du et al., 2016). Under such a scenario, the Nd isotope signal of a water mass may evolve through non-mixing (i.e., non-conservative) processes such as a change in the magnitude and isotope composition of a benthic flux, or a change in the exposure time of bottom water to this flux (which may result with a change in ventilation of a deep water mass) (Abbott et al., 2015a; Haley et al., 2017).

An important implication of a potential benthic control of Nd is that most palaeoceanographic reconstructions discount the possibility of changes in Nd supply that

is not the result of water mass mixing or circulation, treating ε_{Nd} as a fundamentally conservative tracer (Frank, 2002). This assumption may not be valid in locations or during periods where bottom waters are subject to benthic fluxes, for example due to changed weathering regimes (e.g., large inputs of freshly eroded material during periods of deglaciation) or certain environmental conditions (e.g., pH and redox conditions) that would drive elevated fluxes. Moreover, under a benthic flux, authigenic ε_{Nd} records (which are used to reconstruct ocean circulation), may not be exclusively recording seawater signals in certain locations if bottom water ε_{Nd} signals and/or the archives themselves are altered by such a flux (as detailed in the different frameworks for interpreting authigenic ε_{Nd} records in Fig. 1.7) (Abbott et al., 2022; Du et al., 2016; Blaser et al., 2019b). Therefore, more careful evaluations of archived ε_{Nd} signals may be required. However, under a benthic flux driven model of marine Nd cycling, new avenues of applications of marine Nd as a potential ocean kinematic tracer, and as a tracer of continental weathering regimes and climate arise (Abbott et al., 2015a; Haley et al., 2017; Pöppelmeier et al., 2020a, 2022).

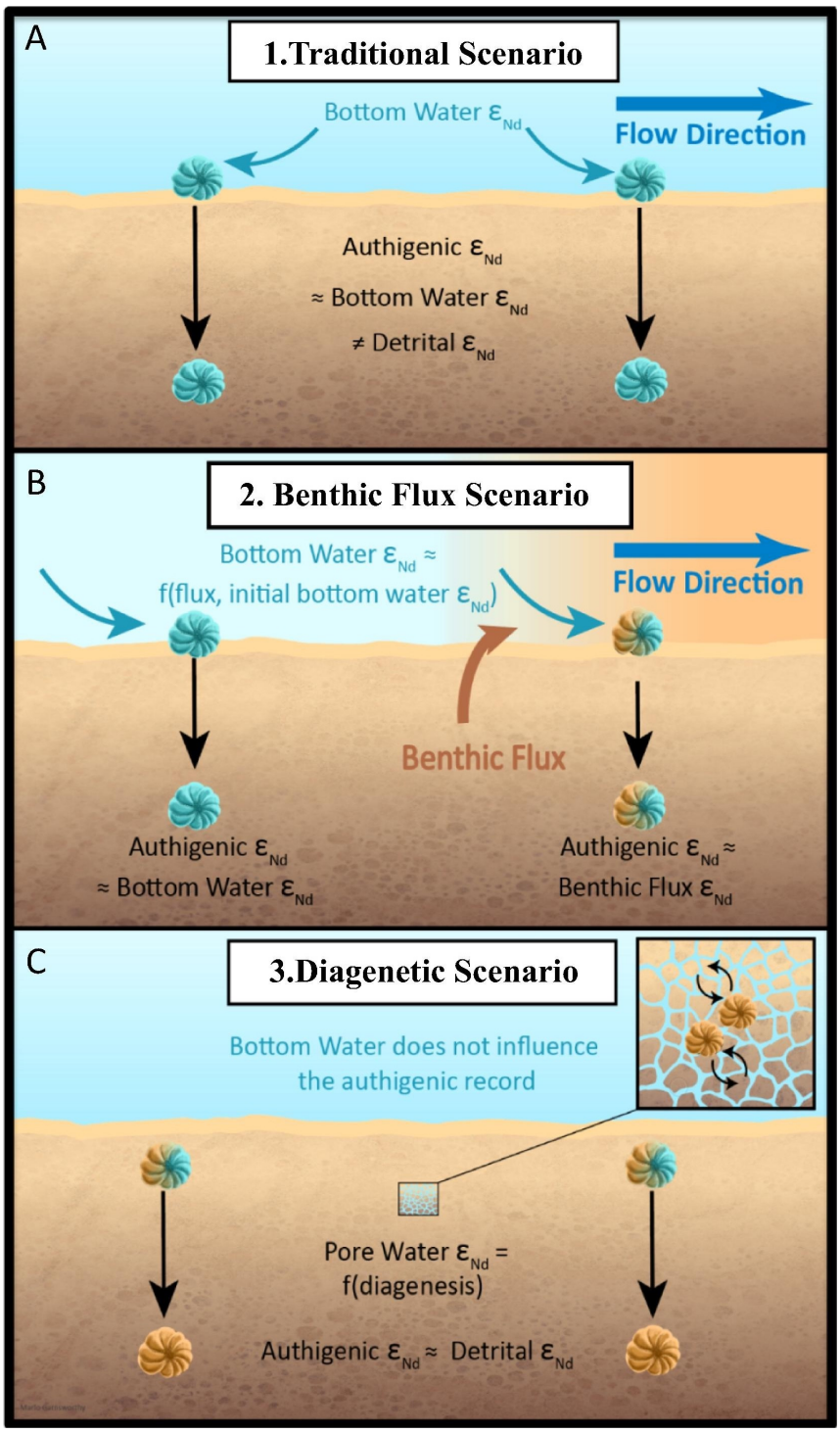

Figure 1.7: Framework for interpreting authigenic ε_{Nd} records, with three end-member scenarios; 1) 'Traditional' Scenario: authigenic ε_{Nd} is strictly a record of bottom water ε_{Nd}, detrital ε_{Nd} has no influence, 2) Benthic Flux Scenario: detrital ε_{Nd} can alter the bottom water ε_{Nd} via a benthic flux, and then the authigenic ε_{Nd} then records that altered bottom water ε_{Nd} (which is a function of the magnitude, exposure and character of a benthic flux), and 3) Diagenetic Scenario: bottom water ε_{Nd} is not preserved in the authigenic ε_{Nd} record which is instead strictly a function of the composition and reactivity of the detrital components, exchanging via pore water. The relative importance of each scenario may vary spatiotemporally. Figure reprinted from Abbott et al. (2022).

Overall, despite a wide acceptance of the water mass tracer properties of ε_{Nd}, universal understanding of the exact mechanisms controlling marine geochemical Nd cycling remains

incomplete; making it hard to define exactly how seawater obtains its Nd isotope signal (Abbott et al., 2015a; van de Flierdt et al., 2016; Tachikawa et al., 2017; Haley et al., 2017). One approach for progressing our understanding of the global marine Nd cycle is to include Nd isotopes in numerical climate models. Isotope enabled ocean models are highly capable of filling in spatiotemporal gaps in both modern and proxy data. Moreover, such models can be used to test assumptions underlying the application of ε_{Nd} as an ocean circulation tracer, and further are suited for exploring emerging hypotheses regarding the influence of certain non-conservative processes (e.g., boundary exchange, benthic flux, and particle scavenging) which may govern marine Nd isotope distributions.

1.1.4 Nd isotopes in numerical climate models

Numerical climate models represent tools designed to investigate and constrain various Earth system processes. Varying substantially in complexity, climate models range from simple conceptual models, designed to study individual processes in the Earth system, to the most sophisticated and current state-of-the-art Earth System Models (ESMs). These ESMs include the representation of biogeochemical cycles, which present important feedback mechanisms in the dynamic response of the Earth and climate system to perturbations (Flato et al., 2013; Shi et al., 2019; Flato, 2011; Anav et al., 2013).

Comprehensive ESMs are thus the best designed models for projecting future climate change throughout the upcoming century under anthropogenic forcings (Flato et al., 2013). However, owing to their complexities, ESMs demand intensive computational resource, rendering them impractical for both large ensembles with perturbed physical parameters (used to investigate physical controls on climate and capture sources of model uncertainty), and for representing long-lived isotopic systems (which require millennia-length simulations) (Shi et al., 2019). Designed more specifically for these types of experiments, a contrasting class of models, known as Earth system Models of Intermediate Complexity (EMICs) exist between the simplest and the most complex climate models. These models have been applied to studies requiring larger (hundred-member) ensembles (Claussen et al., 2002), or for long (multi-millennial) model integrations to investigate slow, millennial scale feedbacks within the Earth system; such as those associated with ice sheet change, stability of ocean circulation, biogeochemistry, and marine sediments (Ganopolski and Rahmstorf, 2001; Flato et al., 2013; Ridgwell et al., 2007; Goosse et al., 2010; Huybrechts et al., 2011). Such EMICs incorporate an almost complete description of all components of the Earth system, but at a cost of a low resolution, reduced dimensionality, or widely idealised and parameterised representations of complex systems.

Low resolution coupled atmosphere-ocean General Circulation Models (AOGCMs) provide a direct line bridging the gap between ESMs and EMICs. This model class is based upon AOGCMs, with parametrisations of physical and dynamical processes almost identical to their parent model, allowing considerable detail in the complexity of Earth system processes to be retained, but capable of running significantly faster due to reduced horizontal and vertical resolution and an increased timestep (Jones, 2003). Examples of low resolution GCMs include the Geophysical Fluid Dynamics Laboratory coupled climate model (GFDL; Dixon et al., 2003), the Flexible Global Ocean-Atmosphere-Land system model (FGOALS; Bao et al., 2010), the low-resolution version of the Community Climate System Model (CCSM3; Yeager et al., 2006), the Commonwealth Scientific and Industrial Research Organisation climate system model (CSIRO Mk3L; Phipps et al., 2011), and the Fast Met Office/U.K. Universities Simulator (FAMOUS GCM; Jones, 2003). These models are advantageous due to their results being directly traceable back to policy relevant sophisticated GCMs, whilst likewise enabling rigorous testing of Earth system processes and for parametric uncertainty quantification (Gregoire et al., 2011; Smith and Gregory, 2009; Gregoire et al., 2015; Smith et al., 2021; Jones et al., 2005).

Although not ordinarily represented in climate models, mostly due to computational

expense, the simulation of marine Nd isotopes can offer insights into aspects of the ocean-climate system. Neodymium isotope enabled models can be used for example to investigate and quantify the processes and fluxes that govern marine ε_{Nd} distributions, establish the ocean circulation tracer properties of ε_{Nd}, and to explore the sensitivity of ε_{Nd} distributions to different biogeochemical cycling and changed weathering regimes. Furthermore, Nd isotope enabled ocean models can be used to diagnose physical model biases by providing information on the pathways and rates of water mass renewal below the surface mixed layer; details which cannot be gained from relying solely on temperature and salinity prognostic variables alone (Broecker and Peng, 1982; England and Maier-Reimer, 2001).

Neodymium isotopes have been previously implemented in numerical climate models (see Table 1.2 for overview and relevant references) and have contributed substantially towards our understanding of the marine Nd cycle. It was initially thought that the predominant lithogenic fluxes of Nd to the ocean were at the surface (aeolian dust and riverine fluxes; Goldstein et al., 1984; Goldstein and Jacobsen, 1987). Earlier modelling studies applying just these surface fluxes reproduced reasonable North Atlantic ε_{Nd} distributions (Bertram and Elderfield, 1993; Tachikawa et al., 1999), yet resulted in an unrealistically high calculated residence time of Nd in seawater on the order of 5,000 years (Bertram and Elderfield, 1993; Jeandel et al., 1995). Tachikawa et al. (2003) applied a simple box model to explore marine Nd budgets, and demonstrated that considering only dust and river surface inputs failed to balance both [Nd] and ε_{Nd} budgets, highlighting a 'missing source' of Nd to seawater that could account for $\approx 90\%$ of the Nd flux to the ocean (Tachikawa et al., 2003). Boundary exchange, which describes strong Nd isotopic interactions between continental margins and water masses through the co-occurrence of sediment dissolution and boundary scavenging, was thereafter suggested as a mechanism to account for this 'missing source'. Following the proposal of boundary exchange processes, realistic global ε_{Nd} distributions were then simulated in a numerical scheme representing boundary exchange as the only Nd source-sink term (Arsouze et al., 2007). Subsequently, boundary exchange along the continental margins has represented the major source of Nd to seawater in more recent global Nd isotope models (Arsouze et al., 2009; Rempfer et al., 2011; Gu et al., 2019).

However, boundary exchange alone cannot explain the measured vertical profiles of [Nd], which are decoupled from ε_{Nd}, and broadly increase with depth (i.e., the 'Nd paradox': Goldstein and Hemming, 2003). Siddall et al. (2008b) first addressed numerically the hypothesis that the 'Nd paradox' can be explained by a combination of lateral advection and reversible scavenging (i.e., where the element is scavenged onto sinking particles at the surface and is subsequently remineralised in the deep ocean) by applying the reversible scavenging model pioneered by Bacon and Anderson (1982) to Nd cycling. Their findings demonstrated that reversible scavenging could drive the increase of [Nd] with depth, but still allow ε_{Nd} to act as an effective water mass tracer. Yet the use of over-simplified fixed surface boundary conditions in the model by Siddall et al. (2008b) limited what could be determined about the full marine Nd cycle.

Amid a recent transition towards increased complexity, both in terms of the type of model used (shifting from simplified box-models to full complexity ocean GCMs) and the increasingly detailed descriptions of the marine Nd cycle, the most sophisticated Nd isotope enabled models now explicitly simulate each Nd isotope (^{143}Nd and ^{144}Nd). This representation of both individual Nd isotopes allows for a simultaneous representation of both [Nd] and ε_{Nd}, facilitating a more direct representation of the major sources, sinks and cycling believed to govern marine ε_{Nd} (Fig. 1.8), and the exploration of its sensitivity to physical ocean circulation.

Table 1.2: Overview of existing Nd modelling studies

Model	Resolution	Levels	Nd Sources (g yr^{-1})				Residence time	Isotope model	Reference
			Dust source	Riverine source	Sediment source	Total Nd source			
Box models									
Based on model described in Keir (1988)	7 boxes	NA	8.0×10^7	NA	NA	8.0×10^7	2900	ε_{Nd} only	Bertram and Elderfield (1993)
PANDORA	10 boxes	NA	4.0×10^8	5.0×10^8	8.1×10^9	9.0×10^9	490	ε_{Nd} only	Tachikawa et al. (2003)
Based on model described in Talley (2013)	4 boxes	NA	1.2×10^8	4.87×10^8	1.12×10^{10}	1.18×10^{10}	350	ε_{Nd} only	Du et al. (2020)
Steady state									
MITgcm2.8	2.8° by 2.8°	15	No explicit Nd model	NA	NA	NA	NA	ε_{Nd} only	Jones et al. (2008)
MITgcm2.8	2.8° by 2.8°	15	Surface boundary condition	NA	NA	NA	500	ε_{Nd} only	Siddall et al. (2008b)
Boundary propagation models									
NA	4° by 4°	33	No explicit Nd model	NA	NA	NA	NA	ε_{Nd} only	Du et al. (2020)
GNOMv1.0 embedded into OCIM v2.0	2° by 2°	24	3.44×10^9	1.35×10^9	4.59×10^9	9.47×10^9	440	[Nd], ε_{Nd}	Pasquier et al. (2021)
General circulation models									
ORCA2	2° by 2°	30	NA	NA	NA	NA	NA	ε_{Nd} only	Arsouze et al. (2007)
ORCA2	2° by 2°	31	1.0E8	2.6×10^8	1.1×10^{10}	1.14×10^{10}	360	^{143}Nd, ^{144}Nd	Arsouze et al. (2009)
ORCA025	0.25° by 0.25°	46	NA	NA	NA	NA	NA	ε_{Nd} only	Arsouze et al. (2010)
Bern3D	36 by 36 grids	32	2.6×10^8	3.4×10^8	5.5×10^9	6.1×10^9	700	^{43}Nd, ^{144}Nd	Rempfer et al. (2011)
POP2	3° by 3°	60	2.1×10^8	1.3×10^9	4.0×10^9	5.51×10^9	785	^{43}Nd, ^{144}Nd	Gu et al. (2019)
Bern3D	36 by 36 grids	32	5.0×10^8	1.77×10^9	3.3×10^9	5.5×10^9	690	^{43}Nd, ^{144}Nd	Pöppelmeier et al. (2020a)
COCO	120 by 128 grids	40	NA	NA	NA	NA	400	[Nd] only	Oka et al. (2021)

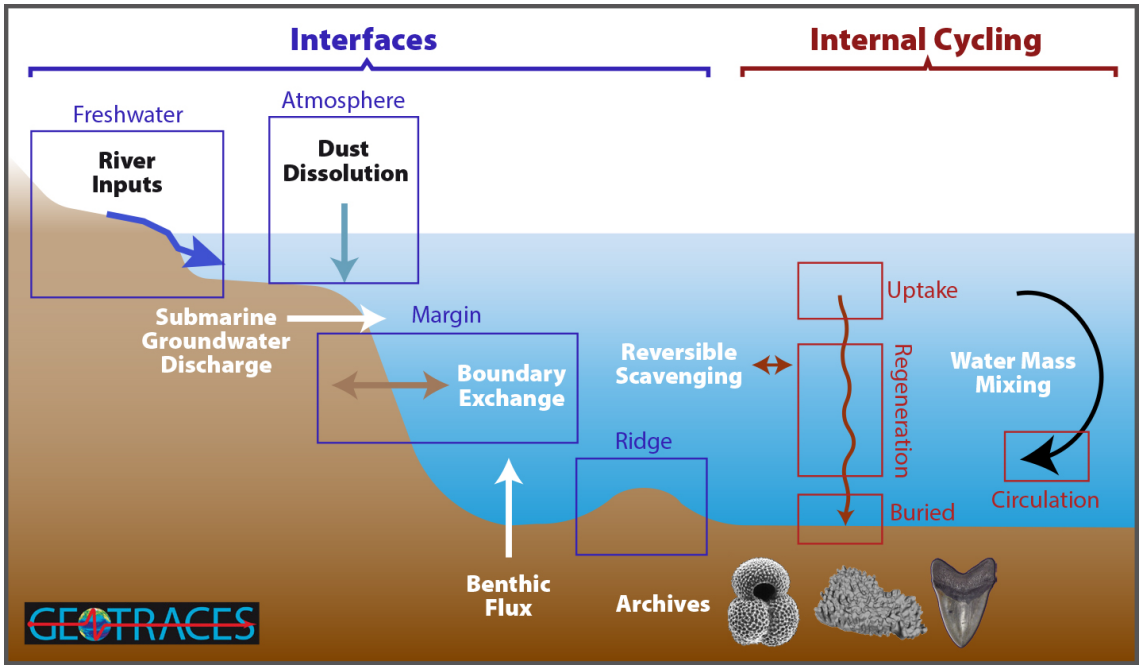

Figure 1.8: A qualitative summary of the major Nd sources and processes believed to govern marine Nd concentrations and isotope distributions. Figure based on data from GEOTRACES (`http://www.geotraces.org/`) and reprinted from Tachikawa et al. (2020) to summarise the oceanic Nd cycle. The relative importance of the various sources/sinks and internal cycling remains unknown.

Arsouze et al. (2009) first applied a fully prognostic coupled dynamic and biogeochemical model to simulate [Nd] and ε_{Nd}, representing individual sources of Nd to seawater from dust deposition, dissolved riverine input, boundary exchange, and a sink of Nd via reversible scavenging and sedimentation. In this study, boundary exchange from the continental margins was found to represent the major source of Nd to seawater (contributing 95% of the total source). However, the high computational cost of the model, alongside time constraints, limited the number of sensitivity tests and model optimisation that could be achieved in this study. Rempfer et al. (2011) thereby extended upon this work, undertaking a more detailed investigation of the marine Nd cycle using a coarse resolution intermediate complexity model (Bern3D ocean model). By performing extensive and systematic sensitivity experiments (running over 250 simulations), the authors here were able to calibrate the scheme and explore the sensitivity of [Nd] and ε_{Nd} to the parameterisation of different sources and sinks of Nd. This scheme was then closely followed by the implementation of Nd isotopes into the ocean component of a more comprehensive Earth System Model (ESM, specifically the Community Earth System Model: CESM1.3) by Gu et al. (2019). This more complex model, which accounts for different deep-water source regions, facilitated idealised hosing experiments used to explore the expected effects of ocean circulation changes on end member ε_{Nd} signals.

Following emerging suggestions that a benthic flux of Nd from sedimentary pore fluids may pose a new, potentially major, seafloor-wide source of Nd to seawater, simple box models have since been employed to investigate, to a first order, the non-conservative effects from such a flux (Du et al., 2016, 2018, 2020; Haley et al., 2017; Pöppelmeier et al., 2020b). Findings from these studies suggest a benthic flux can overprint the ε_{Nd} signal of a deep-water mass, the extent of which being linked to benthic flux exposure time and the difference between the ε_{Nd} of the benthic flux and bottom water. However, these simplistic models lack both a detailed description of the marine Nd cycle and of physical ocean circulation and climate interactions, which are important factors required to determine precisely how, and under what physical/environmental conditions, the benthic flux may govern ε_{Nd} distributions. Commencing more detailed investigations of the benthic flux hypothesis, Pöppelmeier et al. (2021a) updated the Nd isotope scheme in the Bern3D model, hereby removing the depth limitation of the boundary exchange (previously 3 km) to represent a constant seafloor-wide benthic flux. The scheme was then applied to explore non-conservative Nd isotope behaviour under different ocean circulation regimes (Pöppelmeier et al., 2022). Here, the authors demonstrated although the benthic flux was a major source of Nd to seawater, alone it cannot explain all non-conservative marine Nd isotope behaviour, highlighting the importance of downward vertical fluxes via reversible scavenging. Nonetheless, the low horizontal resolution of the intermediate complexity model limits a full resolution of key circulation patterns such as distinct deep-water formation in the Labrador and in the Nordic Seas, inhibiting the capabilities of the scheme to fully capture and explore water mass end member ε_{Nd} distributions.

In closing, despite considerable efforts to explicitly constrain and describe seawater Nd budgets, outstanding questions remain. Moreover, the demand for higher computational power required by the increasing sophistication and complexity of Nd isotope schemes has meant only a handful of studies performed optimisation for their input parameters within their relevant host ocean GCM models (e.g. in the ocean components of the Bern3D model; Pöppelmeier et al., 2020b; Rempfer et al., 2011, and CESM1; Gu et al. 2019). Such schemes applied resource intensive systematic tuning (i.e., running over 100 simulations), using suboptimal space filling design methodologies that may also lead to inefficient exploration of the input space. In addition, some of these calibrated models were restricted by previous assumptions regarding the dominating processes involved in the marine Nd cycle, which limited the development of appropriate model boundary conditions – notably here, an assumption that particle-seawater interaction is constrained to shallow continental margins.

A proliferation of recent investigations into particle-seawater Nd interactions in seawater (e.g., Abbott et al., 2019, 2015a,b; Paffrath et al., 2021; Rahlf et al., 2020, 2021; Rousseau et al., 2015; Stichel et al., 2020; Wang et al., 2021), alongside an ever-growing body of high-quality and highly-resolved seawater measurements of [Nd] and ε_{Nd}, now presents an opportunity to re-evaluate, revise and explore constraints on the marine Nd cycle. Hereby allowing for more detailed investigations to challenge the contemporary paradigms regarding the modern marine Nd cycle.

At present there is a gap in the toolkit for modelling the marine Nd cycle between the class of high complexity, state-of-the-art ESMs (e.g., Gu et al., 2019) and the more efficient intermediate complexity models (e.g., Rempfer et al., 2011; Pöppelmeier et al., 2020a). To bridge this gap, there is a need for a model with the full complexity of an Atmosphere-Ocean General Circulation Model (AOGCM), allowing the exploration of how Nd isotopes vary under changing climate conditions (including extensive palaeoceanographic applications), that is also capable of running very quickly to facilitate efficient parameter space exploration, performance optimisation and long integrations.

1.2 Research aim and overall approach

The overarching aim of this thesis is:

To investigate and constrain the global marine Nd cycle within a fast, full complexity general circulation model, and apply uncertainty quantification techniques to facilitate parameter space exploration and calibration

To address this aim, I present the first implementation of marine Nd isotopes (^{143}Nd and ^{144}Nd) into the UK Met Office Unified Model version 4.5 (UM4.5; Valdes et al., 2017), revisiting and updating the sources, sinks and transformation of this tracer in line with increased measurements and current findings relating to the global marine Nd cycle. Aeolian dust fluxes, riverine inputs, and dissolution of seafloor sediment (i.e., boundary exchange and benthic flux) represent the three major simulated sources of Nd to seawater. Internal vertical cycling and removal of Nd from the ocean is simulated via reversible scavenging onto sinking particles and sedimentation. The Nd isotope scheme is evaluated against modern measurements of Nd concentration and isotope distributions, and the optimised scheme is applied to explore and constrain the global marine Nd cycle.

1.2.1 Choice of model

Chapters 3 and 4 of this thesis use the Fast Met Office/U.K. Universities Simulator (FAMOUS; Jones et al., 2005; Smith et al., 2008; Williams et al., 2013; Smith, 2012), a fast coupled atmosphere-ocean GCM, which is a lower resolution version of the HadCM3 climate model (Gordon et al., 2000; Pope et al., 2000). Both FAMOUS and its parent model HadCM3 are configurations of version 4.5 of the UK Met Office Unified Model (UM4.5: Gordon et al., 2000; Valdes et al., 2017). The atmospheric model is based on quasi-hydrostatic primitive equations, with a horizontal resolution of 5° latitude by 7.5° longitude and has 11 vertical levels on a hybrid sigma-pressure coordinate system, operating on a 1-hour timestep. The rigid-lid ocean model is based upon the widely used Bryan and Cox code (Bryan, 1969; Cox, 1984) and has twice the resolution of the atmosphere, with a horizontal resolution of 2.5° latitude by 3.75° longitude and 20 vertical levels, spaced unequally in thickness from 10 m at the near-surface ocean to over 600 m at deep ocean depths, operating on a 12-hour timestep. The atmosphere and the ocean are coupled once per day, and due to using approximately half the horizontal resolution of HadCM3 alongside an increased timestep, FAMOUS requires around one tenth of the computational resources. Land processes are modelled with either static or dynamic vegetation via the Met Office Surface Exchange Scheme MOSES1 and MOSES2 land

surface scheme (Cox et al., 1999; Essery et al., 2001, 2003).

FAMOUS has been tuned and optimised through various procedures to reproduce the equilibrium climate and climate sensitivity of HadCM3, and to further reduce the original northern high latitude cold bias (Jones et al., 2005; Smith et al., 2008; Gregoire et al., 2011; Williams et al., 2013). Despite its lower resolution, the resultant climatology in FAMOUS performs much greater than expected, yielding a good representation of large-scale features of the climate-system over both terrestrial and marine realms (Jones et al., 2005; Valdes et al., 2017). Notably here the performance of the atmosphere-ocean components, common to both HadCM3 and FAMOUS, and in regard to large-scale climate measures, place them within comparable accuracy of the best performing and policy relevant climate models (e.g. CMIP5 models) (Williams et al., 2013; Valdes et al., 2017). Furthermore, ocean circulation in FAMOUS has simulated maximum Atlantic Meridional Overturning (AMOC) stream functions of 12-17 Sv (Valdes et al., 2017), which are comparable to modern observations of 14-19 Sv (Talley, 2013; Smeed et al., 2014). When run under a full suite of oceanic tracers, FAMOUS is capable of simulating roughly 400 model years per wall clock day or more, more than five times the speed of HadCM3.

The combination of speed and complexity inherent to FAMOUS makes it an invaluable tool that has been widely applied to addressing major research questions regarding Earth system interactions, alongside tackling parametric uncertainty, and forming the main motivation for its use within this thesis. For example, FAMOUS has been successfully applied to simulating the first transient simulation of the last glacial cycle (120 ka) (Smith and Gregory, 2012), the response of the Earth system to the relative roles of greenhouse gas concentrations and orbital forcing during the last deglaciation (21-7 ka) (Gregoire et al., 2016) and to investigate meltwater fluxes (Smith and Gregory, 2009), alongside studies coupled to ice sheet models (Gregory et al., 2012; Smith et al., 2021). Further applications of FAMOUS include investigations of deeper time climate using perturbed parameter ensembles (Early Eocene; Sagoo et al., 2013), studying extra-terrestrial climate impacts (Joshi et al., 2017), assessing the stability of ocean circulation under salinity drifts (Dentith et al., 2019), large initial condition ensembles (Hawkins et al., 2016), and, following the implementation of carbon isotopes into the ocean component of FAMOUS, exploring marine biogeochemical cycles relevant for the marine carbon cycle (Dentith et al., 2020).

Thus, FAMOUS is an ideal and well-suited choice for model development and optimisation involving numerous simulations which require full multi-millennial integrations of the deep ocean circulation. FAMOUS provides an optimal tool for answering outstanding questions and exploring new hypotheses regarding the global marine Nd cycle. Furthermore, the new Nd isotope scheme will be directly transferrable into the higher resolution HadCM3 model for future scientific applications.

1.3 Research questions

The overall aim of this thesis has been broken down to form three research questions which are investigated throughout the work presented in this thesis:

RQ1) How accurately can modern Nd isotope distributions be simulated in a fast coupled atmosphere-ocean general circulation model?

RQ2) What are the limitations of the Nd isotope scheme, and do they challenge the general assumptions underpinning the interpretive framework of marine Nd cycling and its fundamental applications as a robust ocean circulation tracer?

RQ3) To what extent can a seafloor-wide benthic flux explain non-conservative behaviour of Nd isotopes under a global model of marine Nd cycling, and to what extent can global

bulk sedimentary ε_{Nd} distributions represent a labile sedimentary flux to seawater?

1.4 Research objectives

To investigate the research questions identified above (Sect. 1.3), I have identified five research objectives (Table 1.3) to be met by my thesis research chapters; Chapters 2, 3, and 4.

Table 1.3: Research objectives and the chapters in which they are applied

Research objectives	Thesis chapter(s)
OBJ1) Estimate the bulk ε_{Nd} distributions of seafloor detrital sediment across the continental margins and seafloor	2
OBJ2) Implement Nd isotopes into a fast coupled atmosphere-ocean general circulation model, revisiting and updating key source and sink parameters	3
OBJ3) Explore the sensitivity of simulated Nd isotope distributions to different components of the marine Nd cycle	3, 4
OBJ4) Statistically optimise the Nd isotope scheme to best represent the modern marine Nd cycle	4
OBJ5) Investigate the spatial extent and preferential mobilisation of certain reactive sediment components from a benthic flux under a global model of the marine Nd cycle	4

1.4.1 OBJ1: Estimate the bulk ε_{Nd} distributions of seafloor detrital sediment across the continental margins and seafloor

1.4.1.1 Scientific background

In response to increased evidence of intense dissolved/particulate exchange of Nd occurring along the continental margins (i.e. boundary exchange), and suggestions this process is important for governing marine ε_{Nd} distributions, Jeandel et al. (2007) produced a map characterising the global ε_{Nd} signal of the continental margins. The map incorporated a compilation of ≈ 200 published sedimentary ε_{Nd} measurements, and pioneered numerous investigations within numerical schemes that applied the ε_{Nd} distributions as boundary conditions to explore the role of boundary exchange within the marine Nd cycle (e.g., Arsouze et al., 2009, 2007; Gu et al., 2019; Rempfer et al., 2011). However, data limitations when the map was produced meant that broad estimates had to be made when characterising the ε_{Nd} signal of the continental margins, especially around Alaska, northern Eurasia, Pakistan, Cameroon, Somalia, and Brazil. Moreover, this data product is now 15 years old, and since its creation, there has been a substantial increase in the amount and spatial extent of published detrital ε_{Nd} measurements. As such an updated synthesis of all published sedimentary ε_{Nd} to date is needed.

Furthermore, emerging hypotheses that suggest a globally widespread abyssal benthic flux of Nd from seafloor sediment to seawater may govern the marine ε_{Nd} cycle, brings forth the requirement for updated global maps of sedimentary ε_{Nd} (Haley et al., 2017; Abbott et al., 2015b). Now, and to facilitate the exploration of a benthic Nd flux within numerical models, the ε_{Nd} characterisation of the sediment needs to extend across the entire seafloor. Such updated maps would provide the crucial model pre-requisites required to determine whether a shift towards a benthic flux driven model of the marine Nd cycle can represent Nd isotope distributions, and what this means for the water mass tracer properties of ε_{Nd}.

Ideally pore water ε_{Nd} measurements, which record most directly the labile Nd from detrital material into pore waters, would be most representative of Nd interactions across

the sediment-water interface (Du et al., 2020; Abbott et al., 2015a). However, to date these measurements are very spatially limited, with just three published measurements from sites in the North Pacific on the continental margins (Abbott et al., 2015a). Published detrital sediment ε_{Nd} measurements, which are both a lot more abundant and have a greater spatial coverage across the global seafloor, therefore provide the current most practical solution to this global ocean pore water data sparsity.

1.4.1.2 Research approach

Chapter 2 provides a new extensive and up-to-date compilation of over 5,100 terrestrial and marine sediment ε_{Nd} measurements, synthesising both published and new data. Global maps characterising the ε_{Nd} signal of (1) all outcropping rock surrounding the oceans and the continental margins, and (2) abyssal seafloor sediments were produced. Here, the updated database was first filtered to include only Holocene measurements (specifically 11.7 ka to present), and then these discrete points were interpolated to create spatially continuous distributions. The continental margin and seafloor ε_{Nd} maps were then combined to produce high resolution ($0.5° \times 0.5°$) spatially continuous global maps of ε_{Nd} across the entire sediment-water interface.

1.4.2 OBJ2: Implement Nd isotopes into a fast coupled atmosphere-ocean general circulation model, revisiting and updating key source and sink parameters

1.4.2.1 Scientific background

In the early 2000s, there was a concentrated wave of Nd isotope numerical modelling studies which began efforts to quantitively constrain the processes governing the global marine Nd cycle (Tachikawa et al., 2003; Siddall et al., 2008a; Arsouze et al., 2009; Rempfer et al., 2011). However, in light of the recently emerging hypotheses surrounding the dominating mechanisms involved in marine Nd cycling (Abbott et al., 2015a,b; Haley et al., 2017; Rousseau et al., 2015; Stichel et al., 2020; Wang et al., 2021; Rahlf et al., 2020, 2021), alongside a substantial increase in marine ε_{Nd} measurements (GEOTRACES Intermediate Data Product Group, 2021; Tachikawa et al., 2017; van de Flierdt et al., 2016), it is now time to revisit and revise a number of outdated critical parameters (e.g., Nd source functions and distributions and water column processes). By exploring fundamental perceptions used to describe marine Nd isotope distributions, we can develop robust constraints on how, and where, they translate to ocean circulation properties.

1.4.2.2 Research approach

New code to implement Nd isotopes (^{143}Nd and ^{144}Nd) as optional passive tracers into the ocean component of the fast FAMOUS GCM was developed and is presented in Chapter 3, representing three global sources of Nd into seawater: aeolian dust flux, dissolved riverine input and dissolution of seafloor sediment, and represents internal cycling and sedimentation processes via reversible scavenging. The Nd isotope scheme starts from previous implementations (Rempfer et al., 2011; Gu et al., 2019; Pöppelmeier et al., 2020a; Arsouze et al., 2009; Siddall et al., 2008b), but revisits and updates all the model boundary conditions and code in line with increased measurements and recent findings relating to global marine Nd cycling (Blanchet, 2019; Robinson et al., 2021; Haley et al., 2017; Siddall et al., 2008b; Arsouze et al., 2009).

The scheme is validated against the most up-to-date global compilation of seawater measurements of [Nd] and ε_{Nd} to date (Osborne et al., 2015, 2017; GEOTRACES Intermediate Data Product Group, 2021), with a focus on describing the ability of the model to represent appropriate global Nd inventories and key spatial and vertical distributions across ocean basins.

1.4.3 OBJ3: Explore the sensitivity of simulated Nd isotope distributions to different components of the marine Nd cycle

1.4.3.1 Scientific background

Of the major input pathways and cycling of marine Nd in the global ocean (Fig. 1.8), the seafloor sedimentary flux and reversible scavenging represent two major and largely unconstrained non-conservative processes believed to govern marine Nd isotope distributions (Haley et al., 2017). Furthermore, they challenge the simplified conservative assumptions of marine Nd cycling in the open ocean. In detail, a seafloor sedimentary flux, refers to a multitude of 'hard to disentangle' processes occurring across the sediment-water interface, encompassing boundary exchange (Lacan and Jeandel, 2005a), submarine groundwater discharge (Johannesson and Burdige, 2007), and a benthic flux released from pore waters (Abbott et al., 2015a), presenting a direct major deep ocean source of Nd. On the other hand, reversible scavenging refers to absorption/incorporation and desorption/dissolution of Nd onto particle surfaces throughout the water column, which transfers Nd internally into deeper water masses (Bacon and Anderson, 1982; Siddall et al., 2008b). Both these processes, and how they influence marine ε_{Nd} are a hot topic of debate within the community, yet suffer from limited process-based observations (Abbott et al., 2015a; Abbott, 2019; Stichel et al., 2020; Wang et al., 2021), and a lack of consensus regarding complete process descriptions (Homoky et al., 2016). As such, questions remain regarding how much, where, and under what environmental conditions they govern seawater ε_{Nd} distributions, and ultimately what this means for the interpretation of marine ε_{Nd} and its archives as an oceanographic tracer.

Nd isotope enabled ocean models, which explicitly attempt to describe the individual sources and sinks of Nd, are suited to exploring the relative importance of different processes understood to govern the marine Nd cycle. By better understanding model behaviour and performance of isotope enabled schemes, we can aim to determine more completely the locations/conditions where non-conservative processes, such as sedimentary Nd fluxes and reversible scavenging may or may not govern marine ε_{Nd} over water mass mixing.

1.4.3.2 Research approach

Sensitivity experiments were performed using the Nd isotope scheme in FAMOUS in Chapter 3 to isolate and explore the physical effects of systematically varying individual model parameters that represent: (1) the efficiency of reversible scavenging and sedimentation and, (2) the magnitude of the sedimentary flux to seawater. Simulated Nd concentration and isotope distributions were assessed between the sensitivity experiments and against modern seawater measurements (Osborne et al., 2015, 2017; GEOTRACES Intermediate Data Product Group, 2021), exploring how model sensitivity to different parameter values influenced the ability of the model to produce spatial and vertical distributions consistent with the observational data. The results from the sensitivity analysis were contextualised through comparisons to previous Nd isotope schemes and their reported model sensitivities (Rempfer et al., 2011; Pöppelmeier et al., 2020a; Arsouze et al., 2009; Siddall et al., 2008b). Finally, how, and where these parameters can govern marine [Nd] and ε_{Nd} distributions was explored.

In Chapter 4, further sensitivity simulations were performed to explore the spatial extent and preferential mobilisation of certain reactive sediment components under a seafloor-wide sediment source of Nd to seawater (described in detail in OBJ5).

1.4.4 Statistically optimise the Nd isotope scheme to best represent the modern marine Nd cycle

1.4.4.1 Scientific background

The application of Nd isotope enabled ocean models to describe and investigate complex geochemical processes governing its cycling introduces several sources of uncertainty. Despite a general consensus surrounding the broad qualitative descriptions of the major source/sink pathways (Fig. 1.8), a full quantitative model of the marine Nd cycle has yet to be fully established, and hypotheses regarding the dominant processes involved are still emerging (e.g., Abbott et al., 2015a, 2019; Du et al., 2020; Haley et al., 2017, 2021; Jeandel, 2016; Johannesson and Burdige, 2007; Rousseau et al., 2015; Siddall et al., 2008b).

Furthermore, due to model resolution combined with incomplete process knowledge, the representation of different Nd source and sinks in ocean models requires parameterisation (Rempfer et al., 2011; Siddall et al., 2008b; Arsouze et al., 2009; Gu et al., 2019; Pöppelmeier et al., 2020a, 2022). Model parametric uncertainty requires detailed exploration before a new scheme can be confidently utilised for scientific investigation. Moreover, without sufficient exploration of parametric uncertainty, it is not possible to determine if model discrepancy with observations is due to limitations of the scheme or suboptimal tuning.

To date only a few Nd isotope schemes have attempted to systematically optimise their input parameters within their relevant host GCMs in order to best represent modern Nd isotope distributions (e.g. in the ocean components of the Bern3D model; Pöppelmeier et al., 2020b; Rempfer et al., 2011, and CESM1; Gu et al. 2019). Moreover, due to the different architecture and resolution of ocean models hosting Nd isotope schemes, coupled with the various approaches and assumptions applied to represent the sources and sinks of marine Nd (e.g., different imposed boundary conditions, Nd source/sink assumptions), the optimised parameter values for one model will not necessarily represent the optimum parameters for another.

Statistical surrogate models, also known as emulators, have been developed to overcome the demand for time and computational resources necessary for the optimisation of complex numerical models like isotope enabled GCMs. Gaussian Process (GP) emulators describe a stochastic representation of computer code which facilitates a fast prediction of the model response to inputs (model parameters) and a probabilistic quantification of the uncertainty on that prediction (Rasmussen and Williams, 2006; Astfalck et al., 2019). This makes them valuable, flexible, and analytically traceable tools, especially when used with maximised and composite parameter space filling designs that effectively explore model parameter space for model calibration (Williamson, 2015).

To date no Nd isotope scheme has applied a GP emulator to effectively explore the uncertainty and subsequently optimise their key parameter values to best represent the modern marine Nd cycle within a fast full complexity GCM. The benefits from this include improved constraints on marine Nd budgets, the disentangling of key non-conservative processes, and how they govern marine Nd isotope distributions, particularly in light of the recently hypothesised benthic flux driven model of marine Nd cycling (Haley et al., 2017; Abbott et al., 2015a, 2019; Du et al., 2020). Additionally, limitations which cannot be resolved through parameter optimisation can help guide community focus towards resolving certain assumptions which underpin the interpretive framework of marine Nd cycling through more detailed investigations and measurements.

1.4.4.2 Research approach

To statistically optimise the Nd isotope scheme in FAMOUS to best represent the modern marine Nd cycle, a GP emulator was utilised in Chapter 4 to examine the not-ruled-out-yet parameter space of three key previously unconstrained parameters detailing: (1) the

reversible scavenging efficiency, (2) the magnitude of the sedimentary flux to seawater and, (3) a riverine scaling accounting for the additional release of Nd from river particulates.

A multi-wave ensemble approach comprising 23 simulations was applied to the investigation, and combinations of parameter values were selected by applying an effective space filling design methodology (Williamson, 2015). An exploration of where the parameters dominated the simulated variability in model output of global Nd inventory, residence time and model fit to measurements of both Nd concentration and isotope distributions was undertaken. Following the uncertainty investigation, we applied an updated GP emulator to determine the parameter combinations for an optimised reference simulation, based upon minimising a loss function used to define model skill in representing measurements of marine [Nd] and ε_{Nd} (Osborne et al., 2015, 2017; GEOTRACES Intermediate Data Product Group, 2021). The optimised simulation was then assessed in detail against modern seawater measurements to explore how the calibrated scheme captures the global distributions and key features of the modern marine Nd cycle, including where distributions are representative of distinct water mass ε_{Nd} properties.

1.4.5 OBJ5: Investigate the spatial extent and preferential mobilisation of certain reactive sediment components from a benthic flux under a global model of the marine Nd cycle

1.4.5.1 Scientific background

The distinct labelling of seawater ε_{Nd} by lithogenic Nd inputs forms its foundations as an ocean circulation tracer (Goldstein and Hemming, 2003; Frank, 2002). Under a benthic flux driven model of marine Nd cycling, the global distribution of mobile seafloor sedimentary Nd phases effectively sets the 'blueprint' for seawater ε_{Nd}, which is then redistributed via ocean circulation (Robinson et al., 2021; Abbott et al., 2019; Du et al., 2020; Haley et al., 2017). Yet, due to an incomplete understanding of the how these elements fractionate during dissolution (Pearce et al., 2013), there remains no detailed mechanistic model of the sedimentary Nd source to seawater.

Preferential release of Nd from minor 'reactive' components of the bulk sediment have been observed both in seawater and in the laboratory (Wilson et al., 2013; Pearce et al., 2013; Jeandel and Oelkers, 2015; Abbott et al., 2016b; Rousseau et al., 2015; Elmore et al., 2011). In some instances this could result in the pore water ε_{Nd} signal which is interacting with seawater being noticeably different to the bulk sediment signal (Abbott et al., 2015a; Wilson et al., 2013; Du et al., 2016). To better understand the mobile sedimentary Nd phases that could be interacting with seawater, substantial and detailed further analysis of global sediment compositions, inputs, transport history, ageing, mineral chemistry, local pore water chemistry and redox state are necessary, requiring a full community effort (Du et al., 2020).

Furthermore, it remains unknown whether the chemical transfer of Nd across the sediment-water interface occurs primarily across the continental margins (proximal to substantial influxes of distinct and poorly chemically weathered lithogenic sediment, with high eddy kinetic energy, and high detrital and biogenic particle concentrations that drive rapid particle-seawater exchange reactions: Jeandel 2016; Jeandel and Oelkers 2015; Lacan and Jeandel 2005a; Rousseau et al. 2015; Tachikawa et al. 2003), or concentrated across the remote abyssal seafloor (characterised by fine grained sediment with high sediment reactivities and long term benthic flux exposures: Abbott 2019; Abbott et al. 2019, 2015a; Du et al. 2016).

Recent investigations using box models and EMICs are now beginning to explore the non-conservative effect of a benthic flux under a global model of marine Nd cycling on seawater and authigenic ε_{Nd} (Pöppelmeier et al., 2020a, 2022; Pasquier et al., 2021; Du et al., 2020; Abbott et al., 2015a, 2022; Du et al., 2016, 2018). Understanding the response

and sensitivity of seawater ε_{Nd} to different mobile sedimentary Nd isotope distributions using a sophisticated fast GCM can build upon these latest efforts, and further seek to globally contextualise where and under what conditions seawater ε_{Nd} is most sensitive to a benthic flux. Accordingly, exploring regions where simulated seawater ε_{Nd} is most sensitive to modified benthic fluxes can result in a better focus of future studies towards regions where more constraints on the benthic flux are required, and alternatively where fully resolving a benthic flux may not be important for describing seawater ε_{Nd}.

1.4.5.2 Research approach

Quasi-idealised sensitivity studies using the optimised reference Nd isotope simulation in FAMOUS are applied in Chapter 4 to test three different global seafloor sediment ε_{Nd} distributions which are applied as model boundary conditions for the simulated sediment Nd flux to seawater. The first mobile sediment map represents the estimated bulk sediment ε_{Nd} distributions of the continental margins and seafloor as presented in Chapter 2. The subsequent two maps impose modifications of increasing magnitude to the soluble ε_{Nd} from localised regions in the Pacific and North Atlantic, herby exploring where more extreme and highly reactive sediment phases relative to the bulk sediment may be driving global sediment-seawater interactions under a benthic flux model of marine Nd cycling. A final sensitivity experiment explores the response of seawater ε_{Nd} under a continental margin constrained versus a seafloor-wide benthic flux. Simulated ε_{Nd} across ocean basins and depths are analysed between the sensitivity simulations and against modern seawater measurements (Osborne et al., 2015, 2017; GEOTRACES Intermediate Data Product Group, 2021).

1.5 Thesis structure

The subsequent three results chapters form the main body of this thesis (Chapters 2, 3 and 4). They are composed of journal manuscripts at different stages of publication and have either already been published (Chapter 2; Robinson et al. (2021)) or have been submitted to peer-reviewed journals (Chapter 3; Robinson et al. (2022a)) and (Chapter 4; Robinson et al. (2022b)). The results chapters tackle the five research objectives of the thesis (Sect. 1.4) and are ultimately used to answer the three research questions (Sect. 1.3). The research questions transpose across all the results chapters (Chapters 2, 3 and 4) and are addressed in detail in the conclusions chapter (Chapter 5).

Chapter 2/Robinson et al. (2021), *Global continental and marine detrital ε_{Nd}: An updated compilation for use in understanding marine Nd cycling, addresses* OBJ1. This chapter presents an extensive global compilation of publised and new sedimentary Nd isotopic measurements, used to construct gridded global maps characterising the bulk Nd isotope distibutions across the entire sediment-ocean interface. The content of this chapter is from a manuscript published in *Chemical Geology* in 2021 (Robinson et al., 2021).

Chapter 3/Robinson et al. (2022a), *Simulating neodymium isotopes in the ocean component of the FAMOUS general circulation model (XPDAA): sensitivities to reversible scavenging efficiency and benthic source distributions*, addresses OBJ2 and OBJ3. This chapter presents the implementation of Nd isotopes into the ocean component of a fast coupled AOGCM (FAMOUS). The content of this chapter is from a manuscript submitted to *Geoscientific Model Development* (Robinson et al., 2022a).

Chapter 4/Robinson et al. (2022b), *Optimisation of the Nd isotope scheme in the ocean component of the FAMOUS general circulation model*, addresses OBJ2, OBJ4, and OBJ5. This chapter presents an optimisation of the Nd isotope scheme in FAMOUS. The optimised scheme is applied to investigate the spatial extent and regional mobilisation of reactive detrital sediment components. The content of this chapter is from a manuscript

submitted to *Biogeosciences* (Robinson et al., 2022b).

Chapter 2

Global continental and marine detrital ε_{Nd}: an updated compilation for use in understanding marine Nd cycling

Abstract

Understanding the role of sediment-water interactions in the oceanic cycling of neodymium (Nd) isotopes is essential for its reliable use as a modern and palaeoceanographic tracer of ocean circulation. However, the exact processes that control Nd cycling in the ocean are poorly defined and require an up-to-date knowledge of the sources, sinks and transformation of this tracer to and within the ocean (e.g. as per the GEOTRACES core mission). We propose a considerable improvement of Nd source identification by providing an extensive and up-to-date compilation of published terrestrial and marine sedimentary Nd isotopic measurements. From this database, we construct high resolution, gridded, global maps that characterise the Nd isotopic signature of the continental margins and seafloor sediment. Here, we present the database, interpolation methods, and final data products. Consistent with the previous studies that inform our compilation, our global results show unradiogenic detrital Nd isotopic values ($\varepsilon_{\mathrm{Nd}} \approx -20$) in the North Atlantic, ε_{Nd} values of ≈ -12 to -7 in the Indian and Southern Ocean, and radiogenic values ($\varepsilon_{\mathrm{Nd}} \approx -3$ to $+4$) in the Pacific. The new, high-resolution interpolation is useful for improving conceptual knowledge of Nd sources and sinks and enables the application of isotope-enabled ocean models to understand targeted Nd behaviour in the oceans. Such applications may include: examining the strength and distribution of a possible benthic flux required to reconcile global Nd budgets, establishing the potential use of Nd isotopes as a kinematic tracer of ocean circulation, and a general quantification of the non-conservative sedimentary processes that may contribute to marine Nd cycling.

2.1 Introduction/ Background

The Nd isotope composition of seawater is typically expressed in the epsilon notation (ε_{Nd}), denoting the deviation of a sample's $^{143}\mathrm{Nd}/^{144}\mathrm{Nd}$ ratio from the chondritic uniform reservoir (CHUR) or bulk earth ratio of 0.512638 in parts per 10,000 (Jacobsen and Wasserburg, 1980):

$$\varepsilon_{Nd} = \left(\frac{(^{143}\mathrm{Nd}/^{144}\mathrm{Nd})_{\mathrm{sample}}}{(^{143}\mathrm{Nd}/^{144}\mathrm{Nd})_{\mathrm{CHUR}}} - 1 \right) \times 10^4, \tag{2.1}$$

$\varepsilon_{\mathrm{Nd}}$ varies with the age and composition of Earth's crust (Goldstein and Hemming, 2003), such that different regions have distinct $\varepsilon_{\mathrm{Nd}}$ signatures. Older continental crust generally has a more negative (i.e. 'unradiogenic') $\varepsilon_{\mathrm{Nd}}$ signature compared with younger mantle derived material, as demonstrated in the compilation by Jeandel et al. (2007).

This spatial heterogeneity in crustal $\varepsilon_{\mathrm{Nd}}$ and the dominance of crustal sources of Nd to the ocean forms the foundation of the use of $\varepsilon_{\mathrm{Nd}}$ as a water provenance tracer. Neodymium has a shorter deep-ocean residence time than the typical global ocean mixing time ($\approx$ 1,500 years) (Arsouze et al., 2009; Goldstein and Hemming, 2003; Lynch-Stieglitz and Marchitto, 2003; Rempfer et al., 2011). As such, different water masses in the ocean are categorised by distinct $\varepsilon_{\mathrm{Nd}}$ that is derived from chemical weathering of the continents (Goldstein and Hemming, 2003; Lacan and Jeandel, 2005a; Tachikawa et al., 2003). This isotopic signature is then redistributed via advection. Thus, water column $\varepsilon_{\mathrm{Nd}}$ measured in-situ for the present day or in sedimentary/seafloor archives for the past has been observed to track basin-scale ocean transports such as meridional overturning circulation (e.g. Basak et al., 2015; Dausmann et al., 2017; Howe et al., 2016; Hu and Piotrowski, 2018; Jonkers et al., 2015; Pöppelmeier et al., 2020a; Roberts and Piotrowski, 2015; Wilson et al., 2015; Xie et al., 2014) and to reconstruct marine gateway events (Horikawa et al., 2010; Khélifi et al., 2014; Martin and Scher, 2006; Newkirk and Martin, 2009; Scher and Martin, 2006; Sepulchre et al., 2014; Stumpf et al., 2015, 2010). Such interpretations of $\varepsilon_{\mathrm{Nd}}$ rely on the assumption that in the absence of local lithogenic input, $\varepsilon_{\mathrm{Nd}}$ behaves conservatively.

Despite a general acceptance of the water mass tracer properties of $\varepsilon_{\mathrm{Nd}}$, the usefulness of Nd isotopes as a proxy for ocean circulation is hampered by ambiguities in the modern cycling and oceanic budget of Nd, alongside a lack of constraints on the processes governing its marine distribution (Abbott et al., 2015a; Rempfer et al., 2011; Tachikawa et al., 2017). This has led to the ambiguous phrase of a 'quasi-conservative' tracer. Nonetheless, extensive progress has been made in understanding how different water masses acquire their $\varepsilon_{\mathrm{Nd}}$ (to give a few examples: Arsouze et al. 2009; Haley et al. 2017; Jeandel 2016; Jeandel et al. 2013; Lacan et al. 2012; Rempfer et al. 2011; Siddall et al. 2008b; Stichel et al. 2020; Tachikawa et al. 2017, 2003; van de Flierdt et al. 2016, 2012; Wilson et al. 2013). It was initially thought that seawater labelling by lithogenic Nd inputs took place only at the surface via aeolian dust and dissolved riverine inputs (Bertram and Elderfield, 1993), and early modelling studies using the transport-matrix method with surface inputs did reproduce North Atlantic Nd distributions correctly/reliably based on these assumptions (Jones et al., 2008). However, considering surface inputs alone failed to balance both Nd concentration ([Nd]) and $\varepsilon_{\mathrm{Nd}}$ distributions globally, with authors highlighting that there must be a 'missing source' (i.e. missing global Nd flux into seawater; Arsouze et al. 2009; Jones et al. 2008; Rempfer et al. 2011; Siddall et al. 2008b; Tachikawa et al. 2003). Furthermore, a partial decoupling of [Nd] and $\varepsilon_{\mathrm{Nd}}$ in seawater is observed, termed the 'Nd paradox' (Goldstein and Hemming, 2003). That is, while $\varepsilon_{\mathrm{Nd}}$ remains fairly constant, [Nd] becomes more concentrated with increasing depth in the water column, and very generally increases along the circulation pathway, overall being mostly lower in the North Atlantic and higher in the Pacific, displaying broadly what has been described as a 'nutrient-like behaviour' (Bertram and Elderfield, 1993; van de Flierdt et al., 2016). The current debate on the oceanic cycling of Nd is therefore centred around two related issues: (1) constraining the sources, sinks and internal cycling of Nd, and (2) the decoupled behaviour of [Nd] and $\varepsilon_{\mathrm{Nd}}$ ('Nd paradox').

Building on the initial understanding that Nd enters the ocean through continental weathering, an important role for particulates within marine biogeochemical cycling of Nd, especially particulate-seawater exchange occurring within marginal settings, has been observed, and proposed to account for imbalances in the global marine Nd budget and the 'Nd paradox'. This contribution from particulates to marine $\varepsilon_{\mathrm{Nd}}$ and [Nd] may be somewhat unsurprising since the global terrigenous particulate flux to the oceans exceeds

the dissolved flux by a factor of 17-30, and as such, the particulate flux dominates fluvial transport of Nd to the oceans (Jeandel, 2016; Jeandel and Oelkers, 2015). Thus, dissolution of just a small proportion (1-3%) of this particulate material deposited annually into seawater can have a large impact on global marine Nd budgets and cycling (Jeandel and Oelkers, 2015). Chemical transfer reactions among terrestrially derived particles and seawater comprise of adsorption/desorption, ion exchange and dissolution/precipitation (Jeandel, 2016; Jeandel and Oelkers, 2015; Lacan and Jeandel, 2005a; Tachikawa et al., 2003). While desorption and ion exchange are usually relatively rapid processes, driven by the relatively high pH and ionic strength of seawater compared to most river waters, dissolution and precipitation take longer (Jeandel and Oelkers, 2015; Rousseau et al., 2015). Dissolution therefore continues for as long as the minerals remain out of equilibrium with respect to the adjacent fluids, at rates that are commonly proportional to surface area (Jeandel and Oelkers, 2015).

A large proportion of this particle-seawater exchange is thought to occur predominantly within estuarine sediments and on continental margins (Rousseau et al., 2015). Chemical elements released from particle dissolution are available locally here as a result of proximity to lithogenic sources delivering dissolved and particulate material to the ocean, alongside high detrital and biogenic particle concentrations within the water column that act to promote rapid local reprecipitation as secondary phases due to seawater being close to saturated or supersaturated with respect to many mineral phases (Jeandel and Oelkers, 2015; Pearce et al., 2013). Such an exchange, termed 'boundary exchange' is capable of modifying the isotopic signature of a water mass without significantly affecting its concentration, and has been proposed as a major source of Nd into seawater (Arsouze et al., 2009; Jeandel et al., 2007; Rempfer et al., 2011; Tachikawa et al., 2017; van de Flierdt et al., 2016). Investigating this concept further, Arsouze et al. (2007) simulated a realistic global $\varepsilon_{\mathrm{Nd}}$ distribution using boundary exchange as the only source/sink term, demonstrating the potential for this process to be highly important for balancing the oceanic Nd cycle. Subsequent to this 2007 study, the release of Nd from dissolution of continental derived particulate material has been incorporated into global Nd modelling schemes (Arsouze et al., 2009; Gu et al., 2019; Rempfer et al., 2011), contributing 90-95% of the total simulated Nd flux to the ocean and thus providing a mechanism to account for the 'missing source'.

Another possible contributor to the 'Nd paradox' is reversible scavenging; the physical process of adsorption and desorption of Nd onto sinking particle surfaces in the water column, now considered another important feature of the interplay of particulate and dissolved Nd phases in the ocean (Jeandel et al., 1995; Siddall et al., 2008b; Stichel et al., 2020; Tachikawa et al., 1999). Modelling studies show that the observed pattern of increasing [Nd] with depth can be reproduced by parameterising internal cycling using the reversible scavenging approach developed by Bacon and Anderson (1982) (Arsouze et al., 2009; Gu et al., 2019; Pöppelmeier et al., 2020b; Rempfer et al., 2011; Siddall et al., 2008b). These models operate under a steady state assumption, meaning external fluxes from particles are balanced by dissolution and adsorption, which is partitioned according to an equilibrium scavenging coefficient (K_D; Siddall et al., 2008b).

This interplay between dissolved and particulate phases is a key aspect of the biogeochemical cycling of Nd that has sparsely been explored. As a result, K_D values have mostly been derived from research looking into the relationship between adsorbed and desorbed ^{231}Pa and ^{230}Th (Chase et al., 2002; Henderson et al., 1999; Siddall et al., 2007, 2005). Stichel et al. (2020) presented the first regional Nd particle-seawater interaction study in the North Atlantic, here investigating whether particle-seawater exchange occurs beyond settings proximal to where seawater acquires a weathering signal (i.e., does particle-seawater exchange take place in open ocean regions with low particle concentrations?). Comparing the difference in $\varepsilon_{\mathrm{Nd}}$ between the dissolved and particulate phases along the North Atlantic

Deep Water (NADW) flow path, they found that particles become fully equilibrated with ambient seawater in the open ocean and therefore are no longer considered to be particle reactive. However, deep waters that are in contact with the seafloor, where nearly half of the total Nd is present in the particle phase (in comparison to approximately 5% in the open ocean), may present an exception to this condition. Here, increasing [Nd] profiles contrast with the more general observance that particle-seawater exchange is primarily limited to locales close to weathering inputs. This deviation has been attributed to either the reduced deep-water scavenging potential of Nd (Stichel et al., 2020), which would allow dissolved [Nd] to accumulate, or, to a previously neglected benthic source of Nd (e.g. the mobilisation of a secondary pool of reactive Nd; Abbott et al. 2015b; Haley et al. 2017).

Thus, a current branch of literature on Nd cycling now proposes a change from a 'top-down' paradigm of Nd cycling (governed by aeolian dust inputs; dissolved riverine fluxes; boundary exchange, a sediment flux constrained to the continental margins; and internal cycling through reversible scavenging) to incorporate a 'bottom-up' model, whereby benthic fluxes and a sedimentary source at depth exert a significant control over the distribution of seawater Nd (Haley et al., 2017). This alternative model specifically refers to a transfer of Nd from sediment pore water to seawater resulting from early diagenetic reactions, and may explain imbalances in the marine $\varepsilon_{\mathrm{Nd}}$ budget as well as observed decoupling between water mass provenance and Nd isotopes (Abbott et al., 2019, 2016a, 2015b,a; Du et al., 2016; Haley et al., 2017). It was initially offered as an explanation for measurements taken on the north-western Pacific margins, where it was inferred that radiogenic pore water Nd was transferred to overlying shallow and intermediate waters, and has thenceforth been proposed to exert a primary control over deep ocean $\varepsilon_{\mathrm{Nd}}$ (Abbott et al., 2016a, 2015b,a). In particular, a benthic flux provides a mechanism to explain the deep water $\varepsilon_{\mathrm{Nd}}$ alteration in the North Pacific in the absence of deep water formation, where circulation is sluggish, and the sediments contain a considerable amount of volcanic material susceptible to leaching (Pearce et al., 2013). Under this benthic flux framework, $\varepsilon_{\mathrm{Nd}}$ of a water mass becomes determined by a combination of the circulation pathway and also non-mixing processes such as a bottom-sediment source, the influence of which can be determined from the magnitude and $\varepsilon_{\mathrm{Nd}}$ of the sediment flux coupled with the integrated time of exposure to this flux (i.e. exposure time) (Abbott et al., 2015a). In this sense, if benthic exposure time and detrital sediment composition can be reasonably predicted, $\varepsilon_{\mathrm{Nd}}$ may provide additional constraints concerning ocean circulation kinematics (Abbott et al., 2015a; Du et al., 2020; Haley et al., 2017). Since the 2015 north-western Pacific studies, observations of large additions of Nd to the ocean from deep sites have been made in the Angola Basin off the southwest coast of Africa (Rahlf et al., 2020; Zheng et al., 2016) and the Rockall Trough in the North Atlantic (Crocket et al., 2018). Furthermore, measurements from the Tasman Sea revealed a flux of similar magnitude to that inferred for the North Pacific, suggesting regions with dominantly calcareous sediment could also contribute a significant source of Nd (Abbott et al., 2019). This presented an interesting challenge for understanding Nd cycling, since carbonate contains relatively low [Nd] and therefore regions dominated by calcareous sediments were previously considered an unlikely contributor to the benthic flux.

However, the presence of volcanic materials and calcareous sediments at the ocean interface can be highly localised, meaning that any potential Nd inputs from these sources are not seafloor-wide. Clays, on the other hand, are more ubiquitously spread throughout the global ocean, meaning that clay mineral dissolution might facilitate a large, widespread sedimentary Nd source to the ocean. Abbott et al. (2019) evaluated potential sedimentary Rare Earth Element (REE) host phases and concluded a benthic control of REEs, including Nd, could be driven by clay minerals that have high reactivates and large surface areas. The authors suggest that distal, deep ocean sites with fine-grained sediments may have the largest fluxes, as opposed to previous views that most of the Nd sediment source is highly constrained to margins. Consequently, the benthic flux could be widely applicable

across the global ocean, providing another possible origin for the 'missing' Nd source. This model, however, assumes that reactivity and exchange capacity of certain mineral phases is similar across the globe, an assumption that still requires careful testing.

It is apparent that there remains many outstanding questions regarding particle-seawater exchange of Nd, in part due to an incomplete understanding of how these elements fractionate during mineral dissolution and precipitation (Pearce et al., 2013). Firstly, particle-seawater interaction of Nd involves a combination of complex processes (release, removal and exchange) operating under various temporal scales and under specific environmental conditions, for example pH or oxic-anoxic conditions, transport and aging of sedimentary deposits (Wilson et al., 2013). Our understanding of these processes is further complicated by the fact that particulate material is comprised of numerous mineral phases, each with its own distinct dissolution rate and saturation state, and as such, each fraction tends to be incongruently released by particle dissolution (Pearce et al., 2013; Wilson et al., 2013). Additionally, it has been argued that because Nd is commonly present in less reactive minerals, it is likely released to seawater at a slower rate than most other elements, enabling the potential of sediments deposited for a long time in the deepest part of the ocean to be weathered (Abbott et al., 2019).

Notably, it remains unconfirmed and sometimes hotly debated whether or not a benthic flux does exert a strong control on oceanic Nd distributions and what conditions influence the rate of such a flux. Simulating Nd cycling in 3D ocean models has been shown to help contribute to this debate, quantitatively evaluating the importance of different components of Nd cycling (Arsouze et al., 2009, 2007; Gu et al., 2019; Jones et al., 2008; Pöppelmeier et al., 2020b; Rempfer et al., 2011; Siddall et al., 2008b). The most sophisticated global Nd schemes to date are implemented within coupled atmosphere-ocean general circulation models (AOGCMs), with an explicit description of the oceanic sources and sinks (e.g. Arsouze et al., 2009; Gu et al., 2019; Pöppelmeier et al., 2020b; Rempfer et al., 2011). They are currently predominantly based upon a 'top-down' model of marine Nd cycling, with a sediment flux constrained to the continental margins. However, Pöppelmeier et al. (2020b) recently began numerical-modelling investigations of the benthic flux within global marine Nd cycling by updating the Nd isotope enabled Bern3D model initially developed by Rempfer et al. (2011) to explicitly account for a seafloor-wide source of Nd. The refined implementation included dissolution of resuspended riverine material in estuaries (Rousseau et al., 2015), and the removal of the depth limitation for the sediment source (i.e. adapting the model's representation of 'boundary exchange', previously restricted to the upper 3,000 m of the ocean, to thus invoke a benthic flux). The results of this study were useful for demonstrating the potential importance of including a seafloor-wide input of Nd.

Moreover, it has been argued that the 'top-down' and 'bottom-up' views of Nd cycling are not independent of each other (Du et al., 2020; Haley et al., 2017). Both may be essential for understanding and balancing the global marine $\varepsilon_{\mathrm{Nd}}$ budget and solving the 'Nd-paradox'. Despite the still enigmatic nature of Nd cycling in the ocean, a consistent theme to emerge from the expanding body of literature has been increasing evidence of the importance of the sediment-water interface as a dominant control on the marine Nd cycle (Abbott et al., 2015b; Arsouze et al., 2009, 2007; Blaser et al., 2019b; Haley et al., 2017; Rempfer et al., 2011; Tachikawa et al., 2017, 2003; van de Flierdt et al., 2016; Vogt-Vincent et al., 2020). With more Nd delivered to the oceans in the particulate phase relative to the dissolved phase, and just a small fraction of particle dissolution being capable of governing marine $\varepsilon_{\mathrm{Nd}}$ and [Nd] distributions, the dissolution of terrigenous particulate material may be the dominant mechanism by which Nd is supplied to the oceans (Jeandel and Oelkers, 2015). Although this may complicate the use of $\varepsilon_{\mathrm{Nd}}$ as a tracer of ocean circulation, it suggests that global marine cycling of Nd can provide additional constraints as a tracer of continental weathering and climate (Abbott et al., 2019; Jeandel and Oelkers, 2015;

Pearce et al., 2013). If terrigenous particle dissolution does dominate Nd [isotope] input to the ocean, $\varepsilon_{\mathrm{Nd}}$ variations in different water masses could, in some cases, be directly relatable to changes in *sediment* (as opposed to *water*) provenance and the weathering of locally derived material. However, to be able to quantify such effects, it is first necessary to improve our incomplete knowledge of how different particulate Nd phases from diverse sedimentary environments fractionate during mineral dissolution and precipitation.

In short, notwithstanding significant recent advances in the way we think about Nd sources and sinks, sediment-water interactions remain one of the least understood aspects of marine Nd cycling. The proliferation of Nd measurements, and our evolving knowledge of Nd cycling now present an opportunity to test new conceptual and numerical models that explicitly account for the benthic flux occurring across the whole seafloor. This could be used to answer, to a first order, the current key questions around marine Nd cycling. Including, but not limited to: constraining the magnitude and $\varepsilon_{\mathrm{Nd}}$ from sediment-water interaction, testing whether a 'bottom-up' framework is consistent with the observed modern seawater $\varepsilon_{\mathrm{Nd}}$ and [Nd], assessing any overprinting effect a benthic flux may have on bottom waters, and evaluating the possibility that with a strong benthic flux $\varepsilon_{\mathrm{Nd}}$ could be exploited as a kinematic tracer of ocean circulation.

However, all of these investigations require a known global distribution of sedimentary $\varepsilon_{\mathrm{Nd}}$. Numerical modelling studies in particular rely on a spatially-continuous definition of Nd signatures across the whole global sediment-water interface as a model input, essentially filling in the gaps between disparate measurement sites in a geologically robust way. More than a decade ago, Jeandel et al. (2007) produced a seminal map of continental $\varepsilon_{\mathrm{Nd}}$, which fulfilled exactly this purpose, summarising the global fingerprint of continental $\varepsilon_{\mathrm{Nd}}$ inputs to the ocean and enabling numerical schemes to implement a continental margin source. Here, we build on this formative work, taking the opportunity to incorporate a substantial amount of recently published $\varepsilon_{\mathrm{Nd}}$ measurements to update the extrapolated data product for the continental margins and extend it across the whole ocean floor. Our new continuous distributions of $\varepsilon_{\mathrm{Nd}}$ thus provides the detail needed to evaluate a global sediment source of Nd to the ocean, or for the user to apply their own regional constraints depending on water depth, sediment thickness/type etc. In this way, we hope to facilitate a more complete understanding of Nd marine cycling, specifically enabling a first-order examination of the benthic flux in numerical modelling schemes to determine whether a shift towards a 'bottom-up' framework is capable of representing global oceanic Nd distributions.

In the following section, we describe the methods used to characterise the $\varepsilon_{\mathrm{Nd}}$ signature of the global sediment-water interface, including the new data compilation contributed by co-authors, our approach to filtering $\varepsilon_{\mathrm{Nd}}$ measurements and the process for producing the spatially continuous gridded maps (Sect. 2.2). Next, we present our refined continuous ocean sediment $\varepsilon_{\mathrm{Nd}}$ distributions, including $\varepsilon_{\mathrm{Nd}}$ at the continental margin and across the sea floor (Sect. 2.3). We then provide our proposed combination of both datasets and include a discussion about the final boundary conditions, acknowledging the limitations in our approach, and propose the use of these gridded maps as a first step towards a deeper interrogation of the sources and sinks of oceanic Nd, including the possibility of a benthic flux (Sect. 2.4).

The final $\varepsilon_{\mathrm{Nd}}$ maps clearly highlight where there is a wealth and conversely a dearth of Nd measurements, and where those measurements may or may not be representative of the wider oceanographic setting, thereby providing a useful guide for future data acquisition efforts. Furthermore, our methods are reproducible, and we provide full documentation of the protocol to facilitate updating the distributions with new measurements. Thus, we contend that our proposed sediment $\varepsilon_{\mathrm{Nd}}$ maps form an important and much needed step towards improving the understanding and quantification of marine Nd cycling under evolving frameworks and in line with the aims of the international GEOTRACES program,

enabling future modelling efforts to answer the many intriguing questions that remain.

2.2 Methods

2.2.1 Updated database and compilation of published ε_{Nd}

An extensive and updated (relative to Jeandel et al. 2007) database of ε_{Nd} values measured on both terrestrial and marine sediments was initially obtained from Blanchet (2019). This database was built incorporating published Nd values from an extensive literature review, external contributions and retrieval from the SedDB database and includes 1,529 observations. We then identified areas where known additional published data could be added to the database and where observational data was spatially limited, having the potential to impede/bias interpolation across the globe. Notably, we prioritised detailed publications with numerous observations taken around key regions of deep-water formation in the North Atlantic and addressing data scarcity, particularly in the Pacific, Indian and Southern Ocean.

Through co-author contribution and a collective community effort to put forward relevant published datasets, the initial database was expanded to reach a total of 5,107 data points, including 2,671 present day and Holocene rock, river and marine sediment observations, thus capturing a much greater level of spatial detail in the overall larger quantity of constituent data (Fig. 2.1 and Supplementary Table S1). This was achieved first from extensive literature review, adding relevant observations particularly covering the Southwest Atlantic, the Bering Sea, the Southern Ocean, and West Africa. We then added further detail in the Southern Ocean, focusing along the Antarctic coastline, notably in West Antarctica, the Antarctic Peninsula and surrounding the Ross Sea (Cook et al., 2013; Mikhalsky et al., 2013; Pierce et al., 2011; Roy et al., 2007; Simões Pereira et al., 2018; van de Flierdt et al., 2008; Walter et al., 2000). This Southern Ocean compilation also includes a collection of 34 new (i.e. hitherto unpublished) measurements contributed by co-authors; see Supplementary Text S2.1 and Table S2 for information on the collection/measurement techniques. Our compilation of published and new Southern Ocean data is focussed on marine detrital measurements that could be used as an indicator of the ε_{Nd} signal eroded from neighbouring continental rock and also provides measurements from sediments directly in contact with seawater. We obtained even more modern and Holocene detrital measurements from sediments in the Arctic, eastern North Atlantic, West Atlantic, Gulf of Alaska and the Indian and East Pacific Ocean from the global compilation of detrital ε_{Nd} that accompanied the large-scale acquisition of seawater and geologic-archive ε_{Nd} performed by Tachikawa et al. (2017). Additionally, we include data from a recent global core-top compilation published by Du et al. (2020), whom investigated recent changes to Global Overturning Circulation from authigenic and sedimentary ε_{Nd} records, covering particularly the North-West and South-West Atlantic, the Indian and Central Equatorial Pacific Ocean. Finally, we included marine pore fluid ε_{Nd} from three sites in the eastern North Pacific (Abbott et al., 2015b,a).

The database, including the full dataset of ε_{Nd} and associated metadata table is reported in Supplementary Table S1.

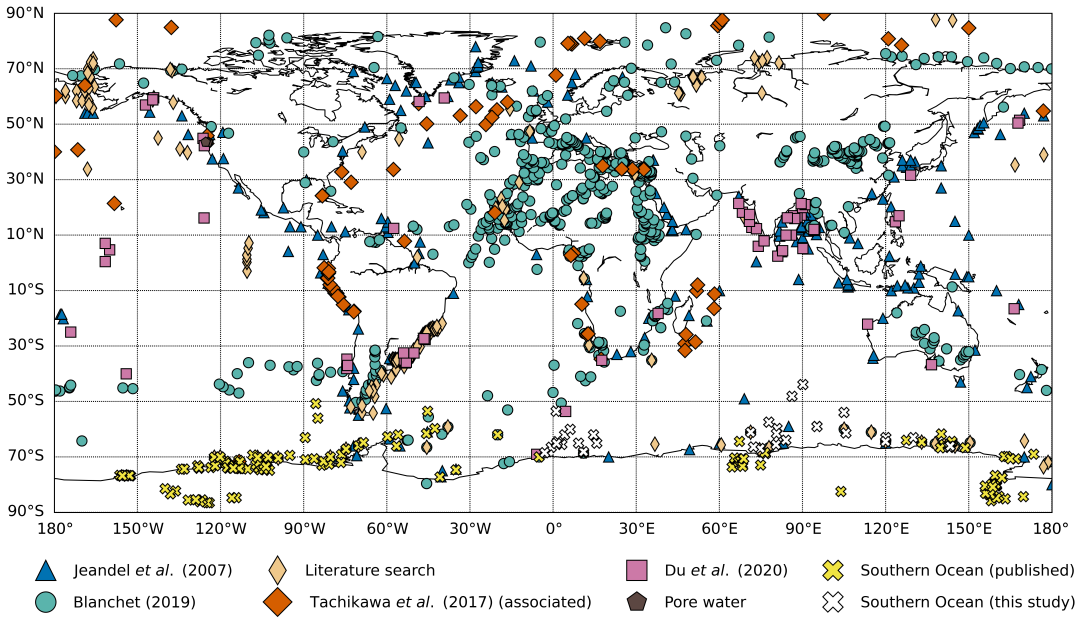

Figure 2.1: Overview of the location of the $\varepsilon_{\mathrm{Nd}}$ samples assembled in the updated continental and marine detrital and porewater database, filtered to show only data from the Holocene (specifically 11.7 ka to present) and the new Southern Ocean data contributed by co-authors and presented in this study. Data are identified as belonging to the initial sediment $\varepsilon_{\mathrm{Nd}}$ compilation by Jeandel et al. (2007) (blue triangles), subsequent additions by Blanchet (2019) (green circles), from further literature review (thin beige diamonds), detrital data associated with the results presented by Tachikawa et al. (2017) (orange diamonds), data compiled by Du et al. (2020) (lilac squares), pore water data from Abbott et al. (2015a) (black pentagon) and Southern Ocean compilation (yellow crosses: published by Cook et al. 2013; Mikhalsky et al. 2013, 2006; Pierce et al. 2011; Roy et al. 2007; Simões Pereira et al. 2018; van de Flierdt et al. 2008; Walter et al. 2000. White crosses: this study).

2.2.2 Continental $\varepsilon_{\mathrm{Nd}}$ map

2.2.2.1 Data selection

The primary aim of this first phase of work is to define as accurately as possible the modern isotopic signatures of the continents surrounding the oceans and continental margins on a global scale. To achieve this aim, we filtered the entries in our new, comprehensive database (Sect. 2.2.1) to only include samples from the Holocene (specifically 11.7 ka to present) as well as the New Southern Ocean samples contributed by co-authors, which in some cases may be older, yet still provide appropriate $\varepsilon_{\mathrm{Nd}}$ for our study (as explained in Supplementary Information: Text S2.1). We include present day (P) samples defined from 1 ka to present or from the upper 1cm/top-core sediment, and Holocene/Marine Isotope Stage 1 (MIS1) samples ranging from 11.7 – 1 ka. This is because we are most confident that the measured values falling within these depositional age ranges are representative of the modern continental $\varepsilon_{\mathrm{Nd}}$ interacting with seawater. This yielded a total of 1,078 observations, which came from three broad sample types: river sediment samples, which deposit on the continental shelf and slope; Holocene marine sediments collected along given margins; and geological material outcropping close to an oceanic margin expected to be weathered. We explain this choice in more detail in Supplementary Information (Sect. 2.6); Text S2.2. All the discrete continental data extracted through this filtering process are reported in Supplementary Table S3 and are displayed in Fig. 2.2a.

We acknowledge the potential for bottom ocean currents to transport fine-grained

sediments to sites distal from their sources (Gorsline, 1984), and this may have a local/regional control on the ε_{Nd} passed on to the overlying water column (Jeandel et al., 2007). With currently available observations, this is difficult to consider comprehensively within a global, objective, numerically-driven framework. Thus, we assume that the effect of bottom-current transport is relatively small for the overall regional-global Nd budget and do not explicitly incorporate the process in our initial interpolation of the discrete data (Sect. 2.2.2.2). Future work that focuses on specific geographical domains would be best suited to investigating the importance and impact of these assumptions in greater detail.

2.2.2.2 Interpolation of continental ε_{Nd} map

Once an extensive compilation of suitable discrete ε_{Nd} observations was obtained, the points were interpolated across the globe, to create a spatially continuous distribution of continental ε_{Nd} proximal to the ocean. It is noted here that we are aiming to produce values that represent broader geological regions and not specific outcrops and singular observations.

Since the ε_{Nd} of continental rocks is closely related to its geological characteristics (i.e. lithology) and age, we used the digital geological map as used by Jeandel et al. (2007) which provided polygons for the (simplified) fields of given geological age and type. This map was used to constrain our interpolation of discrete data points according to the underlying geological units, maintaining a basic level of regional geological consistency in our continuous characterisation of the continental margins. Such an approach is based on the assumption that the seawater ε_{Nd} is equivalent to the ε_{Nd} signature of the weathered source rock, which we deem to be an appropriate premise for the global scale examined here.

The interpolation scheme employed a nearest neighbour analysis, using the digital geological map as a mask to produce spatially continuous continental ε_{Nd} fields from the discrete Nd point measurements. Each geological-unit polygon was attributed an ε_{Nd} value according to the sample that fell within its spatial domain with the nearest distance to the centre of the polygon, or in the absence of any measurements within the domain, according to the nearest sample by distance to the centre of the polygon. This produced a first iteration of the new high resolution, gridded ε_{Nd} for continental margins (see Supplementary Fig. 2.9) based purely on the numerical interpolation methods described above and without any expert 'tuning' of the results to account for any [sampling] biases that may skew the results. It forms the basis of our final continental margin ε_{Nd} distribution with the adaptations summarised below.

Examining this initial output, it is apparent that in some regions, the purely numerically based interpolation failed to capture the real spatial heterogeneity of crustal ε_{Nd}, or produced ε_{Nd} that, from our knowledge, appeared to not represent the broader regional signal, e.g. due to measurements capturing only very localised ε_{Nd} and the numerical interpolation inaccurately dispersing those signals. We therefore performed a small number of manual adjustments to the interpolation in order to improve the final distribution of ε_{Nd} and thus bring it into better accord with available evidence (i.e. the wider published literature) and the expert judgment and field/laboratory experience of our pool of co-authors.

To assess the interpolation and identify where adjustments were needed, we closely interrogated the agreement between the numerically-produced ε_{Nd} and expected (e.g. based on geological age and rock type) ε_{Nd} within geological polygons based on the Sm-Nd evolution of Earth (i.e. age) and Sm/Nd fractionation during mantle melting (i.e. lithology; Goldstein et al. 1984; Taylor et al. 1983). In addition, we compared the signature of similar geographically distal fields (e.g. the same rock type/age, and regions that are

known to have once been physically connected before tectonic plate movement separated them). Overall, we made the fewest possible changes to rectify obtrusive inconsistencies. For full transparency and to enable easy reproducibility of our methods or bespoke editing of our modifications, all changes are documented and explained in Text S2.4, with the precise operational details provided in Supplementary Table 2.2. Furthermore, a visual comparison of the results is made in Supplementary Fig. 2.9, which demonstrates the difference in continental $\varepsilon_{\mathrm{Nd}}$ arrived at using purely the numerical interpolation (i.e. before making manual adjustments) compared with the refinement. Fig. 2.2b shows our final representation of the $\varepsilon_{\mathrm{Nd}}$ of the continents surrounding the ocean.

2.2.2.3 Extrapolation of continental $\varepsilon_{\mathbf{Nd}}$ onto the continental shelf

Once the continental interpolation was finalised, we extrapolated these data out across the marine sectors of the continental margins, adopting the philosophy that the mean $\varepsilon_{\mathrm{Nd}}$ signature on continental margins is similar to that of the neighbouring land surfaces. We define the extent of this extrapolation – that is, how far out to sea/how deep we can reasonably assume that the continental $\varepsilon_{\mathrm{Nd}}$ remains representative of the proximal marine sediments – as being limited to where sediment thickness is greater than or equal to 1,000 m according to GlobSed, a total sediment thickness grid for the world's oceans and marginal seas (Straume et al., 2019). We chose to use sediment thickness to constrain our margin extrapolation as a proxy for the extent to which outcropping fields are weathered, and thus the extent to which it is reasonable to assume a similar $\varepsilon_{\mathrm{Nd}}$ would exist at the sediment-ocean interface. Globally, erosion, proximity to continents, transport and biogenic sedimentation determines the first order structure of sediment thickness (Straume et al., 2019). We compared extrapolating the continental $\varepsilon_{\mathrm{Nd}}$ out to the margins under various sediment thickness constraints ($\geq$ 500 m, $\geq 1,000$ m and $\geq 2,000$ m), detailed in Supplementary Fig. 2.11, to find the most suitable limits of our extrapolation.

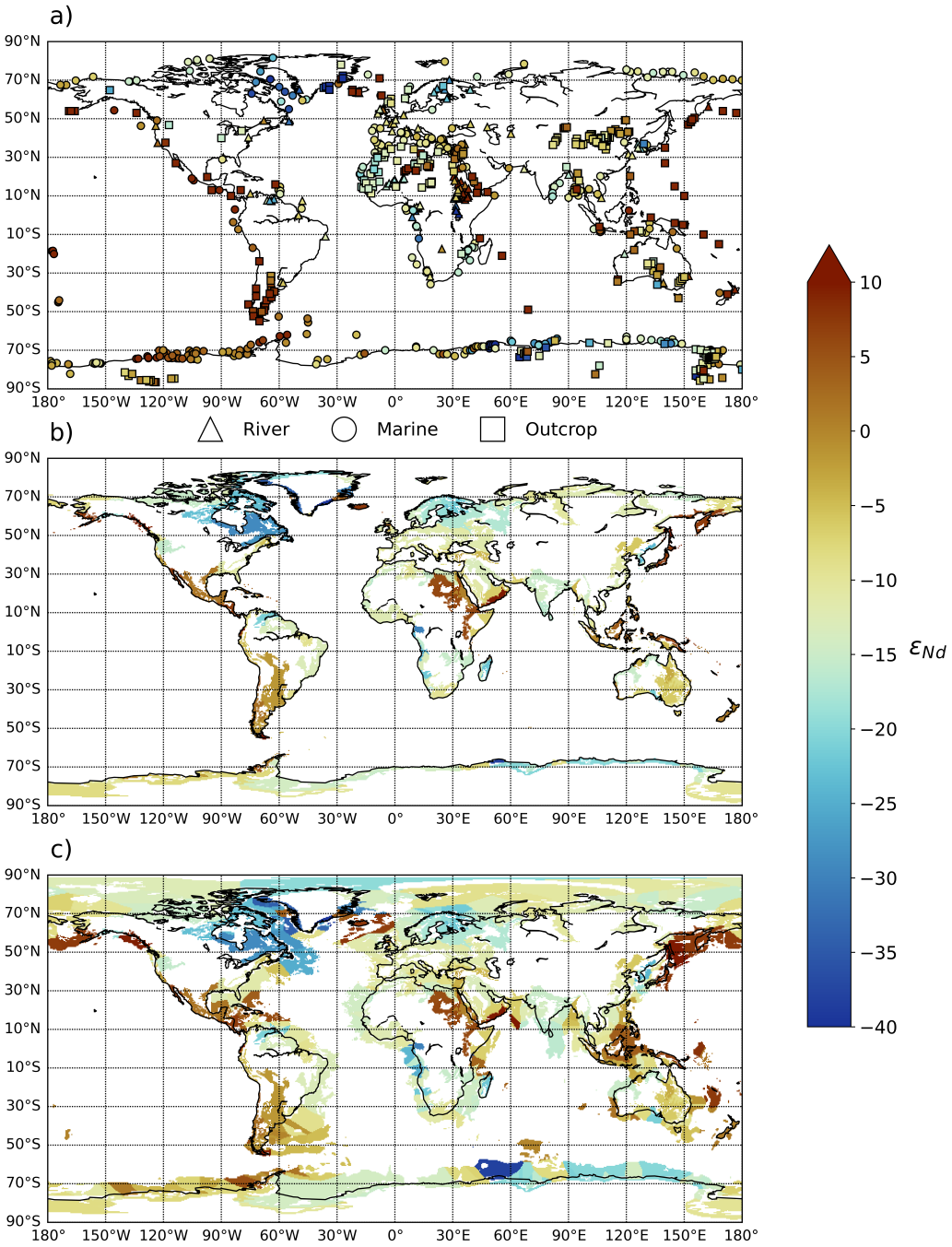

Figure 2.2: Continental and proximal margin $\varepsilon_{\mathrm{Nd}}$ map, showing (a) sample type and $\varepsilon_{\mathrm{Nd}}$ of Nd isotope measurements compiled in Supplementary Table S3, indicating the three broad sample types included in the new compilation: river sediment (triangles), Holocene marine sediments (circles), and geological outcrops (squares), (b) updated continental $\varepsilon_{\mathrm{Nd}}$, and (c) complete $\varepsilon_{\mathrm{Nd}}$ of the continents and proximal margins (constrained to where sediment thickness $\geq 1,000$ m).

Continental margins, which represent approximately 13% of the oceanic area, contain over 42% of the total ocean sediment volume, and have an estimated average sediment cover of 3,044 m, in comparison with ocean crust with an estimated average sediment cover of 404 m (Straume et al., 2019). We choose $\geq 1,000$ m sediment thickness as

our final extrapolation extent to encompass only marginal settings. Sediment thickness $\geq 2,000$ m did not capture all marginal settings, in particular passive margins in the Eastern Pacific and margins surrounding Australia, and we chose not to use a shallower threshold (such as ≥ 500 m) because this extrapolated the continental signal beyond what we deemed representative. This value was close to the average sediment cover of oceanic crust and as a result reached distal oceanic crust, for example in the western North and South Atlantic basins. We acknowledge that lithogenic input via aeolian dust flux may reach further limits than our definition, but we made the pragmatic choice to prioritise the categorisation of marginal sediments and deposits. Constraining what we define as 'continental margins' to $\geq 1,000$ m sediment thickness is, however, a somewhat arbitrary choice. Our transparent approach and fully available input data will allow future user groups to implement a different choice of delimiting sediment thickness, should they wish. The product of our final combined continental and extrapolated marginal sediment $\varepsilon_{\mathrm{Nd}}$ is shown by Fig. 2.2c.

2.2.3 Seafloor $\varepsilon_{\mathrm{Nd}}$ map

2.2.3.1 Data selection

In order to examine the possible role of a benthic flux on global Nd cycling and thus to test mathematically (e.g. through Nd isotope enabled three-dimensional ocean models) the emergent hypothesis that such a flux is driven by Nd released into pore waters from detrital sediment on the seafloor during early diagenesis, the $\varepsilon_{\mathrm{Nd}}$ of the seafloor needs to be represented. This characterisation of $\varepsilon_{\mathrm{Nd}}$ across the entire sediment-water interface is also more broadly useful for investigating Nd cycling, since it allows any user to define their own (and experiment with different) depth or sediment-type boundaries for where Nd is exchanged with the water column. Based on current paradigms, it has been suggested that ideally, pore water measurements of $\varepsilon_{\mathrm{Nd}}$ and [Nd] would be most representative of the Nd interaction between the sediment-water interface, recording the labile Nd from detrital material into pore water (Abbott et al., 2015a; Du et al., 2020). However, to date the measurements of pore water $\varepsilon_{\mathrm{Nd}}$ are very spatially limited; three sites currently, all in the North Pacific, measured in near surface sediments on the continental margins between 500 and 3,000 m water depth (Abbott et al., 2015b,a). An approach that extrapolates the few (three) valuable pore water measurements that do exist would likely over-generalise the distribution of global labile seafloor $\varepsilon_{\mathrm{Nd}}$, failing to capture a sediment-type dependent, realistic distribution even at the broad scale. Further measurements would also be needed to fully verify whether this is true.

Published detrital sediment $\varepsilon_{\mathrm{Nd}}$ measurements provide our most practical solution to this global open ocean pore water data sparsity. Here, we define detrital sediments as the non-authigenic and non-biogenic sediment phases encompassing three main fractions: bulk sediment digests, decarbonated sediment residuals and decarbonated and leached sediments (hereby referred to as the detrital fraction), indicated in Supplementary Table S4 and Fig. 2.3a (Blaser et al., 2016; Du et al., 2016; Wilson et al., 2013). It is hypothesised that detrital sediments interact with pore water on long timescales (hundreds to thousands of years), in large part compensating for slow reaction kinetics and therefore enabling detrital sediment to exert a significant influence on the $\varepsilon_{\mathrm{Nd}}$ of pore water (Du et al., 2016). Furthermore, detrital sediments provide a direct measurement of the sediment $\varepsilon_{\mathrm{Nd}}$ in contact with pore water, albeit in the absence of quantifying exactly the reactive Nd phases. We therefore filtered the updated Nd database to identify marine core-top pore water and detrital sediment $\varepsilon_{\mathrm{Nd}}$ and used this compilation to produce a best estimate of the global distribution of seafloor $\varepsilon_{\mathrm{Nd}}$. Similar to the continental compilation, only core-top sediments (i.e. the upper cm) or sediments deposited during the Holocene (11.7 ka to present), as well as the New Southern Ocean samples contributed by co-authors were considered, yielding a total of 1,479 observations. All the discrete marine detrital

and pore water data utilised in this study are reported in Supplementary Table S4 and are shown by Fig. 2.3a.

Despite the development of several sequential extraction processes for the partitioning of marine sediment fractions, at present there remains no standard chemical procedure for measuring the detrital fraction $\varepsilon_{\mathrm{Nd}}$ of marine sediments (Bayon et al., 2002; Du et al., 2020). As such, the definitions of the three main detrital phases presented here (bulk, decarbonated and detrital) represent a broad classification due to the non-uniformity in extraction methods employed within the literature. Furthermore, between these fractions, the reported $\varepsilon_{\mathrm{Nd}}$ may vary significantly due in part to the specific aims of the individual research efforts. For example, most (if not all) detrital samples were conducted not to establish a benthic flux of Nd to the oceans, but to understand geographical provenance and transport mechanisms (atmospheric circulation of dust, water advection, fluvial erosion, cryospheric dynamics). In all cases, the assumption is that detrital phases retain the isotopic signature of their source rock signature throughout continental weathering, sediment transport and diagenesis (e.g. Basile et al., 1997; Cook et al., 2013; Grousset et al., 1998, 1992, 1988; Innocent et al., 1997; Jones et al., 1994; Nakai et al., 1993; Revel et al., 1996; Simões Pereira et al., 2018; Toucanne et al., 2015; van de Flierdt et al., 2008). Recent work suggests that strong leaching procedures in older studies could lead to loss of reactive detrital phases, which are a potentially important benthic source of Nd, and thus may not be preserved in operationally defined 'detrital residues' (Abbott et al., 2019, 2016a; Blaser et al., 2016; Du et al., 2016; Williamson et al., 2013). Furthermore, the standard protocols used to isolate the Fe-Mn oxyhydroxide phases in leaching procedures have been found to not only target oxyhydroxide phases, but also target clay host phases (Abbott et al., 2019). These conventional leaching methods mobilise significant quantities of silicate hosted REEs, particularly in carbonate poor sediments (Blaser et al., 2016; Wilson et al., 2013). Refined leaching methods, which now employ a gentler approach, can minimise this silicate fraction 'contamination'. Nonetheless, in the absence of a carbonate buffer, they have still been found to mobilise some of the silicate fraction (Blaser et al., 2019b, 2016). Utilising bulk sediment data may avoid this underrepresentation of the more labile $\varepsilon_{\mathrm{Nd}}$ signal and prevent removal of the clay mineral fraction $\varepsilon_{\mathrm{Nd}}$. However, bulk sediment data are also relatively sparse, albeit not as scarce as pore water measurements. Acknowledging the limitations outlined above, decarbonating and leaching procedures aim to remove the preformed seawater/pore water signal in order to isolate specifically the detrital fraction, and improvements have been made towards standardising these procedures. For example, Bayon et al. (2002) presented a robust chemical procedure for separating the detrital material into decarbonated sediment residuals and specific detrital size fractions, resulting in reduced or no loss of specific phases. Within our database, decarbonated and detrital fraction observations are much more abundant, and as such, these samples are also deemed suitable for inclusion in this dataset alongside bulk sediment digests and pore water samples, allowing for a more global representation of direct $\varepsilon_{\mathrm{Nd}}$ measurements covering various seafloor lithologies.

We recognise that under current practical constraints, there is no unique/ideal solution for our sample selection. To use only pore water and bulk sediment fractions would limit the number of observations to too few for producing a useful broad scale representation of the seafloor $\varepsilon_{\mathrm{Nd}}$ source. For example, the 106 bulk sediment observations compiled globally (compared to 541 and 829 decarbonated and detrital observations, respectively) are not only limited in number, but also are heavily biased towards marginal settings and concentrated mainly in the northwest and southwest Atlantic, the Gulf of Alaska and East Antarctica, likely underrepresenting marine sedimentary areas (e.g. deep ocean settings, the Arctic Ocean, and the Indian Ocean). On the other hand, as acknowledged by Blaser et al. (2016); Du et al. (2016) and Wilson et al. (2013), decarbonated sediment residuals and detrital fractions may (at least in some cases) provide a weaker/less significant oceanic Nd flux. Again, the available data are insufficient to fully verify this possibility or

demonstrate in which specific settings it is the case. Balancing these two challenges, we made the decision to include the whole sediment (not favouring any specific detrital phases) as contributing to the sediment-water $\varepsilon_{\mathrm{Nd}}$. Following further data acquisition from more labile fractions and direct comparison between the $\varepsilon_{\mathrm{Nd}}$ yielded by the different detrital phases of the same samples on a global scale, this approach could be revisited in the future.

2.2.3.2 Interpolation of seafloor $\varepsilon_{\mathbf{Nd}}$ map

Once an extensive compilation of suitable discrete detrital and pore water $\varepsilon_{\mathrm{Nd}}$ observations were obtained, the points were then interpolated globally to produce a spatially continuous $\varepsilon_{\mathrm{Nd}}$ signature of seafloor sediments in contact with bottom water. Again, the aim here is to broadly characterise the signature of seafloor sediments, providing a best estimate of global $\varepsilon_{\mathrm{Nd}}$ based on the available [and limited] dataset. Our map thus may not capture localised features and variations.

Adopting the assumption that dominant seafloor lithology types at least partially describe the major sedimentary source and characteristics of detrital $\varepsilon_{\mathrm{Nd}}$, we used a high-resolution gridded map characterising the major lithologies of seafloor sediments in the world's ocean basins (Dutkiewicz et al., 2015). This assumption is based on the notion that $\varepsilon_{\mathrm{Nd}}$ from a possible benthic flux is related to the signature and reactivity of the underlying detrital sediment, and sediments of the same lithology type likely have similar diagenetic environments. Similar to the digital geological map used for continental margin $\varepsilon_{\mathrm{Nd}}$ (Sect. 2.2.2.2), this provided a spatially delimited mask of polygons capturing the broad distribution of seafloor sediment types. We used this mask to inform the interpolation of discrete data onto a continuous high-resolution grid by constraining the nearest-neighbour extrapolation of individual measurements to keep within the limits of each polygon. Thus, we implicitly assume that proximal sediments of the same depositional type contain similar Nd characteristics, with hard boundaries where the sediment type changes, although there is no imposed relationship between distal polygons of the same sediment type in this objective numerical method.

Diagenetic reactions in sedimentary deposits are reliant on the properties of the depositional environment. Biogenic debris in particular are often inherently unstable, with organic matter, carbonate and opaline silica as dominant biogenic solids involved in early diagenetic reactions (Jahnke et al., 1989). Thus, the contribution of particular biogenic phases to early diagenetic processes is highly complex and requires a thorough understanding of the behaviour of each biogenic component and the depositional environment in which digenesis occurs. Recent pore water and water-column [Nd] observations from the Tasman Sea have highlighted the possibility that regions dominated by biogenic carbonates can be important contributors to the global benthic flux (Abbott et al., 2019). Due to low [Nd] in biogenic sediments, these sediment regions had previously been dismissed as a likely contributor to the oceanic Nd budget (Abbott et al., 2015b). However, a diffusive flux of Nd calculated in this region, although smaller, was similar in magnitude to that measured in the low-carbonate samples measured from the North Pacific. Such data may provide evidence for expanding the area over which we consider the benthic flux to be an important contributor to marine $\varepsilon_{\mathrm{Nd}}$, and further suggests that a benthic flux may be driven by a small fraction of the sediment (i.e. dissolution of clay fraction) (Abbott et al., 2019; Abbott, 2019; Huck et al., 2016).

In order to enable the testing of a global benthic flux, an $\varepsilon_{\mathrm{Nd}}$ signature therefore needs to be assigned to all depositional sedimentary environments. Here, we chose not to make assumptions regarding early diagenetic reactions and how they might alter Nd fluxes within different depositional environments, and instead applied the same method to characterise all sediment $\varepsilon_{\mathrm{Nd}}$. This approach was adopted in order to limit the complexity of a method that is necessarily based on sparse data, including reducing the number of

arbitrary assumptions we would otherwise be required to make. This has the benefit of producing a more reproducible data product and methodology, which can then be adapted by any user in the community according to our evolving understanding of the role of particular biogenic phases in early diagenetic processes, the role of a benthic flux within diverse sediment compositions and depositional environments, and the wider acquisition of suitable measurements. Note, that for pore water measurements, we use the mean of all depths in the upper 11.1 cm of seafloor sediment for each site, representing all available data (see Supplementary Table S4). This seems justified as the average $\varepsilon_{\mathrm{Nd}}$ of pore water is found to be near constant with depth at each site (Abbott et al., 2015a).

In certain poorly documented areas and where the interpolation failed to capture a representative $\varepsilon_{\mathrm{Nd}}$ based on what is known to exist, manual adjustments were made. These modifications follow a similar approach to that described in Sect. 2.2.2.2 and are based on available observational and expert evidence, including (i) consideration of the source and location of detrital input to the region, (ii) the assumption that the mathematical means of the available data best represent domains containing a large number of data points, and (iii) spatially constraining localised extreme $\varepsilon_{\mathrm{Nd}}$ signals, e.g. from volcanic island arcs, which are not always captured in the mask of major sediment lithologies. All changes are explained in Supplementary Information (Sect. 2.6); Text S2.4 (with precise operational detail for how to implement/revert them in Supplementary Table 2.3), alongside graphical depictions of the new gridded seafloor $\varepsilon_{\mathrm{Nd}}$ dataset that show the direct output of the numerical interpolation schemes before expert manual adjustments were made compared with the refined version (Supplementary Fig. 2.10). Figure 2.3b shows our final, refined representation of the $\varepsilon_{\mathrm{Nd}}$ of seafloor sediment.

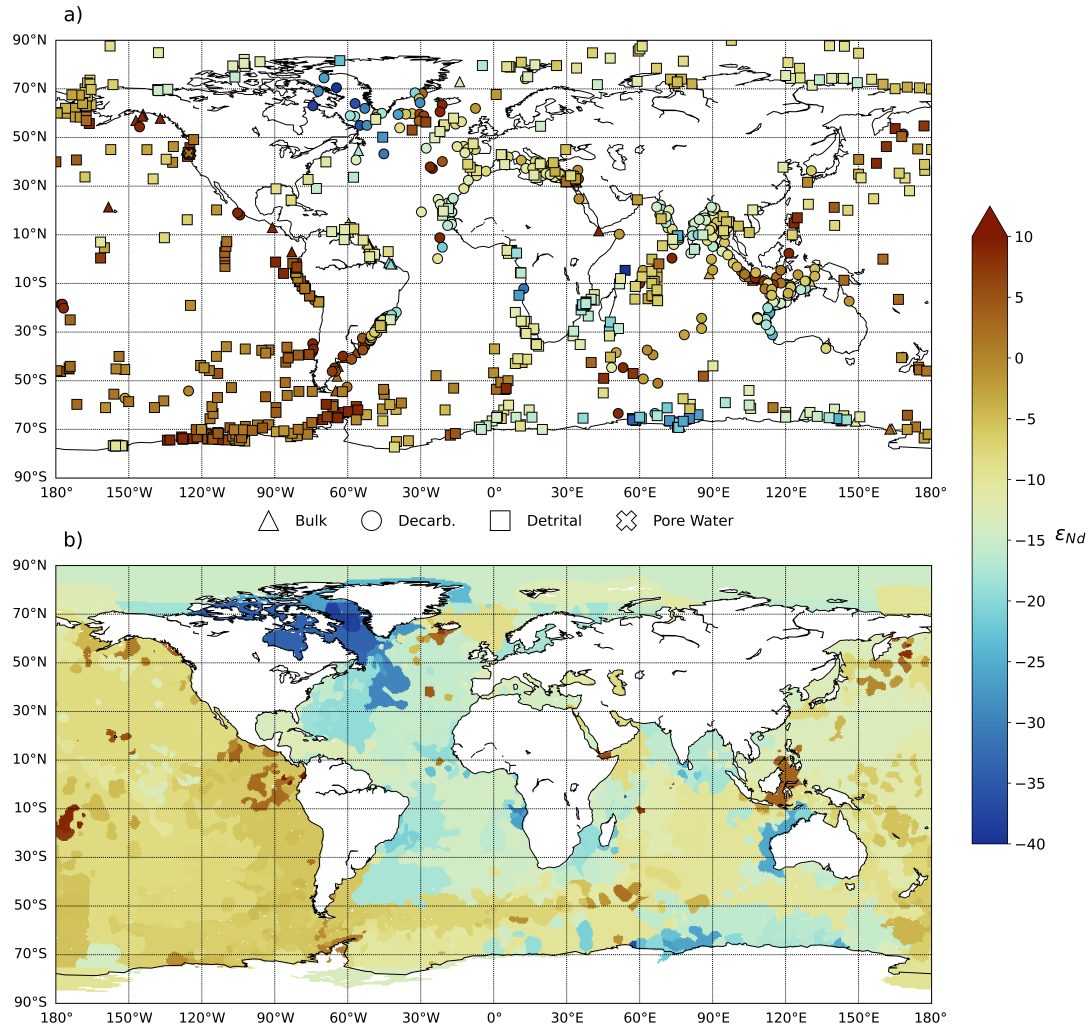

Figure 2.3: Seafloor sediment $\varepsilon_{\mathrm{Nd}}$ map. (a) Location and $\varepsilon_{\mathrm{Nd}}$ of the discrete marine detrital and pore water data compiled in Supplementary Table S4 and used to produce a best estimate of spatially continuous seafloor $\varepsilon_{\mathrm{Nd}}$. The three broad sample types of marine detrital and pore water data included in the compilation are indicated: bulk sediment digests (triangles), decarbonated sediment residuals (circles), specific detrital size fractions (squares), and pore water measurements (crosses). (b) Spatially continuous seafloor $\varepsilon_{\mathrm{Nd}}$ representation interpolated from the discrete data.

2.3 Results

2.3.1 Continental $\varepsilon_{\mathrm{Nd}}$ representation

Similar to Jeandel et al. (2007), we focused our spatially continuous reconstruction of continental $\varepsilon_{\mathrm{Nd}}$ on the regions surrounding the ocean (as shown in Fig. 2.2b), since the main purpose is to provide updated information for examining *marine* Nd cycling. Thus, the continental interiors are largely omitted from our final $\varepsilon_{\mathrm{Nd}}$ distribution.

Examination of the variability in our updated map of continental $\varepsilon_{\mathrm{Nd}}$ reveals the expected pattern of the most negative values corresponding to known provinces of the oldest unradiogenic continental rock worldwide (e.g. the exposed Archean rock comprising the North Atlantic Craton around southwestern Greenland and Paleoproterozoic granites

which constitute the Rae Craton that forms Baffin Island and parts of western Greenland), and positive values corresponding to young volcanic arcs (e.g. convergent margin volcanism in the northwest Pacific) and hotspot/ocean island volcanics (e.g. the Hawaiian Islands Archipelago, the Samoan Islands and the Kerguelen Islands).

For instance, in the high northern latitudes, continental crust surrounding the Hudson Bay and Labrador Sea in eastern Canada and western Greenland display largely unradiogenic ε_{Nd} values of -25 due to the presence of old Archean and Proterozoic units. This characterisation of very negative (-25) ε_{Nd} has been observed recently in a regional North Atlantic marginal ε_{Nd} map produced utilising compiled Holocene bulk surface sediments by Stichel et al. (2020). Similarly, here, the most unradiogenic signals correspond particularly to crust exposed on the North Atlantic Craton, where these lithological units are amid some of the oldest rocks worldwide. Previous investigations from Innocent et al. (1997) on modern and late Quaternary sediments in the northwest North Atlantic further highlight the most unradiogenic ε_{Nd} signals (ranging from -35 to -24) within sediments from terrains belonging to the North American Shield, particularly Baffin Island, Quebec and Labrador regions. Accordingly, these regions are characterised in our continental representation by ε_{Nd} ranging -32 to -23. Conversely, recent volcanic intrusions associated with the younger Cenozoic mafic rocks in Iceland and from the Nansen Fjord in East Greenland yield radiogenic ε_{Nd} signatures ranging from +4 to +7. In particular, exposed Holocene basalts on the continental shelf associated with Icelandic volcanism results in a radiogenic signal of +7 over Iceland, a value consistent with the first-order estimation of the Icelandic detrital Nd source signal to the ocean from Innocent et al. (1997) of +8. Material eroded from Iceland has particularly high [Nd], and so even a small contribution from this mafic sediment to seawater can have an important role governing Nd distributions here and thus an important region to characterise (Stichel et al., 2020).

The Arctic Archipelago displays an east-west gradient in ε_{Nd}, with unradiogenic ε_{Nd} values of -23 in the southeast associated with the oldest rocks of Archean and Proterozoic origin and less unradiogenic ε_{Nd} values of -12 towards the northwest of the archipelago related to Palaeozoic crust. Continental crust of lower Palaeozoic origin in northern Alaska has unradiogenic values of -14 and in northeast Siberia, proximal to the East Siberian Sea, younger Mesozoic units have more radiogenic values of -7. Asahara et al. (2012) analysed detrital fraction ε_{Nd} from marginal sea sediments in the Arctic to identify sources of terrigenous detritus in the Bering and Chukchi Seas. The authors found ε_{Nd} in detrital fractions in the Chukchi Sea range from -10 to -8, which they attributed to terrigenous detritus material derived from north-eastern Siberia (-9), and additionally from the Mackenzie River basin including the Canadian Shield (-14). Detrital fractions in the eastern Bering Sea are varied, though generally more radiogenic (-9 to +3), representing terrigenous input from the Yukon basin, underlain by Mesozoic and Palaeozoic rocks from Alaska (-9) and the Aleutian-arc volcanics (+7). Our continental representation in this region corresponds well to these previous estimations, suggesting that the spatial heterogeneity within continental ε_{Nd} in this region is captured reasonably well, which is especially important for the Arctic Ocean, whose water column Nd distributions are distinctly and generally influenced by the broad, surrounding continental shelves (Porcelli et al., 2009).

There is less spatial ε_{Nd} variability in the rest of the Siberian margin, central and southern Europe, and North, West and South Africa, which all display a relatively spatially homogenous ε_{Nd} signal between -11 and -7, with the more radiogenic values associated with widespread Cenozoic and Mesozoic rocks in these regions. A previous study by Revel et al. (1996) measured the ε_{Nd} of lithogenic particles from a sediment core in the Icelandic basin to trace its detrital origin. The authors reported ε_{Nd} of -12 originating from the British Isles, a value consistent with our characterisation (-12 to -11). Measurements from Scandinavia, on the other hand, are quite unradiogenic, with the most negative ε_{Nd}

values of -23 found in Archean rock in Finland and values of -22 to -14 in Proterozoic rocks within Norway and Sweden. These unradiogenic values correspond to findings by Bayon et al. (2015) who assessed the $\varepsilon_{\mathrm{Nd}}$ of sediments collected in Finland near the Kiiminkijoki river mouth, which drains the Precambrian shields of Fennoscandia, reporting $\varepsilon_{\mathrm{Nd}}$ of -23. Further, Revel et al. (1996) reported $\varepsilon_{\mathrm{Nd}}$ in lithogenic particles on the Norwegian margin around -19, consistent with our continental characterisation here.

Looking at the African continent, Scheuvens et al. (2013) reported bulk $\varepsilon_{\mathrm{Nd}}$ of dust in northern Africa to evaluate lithogenic sediments, measuring $\varepsilon_{\mathrm{Nd}}$ of -15 to -10 in Southern Algeria and northern Mali. Furthermore, samples collected off the west coast of northern Africa ranged between -16 and -8, these values are in agreement with our continental representation of this region (-14 to -13) illustrating the $\varepsilon_{\mathrm{Nd}}$ characteristics here have been effectively captured. On the other hand, north-eastern Africa displays quite a comprehensive picture of positive $\varepsilon_{\mathrm{Nd}}$, in particular around the Ethiopian Highlands and the Red Sea region, related to magmatic rifting (0 to +6). Overall, across the mainland of northern African a eastward tendency of increasing $\varepsilon_{\mathrm{Nd}}$ occurs. This gradient has been observed previously in detailed studies of terrestrial and marine sediments (Blanchet, 2019; Scheuvens et al., 2013).

The east coast of USA, Brazil and Uruguay are similar in regard to the intermediate values across the majority of Europe and West Africa, with $\varepsilon_{\mathrm{Nd}}$ generally falling within the -14 to 10 range, here Caledonian and Hercynian rocks cover the majority of these continental areas and so share broadly similar $\varepsilon_{\mathrm{Nd}}$ characteristics (Jeandel et al., 2007). However, characterisation of the east American continent is based on few observations and may underrepresent the true spatial variability of those regions. Examining river sediment $\varepsilon_{\mathrm{Nd}}$ from the Amazon and Mississippi river mouths, Bayon et al. (2015) reported values of -11 and -12 to -11 respectively, which correlate well with the continental $\varepsilon_{\mathrm{Nd}}$ interpolation at the location of these two river mouths. This is an important feature to capture, because these large river systems deliver large inputs of terrestrial particulate material to the ocean.

The geology of the west coast of the Americas and throughout central America is complex, associated with divergent and transform boundaries. Nonetheless, $\varepsilon_{\mathrm{Nd}}$ measurements on the Pacific Rim are consistently radiogenic, ranging from around +2 to +10 in the Cenozoic units there. Grasse et al. (2012) reported radiogenic measurements of $\varepsilon_{\mathrm{Nd}}$ (-2 to +3) and increased [Nd] in surface waters in the Eastern Equatorial Pacific, indicating exchange with either volcanic particles in the water column or highly radiogenic shelf sediments. These surface waters are characterised by increasingly radiogenic $\varepsilon_{\mathrm{Nd}}$ as we head northwards up the coast from Peru to Ecuador. A radiogenic gradient in continental $\varepsilon_{\mathrm{Nd}}$ is also represented here, ranging from -5 in Peru to +7 in Ecuador. Out in the Pacific, the Hawaiian island chain and other active volcanic island chains yield $\varepsilon_{\mathrm{Nd}}$ values at the top end of our scale (+8 to +10). Here, values for the volcanic islands on the Hawaiian plume (+7 to +9) are in agreement with present day (0 ka) $\varepsilon_{\mathrm{Nd}}$ measurements compiled and summarised by Bryce et al. (2005), with mean $\varepsilon_{\mathrm{Nd}}$ values measured on Mauna Loa (+5), Hualalai (+6), Kilauea (+7) and Mauna Kea (+8). The detail of these small volcanic island chains (including Hawaii, Tahiti, Gallapagos, etc.) is not fully evident in the global image shown in Fig. 2.2b, but can be accessed by downloading the high-resolution vector datasets accompanying this study (Supplementary Dataset S1).

India and Sri Lanka are characterised by a relatively homogenous unradiogenic $\varepsilon_{\mathrm{Nd}}$ signal of -16 associated with Proterozoic and Pan-African rocks. Chemical weathering of the Himalayan system exports large sediment loads to coastal regions via the Ganges-Brahmaputra Rivers. Lupker et al. (2013) compiled measurements of $\varepsilon_{\mathrm{Nd}}$ in river sediments in the Ganges and Brahmaputra Rivers highlighting unradiogenic values of -18, and a range of -14 to -19 respectively. Our continental characterisation in margins surrounding the Bay of Bengal (-15) falls within the range of $\varepsilon_{\mathrm{Nd}}$ characteristics from these major river systems. Moreover, Thailand, with predominantly upper Palaeozoic units,

is characterised by values of -14, and younger crust (predominantly of Mesozoic origin) comprising Cambodia and Vietnam have values of -9. A previous study by Peucker-Ehrenbrink et al. (2010) explored the relationship between bedrock lithology and age to estimate the ε_{Nd} of large-scale continental drainage regions. Here, the ε_{Nd} of Southeast Asia was estimated to be -14. Palaeozoic crust in North and South Korea yield more unradiogenic ε_{Nd} values of -20 to -16, whereas Japan, Indonesia and the Philippines bear a very radiogenic signal around +5, associated with active plate tectonics and recent Cenozoic formations. The basaltic composition of numerous islands located in the southwestern inter-tropical Pacific (e.g. Papua New Guinea, Solomon Islands, Fiji) yield radiogenic ε_{Nd} (ranging +5 to +7). Grenier et al. (2013) compiled ε_{Nd} data from rock and sediment samples to characterise the average ε_{Nd} of such islands. Radiogenic mean ε_{Nd} of +8, +7 and +8 were attributed to Fiji, Vanuatu and Tonga respectively, in accordance with our representation of ε_{Nd} here. The authors further suggest that these islands provide an important lithogenic supply of radiogenic ε_{Nd} to the southwestern Pacific. In comparison, the geology of Australia is broadly characterised by several Archean and Middle Proterozoic cratons, with younger formations of Phanerozoic age occurring mainly in north Australia (Ehlert et al., 2011). In our continental ε_{Nd} representation, north-eastern and eastern Australia and Tasmania display a relatively homogenous signal with Cenozoic and Mesozoic rocks dominating, and thus yielding values of around -8 to -6. The presence of Proterozoic to Archean units in north-western Australia and southern Australia provide two relatively spatially constrained regions of quite unradiogenic ε_{Nd} (-20 to -15).

Antarctica displays a high degree of spatial heterogeneity, this heterogeneity has been observed previously in studies documenting the variability of Antarctic sediment sources using $^{40}Ar/^{39}Ar$ ages and bulk $< 63\mu$m Sm/Nd isotopes (Roy et al., 2007; Simões Pereira et al., 2018). This observed systematic variability is in agreement with known major geological events that characterise Antarctica's bedrock. Broadly the geology of Antarctica is naturally divided into East and West Antarctic domains, East Antarctica is a complex Precambrian craton comprising Archean terrains separated by Proterozoic units, while West Antarctica is characterised through abundant late Mesozoic-Cenozoic intrusive volcanic rocks around Palaeozoic and Mesozoic crust (Roy et al., 2007). In our continental ε_{Nd} representation here, the most unradiogenic values occur across East Antarctica, with a general signal around -20 within predominantly Proterozoic and Archean crust, the most unradiogenic signal of -38 is found within the Archean units of Enderby Land. Radiogenic values around -5 are found in West Antarctica, representing younger crustal ages of Mesozoic and Cenozoic rock, with the most radiogenic signal in this region (+5) occurring within Cenozoic and extrusive volcanic rocks on the Antarctic Peninsula. Intermediate values occur in our characterisation of continental and marginal rocks surrounding the Weddell Sea (-14) and the Ross Sea (-8). In these regions, there is a degree of variability among Holocene marine sediments (ranging -10 to +2 [detrital fraction] and -28 to 11 [in decarbonated and detrital fractions] within the Weddell Sea and Ross Sea respectively), which is important, because they are the main sample types used to characterise these regions. In the Weddell Sea, this variability likely represents detrital contributions from proximal rocks off the Antarctic Peninsula (in the absence of continental samples, the nearest marine sediments [detrital fraction] to these rocks range from -6 to +1), and bordering crust from East Antarctica (nearby marine sediments [detrital fraction] to the continents range -15 to -10). In the Ross Sea, the variability likely reflects detrital inputs from the bordering continental crust of East Antarctica (-15 to -6 in bulk rock samples) and West Antarctica (-9 within bulk rock samples).

2.3.2 Seafloor ε_{Nd} representation

Consistent with the distribution of continental ε_{Nd}, the most unradiogenic sediment in our seafloor compilation (summarised in Fig. 2.3b) is found in the northernmost North

Atlantic sector, specifically in Baffin Bay, the Hudson Bay and the Labrador Sea, where $\varepsilon_{\mathrm{Nd}}$ values range from approximately -28 to -25, reflecting deep-sea detrital input from surrounding unradiogenic continental crust. Similarly, but at the opposite end of the scale, more radiogenic $\varepsilon_{\mathrm{Nd}}$ of +3 to +7 is observed in the ocean sediment surrounding Iceland as a result of detrital input from recent volcanism. Further south and away from the coast, our interpolation produces a generally more moderate $\varepsilon_{\mathrm{Nd}}$ signal of -13 to -11 in the Atlantic Ocean sediments. The Gulf of Mexico/Caribbean Sea contain some of the more radiogenic sediments (-10 to -9), but otherwise in the open Atlantic, there is a slight gradient from more unradiogenic values in the northwest to more radiogenic values approaching the Southern Ocean and Namibia/South Africa in the southeast. However, we note that the deep Atlantic Ocean is the most data sparse region in our database, especially in the open South Atlantic. Further data acquisition in this area could alter our results.

The Mediterranean region is data rich, due to the detailed wealth of published observations gathered by Blanchet (2019) in addition to detrital measurements accompanying the data presented by Tachikawa et al. (2017). The Mediterranean Sea is mainly characterised by an unradiogenic sediment signal of -11, consistent with the majority of observations here, with an exception being in the east of the basin, located north of Egypt, at the mouth of the Nile River. Here, multiple observations range from -5 to -2 and the area is broadly characterised by an $\varepsilon_{\mathrm{Nd}}$ signal of -3. These higher values trace the delivery of radiogenic sediments by the Nile River to the Eastern Mediterranean from Cenozoic volcanic plateaus of the Ethiopian Highlands (Fielding et al., 2017). The Mediterranean Sea communicates with the eastern North Atlantic via the Strait of Gibraltar, with Mediterranean Outflow Water believed to be an important modulator of the North Atlantic salt budget (Tachikawa et al., 2004; Voelker et al., 2006). This water mass forms seasonally in the east of the basin, where an $\varepsilon_{\mathrm{Nd}}$ gradient towards more radiogenic values occurs, and is thus an important feature for understanding the sediment-water interaction on the $\varepsilon_{\mathrm{Nd}}$ of Mediterranean Outflow and Atlantic Surface Water in the Mediterranean (Ayache et al., 2016; Tachikawa et al., 2004).

In the Indian Ocean, as already described in Sect. 2.3.1, unradiogenic detrital sediment is sourced by chemical weathering in the Himalayan system transported to the oceans via the Ganges-Brahmaputra Rivers (Lupker et al., 2013), and provides a localised source of -14 in the Bay of Bengal, a similar signal also persists close to the western coast of India. Notwithstanding, most of the Indian Ocean away from the continents is characterised by a more intermediate signal ranging from -9 to -7. In proximity to the western coast of Australia, the $\varepsilon_{\mathrm{Nd}}$ of clay size sediment fractions range from -22 to -8, a result of erosional supply off adjacent landmasses and surface hydrography, with the most unradiogenic (decarbonated) detrital sample (-22) off Cape Basin reflecting riverine input of weathered Archean rock from the Pilbara Craton (Ehlert et al., 2011). Overall, the seafloor sediment in this region is characterised by an $\varepsilon_{\mathrm{Nd}}$ of -21 due to the transport of weathered fine-grain material from coastal Proterozoic and Archean regions of northwest and west Australia, by the southward flowing Leeuwin Current, which is the dominant poleward near-coastal current in this region (Ehlert et al., 2011).

Much more radiogenic signals (+4) are observed surrounding Indonesia and the Philippines, reflecting detrital input derived from surrounding radiogenic Cenozoic units forming the Indonesian Archipelago, particularly arc, hotspot volcanics and oceanic plateaux in eastern Indonesia (in particular, the Ontong Java Plateau), and further detrital input from the Philippine Islands, one of the main sources of deep-sea sediment in the west Philippine Sea (Hall, 2002; Zhang et al., 2020). Radiogenic signals (+6) are observed locally in the Arabian Sea of the Indian Ocean surrounding the Maldives, caused by detrital input from the Maldives and surrounding basalts underlying the atolls, which formed in the Mesozoic Era (Gischler, 2006). In the western and north-central Pacific, aeolian dust

from Asia, the second largest dust source area on Earth, contributes significant terrigenous material to the seafloor (Han et al., 2011; Nakai et al., 1993), providing an ε_{Nd} signal of approximately -10. On the other hand, eastern Equatorial and South Pacific sediments are more radiogenic, ranging from -6 to -4 in the deep ocean, with more radiogenic signals observed closer to the continents and on the circum-Pacific ring of fire.

For the high latitudes, in the Arctic Ocean, away from the continental margins, the seafloor has an ε_{Nd} of -12, consistent with the majority of detrital observations here. In the basin of the Chukchi Sea, ε_{Nd} is -7, influenced here by terrigenous detrital input from north-eastern Siberia, input from the Yukon River via Bering Strait inflow and from the Mackenzie River Basin containing input from the Canadian Shelf (Asahara et al., 2012; Haley and Polyak, 2013). Surrounding the western edge of the broad Eurasian shelf and Svalbard seafloor sediment ε_{Nd} is -10, whereas north of Greenland ε_{Nd} is characterised by a more unradiogenic signal of -20, resultant from detrital input from surrounding continental sources (Maccali et al., 2013). The Nordic Seas have a predominant ε_{Nd} signal ranging from -13 to -11, with a less negative signal (-6) observed in ocean sediment within the Irminger Basin, associated with detrital input from mafic source rock from Iceland and Western Greenland (Stichel et al., 2020). Based on the available data, we characterise much of the Southern Ocean seafloor ε_{Nd} to have a relatively intermediate signature (typically -8 to -5), but with more unradiogenic values of -12 proximal to East Antarctic shorelines and more radiogenic values of around -4 surrounding West Antarctica.

2.4 Discussion

2.4.1 Combined representation of the ε_{Nd} signal at the sediment-water interface

In this study, we have presented an updated compilation of current measurements of a range of possible sources of Nd isotopes to the ocean, and we have used this new synthesis to produce a spatially continuous dataset of seafloor and continental margin ε_{Nd}. In so doing, we provide suitable data products to facilitate a step-change in our ability to address outstanding questions concerning marine Nd cycling (e.g. through new conceptual or three-dimensional ocean modelling) and a methodology for reproducing/adapting our results.

The possible existence of a benthic flux of Nd to overlying waters, or simply a less spatially constrained boundary exchange at the sediment-water interface than has previously been adopted in most modelling studies (Arsouze et al., 2009, 2007; Gu et al., 2019; Rempfer et al., 2011) brings forth the requirement for global mapping of seafloor ε_{Nd}. We undertook this exercise, utilising all of the available data that we are aware of at the time of writing to produce our final, spatially continuous distribution (Fig. 2.3b). However, we acknowledge that we may have missed some sites, and we hope that when spotted, others will contribute these to the continually evolving database first published by Blanchet (2019). There are most certainly underrepresented regions in our compilation of measurements – notably, huge swathes of the open Atlantic Ocean, deep Pacific, and southern Indian Ocean – which we hope may become better represented in time (notwithstanding the practical difficulties associated with very deep ocean sampling), thus enabling a more thorough capturing of the spatial distribution of seafloor ε_{Nd}. Furthermore, as research continues, it may become more practical to further filter the available data to use only the most suitable sediment sources (ultimately, pore waters or specifying precisely the labile Nd fractions; see discussion in Sect. 2.2.3.1, above). Nonetheless, it is a testament to the hard work of the wide research community that so many observations do already exist, enabling us to produce our best estimate of seafloor ε_{Nd} from these data.

The final step is to bring the two data products together, and Fig. 2.4 shows our combination of the continental margin and seafloor $\varepsilon_{\mathrm{Nd}}$ distributions. This dataset can be considered to be our best estimate of the global distribution of $\varepsilon_{\mathrm{Nd}}$ at the entire sediment-water interface to date. To produce this final characterisation of global seafloor sediment $\varepsilon_{\mathrm{Nd}}$ distributions, we used the continental $\varepsilon_{\mathrm{Nd}}$ map extrapolated to where sediment thickness $\geq 1,000$ m, and the remaining sediment regions are represented using the seafloor $\varepsilon_{\mathrm{Nd}}$ map. The signal varies spatially, but in *very* general terms, the North Atlantic provides an unradiogenic signal, intermediate values occur in the Indian and Southern Oceans, and the most radiogenic values occur in the Eastern Equatorial Pacific, Southern Pacific, and circum-Pacific ring of fire.

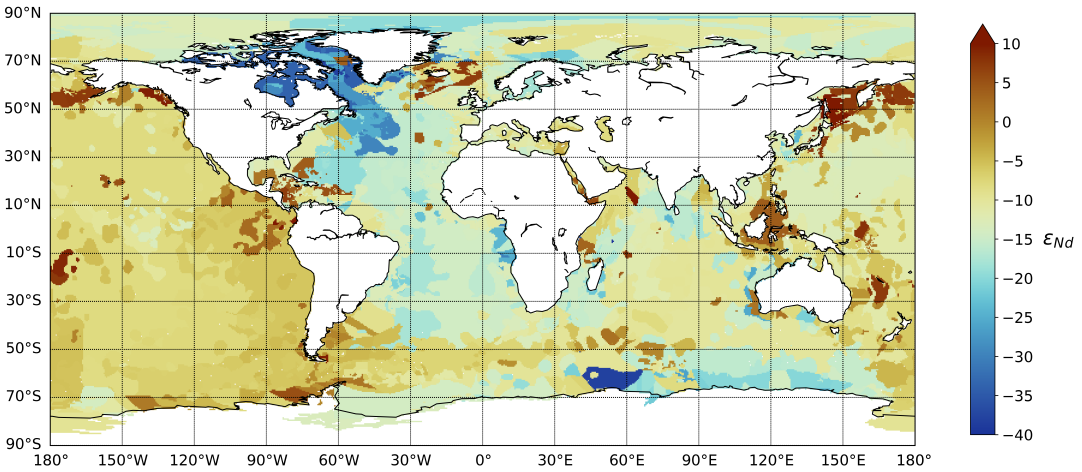

Figure 2.4: Nd isotope signature of the global sediment-water interface, showing the combination of the seafloor $\varepsilon_{\mathrm{Nd}}$ and the continental margin $\varepsilon_{\mathrm{Nd}}$ maps. This final characterisation of global $\varepsilon_{\mathrm{Nd}}$ distributions at the sediment-ocean interface uses the continental $\varepsilon_{\mathrm{Nd}}$ map extrapolated to where sediment thickness $\geq 1,000$ m, and the remaining sediment regions are represented using the seafloor $\varepsilon_{\mathrm{Nd}}$ map.

2.4.2 Comparison with previous compilation of continental margin $\varepsilon_{\mathrm{Nd}}$

Fig. 2.5 shows the difference in $\varepsilon_{\mathrm{Nd}}$ between the previous, seminal map of continental $\varepsilon_{\mathrm{Nd}}$ produced by Jeandel et al. (2007) and the new distribution presented here. With positive [negative] values showing regions where our newer $\varepsilon_{\mathrm{Nd}}$ representation has a more radiogenic [unradiogenic] signal compared with the previous map. In this section, we discuss key updates to the original continental $\varepsilon_{\mathrm{Nd}}$ map, addressing improvements and further illustrating regions where data limitation causes outstanding uncertainty. Overall, our updated compilation has vastly increased the number of suitable continental $\varepsilon_{\mathrm{Nd}}$ observations and also improved the spatial coverage of $\varepsilon_{\mathrm{Nd}}$ observations, with an extra 855 samples in addition of those used in Jeandel et al. (2007). This has enabled a more data constrained representation of continental $\varepsilon_{\mathrm{Nd}}$ (see Supplementary Fig. 2.12).

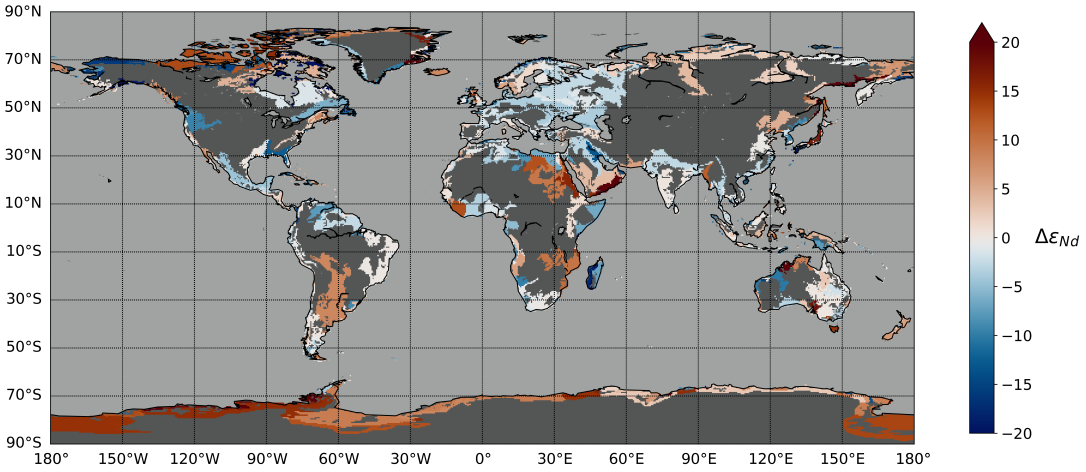

Figure 2.5: Difference in $\varepsilon_{\mathrm{Nd}}$-units between the continuous representation of continental $\varepsilon_{\mathrm{Nd}}$ presented in this study and the previous map produced by Jeandel et al. (2007). Positive [negative] values show regions where our newer $\varepsilon_{\mathrm{Nd}}$ interpolation has a more radiogenic [unradiogenic] signal compared with the previous map; no data regions are coloured dark grey (land) and light grey (ocean).

Broadly in comparison to Jeandel et al. (2007), the new continental $\varepsilon_{\mathrm{Nd}}$ map is more radiogenic in the Arctic Shield, Northern Eurasia, South America, north-eastern Africa and Antarctica, and has more unradiogenic values over southern Greenland, north-eastern Europe, western and eastern Africa and parts of the Americas. Jeandel et al. (2007) noted that in the previous $\varepsilon_{\mathrm{Nd}}$ representation, certain regions were data limited and so broad estimations had to be made, for example continental rock in Alaska, northern Eurasia, Pakistan, Cameroon, Somalia and Brazil. In Fig. 2.6, we show the new continental $\varepsilon_{\mathrm{Nd}}$ representation in regions where we consider a higher number of observations have improved the characterisation of $\varepsilon_{\mathrm{Nd}}$ relative to Jeandel et al. (2007), as explained in more detail below, with a particular focus on regions considered important for deep-water formation and thus potential $\varepsilon_{\mathrm{Nd}}$ labelling of water masses by continental erosion.

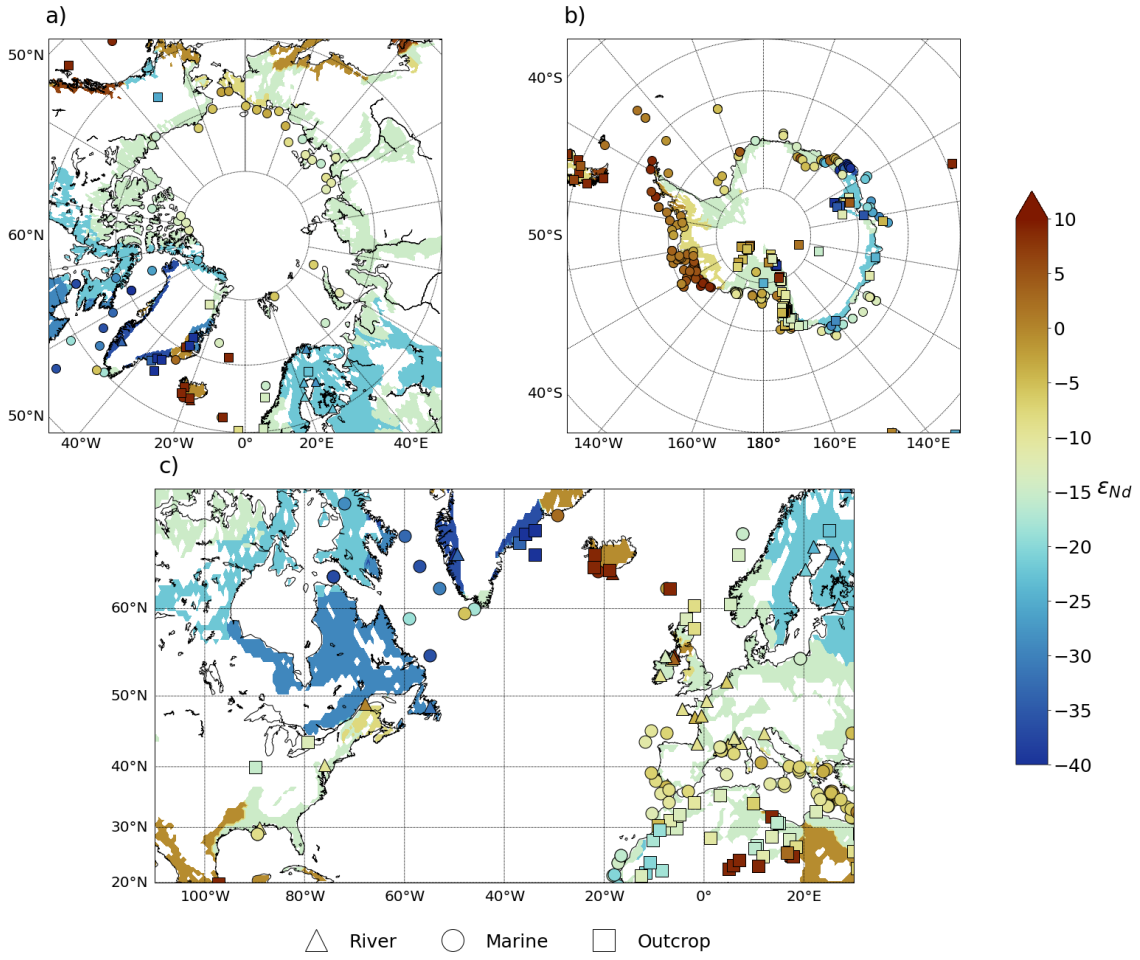

Figure 2.6: Regional analysis of the new continental $\varepsilon_{\mathrm{Nd}}$ map, with particular focus on regions important for deep-water formation and thus potential $\varepsilon_{\mathrm{Nd}}$ labelling of water masses by continental erosion. The displayed regions have reduced uncertainty in the characterisation of $\varepsilon_{\mathrm{Nd}}$ relative to the original maps produced by Jeandel et al. (2007, not shown) in large part due to an increased number of observations. (a) The polar Arctic region, (b) Antarctica, and (c) the North Atlantic, overlain by the discrete $\varepsilon_{\mathrm{Nd}}$ measurements used in the interpolation presented here and also indicating the three broad sample types included in the new compilation: river sediment (triangles), marine sediments (circles), and geological outcrops (squares). For further context, an equivalent version for the new complete $\varepsilon_{\mathrm{Nd}}$ representation of the sediment-ocean interface (i.e. including the whole ocean floor), both from the seafloor-only data and from combining the seafloor and continental interpolations based on sediment thickness (see Sect. 2.4.1), is provided in Supplementary Fig. 2.13.

Newly compiled observations around the Arctic within this study (Fig. 2.6a) have led to a more detailed representation of the continental $\varepsilon_{\mathrm{Nd}}$ in the new map. This was a particular region of uncertainty in Jeandel et al. (2007), especially across northern Alaska and north-eastern Eurasia where there were previously no observations. These areas now have a multitude of continental measurements and the region is characterised by a more radiogenic signal than was previously estimated, with the signal from northern Alaska updated from -29 to -15 and north-eastern Eurasia from -14 to -12. The additional seafloor $\varepsilon_{\mathrm{Nd}}$ map adds further previously uncharacterised detail to the region, utilising additional marine detrital samples from seafloor sediment in the Arctic (shown Supplementary Fig. 2.13a). Here, the Arctic seafloor sediment-water interface is broadly characterised by an $\varepsilon_{\mathrm{Nd}}$ of -12, with more unradiogenic marginal values (-20) north of the Canadian Shield

and northern Greenland.

A large contrast and increased spatial detail occur in the Antarctic region (Fig. 2.5), driven by the greater number of observations now available (Supplementary Fig. 2.12). Fig. 2.6b highlights the improved data density and coverage of observations, particularly in East Antarctica (notably around Prydz Bay and Enderby Land), Victoria Land, the Ross Ice Shelf and the Antarctic Peninsula (especially to the west of the peninsula, surrounding the Bellingshausen Sea). Enhanced availability of data has enabled a better constrained characterisation of the ε_{Nd} of Antarctica. However, there still remains data scarcity around Ronne Ice Shelf in the Weddell Sea, and so our representation of ε_{Nd} is more uncertain here. In comparison to the Antarctic ε_{Nd} presented by Jeandel et al. (2007), the Antarctic Peninsula, the Ross Sea and the Weddell Sea are much more radiogenic in our interpolation of measured ε_{Nd}; +5, -8 and -14 respectively as opposed to the previous more homogenous estimate of -23. East Antarctica remains unradiogenic with values around -20, and the most unradiogenic signal (-38) occurs in the Archean Napier Complex of Enderby Land, East Antarctica.

Antarctic Bottom Water ε_{Nd} measured close to the Antarctic shelf is believed to be influenced by marginal sediment inputs, evidenced by increased [Nd] closer to the continent. Lambelet et al. (2018) found seawater measurements in proximity to the Antarctic coast also display spatial heterogeneity, carrying Nd isotope fingerprints that are characteristic of their formation area and consistent with the heterogenous ε_{Nd} signal presented in our continental representation. In this study, Adélie Land Bottom Water samples were found to reflect unradiogenic ε_{Nd} of surface sediments collected around East Antarctica, particularly detrital measurements from the Adélie Craton (-20). Ross Sea Bottom Water reflected the radiogenic fingerprint of West Antarctic lithologies, with detrital measurements ranging from -6 to +2 and newly formed Weddell Sea Bottom water was influenced by unradiogenic inputs from old continental crust in the East Antarctic part of the Weddell Embayment.

This better constrained representation of Antarctic and Southern Ocean ε_{Nd} may be an important update for understanding ε_{Nd} cycling in the ocean, especially if these data are used as boundary conditions for Nd isotope models. The updates from our compilation and interpolation are particularly useful because the formation of modern Antarctic Bottom Water (AABW), which is a key component of the global oceanic overturning circulation, forms predominantly in the Ross and Weddell Seas and around the much more unradiogenic East Antarctic margin from the Adélie Coast to Prydz Bay. Thus, here, the ε_{Nd} signal from the continents and seafloor sediment may exert a strong influence on seawater ε_{Nd} provinciality, as pointed out by Lambelet et al. (2018). Furthermore, the strength and location of the boundaries of the Antarctic Circumpolar Current (ACC) are important parameters for understanding the role of the Southern Ocean in global climate change (Hemming et al., 2007). For example, it has been suggested that glacial stratification and/or variations in sea-ice cover in the circum-Antarctic may play an important role in glacial variations in atmospheric pCO_2 (Sigman et al., 2004; Stephens and Keeling, 2000). In this context, northward displacement of the westerlies during glacial periods may have caused reduced ventilation of deep waters around the perimeter of Antarctica, possibly resulting in an important feedback loop for glacial-interglacial pCO_2 changes (Toggweiler et al., 2006). This may be the kind of circulation shift that will be easier to discern with an accurate and precise map of ε_{Nd} sources, helping to identify possible glacial northward shifts of the ACC major frontal boundaries, for example. Moreover, the evolution of grounded ice delivering large quantities of eroded sediment to the ocean may also be easier to interpret with well-characterised continental ε_{Nd}, shedding light on local-regional glacial dynamics. Although, it will always be challenging to determine the Nd (or other) characteristics of currently subglacial source material. In any case, further constraints on how sediment-water Nd interactions coupled with advection by

Southern Ocean currents determine seawater ε_{Nd} distributions, and how these may vary under modern/interglacial and glacial weathering regimes (including the ability to relate measured ε_{Nd} to seawater exposure time, and hence estimate possible deep storage in a highly stratified ocean), can assist in reaching an improved understanding of fundamental climate dynamics on glacial-interglacial timescales.

The important regulating role of the Atlantic Meridional Overturning Circulation (AMOC) on the global climate means that it is the focus of numerous Nd isotope studies aiming to reconstruct changes in Atlantic Ocean water mass mixing during the recent (and more distal) geological past, utilising geological archives (e.g. Howe et al., 2017; Lippold et al., 2016; Piotrowski et al., 2012; Roberts et al., 2010) and through Nd isotope-enabled climate modelling (e.g. Arsouze et al., 2010, 2008; Pöppelmeier et al., 2020b; Rempfer et al., 2012). The North Atlantic is thus an important region to characterise well, and in the new ε_{Nd} representation, there are a number of moderate updates (Fig. 2.5). Namely, continental rock to the north of Baffin Bay in north-western Greenland and further in southern Greenland generally has a more unradiogenic representation of -34, compared to -30 in Jeandel et al. (2007). Continental crust surrounding the south and east of the Hudson Bay remain mostly unchanged. However, rock to the north of the bay overall has a more radiogenic signal than previously estimated, the unradiogenic signal here has been changed from -27 to -23 within continental crust directly in contact with seawater here. Over northern Europe, Iceland now has a more radiogenic signal of +7 compared to 0 in the earlier map, but much of the continental crust in north-western Europe and in addition north-western Africa that is directly in contact with seawater remains largely unchanged.

The discrete ε_{Nd} measurements interpolated to produce the continental map in the north-western Atlantic (shown in detail in Fig. 2.6c) were mainly the same as used in Jeandel et al. (2007) (not shown here, see Supplementary Fig. 2.12), with a limited addition of samples added to the north of Baffin Bay and Greenland. However, in producing the novel complementary seafloor map, additional marine detrital samples were collected in this important region (Supplementary Fig. 2.13c), adding greater spatial representation of observations and thus additional constraints in the Labrador Sea and the North Atlantic Ocean to improve our overall characterisation of the sediment-water interface here. Again, these changes may be important when modelling water mass mixing or interpreting ε_{Nd} data in terms of ocean water provenance, the Labrador and Nordic Seas are known sites of North Atlantic Deep Water formation, thus northern-sourced waters in the Atlantic likely obtain their ε_{Nd} signature from weathering of this continental crust and interaction with seafloor sediment (e.g. Stichel et al., 2020).

A marked increase in observations throughout eastern and southern Europe (particularly the Mediterranean region), and much of the African continent has been achieved (Supplementary Fig. 2.12), which has directly addressed previous regions of data sparsity in the former compilation by Jeandel et al. (2007). For example, our new compilation includes river sediment measurements taken from the Sanaga Basin in Cameroon bordering the South Atlantic (Weldeab et al., 2011), an area which was previously absent of observations. Nonetheless, notable regions of data sparsity persist in our compilation, and thus there remains some significant uncertainty in our continental ε_{Nd} characterisation in those areas, which include eastern Africa (notably Somalia), Oman, Pakistan, western India and eastern Brazil. It is advised that in these regions, users consider this data limitation and uncertainty in ε_{Nd} when applying/interpreting results.

In summary, our new continental map has incorporated an extensive and up-to-date compilation of published ε_{Nd} observations. It has considerably improved upon the previous version, primarily through a vast increase in the number and spatial coverage of ε_{Nd} observations and directly addressing key regions of data scarcity. This now allows for more accurate and data-constrained interpretations of ε_{Nd} measurements, both in terms

of Nd cycling and for use as a water provenance and weathering tracer.

2.4.3 Improvements to previously utilised seafloor ε_{Nd} distribution

Du et al. (2020) noted some inaccuracies of previous model schemes for margin ε_{Nd} boundary conditions that represented a simplified characterisation of seafloor ε_{Nd} distributions produced by linearly extrapolating the data presented by Jeandel et al. (2007). In some locales, this technique did not appropriately capture the distribution suggested by core-top detrital measurements, for example extrapolating observations from southeast Greenland to a wider geographical area yielded extremely unradiogenic ε_{Nd} (-35) in the Irminger Sea where core-top measurements suggested a much more radiogenic signal (-5). Adopting a similar linear extrapolation approach, adding in further constraints by Blanchet (2019); Pöppelmeier et al. (2020b) imposed a global seafloor sediment ε_{Nd} map within a global Nd isotope enabled model. This was done to explore the possible role of a benthic flux in accurately simulating global marine ε_{Nd} and [Nd], and investigating regionally elevated benthic fluxes in the Northwest Atlantic to test how localised inputs of poorly weathered detrital material could explain the observed early Holocene seawater ε_{Nd} anomaly (Howe et al., 2017; Lippold et al., 2016; Pöppelmeier et al., 2020b, 2019). Through inclusion of a benthic flux, Pöppelmeier et al. (2020b) found an improved global modern model-data fit for [Nd] was produced relative to previous schemes, as well as an equivalent level of skill in predicting seawater ε_{Nd} compared to previous studies.

With the addition of over 3,500 extra observations to the initial Nd compilation by Blanchet (2019), including an additional 842 relevant Holocene samples than utilised in this most recent study from Pöppelmeier et al. (2020b), we have vastly increased the number and the spatial coverage of appropriate observations in order to characterise the ε_{Nd} of the entire sediment-water interface. This particularly includes the addition of more distal seafloor detrital observations, notably covering the eastern North Atlantic, Central Pacific, northern Indian Ocean and the Southern Ocean (Fig. 2.1). As a result, we have overcome, or at least greatly limited the occurrence of extrapolation biases highlighted in previous model boundary conditions within our new, detailed and constrained seafloor ε_{Nd} maps. Furthermore, in producing a broadly representative global seafloor ε_{Nd} distribution, under the consideration of margin-seafloor continuity and inclusion/application of state-of-the-art knowledge within our methodology (though acknowledging the limitations of persistent data scarcity), we have improved markedly upon earlier work. For example, our seafloor ε_{Nd} representation in the Irminger Sea is -6, which is more consistent with local core-top observations and representative of radiogenic detrital input from the Iceland hotspot. The unradiogenic signal of -23 and -33 associated with Proterozoic and Archean crust respectively in southeastern Greenland, which has previously been extrapolated out to the Irminger Sea, is now constrained to coastal margins. Furthermore, in the seafloor sediment boundary conditions presented by Pöppelmeier et al. (2020b), extrapolation of observations from the Antarctic into the deep South Pacific Ocean give it a very unradiogenic signal of -20, whereas our more radiogenic ε_{Nd} characterisation of -6 is more consistent with detrital observations and with the geology of this area (i.e. proximity to the East Pacific Rise). We were able to achieve this improvement by refining the spatial variability around Antarctica compared to earlier work using a larger compilation (as discussed Sect. 2.4.2) and by including additional marine detrital observations in the South Pacific.

The presented seafloor ε_{Nd} maps therefore provide a considerable improvement upon previous simplified linear extrapolation methods. Our key ambition in this regard is to enable users ease of access to appropriate boundary conditions and thus to facilitate future improved model ε_{Nd} representation. By doing so, we hope to have empowered the community to progress our understanding of sediment-water interaction of Nd and further to build upon this established database, incorporating further understanding of

the sediment ε_{Nd} distributions and its role in governing the Nd characteristics of seawater.

2.4.4 Modelling applications and future work

We envisage that one of the major applications of our new ε_{Nd} distributions will be for designing/implementing the boundary conditions required for Nd isotope models. Such models could range in complexity from relatively simple box-models to full complexity general circulation models. What all have in common, is the need for pre-defined Nd sources. With the emergent (but still debated) benthic flux hypothesis, future models will require knowledge of the ε_{Nd} of seafloor sediment to be able to constrain a benthic flux and model the non-conservative processes involved in marine Nd cycling.

The new datasets presented in this study are therefore useful for further modelling applications like the research undertaken by Pöppelmeier et al. (2020b) in exploring sedimentary Nd sources. For example, they can be used to examine the nature and magnitude/rate of a benthic flux, and to produce quantitative estimates of a global benthic Nd flux into seawater. Our work will facilitate the community to build upon previous modelling efforts (Arsouze et al., 2009; Gu et al., 2019; Pöppelmeier et al., 2020b; Siddall et al., 2008b) and explicitly, quantitatively test the range of proposed major sources, sinks and internal cycling mechanisms that govern modern marine Nd distributions. In this way, our new maps, which span the whole ocean-sediment interface, can be employed to examine current paradigms in Nd cycling, including the geographical and geochemical extent of sediment-ocean Nd interactions, and additionally may be used to better estimate Nd ocean residence time. Specifically, it will be more straightforward to systematically explore the sensitivity of ε_{Nd} and [Nd] to different benthic source parameterisations and distributions. This could be achieved, for example, by (i) examining a range of sediment fluxes, (ii) exploring further regional elevated sources from poorly chemically weathered material, and/or (iii) estimating the non-conservative sedimentary processes and the validity of such schemes in producing realistic modern ε_{Nd} and [Nd] distributions. Our new maps additionally enable sensitivity tests in models to explore how physical changes to the strength and structure of ocean circulation impact marine ε_{Nd} and [Nd] under a bottom-up model of marine Nd cycling. Such investigations would undoubtedly provide useful information towards constraining marine Nd budgets, which is essential for robust interpretation and continued application of Nd isotopes as a useful tracer of ocean circulation.

The modern North Pacific represents a key location for testing the benthic flux hypothesis, and thus an important region for modelling applications since the first benthic flux measurements from Abbott et al. (2015b) were taken on the Pacific margin, providing direct evidence for a sedimentary Nd source here. Further, under modern sluggish circulation in the deep Pacific, and alongside detrital input of labile volcanic material into the region, we believe it is an important region to test the potential relabelling of bottom water masses by a benthic flux, and could even be suitable to explore the use of ε_{Nd} as a kinematic tracer. Our seafloor sediment ε_{Nd} distribution presented here now enables more detailed exploration within the Pacific, and thus may enable a new perspective on what could be considered a previously overlooked, but potentially important region for understanding global marine Nd cycling. Further, although not a modern region of deep water formation, the North Pacific may have been a significant contributor to global overturning at times in the past (e.g. Hague et al., 2012; Rae et al., 2014), here conceptual studies could be used to explore changes in ε_{Nd} distributions as a result of enhanced convection and the presence of Pacific Deep Water formation. These could provide a context for how sedimentary controls govern seawater ε_{Nd} under various idealised palaeo reconstructions of circulation states, it must be noted, however, that utilising the global sediment ε_{Nd} maps presented here for such experiments would be limited by the assumption of stable sedimentary Nd fluxes through time (e.g. not accounting for changes in sedimentation

rates and/or distribution of detrital sediment). Regardless, such studies would provide an important first step towards quantifying the potential overprinting affect that a benthic flux may have on bottom waters under various circulation regimes.

The seafloor ε_{Nd} maps presented here also create the opportunity to test further hypotheses related to constraining particle-seawater interaction in marine Nd cycling. Haley et al. (2017) suggested that a large difficulty in resolving the Nd paradox could be a result of undue emphasis placed on reversible scavenging, with the mass transfer required via vertical water column processes being implausible to explain fully the observed [Nd] increases with depth. The sediment ε_{Nd} distributions presented here would enable global sensitivity experiments to utilise these maps, in conjunction with the comprehensive nature of GEOTRACES seawater Nd sampling, to constrain further both water column and sedimentary processes that govern marine Nd.

Further applications could also involve testing the role of a benthic flux on seawater ε_{Nd} in the North Atlantic under different circulation regimes. Under the benthic flux hypothesis the limited expression of non-conservative behaviour in the modern North Atlantic has been attributed not to a lack of sedimentary source, but as a result of a short benthic flux exposure time relative to high ventilation rates (Du et al., 2020; Haley et al., 2017). This behaviour cannot always be assumed, particularly during times when the AMOC was believed to be much weaker in the recent geological past (McManus et al., 2004). As such, idealised studies, for example analysing Atlantic end member ε_{Nd} under a current (high ventilation) and also a reduced AMOC state, would provide valuable information on how benthic flux exposure times may influence seawater ε_{Nd}, useful especially for interpreting palaeoceanographic ε_{Nd} records.

The high-resolution ($0.5° \times 0.5°$) gridded maps of the continental and seafloor detrital ε_{Nd} are provided in Supplementary Dataset S1 and S2, the maps are also available in vector format, and so can be accessed at different spatial resolutions to suit specific user applications. These observations thus form the basis of exploring the benthic flux hypothesis in numerical models in order to understand and quantify its potential role in controlling the marine distribution of Nd isotopes, working towards solving the 'Nd paradox'. These data products have been designed to facilitate more modelling and sensitivity studies, with a future aim of coordinating a Nd isotope enabled model intercomparison study.

In closing, appropriate to current understanding of sedimentary Nd sources, we chose to represent the dominant ε_{Nd} signal using lithology and sediment types to inform the origin, age distribution and environment of sediment particles in contact with the ocean, as a first order approach to quantifying the sediment reactive Nd signal. The application of such a method in this work is supported by results from Du et al. (2020), who used a conceptual model to relate the non-conservative ε_{Nd} to published core-top detrital sediment, finding that these two characteristics are well correlated globally. Nonetheless, there still remains uncertainty regarding sediment-water exchange of Nd, especially an incomplete understanding of the controls on dissolved ε_{Nd} distribution in the deep ocean (Wilson et al., 2013), and with particular regard to assessing the main reactive Nd phases in the sediment, which ultimately interact the most with the overlying water column. To narrow down or eliminate these uncertainties, detailed further analyses of global sediment compositions, inputs, transport history, ageing, mineral chemistry, local pore water chemistry and redox state are required (Abbott et al., 2019; Abbott, 2019; Wilson et al., 2013). Such additional research would better inform the work we have undertaken and could be used to refine our proposed ε_{Nd} distributions, assuming there are a sufficient number of available ε_{Nd} measurements from the identified reactive phases. In such a case, it would be useful to perform sensitivity studies on both the regional distribution of ε_{Nd} arrived at by interpolating different selections of sediment types and reactive phases, and on numerically predicted water column ε_{Nd} achieved by utilising those different

distributions as model inputs. The compilation and data products presented here do not seek to estimate the reactive sedimentary Nd phases, and we have avoided making complex assumptions about how such phases may behave differently. However, by highlighting this discussion, and visualising the distribution of seafloor ε_{Nd} surmised from currently available data, our work draws attention to current gaps in the observational record and their potential effect on our collective perspective of sedimentary Nd sources to the ocean. Moreover, we hope this will pave the way towards reaching a better understanding of the lability of Nd in deep sea sediment as well as its role in marine Nd cycling and continue the application of ε_{Nd} as a valuable tool for palaeoceanographic reconstruction.

2.5 Summary and Conclusion

The important role of sediment-water interaction in governing oceanic Nd sources and sinks is widely accepted. However, the detail of these processes remain some of the least understood aspects of marine Nd cycling. The updated compilation of sedimentary ε_{Nd} measurements from the continental margins and deep ocean presented here build upon the work of Jeandel et al. (2007), extending the remit of the previous study to include measurements from pore waters and deep seafloor detrital samples in order to improve the characterisation of global ε_{Nd} distributions at the entire sediment-ocean interface. Thus, our new continuous, global, gridded datasets provide the opportunity to explore the non-conservative sedimentary processes that control global Nd cycling. Our results are especially designed for investigating marine Nd cycling, particularly to aid in constraining the magnitude and ε_{Nd} from sediment-water interaction and constrain how this influences the distribution of marine ε_{Nd}. The maps can be used in the implementation of Nd isotopes in numerical models to perform sensitivity and palaeo-experiments, enabling the explicit simulation and quantification of non-conservative sedimentary Nd sources (e.g. testing of a possible benthic flux) and examining the relationship between circulation speed, detrital sediment composition and magnitude of sedimentary inputs under modern and recent (i.e. Quaternary) palaeoceanographic reconstructions. All of this offers a concrete way forward to improve the application of Nd isotopes as a useful tracer of water provenance and mixing, and potentially also as a kinematic tracer of ocean circulation. Future work may aid more rigorous, process-based corrections to evolve this tool. Specifically, once Nd sediment-water interactions within under-studied oceanic regions and sediment types have been more widely analysed, this work will lead to a better understanding of the mechanisms of sediment composition on upward Nd fluxes into seawater.

2.6 Supplementary Information

The presented database of ε_{Nd} measurements, along with the global, gridded datasets and all input files for reproducing the maps are available via the Research Data Leeds Repository at (`https://doi.org/10.5518/928`; Dataset S1-S2, Table S1-S4 and Directory S1-S2).

Dataset S1: Continental ε_{Nd} map: gridded ($0.5° \times 0.5°$) and vector format.

Dataset S2: Seafloor ε_{Nd} map: gridded ($0.5° \times 0.5°$) and vector format.

Table S1: Full ε_{Nd} compilation presented in this study. See Tables S3 and S4 for the specific data used for each component of the high resolution, spatially continuous ε_{Nd} distribution presented here.

Table S2: New Southern Ocean ε_{Nd} data, contributed by co-authors for the < 63 μm fraction of Holocene samples from East Antarctica (see Text S2.1and Fig. 2.7 for methods and location).

Table S3: Continental ε_{Nd} observations utilised in the spatially continuous continental

ε_{Nd} distribution.

Table S4: Marine detrital and pore water ε_{Nd} observations used in the spatially continuous seafloor sediment ε_{Nd} representation.

Directory S1: Files required for the continental ε_{Nd} interpolation.

Directory S2: Files required for the seafloor ε_{Nd} interpolation.

Text S2.1 Methods for producing the new Southern Ocean measurements contributed by co-authors

Sites were chosen to represent different sediment provenance sectors surrounding East Antarctica and different depositional settings (proximal continental shelf, continental slope, submarine highs – e.g. Maud Rise and Kerguelen Plateau – and distal deep ocean basins). No samples were available offshore of Enderby Land.

The majority of sediment samples were taken from between 10 and 42 cm below core-top to avoid anthropogenic Pb contamination since Pb isotopes were also being examined (not reported here). Most sampled sediments were composed of fine-grained clays and silts. Fractions < 63 μm were analysed to minimise potential supply of detrital material from distally sourced icebergs, but we recognise that this fraction can also contain fine grained IRD.

Bulk sediments were wet sieved into < 63 μm and > 63 μm fractions using nylon sieves. Approximately $\sim$1.5 g of the < 63 μm fraction was weighed into cleaned 50 ml centrifuge tubes. Sediments were leached of carbonate using 30 ml of buffered acetic acid (pH 5) for 12 hours. This process was repeated until the sediment no longer reacted. The remaining material was then washed with ultraclean water three times and then subsequently leached in 10 ml of 0.5 M hydroxylamine hydrochloride in 10% glacial acetic acid (HH) for 24 hours to remove Fe-Mn oxide-oxyhydroxides coatings (modifed from Gutjahr et al. 2007). The residues were then washed three to five times in ultraclean water, dried, and gently crushed in a pestle and mortar. Despite the high biogenic opal contents of some Holocene Southern Ocean marine sediments, samples were not subjected to opal removal. This is because trace elements in biogenic opal are mainly sourced from detrital grains incorporated into frustules, and elemental concentrations of rare earth elements (REE's) and U, Th and Pb in pure opal are very low (Andersen et al., 2011; Goldberg et al., 2008; Phedorin et al., 2000). Approximately 50 mg of the > 63 μm fractions was weighed into clean Teflon vials and digested on a hotplate for several days using concentrated HF and HNO_3 (3:1).

Dissolved samples were dried and run through columns to isolate Nd. The REEs were concentrated using TRU-Spec resin ($100 - 120$ μm bead size; modified after Pin and Santos Zalduegui (1997)). Samples were loaded in 1M HNO_3, and bulk REE were subsequently eluted using 1M HCl. Neodymium was then isolated by loading the REE cut onto an Ln-Spec resin column ($50 - 100$ μm bead size; modified after Pin and Santos Zalduegui (1997) and eluted volumetrically with 0.2 M HCl. Nd separates were converted to HNO_3 in preparation for mass spectrometry and analysed on a Nu Plasma MC-ICPMS at the University of Florida over an 11-month period using a time-resolved analysis method (Kamenov, 2008). Nd fractions were diluted with 2% HNO_3 to obtain a 4-6 V beam on ^{144}Nd and aspirated into the source using a DSN-100 nebulizer. A $^{146}Nd/^{144}Nd$ ratio of 0.7219 was applied to correct for instrumental mass bias following the exponential law. Tests showed that interferences from ^{144}Sm are adequately corrected if the ^{144}Sm contribution is less than 0.1% of the ^{144}Nd signal. Samarium contributions of all samples were significantly below that level. The JNdi-1 standard was run between every five to six samples and the difference between the daily average of these standard runs and the published value of 0.512115 for JNdi (Tanaka et al., 2000) was used to correct all measured $^{143}Nd/^{144}Nd$ ratios. Procedural blanks were routinely less than 20 pg or less than 0.1% of total estimated Nd concentration for measured samples. All samples, and associated meta

data are reported in Table S2 and Fig. 2.7 shows the location and ε_{Nd} of all observations.

Most samples reported here are of Holocene age (deposited during the past 11.7 ka), and so those samples located within our 3° coastline buffer were included as marine sediments in our continental database (11 samples: shown in Table S3, full details on continental selection criteria in Sect. 2.2.2.1 of the main text and Text S2.2 below), and all samples were included in our seafloor database (Table S4). As highlighted above, data listed from Cook, Martin et al. (unpublished) were collected from 10-42 cm subsurface to avoid anthropogenic contamination for another aspect of the study. Thus, some of these samples may be older than Holocene. However, in terms of detrital data, they likely represent material sourced from the major proximal geologic terranes and therefore still represent appropriate ε_{Nd} for inclusion in our study.

Text S2.2: Continental ε_{Nd} data collection and representation: sample types

As outlined in Sect. 2.2.2.1 of the main text which describes the data selection and filtering methods for establishing our suitable discrete ε_{Nd} continental data, we selected Holocene (specifically 11.7 ka to present) observations which came from three broad sample types: river sediment samples, which deposit on the continental shelf and slope; Holocene marine sediments collected along given margins; and geological material outcropping close to an oceanic margin expected to be weathered. Below we detail the evidence behind selecting these sample types for inclusion in our continental dataset.

River sediments samples: Suspended river load, delta, shelf and fan deposits are considered a significant potential input of Nd to the ocean (Jeandel et al., 2007; Rousseau et al., 2015). As products of weathering and erosion, river sediments deposited on the continental margin likely capture the mean isotopic signature of their drainage basins (Goldstein and Jacobsen, 1987; Goldstein et al., 1997, 1984). Once released in the oceanic realm, fluvial sediments will interact with seawater and are therefore representative of the ε_{Nd} signature of the margin-ocean interface.

Marine sediments: Surface sediment samples provide direct information on the ε_{Nd} of material in contact with seawater. Samples representative of this present-day interface were chosen using a set of criteria: a) core-top samples, defined as the upper centimetre of sediment deposited, or b) sediments of Holocene age, i.e., deposited during the past 11.7 ka, and c) sites within $\approx$ 300 km of the coastline (defined via a 3° buffer from coastlines). It is assumed here that sediment provenance and thus detrital input is rather invariant during this time period. This decision is supported by evidence in the North Atlantic, where Holocene sediment core-top calibrations to seawater yield a general good agreement throughout this time period (Howe et al., 2017; Lippold et al., 2016; Pöppelmeier et al., 2020a, 2019). However, it is worth noting that there are occasional, and relatively localised exceptions. For example, temporal excursions in sediment ε_{Nd} constrained to the northwest Atlantic during the Bølling-Allerød and early Holocene have been observed, explained by the potential redistribution of sediment by benthic nepheloid layers or through pulses of poorly chemically weathered detrital sediment from the retreat of the Laurentide Ice Sheet (Howe et al., 2017, 2016; Pöppelmeier et al., 2019). Nonetheless, and with these exceptions aside, the marine sediment measurements from sites proximal to the continents are known to broadly trace the average composition of the crust exposed to weathering and erosion and thus capture a more spatially representative distribution of ε_{Nd} than might otherwise be expected from a single site (McLennan et al., 1990). Older samples are disregarded as the ε_{Nd} may vary due to different climatic and oceanographic conditions (Blanchet, 2019).

Continental geology: Outcropping fields (soils, surface sediment and rocks) provide indirect data for constraining the continental input of Nd to the oceans. That is, the outcrops themselves are not in contact with water masses, but the ε_{Nd} from these samples

capture large sediment regions surrounding the coasts, which may be eroded and subsequently their ε_{Nd} signatures be delivered to the ocean. Therefore, these samples are likely to provide a representative signal of adjacent weathered continental margin sediments (Goldstein et al., 1984). This assumption is supported by comparisons between the sediment province and ε_{Nd} from core-tops (see above), which suggest that sediments deposited along a given margin have an isotopic signature similar to the surrounding outcropping fields exposed to weathering (McCulloch and Perfit, 1981; Plank and Langmuir, 1998).

Text S2.3: User manual for the interpolation methods to produce gridded continental and seafloor ε_{Nd} representations

S2.3.1: Overview, file location and software

The interpolation methods presented here provide a clear outline of which files are required to reproduce our data, which software we used to create the spatially continuous datasets, and our precise methodological process for undertaking the interpolation of discrete ε_{Nd} observations. All files required to produce each of the final spatially continuous ε_{Nd} maps are packaged together with the final datasets they were used to create; zipped Directory S1 for the continental margin ε_{Nd} and zipped Directory S2 for the seafloor ε_{Nd}. We took specific care to utilise freely available software and supply all input data in the attached files, alongside a detailed description of how we used these to create our refined ε_{Nd} distributions (below), thus providing a fully transparent methodology to facilitate accurate reproducibility of the final data products. The contribution of further observations to the continually evolving database first published by Blanchet (2019) is encouraged. It is hoped these data products (and the methods described below) become an evolving tool.

To create the ε_{Nd} maps, we utilised QGIS, a free open-source desktop geographic information system (GIS) application. The files that we loaded into QGIS to perform the interpolation are listed below. The discrete observational ε_{Nd} data that form the basis of the interpolation are stored in a delimited text file (.csv). The continental and marine lithologies, which are used to constrain the interpolation of these discrete data according to underlying geological/lithological units, are stored as geospatial vector data (.shp).

Files for the continental ε_{Nd} interpolation, can be accessed from zipped *Directory S1: Continental*

- Discrete continental ε_{Nd}:
  /discrete_observations/continental_database.csv
- Continental lithology file:
  /lithology/continental_lithology_revised.shp

Files for the marine detrital and pore water ε_{Nd} interpolation, can be accessed from zipped *Directory S2: Seafloor*

- Discrete detrital and pore water ε_{Nd}:
  /discrete_observations/detrital-porewater_database.csv
- Seafloor lithology file:
  /lithology/seafloor_lithology_revised.shp

S2.3.2: Creation of the continental lithology map

The digital geological map as used in Jeandel et al. (2007) can be downloaded from Directory S1: */lithology/continental_lithology_original.shp*.

It is in geospatial vector data (.shp) format and provides polygons delimiting the (simplified) distribution of the main various geological units comprising Earth's continental

surface. This map was used to constrain our interpolation of discrete data points according to the underlying geological units (i.e., providing hard boundaries to the interpolation of individual discrete data) in order to maintain a basic level of regional geological consistency in our continuous characterisation of continental margin ε_{Nd}.

The polygons representing the interior of Greenland and Antarctica, classified as 'glacier', were removed from this file due to the presence of extensive ice sheets in these regions, which hinder the acquisition of in-situ crustal ε_{Nd} measurements and hence prohibit an accurate estimation of underlying ε_{Nd} characteristics. Moreover, since these regions are not directly in contact with seawater, they were not required for representing the ε_{Nd} of the sediment-water interface. The revised lithology map used in our final interpolation can be downloaded from Directory S1:
/lithology/continental_lithology_revised.shp.

S2.3.3: Creation of the seafloor lithology map

The seafloor lithology high resolution gridded map from Dutkiewicz et al. (2015), can be downloaded (.shp format) from Directory S2: */lithology/seafloor_lithology_original.shp.* This file provided polygons for the dominant seafloor lithologies. Adopting the assumption that the seafloor lithological types at least partly describe the major sedimentary source and characteristics of detrital and pore water ε_{Nd} (see discussion in Sect. 2.2.3.2 of the main text), this map was used to spatially delimit the interpolation of discrete data points, allowing us to continuously characterise the seafloor within depositional sediment types assumed to contain similar Nd characteristics.

Notably, the GlobSed map does not capture some key features in seafloor lithology that we anticipated would significantly affect the resulting ε_{Nd} distribution in the interpolation. We therefore needed to make some manual adjustments to seafloor_lithology_original.shp in order to take account of these important features:

L1: Globsed does not have full global coverage in the polar Arctic region, only extending to 75° N. It was therefore necessary to extend the map to cover marine regions north of this extent to allow full global coverage, here we allocated the associated new polygons a 'no data' lithology. However, to avoid producing an overly homogenous signal in the Arctic (i.e. where a single ε_{Nd} value is assigned to the entire 'no lithology' polygon here) and allow the subsequent ε_{Nd} interpolation to reasonably capture the spatial variability evident in the measurements, we then split up the Arctic into several smaller polygons according to largescale differences in the characteristics of the broad shelf areas and including significant fluvial influence (Asahara et al., 2012; Haley and Polyak, 2013; Maccali et al., 2013).

L2: In the region comprising the Azores volcanic island chain basin, detrital input from volcanic basalts which lie on the lateral branch of the Mid-Atlantic Ridge, need to be spatially confined. Here we maintain the regions distinct characteristics by introducing an extra, small polygon into a large spatial area domain characterised by calcareous sediment within the central North Atlantic. This ensures we represent the local radiogenic detrital characteristics of this area but means that observations here are not extrapolated across large areas (Grousset et al., 1988).

L3: In the region surrounding the Maldives, detrital input from basement basalts underlying the atolls, which formed in the Mesozoic Era (Gischler, 2006), need to be spatially confined to keep the signal local, ensuring that neighbouring regions do not pick up the very radiogenic signal from these samples in the numerical interpolation as they are not likely directly exposed to the radiogenic sedimentary source. We therefore introduced an extra, small polygon to encircle the detrital input from these basalts and spatially confine the radiogenic ε_{Nd} measured there.

L4: In the region surrounding the Seychelles, detrital input from the granitic islands

of the Seychelles Plateau, including crust of Precambrian origin (Hammond et al., 2013), need to be spatially confined to keep the signal local. Again, ensuring the neighbouring regions, particularly here classified with large lithology field domain areas, do not pick up the unradiogenic signal from these samples in the numerical interpolation, as they are not directly exposed to it. Instead, they can be assigned an ε_{Nd} which is more consistent with the marine samples within that wider domain. Here we introduced an extra, small polygon to encircle the detrital input from these granitic islands and spatially confined the unradiogenic ε_{Nd} measured there.

L5: Globsed does not have full global coverage in the polar Antarctic regions, only extending down to 75° S. It was therefore necessary to extend the map to cover marine regions south of this extent to allow full global coverage, here we allocated the associated new Antarctica polygon a 'no data' lithology.

The resulting revised lithology map from all of these seafloor lithology changes (summarised in Supplementary Table 2.1: L 1-5 and shown in Fig. 2.8), which is the final version used for our interpolation, can be downloaded from Directory S2: */lithology/seafloor_lithology_revised.shp*.

S2.3.4: Key assumptions

In order to choose a suitable interpolation technique for transforming discrete (and in many cases spatially sparse) observations into continuous fields, careful consideration of the present understanding of ε_{Nd} characteristics in rock and detrital sediment was made, accepting some practical limitations both in the extent of this knowledge and available numerical methods. Outlined below are the main assumptions underpinning our choice of interpolation alongside uncertainties arising from incomplete knowledge, especially relating to the understanding of depositional seafloor sediments.

For continental ε_{Nd}, our interpolation relies on the current knowledge that isotopic Nd characteristics are closely related to the host rock's age and composition (Jeandel et al., 2007). For example, according to the Nd-model age relationship, which describes the crustal residence age (Goldstein et al., 1984; Goldstein and Hemming, 2003; Taylor et al., 1983), generally older continental crust will be more unradiogenic than younger crust. Here, we assume that these characteristics dominate any other influence on ε_{Nd}, and thus ε_{Nd} is homogenous within each local lithological unit. As outlined in Sect. 2.2.2.1 of the main text (description of 'filtering') and Text S2.2, the discrete observational data employed for the interpolation were carefully selected so as to be representative of the average ε_{Nd} of the coastal continental region it came from and not of any specific intrusions or otherwise peculiar samples. Although this does simplify the spatial variability of ε_{Nd}, it does produce a broadly accurate distribution and we therefore deemed it unnecessary to introduce further arbitrary complexities to our approach.

For the marine detrital and seafloor interpolation, we assume that modern seafloor detrital phases retain the isotopic signature of their source rocks throughout weathering, sediment transport and diagenesis (Grousset et al., 1998, 1988; Nakai et al., 1993). As such, within regional lithological units, for example an area dominated by clay sediments in the North Atlantic, we assume that the detrital material has the same source and thus that the ε_{Nd} characteristics are similar (relating to source rock age and composition). This assumption is justified in areas such as the North Pacific, a region dominated by red clay, that has a relativity homogenous ε_{Nd} signal (-10) in detrital material associated with input from Asian dust (Nakai et al., 1993). It must be noted, however, that the sediment composition map used is heavily biased towards biogenic phases (i.e. large regions dominated by opal and calcareous oozes) (Dutkiewicz et al., 2015). As such, our interpolation assigns an ε_{Nd} value to biogenic sediments based on detrital observations and thus may not necessarily represent the ε_{Nd} signal from the dominant biogenic phases.

Nevertheless, the ε_{Nd} from a possible seafloor flux will depend on the reactivity of the underlying detrital sediment, which can be driven by only a small fraction of the sediment (i.e. clay dissolution) – see discussion in the main text (Sect. 2.2.3.1) – and therefore our approach may not introduce such a strong bias as would otherwise be the case. Moreover, it has been found that ε_{Nd} measurements on bulk sediment, including carbonates, do not appear distorted by the seawater/biological signal (Bayon et al., 2002), most likely due to there being low [Nd] in biological sediment. Thus, we deemed detrital samples as being sufficiently representative (and our best option) for broadly characterising the signature of seafloor sediments to provide a best estimate of global ε_{Nd} from the available data.

S2.3.5 Nearest neighbour analysis

Considering the current knowledge of crustal and sedimentary ε_{Nd}, and the limitations described above, we chose to use nearest neighbour analysis to interpolate the discrete ε_{Nd} observations onto a high resolution, global grid. Nearest neighbour interpolation assigns the lithology fields an ε_{Nd} value based on the observational value which rests within the field or is closest to it. We did not apply any weighting criterion or generate intermediate values based on complex rules and [potentially incorrect] assumptions. We recognise that the described approach won't capture all features of ε_{Nd} at the ocean-sediment interface, but we deemed it to be the best approach as it allowed us to exploit all the evidence we are aware of and make only a most basic level of assumptions (outlined in Text S2.3.4) while avoiding incorporating less supported suppositions. It also provides a clear foundation for more detailed and complex approaches to investigate specific aspects of our final ε_{Nd} distribution or methodological assumptions in the future.

In QGIS, we used the Nearest Neighbour Join (NNJoin) plugin. This joined the two vector layers (the input and the join layer) based on nearest neighbour relationships. More explicitly, a feature from the input layer is joined to the nearest feature in the join layer, resulting in a new vector layer with the same geometry type and coordinate reference system as the input layer. For our application, NNJoin attaches the discrete observational points to the lithology fields and assigns each geological/lithological-unit polygon an ε_{Nd} value according to the sample that fell within its spatial domain with the nearest distance to the centre of the polygon, or in the absence of any measurements within the domain, according to the nearest sample by distance to the centre of the polygon.

S2.3.6: QGIS Nearest Neighbour methods

S2.3.6.1: Continental ε_{Nd} initial interpolation

For the continental map, in a QGIS project file, the discrete ε_{Nd} observations and lithology files (*continental_database.csv* and *continental_lithology_revised.shp*, respectively) are loaded. From there, the NNJoin plugin is selected (the plugin can be installed directly via the QGIS Plugins Manager), and once opened, the following options are selected to perform the initial 'raw' interpolation:

Input vector layer: *continental_lithology_revised.shp*

Join vector layer: *continental_database.csv*

Neighbour distance field: *distance*

Then, the nearest neighbour analysis can be run (select 'ok'), creating a new vector layer containing the raw continental interpolation. The vector layer contains a variety of metadata detail, including lithological type, Nd sample information and the distance (decimal degrees) between the centre of the lithology polygon and its nearest input ε_{Nd} measurement.

S2.3.6.2: Marine detrital and pore water ε_{Nd} initial interpolation

The same method as described in Text S2.3.6.1 is applied to generate the seafloor ε_{Nd} representation, with the following selected via the NNJoin plugin to perform the raw interpolation:

Input vector layer: *seafloor_lithology_revised.shp*

Join vector layer: *detrital-porewater_database.csv*

Neighbour distance field: *distance*

Once the nearest neighbour analysis is run, a new vector layer is generated containing the raw seafloor detrital and pore water interpolation and the same metadata as for the continental margin counterpart (see above). Both the raw interpolation of the continental and marine sediment data can be accessed from */intial_interpolation/* within Directory S1 and S2, respectively.

S2.3.7: Revision of initial interpolation

The initial, raw interpolation of both maps allowed a global characterisation of the general ε_{Nd} of the continents and seafloor sediment based on representative observations. However, there are inherent errors in these distributions arising from the simple and purely numerically based interpolation. Text S2.4 describes and explains all of the expert manual adjustments made to reduce these errors and improve the interpolation for both maps. Supplementary Tables 2.2 and 2.3 contain a summary of these modifications and, where relevant, the calculation of mean ε_{Nd} within specified domains. We made a small number of manual adjustments to the interpolation, focusing these efforts on the major changes required to bring it into broadly better accord with available evidence (i.e., the wider published literature) and the expert judgement and field/laboratory-experience of co-authors. The adjustments were only performed where the interpolation had failed to capture the real spatial heterogeneity in crustal and marine sediment ε_{Nd} or produced ε_{Nd} that (as stated in the main manuscript), from our knowledge and experience base, appeared to not represent the broader regional signal, e.g., due to measurements capturing only very localised ε_{Nd} and the numerical interpolation inaccurately dispersing those signals. In marine lithological domains, manual adjustments were also made in instances where there were numerous datapoints within large lithology polygons. Here, an ε_{Nd} was assigned from calculating the mathematical mean of all datapoints within its domain, utilising the abundance of observations to assign a more typical ε_{Nd}, which the NNJoin approach does not automatically do. Modifications were likewise made to areas around spatially constrained localised extreme ε_{Nd} signals, e.g., from volcanic island arcs, ensuring the localised signals are represented but they do not extend into sediment regions not directly exposed to such detrital input. See below for details.

Text S2.4: Detailed description of the expert adjustments made to the initial purely numerical interpolation

All manual adjustments made to the continental and seafloor detrital and pore water ε_{Nd} interpolation are documented below in detail and then summarised in Supplementary Table 2.2 and Table 2.3, respectively. Where the adjustment involved taking the mathematical mean of the available data, in order to best represent domains containing a large number of data points, the ε_{Nd} of all samples are listed in Supplementary Table 2.3 alongside the mean and standard deviation.

S2.4.1: Continental ε_{Nd} representation: manual adjustments to the initial ε_{Nd} interpolation

C1: A thorough comparison of the outcropping geological fields surrounding the Hudson Bay was made with the initial interpolation and following a recent map representing

bulk surface sediment ε_{Nd} in the North Atlantic (Stichel et al., 2020). It was found that most domains assigned an ε_{Nd} were consistent with the spatial distribution of ε_{Nd} represented in Stichel et al. (2020), capturing the unradiogenic features here related to old continental Archean crust and the North Atlantic Craton. A change was made to a Proterozoic domain on the east coast of Newfoundland, correcting a radiogenic bias from -5.3 to -27.7, matching that of proximal Proterozoic fields, and through considering the signature of adjacent Archean fields.

C2: A radiogenic bias in Archean rock surrounding the south of the Hudson Bay was alleviated by assigning the domain here a more unradiogenic value, consistent with the ε_{Nd}-continental age relationship, the geology of the domain and the ε_{Nd} of similar Archean and Proterozoic fields north of the Hudson Bay. The ε_{Nd} value was corrected from -5.3 to -23.1.

C3: A radiogenic bias also occurred in lower Palaeozoic rock in the south of the Hudson Bay (adjacent to the Archean rock detailed in C2 above), this occurred due to data limitation in the region meaning a more radiogenic datapoint to the southeast from Toronto, Canada was extrapolated to this region. Here the bias of -13.3 was corrected to -28.9. Matching that of a marine margin observation within the Hudson Bay.

C4: Due to Greenland being located near modern North Atlantic Deep Water (NADW) formation, the attributed ε_{Nd} fields were closely analysed through comparison with a high resolution stratigraphy map from the Geological Survey of Denmark and Greenland (GEUS), accessed from (`https://eng.geus.dk/`), and the bulk surface sediment ε_{Nd} representation in the North Atlantic from Stichel et al. (2020). An unradiogenic bias of -25.8 in western Greenland Cenozoic units were corrected towards a more radiogenic value of +4, consistent with the younger rock age and matching the ε_{Nd} of proximal Cenozoic rocks in eastern Greenland.

C5: The unradiogenic ε_{Nd} value of -34 from north-western Greenland was extended to include all Proterozoic domains up the coastline, sharing similar characteristics in terms of age and lithology, these were initially assigned a more radiogenic value of 19.5 due to a discrete data point to the north situated within a younger Palaeozoic field.

C6: In north-eastern Greenland, a radiogenic bias was corrected by changing Lower Palaeozoic rock from -13 to -19, matching that of similar, proximal fields in the north and northwest of Greenland.

C7: Two Archean domains surround a Proterozoic unit at the most southerly tip of Greenland, the Archean domain to the east of the Proterozoic unit was originally ascribed a more radiogenic value of -8.8 due to a bias from a proximal marine sample. Here we adjusted the Archean units on the east of the southerly tip from -8.8 to -33, matching that of a river sediment sample measured in the neighbouring Archean rock and consistent with the ε_{Nd} from the Archean rock to the west of the tip, deemed to have similar characteristics due to lithology type and proximity.

C8: The interpolation produced a radiogenic bias to Proterozoic rock within Australia's Northern Territory (Kakadu National Park), here ε_{Nd} was modified from -9.3 to 15.4, representing the same value as neighbouring Proterozoic rock deemed to have similar geological characteristics.

C9: Another radiogenic interpolation bias occurred in a Proterozoic domain around Adelaide, South Australia. Considering the ε_{Nd} from neighbouring Proterozoic domains, ε_{Nd} was modified from -8 to -12.1, this was more consistent with the ε_{Nd}-continental age relationship and the underlying geology of this region.

C10: The ε_{Nd} of a polygon characterised as 'glacier' surrounding the coast of the west Ross Sea was modified to match the ε_{Nd} signal from the 'glacier' surrounding the

east of the Ross Sea basin, where discontinuities in the lithology file failed to wrap around the International Date Line. Here, ε_{Nd} was modified from -20.0 to -9.6.

C11: In East Antarctica an unradiogenic bias in Proterozoic rock was corrected for, modifying ε_{Nd} from -20.2 to -8.1. This added more spatial heterogeneity into the region which is evident within the detailed observations and varying lithologies in this region.

S2.4.2: Seafloor ε_{Nd} representation: manual adjustments to the initial ε_{Nd} interpolation

SF1: In the Arctic, the large polar domain located away from the continental shelves was assigned a value of -11.7, which is the mean of the 21 data points within (ranging from -15.9 to -9.9), as documented in Supplementary Table 2.3. Here we assumed that the mathematical mean of the available data best represents the ε_{Nd} of this domain with a large spatial area, containing a large number of measurements.

SF2: The shelf environment in the Arctic Ocean off northern Greenland was modified to remove the radiogenic bias (-3.8) introduced by a data point to the southeast of Greenland. It was corrected towards a more representative value for detrital input from unradiogenic Lower Palaeozoic continental crust based on neighbouring marine sedimentary ε_{Nd} in the northwest of Greenland in the adjacent field, dropping the ε_{Nd} to -19.5.

SF3: Off the coast of Southeast Greenland, we modified ε_{Nd} to be more unradiogenic (-23 compared with the initial -7.9), matching nearby measurements and in closer agreement with the Archean and Proterozoic lithology of the continental rock that provides a likely unradiogenic source of detrital input to this ocean region.

SF4: The east Bering Sea was modified to match the ε_{Nd} signal from the west Bering Sea, where discontinuities in the gridded lithology file failed to wrap around the International Date Line. Here, ε_{Nd} was modified from -9.9 to -8.7.

SF5: In the North Atlantic, a region of fine-grained calcareous sediment, considered to have a large area domain had a radiogenic bias of -2.3, which we adjusted to -12.3. This was the signature of another observation within the field, which was in closer agreement with the two other measurements that lie within the domain (ε_{Nd} of -13.1 and -11.1) and the signature of the surrounding fields. The radiogenic signal of -2.3 ε_{Nd} is still preserved within a neighbouring clay domain with a smaller area.

SF6: In the central North Atlantic, a region of calcareous sediment covering a large spatial area had a radiogenic bias of +4.9. The two radiogenic measurements in this region (ε_{Nd} of +3.9 and +4.9) were spatially isolated in order to constrain the signal more locally to the sample sites located in the Azores archipelago basin (see adjustment L.2 in Text S2.3.3). The Azores lies on the lateral branch of the Mid-Atlantic Ridge and associated ridge-hotspot activity gives detrital sediment a localised radiogenic signal here (Grousset et al., 1988). We then allocated the remaining larger domain a ε_{Nd} value of -12.6, taking the mean of the remaining (18) data points from within the domain as a more representative value (-12.6; with a range of -14.8 to -11), documented in Supplementary Table 2.3.

SF7: Unradiogenic inputs (-17.1) of detrital material off the east coast of South America (northeast Brazil) where Precambrian rock surrounds the coastlines, were also spatially constrained to marginal regions, here we assume the coastal regions and associated ε_{Nd} is likely unrepresentative of distal sediment in the central South Atlantic Ocean, restricting the extent of the extrapolation of coastal observations. Here the fine-grain calcareous sediment domain which neighboured the coastal sand and calcareous ooze domains containing the unradiogenic measurements was assigned an ε_{Nd} of -14.1. from -17.1. This was the value of a proximal detrital observation to the northeast of

the domain, deemed more representative and consistent with the wider deep Atlantic ε_{Nd} distribution.

SF8: Unradiogenic (-24.9) inputs of detrital Archean material from the Angolan coast, western Africa, was spatially constrained to coastal and marginal regions. This is because the unradiogenic Angolan-sourced ε_{Nd} is likely unrepresentative of the sediment in the central South Atlantic Ocean, which we reassigned with ε_{Nd} more consistent with measurements in the surrounding deep ocean. Here we reassigned a silt and clay domain adjacent to Angolan coastal fields a more radiogenic signal of -11 from -24.9, this was consistent with detrital observations within the neighbouring domain to the north and more consistent with deep Atlantic observations. However, we note that the deep Atlantic Ocean is the most data sparse region in our database, and this decision may need to be revised following further data acquisition in the region, especially in the open South Atlantic.

SF9: A clay domain in the central-western Pacific was modified from -8.7 to 10.1. This new value comes from a measurement within the same polygon that we deemed to be more representative of surrounding samples, which range from -11 to -8. It is also more consistent with the mean of north Central Pacific detrital samples (10.2), which has been attributed to a terrigenous source from aeolian dust input off the Asian continent, a major source of detrital material into the region (Nakai et al., 1993).

SF10: In the central Pacific a radiogenic bias was corrected for, located to the west of Hawaii. Here the interpolation has extrapolated a radiogenic detrital sample (+5.6) taken from the Hawaiian Basin, which is a region of recent localised volcanic hotspots, out into a domain in the open ocean. This domain was reassigned a value of -5.9, consistent with the fields encompassing the domain and more consistent with detrital observations taken within the open central Pacific.

SF11: In the central-equatorial Pacific a small modification was made to a domain with an unradiogenic bias, here the interpolation assigned a value from a datapoint outside the domain, but closer to the centre of the polygon. The domain was reassigned a value of -7.52 from -10.3, this value was consistent within the surrounding domains and more representative of the three observations within the domain, which ranged -7 to -4.3. Within such a data limited region, it was considered the best approach to remove such a numerical interpolation artifice.

SF12: In the South Pacific, off the Peruvian coast, a radiogenic bias was corrected for, this occurred as a result of the extrapolation of a radiogenic detrital sample located on the Peruvian margins into a domain in the open ocean. Here the domain was reassigned a value of -3.8 from +4.4. This maintained, but constrained the radiogenic signal observed in marginal settings. As such the open ocean domain, considered not to be located in a region susceptible to such radiogenic detrital input, was more consistent with surrounding fields.

SF13: A highly unradiogenic sample (-33.6) located in the Seychelles was constrained to the archipelago, localising this unradiogenic signal to coastal areas surrounding the granitic islands of the Seychelles Plateau, where detrital input of crust from Precambrian origin occurs (Hammond et al., 2013), detailed in adjustment L3 Text S2.3.3. The surrounding sediment, with a large field domain area in the Indian Ocean, was then reassigned a value of -12.6, the value of an observation within the remaining domain which is more consistent with the surrounding continental ε_{Nd} and the marine detrital samples within that wider domain.

SF14: Radiogenic samples (+7.3) associated with the Maldives were spatially isolated, detailed in adjustment L4 Text S2.3.3. This preserves the detrital signal from input from the Maldives and the surrounding basement basalts underlying the atolls, which

formed in the Mesozoic Era (Gischler, 2006), but confines the signal to a relatively localised area to avoid introducing a more geographically widespread radiogenic bias through over-extrapolation into the nearby marine sediments, which are not likely directly exposed to the radiogenic sedimentary source. The remaining domain was reassigned an ε_{Nd} value of -9.1 from a datapoint within the centre of the domain, which is representative of the other observations here which lie away from the Maldives basin (ranging -9.8 to -7.2).

SF15: In the Bay of Bengal, the ε_{Nd} was modified from -7.4 to a more unradiogenic signal of -13.3, consistent with the majority of samples within the domain and the surrounding continental signatures that are relevant here due to the large fluvial sediment load from the Ganges-Brahmaputra Delta. The ε_{Nd} value assigned was the mean calculated from 22 samples within the polygon, ranging from -18.2 to -7.1, documented in Supplementary Table 2.3. This was done to take advantage of the wealth of observations in this region.

SF16: In the eastern Indian Ocean, an unradiogenic bias was corrected for, modifying ε_{Nd} from -20.3 to -11.9. The bias was introduced by the numerical interpolation of unradiogenic measurements taken close to the coast in Western Australia, these observations capture the transport of weathered material from the coastal areas of northwest and west Australia, characterised by the presence of Proterozoic and Archean units, by the southward flowing Leeuwin Current, the dominant poleward flowing near-coastal current in this region (Ehlert et al., 2011). This constrained coastal signal does not accurately represent more distal marine sediment and its associated ε_{Nd}. The newly assigned ε_{Nd} is consistent with the signature of proximal marine observations in the eastern Indian Ocean away from the margins.

SF17: In the Indian Ocean sector of the Southern Ocean a diatom ooze polygon had a radiogenic bias of -2.7, this was adjusted to the value of an observational point to the south of the polygon which was more consistent with the surrounding observations and the unradiogenic features of Antarctica's proximal coastline. The value was adjusted from -2.7 to -12.8.

SF18: A coastal domain within the Ross Sea (bordering West Antarctica) was modified to match the signal from the western Ross Sea, where discontinuities in the gridded lithology file failed to wrap around the international date line. Here, ε_{Nd} was modified from -10.9 to -7.3.

SF19: Around West Antarctica, radiogenic values of +0.31 were constrained to the Wrigley Gulf. Here, we assumed that the radiogenic input of detrital material from Cenozoic intrusions are spatially constrained to the coastlines and should not influence the wider region. The adjacent and deeper sea settings off the Wrigley Gulf were reassigned to a more unradiogenic ε_{Nd} value of -4.6 which is consistent with observations and neighbouring fields away from coastal margins.

Table 2.1: Summary of manual adjustments to the high resolution seafloor lithology gridded map from Dutkiewicz et al. (2015) used to create the spatially continuous seafloor ε_{Nd} map (see Text S2.3.2), including descriptor of polygon location ('Region'), brief justification for the adjustment ('Reason for modification'), geographical coordinates of the centre of the new polygon ('New polygon centre coordinate') and the colour of polygon outlined in Fig. 2.8 ('Colour of polygon in Fig. 2.8').

Adjustment reference	**Region**	**Reason for modification**	**New polygon centre coordinate**	**Colour of polygon in Fig. 2.8**
L1	Arctic	Extend map to polar regions and represent spatial heterogeneity	0° E, 90° N	Blue shades
L2	Azores	Spatially confine volcanic basalts	−27.6° E, 38.5° N	Green
L3	Maldives	Spatially confine basement basalts	60.2° E, −10.2° N	Orange
L4	Seychelles	Spatially confine granitic islands	53.8° E, −4.7° N	Red
L5	Antarctica	Extend map to polar regions	−40° E, −80° N	Purple

Table 2.2: Summary of expert adjustments to the ε_{Nd} of individual polygons comprising the spatially continuous continental ε_{Nd} map (see Text S2.4.1), including descriptor of polygon location ('Region') and lithology ('Lithology'), brief justification for the adjustment ('Reason for modification'), geographical coordinates of the centre of the polygon ('Polygon centre coordinate') and the raw and refined ε_{Nd} ('Previous value' and 'Adjusted value', respectively).

Adjustment reference	**Region**	**Lithology**	**Reason for modification**	**Polygon centre coordinate**	**Previous value (ε_{Nd})**	**Adjusted value (ε_{Nd})**
C1	Hudson Bay (east)	Proterozoic	Radiogenic bias	−65.32° E, 52.14° N	-5.3	-27.7
C2	Hudson Bay (south)	Archean	Radiogenic bias	−72.55° E, 56.7° N	-5.3	-23.1
C3	Hudson Bay (south)	Lower Palaeozoic	Radiogenic bias	−88.41° E, 55.3° N	-13.3	-28.9
C4	western Greenland	Cenozoic	Unradiogenic bias	−54.73° E, 71.52° N	-25.8	+4
C5	north-western Greenland	Proterozoic	Radiogenic bias	−58.84° E, 75.87° N	-34	-19.5
C6	north-eastern Greenland	Lower Palaeozoic	Radiogenic bias	−32.80° E, 64.01° N	-13	-19
C7	south Greenland	Archean	Radiogenic bias	−49.18° E, 62.24° N	-8.8	-33
C8	Australia's Northern Territory	Proterozoic	Radiogenic bias	124.25° E, −22.24° N	-9.3	-15.4
C9	South Australia	Proterozoic	Radiogenic bias	133.97° E, −31.31° N	-8	-21.1
C10	Ross Sea	Glacier	Discontinuity across the International Date Line	156.7° E, −84.3° N	-20	-9.6
C11	East Antarctica	Proterozoic	Unradiogenic bias	35.95° E, −70.18° N	-20.1	-8.1

Table 2.3: Summary of expert adjustments to the ε_{Nd} of individual polygons comprising the spatially continuous seafloor ε_{Nd} map (see Text S2.4.2), including descriptor of polygon location ('Region') and lithology ('Lithology'), brief justification for the adjustment ('Reason for modification'), where relevant the ε_{Nd} of the samples within the polygon, the mathematical mean and standard deviation taken ('ε_{Nd} of samples', 'mean ε_{Nd}', and 'SD' respectively), relevant geographical coordinates of the centre of the polygon ('Polygon centre coordinate') and the raw and refined ε_{Nd} ('Previous value' and 'Adjusted value', respectively).

Adjustment reference	**Region**	**Lithology**	**Reason for modification**	**ε_{Nd} of samples**	**Mean ε_{Nd}**	**SD (ε_{Nd})**	**Polygon centre coordinate**	**Previous value (ε_{Nd})**	**Adjusted value (ε_{Nd})**
SF1	Arctic Ocean (away from continental shelves)	No data	Average of 21 samples within the field	-15.9, -14., -13.3, -13.3, -12.5, -12.2, -11.9, -11.4, -11., -11., -11., -10.9, -10.9, -10.6, -10.6, -10.4, -10.2, -10., -9.9, -9.7	-12	1.62	0° E, 85° N	-9.7	-12
SF2	Arctic Ocean (north of Greenland)	No data	Radiogenic bias	N/A	N/A	N/A	−37.7° E, 84.22° N	-3.8	-20
SF3	off the coast of Southeast Greenland	Gravel and coarser	Radiogenic bias	N/A	N/A	N/A	−37.23° E, 64.35° N	-7.9	-23
SF4	Bering Sea	Sand	Discontinuity across the International Date Line	N/A	N/A	N/A	157.39° E, 45° N	-9.9	-8.7

SF5	North Atlantic	Fine-grained calcareous sediment	Radiogenic bias	N/A	N/A	N/A	−19.9° E, 40.3° N	-2.3	-12
SF6	central North Atlantic	Calcareous ooze	Isolated two radiogenic points, took average of the remaining 18 samples within the field	-14.84, -14.6, -14.5, -13.6, -13.55. -13., -12.9, -12.6, -12.47, -12.2, -11.8, -11.6, -11.5, -11.4, -11., -10.88, -10.2	-13	1.4	−32.7° E, 36.5° N	4.9	-13
SF7	off the east coast of South America	Calcareous ooze	Constrained unradiogenic signal to coastal regions	N/A	N/A	N/A	−34.26° E, 9.02° N	-17.1	-14.1
SF8	off the coast of western Africa	Clay	Constrained unradiogenic signal to coastal regions	N/A	N/A	N/A	−17.7° E, −46.2° N	-24.89	-11

SF9	central-western Pacific	Clay	Unradiogenic bias, changed to be consistent with Pacific detrital evidence from predominant Asian dust source	N/A	N/A	N/A	151.9° E, 35.2° N	-8.69	-10.2
SF10	Central Pacific	Calcareous ooze	Radiogenic bias, due to extrapolation of detrital point within Hawaiian Basin into unrepresentative open ocean region	N/A	N/A	N/A	−170.6° E, 20° N	+5.6	-5.9
SF11	central-equatorial Pacific	Calcareous ooze	Unradiogenic bias	N/A	N/A	N/A	−145.1° E, −3.4° N	-10.3	-7.52
SF12	South Pacific	Calcareous ooze	Constrained radiogenic signal to margins	N/A	N/A	N/A	−93.1° E, −13.8° N	+4.4	-3.8
SF13	Seychelles	Clay	Constrained unradiogenic signal	N/A	N/A	N/A	50.47° E, −4.75° N	-33.6	-12.6

SF14	Maldives	Calcareous ooze	Constrained radiogenic signal	N/A	N/A	N/A	64.67° E, −11.05° N	+7.3	-9.1
SF15	Bay of Bengal	Clay	Average of 22 samples within the field	-18.2, -16.7, -16.2, -16.1, -15.5, -15.3, -15.1, -14.7, -14.5, -14.3, -12.8, -12.6, -12.5, -12.5, -11.5, -11.3, -10. -9.2, -9., -8.6, -7.1	-13	3.07	87.17° E, 16.87° N	-7.4	-13
SF16	eastern Indian Ocean	Calcareous ooze	Unradiogenic bias	N/A	N/A	N/A	107.4° E, −43.9° N	-20.3	-12
SF17	Southern Ocean (Indian Ocean sector)	Diatom ooze	Radiogenic bias	N/A	N/A	N/A	87.9° E, −55.3° N	-2.7	-12.8
SF18	Ross Sea (boarding West Antarctica)	No data	Discontinuity across the International Date Line	N/A	N/A	N/A	−171.4° E, −79.1° N	-10.9	-7.3
SF19	Wrigley Gulf, Antarctica	Gravel and coarser	Constrained radiogenic signal to coastal regions	N/A	N/A	N/A	−141° E, −72.1° N	+0.31	-4.6

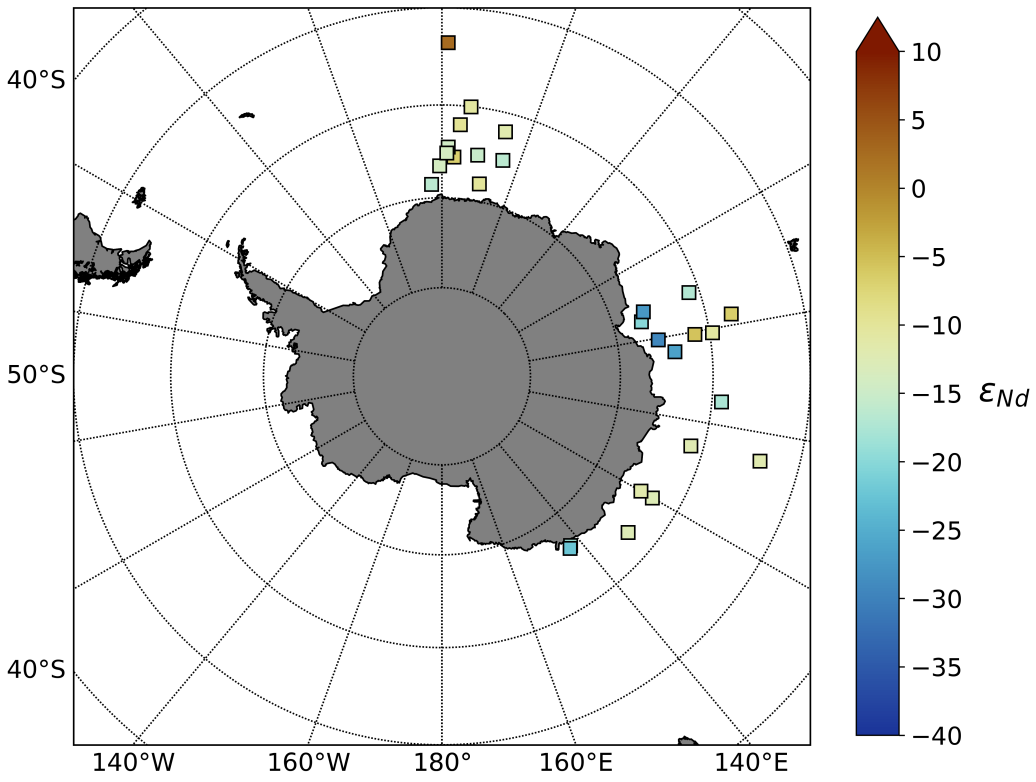

Figure 2.7: Location and ε_{Nd} of the new discrete marine Southern Ocean ε_{Nd} data, contributed by co-authors, for the < 63 μm fraction of Holocene detrital fraction samples from East Antarctica. Methods for the data collection and relevant information are detailed in Text S2.1 and Table S2 respectively.

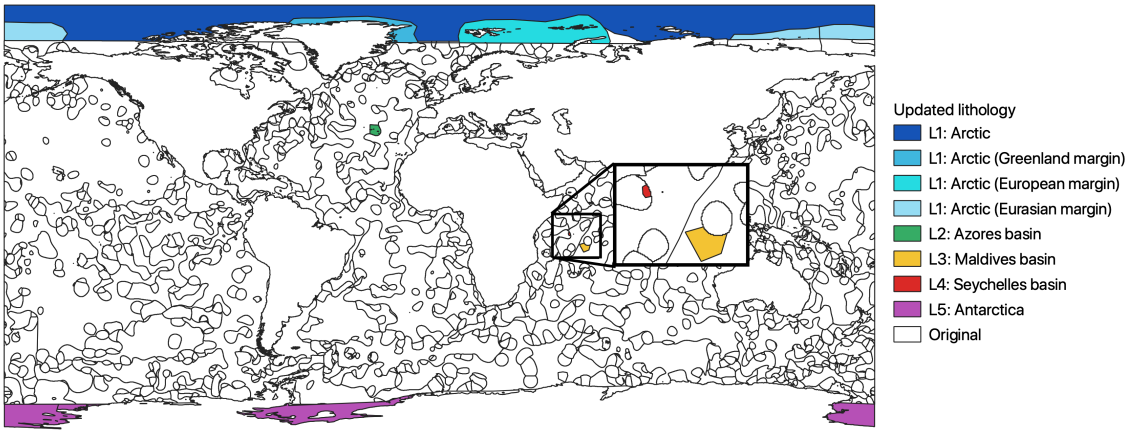

Figure 2.8: Location of manual adjustments (detailing extensions and isolated lithological regions) to the high resolution gridded lithology file from Dutkiewicz et al. (2015). Showing the extension of the map in the Arctic regions (blue shades) (with subsequent addition of spatial heterogeneity near coastal margins, Arctic [Greenland margin] (blue), Arctic [European margin] (turquoise) and Arctic [Eurasian margin] (light blue)), isolated lithological regions, Azores basin (green), Maldives basin (orange), Seychelles basin (red), and extension of the map in Antarctica (purple). Full details of the manual adjustments (L1-5) are documented in Text S2.3.3 and summarised in Supplementary Table 2.1. Inset map highlights the Seychelles and Maldives basins with small polygon areas.

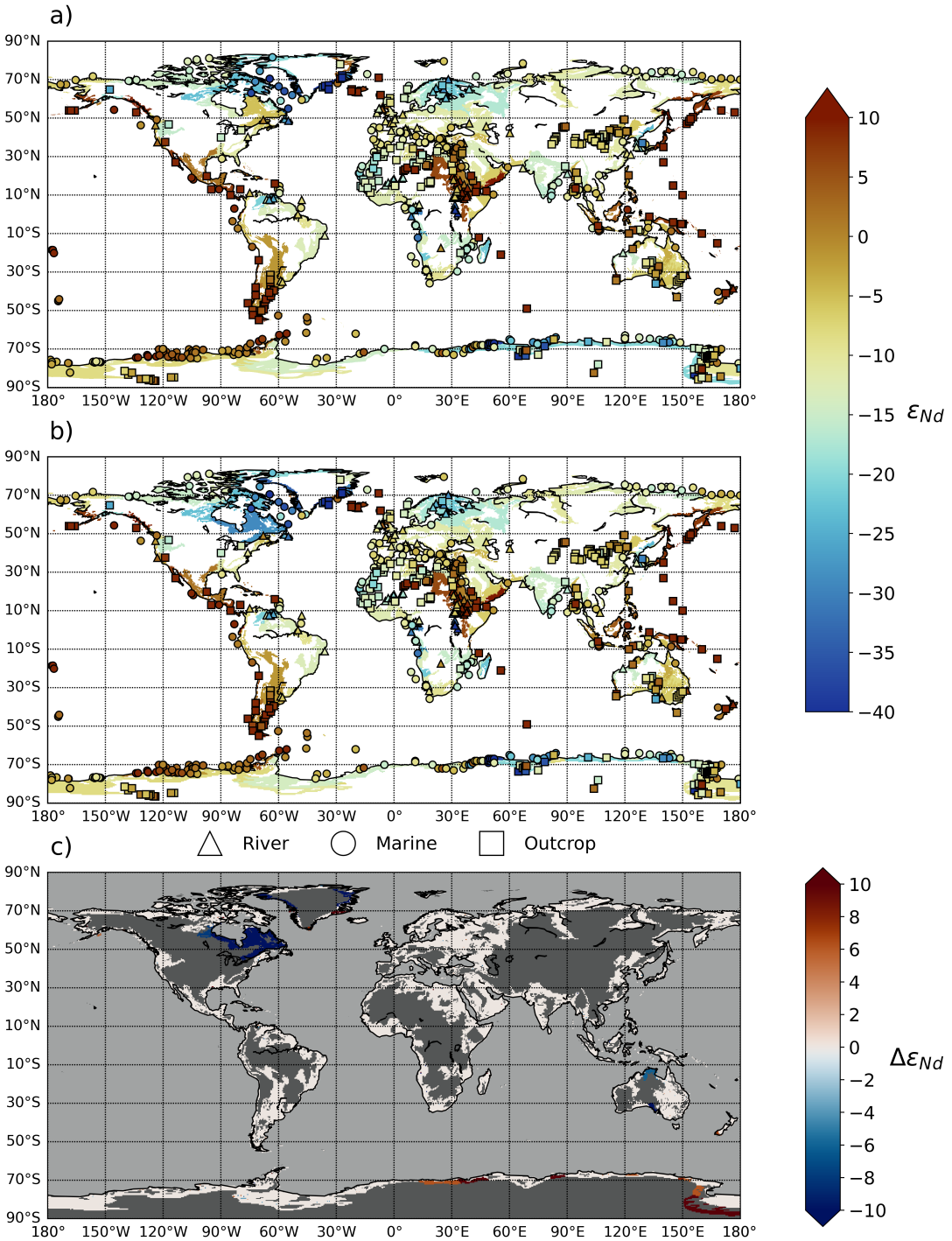

Figure 2.9: Comparison of the spatially continuous continental ε_{Nd} produced by (a) the initial 'raw' numerical nearest neighbour interpolation and (b) expert refinement of (a) as described in Text S2.4 and summarised in Supplementary Table 2.2, the location and ε_{Nd} of the discrete data are indicated, along with the broad sample type in (a) and (b): river sediment (triangles), Holocene marine sediment (circles), and geological outcrops (squares). (c) The changes to ε_{Nd} made through expert refinement (b minus a). Note refinement was centred in Greenland, the Hudson Bay, Australia, and East Antarctica; no data regions are coloured dark grey (land) and light grey (ocean).

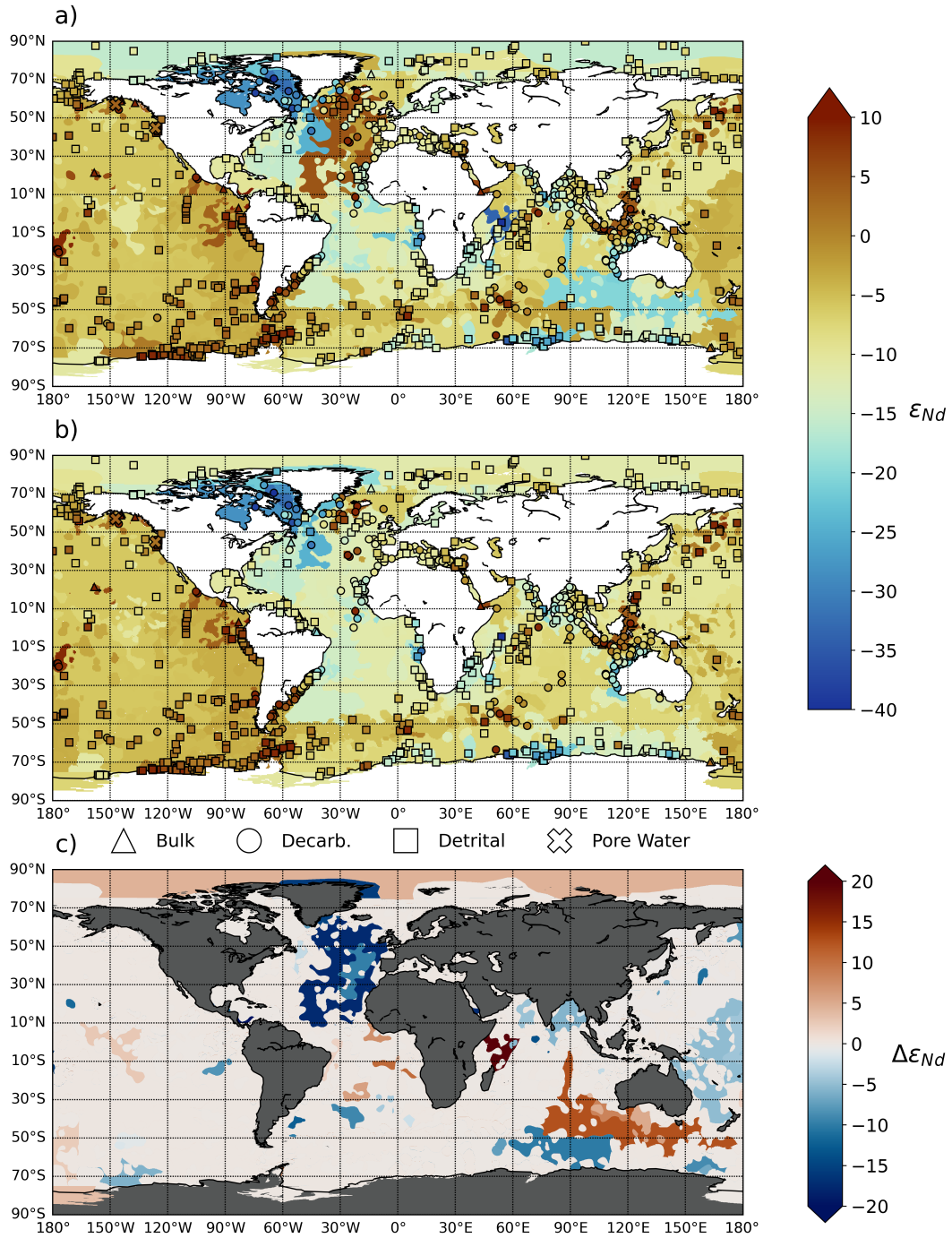

Figure 2.10: Comparison of the spatially continuous seafloor ε_{Nd} produced by (a) the initial 'raw' numerical nearest neighbour interpolation and (b) expert refinement of (a) as described in Text S2.4 and summarised in Supplementary Table 2.3, the location and ε_{Nd} of the discrete data are indicated, along with the broad sample types of marine detrital data in (a) and (b): bulk sediment digests (triangles), decarbonated sediment residuals (circles), specific detrital size fractions (squares), and pore water measurements (crosses). (c) The changes to ε_{Nd} made through expert refinement (b minus a); no data regions are coloured dark grey (land).

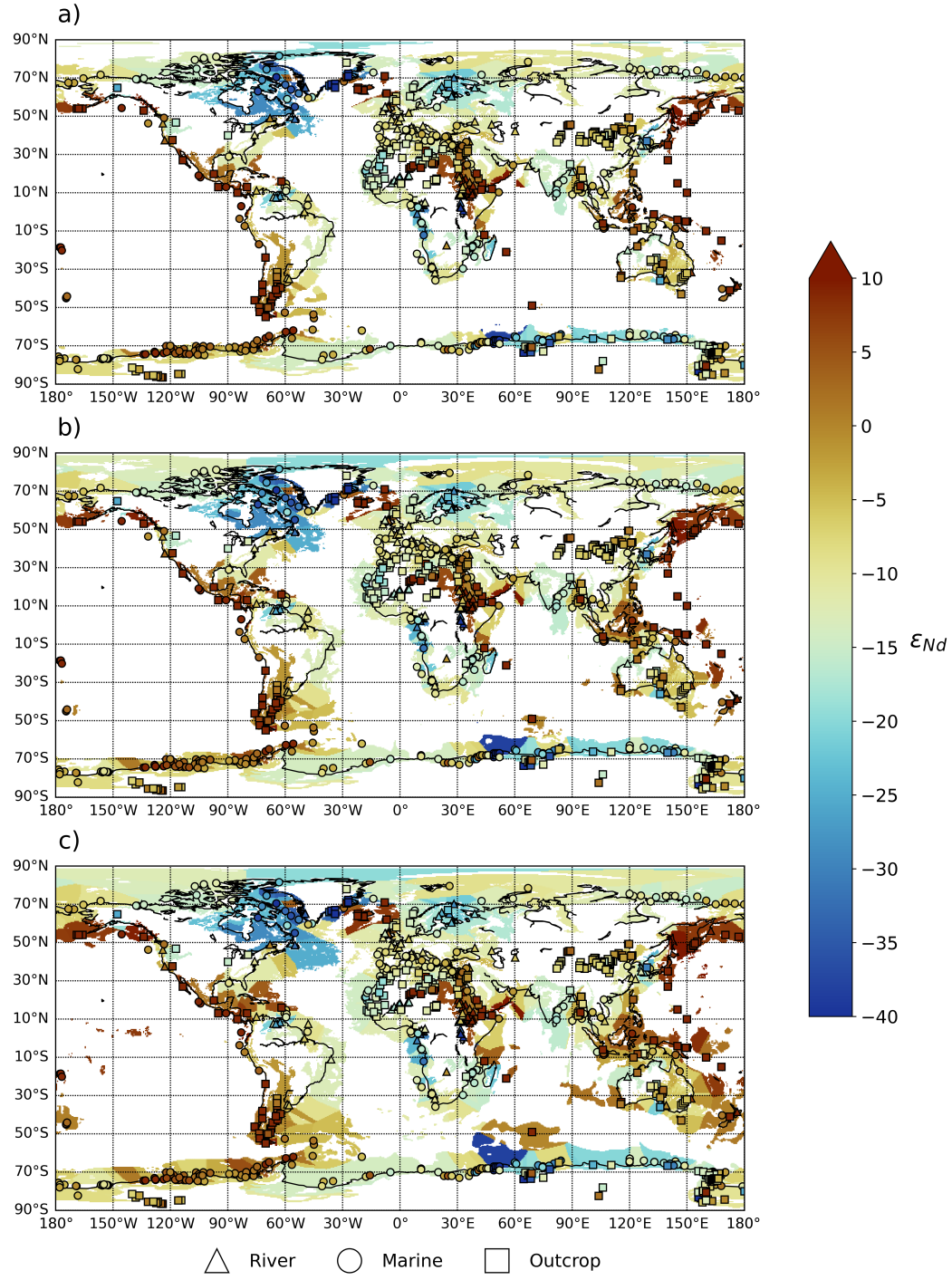

Figure 2.11: Comparison of the complete ε_{Nd} of the continents and proximal margins under three definitions of continental margin extent, all using sediment thickness to constrain the outer limits of the extrapolation: where sediment thickness is (a) $\geq 2,000$ m, (b) $\geq 1,000$ m and (c) ≥ 500 m. The location and ε_{Nd} of the discrete data are indicated, along with the broad sample type: river sediment (triangles), Holocene marine sediment (circles), and geological outcrops (squares). Various sediment thickness definitions were tested to find the most suitable limits of the extrapolation- that is, how far out to sea we can reasonably assume that the continental ε_{Nd} remains representative of the proximal marine sediments as discussed in methods Sect. 2.2.3.3.

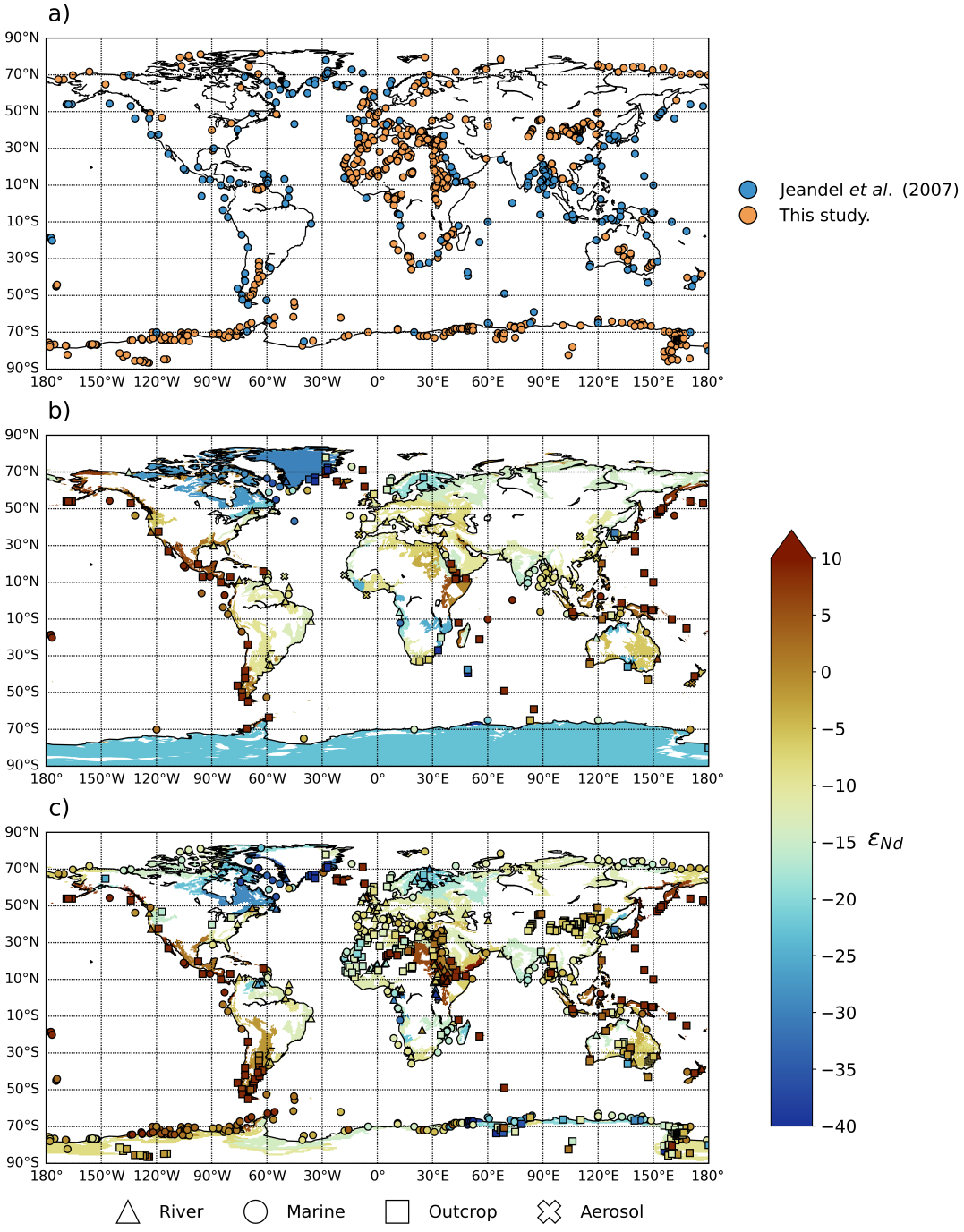

Figure 2.12: Comparison of the original (Jeandel et al., 2007) and new (this study) ε_{Nd} observations and continental margin representation. (a) Overview of the location of the samples assembled for the continental margin ε_{Nd} map by Jeandel et al. (2007) (blue circles) and the additional observations used for the continental representation in this study (orange circles). ε_{Nd} of discrete measurements and the continuous continental margin interpolation produced (b) by Jeandel et al. (2007); and (c) for this study, which uses both blue and orange data from panel (a). The broad sample types included in both compilations are indicated: river sediment (triangles), Holocene marine sediments (circles), geological outcrops (squares) and aerosols (crosses). Note that particular samples from Jeandel et al. (2007) were not used in this study, such as aerosol samples, alongside sites located out of range of our 3° coastline buffer, because these samples were deemed unrepresentative for our filtering criteria as outlined in the methods Sect. 2.2.2.1 and detailed in Text S2.2.

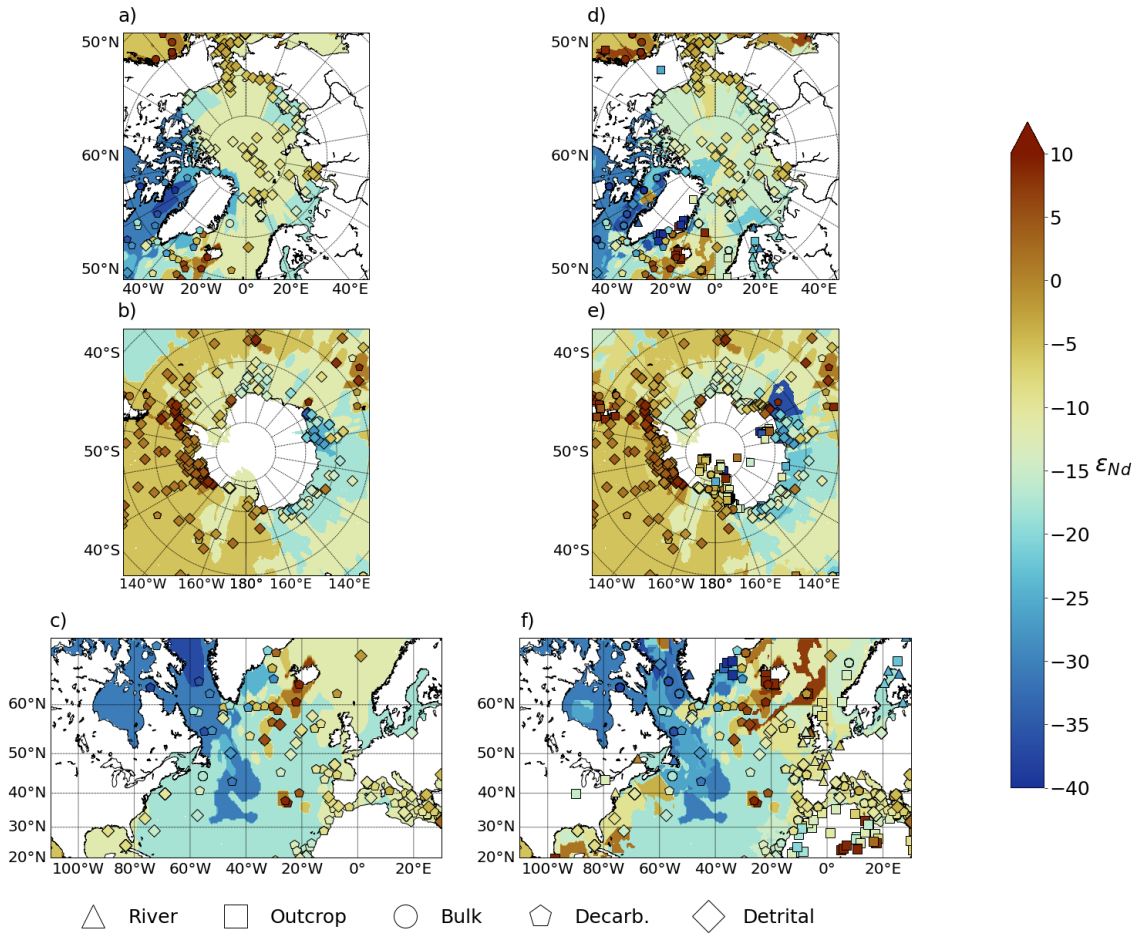

Figure 2.13: Regional analysis of the seafloor and the final combined sediment-ocean interface ε_{Nd} representation (continental ε_{Nd} map extrapolated to where sediment thickness $\geq 1,000$ m and remaining regions characterised by the seafloor ε_{Nd} map), with particular focus on regions important for deep-water formation and thus potential ε_{Nd} labelling of water masses by sedimentary inputs: the polar Arctic region, Antarctica, and the North Atlantic. (a-c) show the seafloor interpolation. (d-f) show the combined seafloor and continental margin interpolation. The continuous interpolations are overlain by the discrete ε_{Nd} measurements, the five broad sample types included in the new compilation are also indicated: river sediment (triangles), geological outcrops (squares) and Holocene marine sediments which are categorised into: bulk sediment digests (circles), decarbonated sediment residuals (pentagons), and specific detrital size fractions (diamonds).

Chapter 3

Simulating neodymium isotopes in the ocean component of the FAMOUS general circulation model (XPDAA): sensitivities to reversible scavenging efficiency and benthic source distributions

Abstract

The neodymium (Nd) isotopic composition of seawater is a widely used ocean circulation tracer. However, uncertainty in quantifying the global ocean Nd budget, particularly constraining elusive non-conservative processes, remains a major challenge. A substantial increase in modern seawater Nd measurements from the GEOTRACES programme coupled with recent hypotheses that a seafloor-wide benthic Nd flux to the ocean may govern global Nd isotope distributions (ε_{Nd}) presents an opportunity to develop a new scheme specifically designed to test these paradigms. Here, we present the implementation of Nd isotopes (^{143}Nd and ^{144}Nd) into the ocean component of the FAMOUS coupled atmosphere-ocean general circulation model, a tool which can be widely used for simulating complex feedbacks between different Earth system processes on decadal to multi-millennial timescales.

Using an equilibrium pre-industrial simulation tuned to represent the largescale Atlantic Ocean circulation with appropriate skill, we perform a series of sensitivity tests evaluating the new Nd isotope scheme. We investigate how Nd source/sink and cycling parameters govern global marine ε_{Nd} distributions, and provide an updated compilation of 6,048 Nd concentration and 3,278 ε_{Nd} measurements to assess model performance. Our findings support the notions that reversible scavenging is a key process for enhancing the Atlantic-Pacific basinal ε_{Nd} gradient, and is capable of driving the observed increase in Nd concentration along the global circulation pathway. A benthic flux represents a major source of Nd to the deep ocean. However, model-data disparities in the North Pacific highlight that the source of ε_{Nd} from seafloor sediment is too unradiogenic in our model with a constant benthic flux. Additionally, model-data mismatch in the northern North Atlantic suggests a missing source of Nd that is much more unradiogenic than the bulk sediment, alluding to the possibility of preferential contributions from 'reactive' detrital sediments under a benthic flux driven model of marine Nd cycling

The new Nd isotope scheme forms an excellent tool for exploring global marine Nd cycling and the interplay between climatic and oceanographic conditions under both

modern and palaeoceanographic contexts.

3.1 Introduction

The Neodymium (Nd) isotope composition of seawater shows a clear provinciality between different ocean basins and is often used as a water mass provenance tracer (e.g., Frank 2002; Goldstein and Hemming 2003). The measured $^{143}Nd/^{144}Nd$ ratio is denoted relative to the bulk earth standard:

$$\varepsilon_{Nd} = \left(\frac{(^{143}Nd/^{144}Nd)_{\text{sample}}}{(^{143}Nd/^{144}Nd)_{\text{CHUR}}} - 1 \right) \times 10^4, \tag{3.1}$$

where $(^{143}Nd/^{144}Nd)$CHUR relates to the Chondritic Uniform Reservoir (CHUR; 0.512638: Jacobsen and Wasserburg 1980). Distinct variations in the Nd isotope signal of water masses originate from different continental regions and their isotopic fingerprints, and subsequent influence by ocean circulation, water mass mixing and particle cycling, as well as interaction with sediments (e.g. Tachikawa et al. 2017; van de Flierdt et al. 2016 for recent reviews). Neodymium in the deep ocean has a residence time that is shorter than the global overturning of the deep ocean (Arsouze et al., 2009; Rempfer et al., 2011; Gu et al., 2019; Pöppelmeier et al., 2020a, 2021b; Tachikawa et al., 2003). Unlike other tracers of ocean circulation (e.g. $\delta^{13}C$, $\Delta^{14}C$), the measured Nd isotope composition of seawater is not actively involved marine biological cycling, giving rise to its promise as a carbon cycle independent ocean circulation tracer (Blaser et al., 2019b). Yet, a fundamental caveat in the application of ε_{Nd} as a reliable oceanographic tracer is that a universal understanding of the exact mechanisms controlling marine geochemical Nd cycling remains incomplete (Abbott et al., 2015a; Haley et al., 2017; van de Flierdt et al., 2016).

Numerical models are useful tools for investigating Nd cycling since they can specify the processes that govern the spatiotemporal variability in Nd isotope distributions in the ocean. Neodymium isotopes have been simulated in a range of different modelling studies testing specific hypotheses relating to Nd fluxes and thermohaline redistribution (Pöppelmeier et al., 2020a; Arsouze et al., 2009; Rempfer et al., 2011; Siddall et al., 2008b; Jones et al., 2008; Roberts et al., 2010; Tachikawa et al., 2003; Ayache et al., 2016; Gu et al., 2019; Oka et al., 2021, 2009; Pöppelmeier et al., 2022; Ayache et al., 2022; Pasquier et al., 2021; Du et al., 2020). However, recent work suggests that a seafloor wide benthic flux, resulting from early diagenetic reactions, may dominate the marine Nd cycle (Haley et al., 2017; Abbott, 2019; Abbott et al., 2015a,b, 2019; Du et al., 2016). These observations, alongside an ever-growing body of high-quality and highly-resolved measurements of dissolved seawater Nd concentrations ([Nd]) and ε_{Nd} from the GEOTRACES programme (GEOTRACES Intermediate Data Product Group, 2021), present an opportunity to re-evaluate, revise and explore constraints on the marine Nd cycle.

Initially, the predominant lithogenic fluxes of Nd to the ocean were believed to be only at the surface (aeolian dust and riverine fluxes; Goldstein et al. 1984; Goldstein and Jacobsen 1987). Early modelling studies applying surface fluxes reproduced reasonable ε_{Nd} in the North Atlantic (Bertram and Elderfield, 1993; Tachikawa et al., 1999). However, considering only dust and river fluxes alone led to an unrealistic calculated residence time of Nd in seawater on the order of 5,000 years (Bertram and Elderfield, 1993; Jeandel et al., 1995). Through applying a simple box model to calculate the oceanic Nd budget, it was then found that considering dust and river surface inputs alone failed to balance both [Nd] and ε_{Nd}, thus indicating a 'missing source' of Nd to the ocean that accounted for $\approx 90\%$ of the Nd flux to the ocean (Tachikawa et al., 2003). This led to a new hypothesis relating to other Nd sources to seawater that could account for this 'missing source', including submarine groundwater discharge (SGD) (Johannesson and Burdige, 2007), and

input from the dissolution of sediment deposited on the continental margins (Lacan and Jeandel, 2005a). The term 'boundary exchange' was coined to describe strong Nd isotopic interactions between continental margins and water masses though the co-occurrence of sediment dissolution and boundary scavenging (Lacan and Jeandel, 2005a). Arsouze et al. (2007) simulated realistic global ε_{Nd} distributions using boundary exchange as the only source-sink term, and since then, boundary exchange along continental margins has represented the major flux of Nd to seawater in recent global Nd isotope models (Arsouze et al., 2009; Rempfer et al., 2011; Gu et al., 2019).

Nonetheless, boundary exchange alone cannot fully reconcile the global marine Nd cycle. Specifically, it cannot explain the observed vertical profiles of [Nd], which are decoupled from ε_{Nd} (i.e., the 'Nd paradox': Goldstein and Hemming 2003), with low concentrations near the surface increasing with depth. This is a common characteristic of isotopes/elements (e.g. thorium) that are reversibly scavenged (i.e., where the element is scavenged onto sinking particles at the surface and is subsequently remineralised in the deep ocean) (Bertram and Elderfield, 1993; Bacon and Anderson, 1982). Siddall et al. (2008b) first addressed numerically a hypothesis that the 'Nd paradox' can be explained by a combination of lateral advection and reversible scavenging by applying the reversible scavenging model pioneered by Bacon and Anderson (1982) to Nd cycling. In their study, both [Nd] and ε_{Nd} were modelled simultaneously and explicitly to explore internal cycling of Nd in the ocean. Their findings demonstrated that scavenging and remineralisation processes are important active components in the marine cycling of Nd, driving the increase of [Nd] with depth, but still allowing ε_{Nd} to act as an effective water mass tracer.

Although inclusion of reversible scavenging can explain aspects of marine Nd cycling, the use of over-simplified fixed surface [Nd] and ε_{Nd} boundary conditions in the model by Siddall et al. (2008b) limited what could be determined about the full marine cycling of Nd and hence the 'Nd paradox'. The most comprehensive Nd isotope enabled ocean models to date now explicitly represent and quantify a wider range of distinct Nd fluxes that are both external and internal to the marine realm. For example, Arsouze et al. (2009) used a fully prognostic coupled dynamic and biogeochemical model to simulate [Nd] and ε_{Nd}, considering dust fluxes, dissolved riverine sources, boundary exchange and reversible scavenging. In their study, a boundary source from the continental margins represented the major source of Nd to seawater ($\approx 95\%$ of the total source). Rempfer et al. (2011) continued this work, undertaking a more detailed and comprehensive investigation of Nd sources and particle scavenging using a coarse resolution intermediate complexity model (Bern3D ocean model) and extensive sensitivity experiments. This later scheme was then closely followed by Gu et al. (2019) for the implementation of Nd isotopes in the ocean component of a more comprehensive Earth System Model (ESM, specifically the Community Earth System Model: CESM1.3) to explore in detail the changes to end-member ε_{Nd} signatures in response to ocean circulation and climate changes. Overall, these comprehensive models, capable of quantifying the major sources implicated in marine Nd cycling indicated that dust and river fluxes were important for representing [Nd] and ε_{Nd} distributions in the surface, but that the main flux of Nd to seawater is via a boundary source operating along the continental margins.

Recent pore fluid concentration profiles measured on the Oregon margin in the Pacific Ocean indicate that there may be a benthic flux of Nd from sedimentary pore fluids, presenting a new, potentially major seafloor-wide source of Nd to seawater (Abbott et al., 2015b,a). Additional measurements from the Tasman Sea suggest the likely presence of a benthic source of similar magnitude to that inferred for the North Pacific, which may indicate that regions with dominantly calcareous sediment also contribute a significant benthic source of Nd (Abbott et al., 2019). Evidence of this previously overlooked abyssal benthic sedimentary source of Nd has led to a shifting paradigm that challenges the current 'top down' model of marine Nd cycling to one of a 'bottom up' model (Haley et al., 2017).

The bottom up model contends that the dominant addition of Nd to the ocean is from a diffuse sedimentary source at depth, rather than surface point sources from rivers and dust and the shallow continental margins ('top down'). The benthic flux hypothesis provides a compelling yet unproved mechanism to explain deep water ε_{Nd} alteration alongside vertical [Nd] gradients in the North Pacific in the absence of modern deep-water formation, via exposure of old bottom water to a substantial benthic flux (Abbott et al., 2015a; Du et al., 2016).

Simple box models have been employed to investigate, to a first order, the non-conservative effects from a benthic flux (Du et al., 2016, 2018, 2020; Haley et al., 2017; Pöppelmeier et al., 2020b), suggesting overprinting of deep water mass ε_{Nd} is linked to benthic flux exposure time and the difference between the Nd isotope composition of the benthic flux and the bottom water (Abbott et al., 2015a; Du et al., 2018). However, these models lack comprehensive descriptions of both the marine Nd cycle and of physical ocean circulation and climate interactions, limiting a clear interpretation of precisely how (and under what physical/environmental conditions) the benthic flux may determine global marine Nd distributions. Applying an intermediate complexity model, Pöppelmeier et al. (2021a) investigated the benthic flux hypothesis in more detail by updating the Nd isotope enabled Bern3D model (Rempfer et al., 2011) to represent recent observations that indicate a Nd flux from bottom waters could occur across the entire seafloor. This was done by removing the depth limitation of the boundary exchange (previously 3 km) and invoking a constant benthic flux that escapes from all sediment-water interfaces. The scheme was further extended by revising key source-sink parameterisations, for subsequent investigation of non-conservative Nd isotope behaviour under different ocean circulation states (Pöppelmeier et al., 2022). The authors demonstrate substantial non-conservative effects occur even under strong circulation regimes with low benthic flux exposure times, and are not strictly limited to the deep ocean. This work highlights the importance of downward vertical fluxes via reversible scavenging alongside the benthic flux to describe non-conservative marine Nd isotope behaviour. Nonetheless, the low horizontal resolution of the intermediate complexity model limits full resolution of key circulation patterns such as distinct deep-water formation in the Labrador and in the Nordic Seas, inhibiting the capabilities of the scheme to fully capture and explore water mass end member ε_{Nd} distributions.

Thus, despite substantial progress to explicitly describe seawater Nd budgets, it is apparent that outstanding questions remain, alongside divergent lines of argument amongst subject specialists, limiting a full, quantitative description of marine Nd cycling. The decoupled nature of marine [Nd] and ε_{Nd}, which is yet to be fully understood, and new emerging observations (e.g., Stichel et al. 2020) emphasise the critical need to progress our understanding of modern marine Nd cycling, in the light of continued use of ε_{Nd} as a valuable tracer of ocean circulation. In this context, Nd isotope enabled ocean models remain an effective way to progress with testing and constraining processes governing marine Nd cycling, which can then feedback key information to the wider GEOTRACES and ocean-tracer modelling community.

With this is mind, there is a current gap in the toolkit for modelling marine Nd cycling between the class of high complexity, state-of-the-art ESMs (e.g., Gu et al. 2019) and the more efficient intermediate complexity models (e.g., Rempfer et al. 2011; Pöppelmeier et al. 2020a). To bridge this gap, there is a need for a model with the full complexity of an Atmosphere-Ocean General Circulation Model (AOGCM), allowing the exploration of how Nd isotopes vary under changing climate conditions (including extensive palaeoceanographic applications), that is also capable of running very quickly to facilitate efficient parameter space exploration, performance optimisation and long integrations. The FAMOUS GCM fills this gap (Smith et al., 2008; Jones et al., 2005; Smith, 2012; Jones et al., 2008).

Here we present the new global marine Nd isotope scheme implemented in FAMOUS.

We utilise the new sediment ε_{Nd} maps from Robinson et al. (2021) as boundary conditions for a mobile global sediment Nd flux, with the end-goal of further constraining the major sources, sinks and cycling of Nd isotopes, and exploring instances of non-conservative behaviour related to changes in Nd source distributions and scavenging processes. We develop sensitivity experiments (Sect. 3.3) to isolate the physical effects of varying two key parameters that detail major Nd fluxes and cycling to the global ocean, verifying foremost that the new isotope scheme is responding to Nd source/sink and biogeochemical processes as expected, and contextualising how, and where, reversible scavenging processes and the benthic flux can govern marine [Nd] and ε_{Nd} distributions. Finally (Sect. 3.3 and 3.4), we evaluate overall model performance through comparison with modern measurements and assess the model's ability to simulate observed spatial and vertical gradients between ocean basins, encompassing underling structural uncertainty/model bias.

3.2 Methods

3.2.1 Model description

We use the FAMOUS GCM (Smith et al., 2008; Jones et al., 2005; Smith, 2012; Jones et al., 2008), a fast coupled AOGCM, derived from the Met Office's Hadley Centre Coupled Model V3 (HadCM3) AOGCM (Gordon et al., 2000). The atmospheric component of FAMOUS is based on quasi-hydrostatic primitive equations and has a horizontal resolution of 5° latitude by 7.5° longitude, 11 vertical levels on a hybrid sigma-pressure coordinate system and a 1-hour timestep. The ocean component is a rigid-lid model, with a horizontal resolution of 2.5° latitude by 3.75° longitude and 20 vertical levels, spaced unequally in thickness from 10 m at the near-surface ocean to over 600 m at depth, and a 12-hour timestep. The ocean and atmosphere are coupled once per day.

FAMOUS's parameterisations of physical and dynamical processes are almost identical to those of HadCM3, but it has approximately half the spatial resolution and a longer timestep, allowing it to run ten times faster. Thus, FAMOUS achieves a current speed of up to 650 model years per wall clock day on 16 processors, making it ideal for running large ensembles (Gregoire et al., 2011, 2016), more bespoke sensitivity studies (Smith and Gregory, 2009; Gregoire et al., 2015), and multi-millennial simulations, e.g. to examine ice sheet behaviours (Gregoire et al., 2012, 2016, 2015), ocean drifts (Dentith et al., 2019) and biogeochemistry (Dentith et al., 2020).

We added Nd isotopes (^{143}Nd and ^{144}Nd) as optional passive tracers into the ocean component of FAMOUS, using a version of the model with the Met Office Surface Exchange Scheme (MOSES) version 1 (Cox et al. 1999: FAMOUS-MOSES1). It was a pragmatic choice to avoid the more recent FAMOUS-MOSES2.2 configuration (Essery et al., 2003; Valdes et al., 2017; Williams et al., 2013; Essery et al., 2001), because evaluation of our new Nd scheme would be hindered by the collapsed Atlantic Ocean convection and strong deep Pacific MOC produced by FAMOUS-MOSES2.2 under pre-industrial boundary conditions (see Dentith et al. 2019). Nonetheless, the Nd isotope code implementation presented here is directly transferable to other versions of the UK Met Office Unified Model (UM) version 4.5, including HadCM3/L or FAMOUS-MOSES2.2.

3.2.2 A new reference simulation for this study

The use of Nd isotopes as a water provenance tracer comes from measurements of distinct ε_{Nd} signatures in different water masses. This is perhaps best demonstrated in the south Atlantic 'zig-zag' depth profiles, where ε_{Nd} displays large heterogeneity and distinguishes southward flowing North Atlantic Deep Water (NADW) from northward flowing Antarctic Intermediate Water (AAIW) and Antarctic Bottom Water (AABW) (Goldstein and Hemming, 2003; Jeandel, 1993). As such, it is desirable to implement the Nd isotope scheme in a

version of FAMOUS that more suitably positions these basinal water masses in the correct locations.

The standard pre-industrial FAMOUS setup (XFHCC; Smith 2012) has certain known limitations, including over-ventilated abyssal Atlantic waters characterised by strong, over-deep NADW formation, with 'North Atlantic' convection occurring only in the Norwegian-Greenland Sea (there is no deep water formation in the Labrador Sea), and insufficient Atlantic sector AABW formation (Dentith et al., 2019; Smith, 2012). This known physical bias would dominate simulated Nd distributions, thus hampering validation of the new Nd isotope scheme against modern measurements. To mitigate this, we chose to employ a new reference simulation with more appropriate basin-scale physical ocean circulation. This simulation was obtained from a perturbed parameter ensemble varying 13 physical tuning parameters (see Supplementary Sect. 3.5: Text S3.1 and Table 3.6 for brief description and for a list of perturbed parameters from this multi-sweep ensemble of FAMOUS MOSES1: Smith 1990, 1993; Crossley and Roberts 1995). We screened the resulting 549 simulations based on a set of pre-defined targets, with a particular focus on Atlantic Ocean structure and water mass composition. Specifically, we sought a simulation with appropriate modern AMOC strength (14-19 Sverdrup, Sv; where 1 Sv = $10^6 m^3\ s^{-1}$) (Frajka-Williams et al., 2019), AMOC structure (Talley et al., 2011), regions of AMOC convection as indicated by mixed layer depth (specifically in both the Labrador Sea and the Nordic Seas as these represent key regions for NADW formation and the resultant end member Nd isotope compositions; Lambelet et al. 2016), depth of maximum overturning ($\approx 1,000$ m), and presence of AABW in the abyssal Atlantic (Frajka-Williams et al., 2019; Talley et al., 2011; Kuhlbrodt et al., 2007; Ferreira et al., 2018). Furthermore, we assessed the capabilities of the simulation to represent appropriate water mass structure in the Pacific (Talley et al., 2011). Through this approach, we identified four possible candidate simulations from the large ensemble as the basis for the new Nd isotope scheme: XPDAA, XPDAB, XPDAC and XPDEA, here denoted by their unique five-letter Met Office UM identifier. See Supplementary Sect. 3.5: Table 3.7 for initial boundary conditions, and Figures 3.18-3.21 for Atlantic meridional stream function and mixed layer depth for the four experiments.

These simulations were integrated for a further 5,000 years to ensure adequate spin-up of the physical circulation. They were then assessed for their ability to simulate global modern observations of salinity and temperature (compared to the NOAA World Ocean Atlas salinity and temperature database; Locarnini et al. 2018; Zweng et al. 2019) as an objective and quantitative basis for selecting the parameter configuration to be our control (Fig. 3.1).

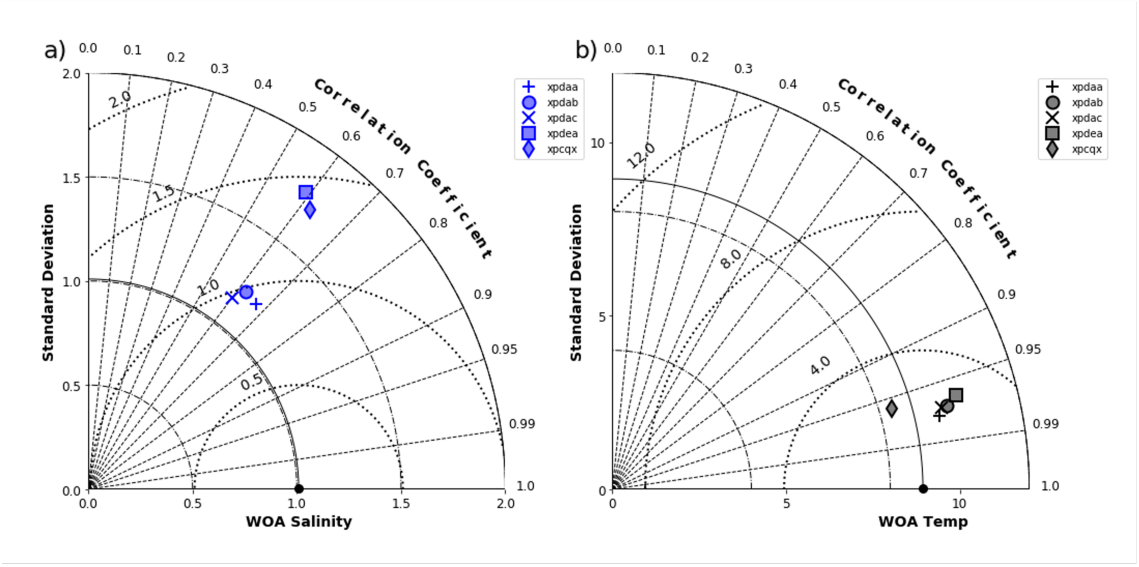

Figure 3.1: Taylor diagrams summarising the performance of the four control-candidate simulations (XPDAA, XPDAB, XPDAC, XPDEA) in terms of their correlation, centred root mean square error, and ratio of their variances to the NOAA World Ocean Atlas (a) salinity and (b) temperature databases (Locarnini et al., 2018; Zweng et al., 2019). The simulations were selected from a large FAMOUS pre-industrial perturbed parameter ensemble following the circulation performance screening described in Sect. 3.2.2. XPCQX represents the initial experiment, upon which the four control-candidates aim to improve.

From this analysis, XPDAA returned the lowest root mean square error (Fig. 3.1) for simulating both salinity and temperature and so was used as our control simulation (Fig. 3.2).

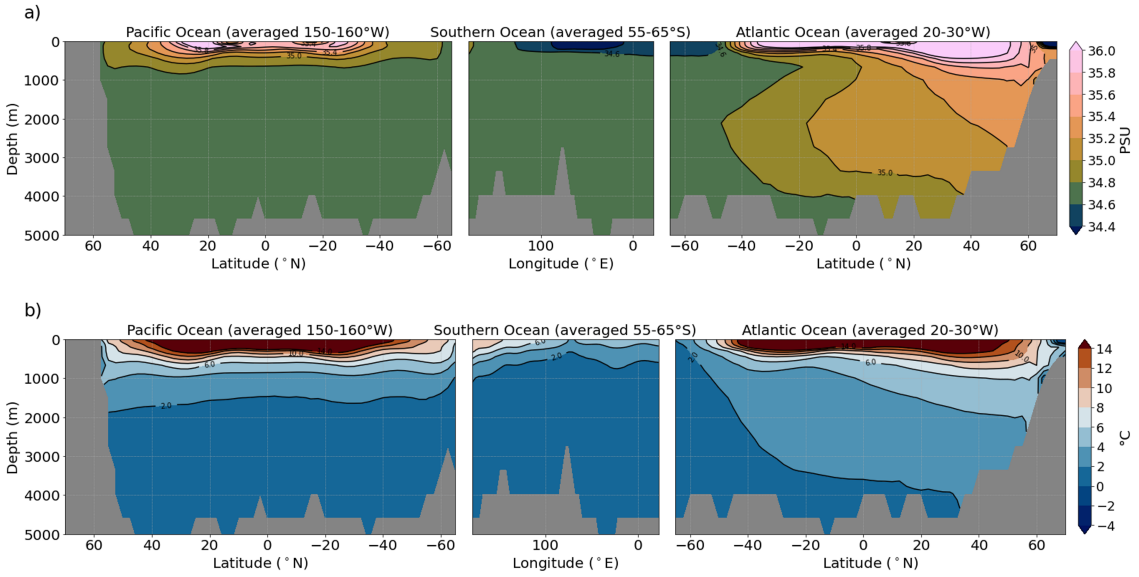

Figure 3.2: (a) Salinity and (b) temperature profiles for the control simulation (centennial mean from final 100 years of a 5,000-year simulation) along a transect crossing the Pacific-Southern-Atlantic Ocean.

The simulated steady state AMOC strength in FAMOUS under fixed pre-industrial

boundary conditions is approximately 17 Sv (Fig. 3.3a), which we consider to be in agreement with direct modern AMOC observations from the RAPID AMOC array at 26.5° N of 17.2 Sv from April 2004-October 2012, and the depth of maximum meridional stream function at 26.5° N is around 800 m (Fig. 3.3b), slightly shallower than RAPID observations of 900-1,100 m (McCarthy et al., 2015; Sinha et al., 2018). In terms of the Atlantic circulation structure, the overturning cell of NADW descends to depths of 3,000 m as it bridges into the South Atlantic, and AABW fills the bottom of the Atlantic basin with southern-sourced waters up to 20° N. For the Nd isotope implementation, all sensitivity studies and model tuning described subsequently are based upon this simulation, XPDAA.

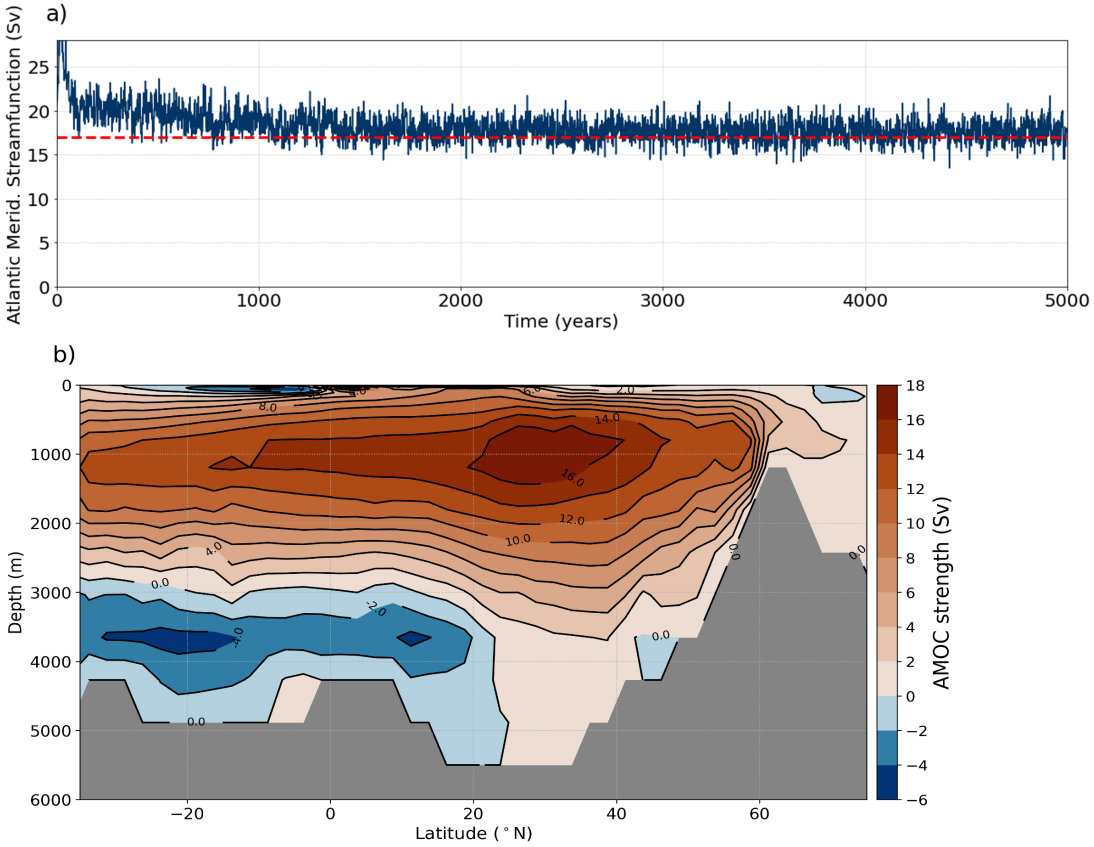

Figure 3.3: Atlantic Meridional streamfunction for a 5,000-year simulation using control (XPDAA), showing (a) the maximum in time series (red dashed line indicates RAPID-AMOC 2004-2012 averaged AMOC strength at 26.5° N of 17.2 Sv; McCarthy et al. 2015), and (b) the zonal integration calculated from the last one hundred years.

3.2.3 Neodymium isotope implementation in FAMOUS

In our simulated Nd isotope scheme, we represent three different global sources of Nd into seawater: aeolian dust flux, dissolved riverine input and dissolution of seafloor sediment. Neodymium (Nd) here refers to the sum of ^{143}Nd and ^{144}Nd, and the isotopic ratio (IR) relates to the ratio of ^{143}Nd to ^{144}Nd, as shown:

$$Nd = {}^{143}Nd + {}^{144}Nd \tag{3.2}$$

$$IR = \frac{{}^{143}Nd}{{}^{144}Nd} \tag{3.3}$$

By rearranging Eq. (3.2) and using the isotopic ratio (IR: Eq. (3.3)), individual fluxes of each isotope can be calculated (Eq. (3.4) and Eq. (3.5)) using information about Nd

fluxes from each specific source and their associated IR distributions:

$$^{143}Nd = \frac{Nd}{(1 + (1/IR))} \tag{3.4}$$

$$^{144}Nd = \frac{Nd}{(IR + 1)} \tag{3.5}$$

Neodymium isotopes are thus simulated and transported individually and independently as two separate tracers in our scheme, explicitly resolving the concentration and distribution of each Nd isotope, allowing for [Nd] and ε_{Nd} to be calculated offline from the model output. It should be noted that of the Nd isotopes, ^{143}Nd and ^{144}Nd together only account for 36% of total Nd. As such, obtaining absolute fluxes of ^{143}Nd and ^{144}Nd from total Nd fluxes requires a scaling of 0.36, and correspondingly, to compare the total simulated Nd from Eq. (3.2) with observed total Nd requires scaling by 1/0.36. Due to this counteraction, unscaled fluxes can be used, i.e. total Nd fluxes are used in the model and as such, the sum of the simulated $^{143}Nd + ^{144}$Nd (Eq. (3.2)) can be easily converted to observed [Nd] for direct comparison, as carried out previously by Gu et al. (2019); Pöppelmeier et al. (2020b); Rempfer et al. (2011).

The implementation of each source/sink term is described in detail in the following sections. To summarise these different components, Nd sources from aeolian dust fluxes and dissolved riverine input enter the ocean only via the uppermost near-surface ocean layer of the model. Seafloor sedimentary fluxes, an umbrella term that refers to a multitude of processes encompassing boundary exchange (Lacan and Jeandel, 2005a), submarine groundwater discharge (Johannesson and Burdige, 2007), and a benthic flux released from pore waters (Abbott et al., 2015a), are simulated via a combination of a sedimentary source applied across sediment-water interfaces together with a separate sink occurring via particle scavenging. Removal of Nd from the ocean model occurs when Nd scavenged/adsorbed onto sinking biogenic and lithogenic (dust) particles reaches the seafloor via vertical fluxes and undergoes sedimentation, removing the particle-associated Nd from the ocean.

In the model numerics, fluxes of each Nd isotope into the ocean (kg m^{-3}s^{-1}) are multiplied by a factor of 10^{18}. This technique minimises the mathematical error associated with carrying small numbers, and so concentrations of each Nd isotope in model units are in (10^{18} kg (Nd) m^3). A full list of all variables described in the text and their abbreviations are given in Table 3.1.

Table 3.1: Nd scheme model parameters, abbreviations, fixed model parameter values, and units.

Variable	Abbreviation	Fixed parameter value	Unit
Total Nd concentration	$[Nd]_t$	-	pmol kg^{-1}
Dissolved Nd	$[Nd]_d$	-	pmol kg^{-1}
Particle-associated Nd	$[Nd]_p$	-	pmol kg^{-1}
Nd source, total	f_{total}	-	g Nd yr^{-1}
Nd source, density	S_{total}	-	g Nd m^{-3}yr^{-1}
Dust source, total	f_{dust}	3.3×10^8	g Nd yr^{-1}
Dust source, density	S_{dust}	-	g Nd m^{-3}yr^{-1}
Flux of dust	F_{dust}	2D horizontal global field from Hopcroft and Valdes (2015)	g m^{-2}yr^{-1}
Nd concentration dust	$\overline{C}_{dust}$	20	μg g^{-1}
Nd dust dissolution	β_{dust}	0.02	

Riverine source, total	f_{river}	4.4×10^8	g Nd yr^{-1}
Riverine source, density	S_{river}	-	g Nd $m^{-3}yr^{-1}$
River discharge	RIVER	-	g $m^{-2}yr^{-1}$
Riverine scaling factor	α_{river}	1	
Nd concentration river	C_{river}	-	μg g^{-1}
Nd removal, estuaries	$\overline{\gamma}_{river}$	0.7	
Sediment source, total	f_{sed}	-	g Nd yr^{-1}
Sediment source, density	S_{sed}	-	g Nd $m^{-3}yr^{-1}$
Total sediment surface	A_{total}	-	m^2
Gridbox sediment surface	$A(i,k)$	-	m^2
Gridbox volume	$A(i,k)$	-	m^3
Thickness of euphotic layer	z_{eu}	81	m
Penetration depth of opal	l_{opal}	10,000	m
Penetration depth of $CaCO_3$	$l_{calcite}$	3,500	m
Particle settling velocity	ω	1,000	m yr^{-1}
Ratio $[Nd]_p$ to $[Nd]_d$	$[Nd]_p/[Nd]_d$	-	
Global average density of seawater	p	1,024.5	kg m^{-3}
Reversible scavenging, density	S_{rs}	-	g Nd $m^{-3}yr^{-1}$
Ratio between average POC concentration and density of seawater	R_{POC}	2.93×10^{-9}	
Ratio between average $CaCO_3$ concentration and density of seawater R_{CaCO_3}	6.27×10^{-9}		
Ratio between average opal concentration and density of seawater	R_{opal}	5.21×10^{-9}	
Ratio between average dust concentration and density of seawater	R_{dust}	1.73×10^{-9}	
Total Nd inventory after equilibrium	$Nd(I)$	-	10^{12} g

3.2.3.1 Dust source

Surface dust deposition (F_{dust}) is prescribed in the model from the annual mean dust deposition for the pre-industrial as simulated by the atmosphere component of the Hadley Centre Global Environmental Model version 2 (HadGEM2-A) GCM (Collins et al., 2011) (Fig. 3.4a). The dust deposition scheme (described by Woodward 2011) has been shown to be in generally good agreement with observations, with concentrations in the Atlantic well simulated across the whole of the Saharan dust plume, although some discrepancies occur, including an overestimation at some Pacific sites during spring (Collins et al., 2011). The simulation of pre-industrial climate conditions within HadGEM2 are described by Hopcroft and Valdes (2015), and the dust results specifically are described in full by Hopcroft and Valdes (2015). Based on these simulated dust fluxes, we apply an Nd source per volume (S_{dust} : g $m^{-3}yr^{-1}$) in the uppermost layer of the ocean model, assuming a global mean concentration of Nd in $\overline{C}_{dust}$($\overline{C}_{dust}$ = 20 μg g^{-1}) (Goldstein et al., 1984; Grousset et al., 1988, 1998) from which only a certain fraction β_{dust}(β_{dust} = 0.02: Greaves et al. 1994) dissolves in seawater.

$$S_{dust}(i,k) = \frac{F_{dust}(i,1) \times \overline{C}_{dust} \times \beta_{dust}}{dz(i,1)} \tag{3.6}$$

Here i, k represents the horizontal and vertical indexing of model grid cell and dz is the grid cell's thickness (10 m in the uppermost surface layer where $k = 1$). The total global flux of Nd from surface aeolian dust deposition to seawater (f_{dust}) is 3.3×10^9 g(Nd) yr^{-1}. Although we use an updated dust deposition field compared to previous studies, prescribed $\overline{C}_{dust}$ and β_{dust} are broadly consistent with earlier Nd isotope schemes, providing a comparable total Nd dust source (1.0×10^8 g $- 5.0 \times 10^8$ g(Nd) yr^{-1}; Arsouze et al. 2009; Gu et al. 2019; Pöppelmeier et al. 2020b; Rempfer et al. 2011; Tachikawa et al. 2003).

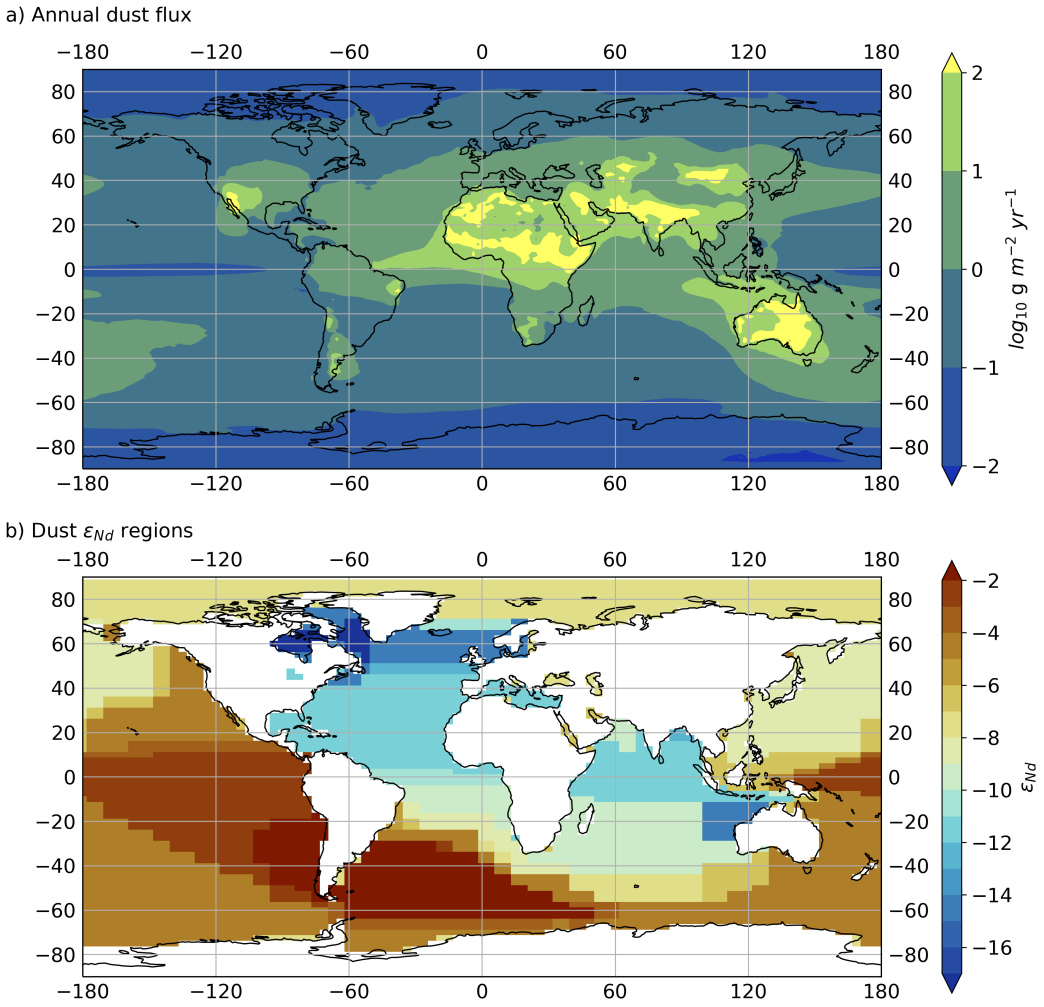

Figure 3.4: (a) Annual dust deposition taken from the pre-industrial annual mean dust deposition simulated by HadGEM2-A GCM (Hopcroft and Valdes, 2015), and (b) ε_{Nd} signal from dust deposition following Tachikawa et al. (2003) and updated with information from Mahowald et al. (2006) and Blanchet (2019).

For the Nd isotope compositions of the dust flux, we started with the first-order estimate by Tachikawa et al. (2003), as follows: North Atlantic $> 50°$ N; $\varepsilon_{Nd} = -15$, Atlantic $< 50°$ N: $\varepsilon_{Nd} = -12$, North Pacific $> 44°$ N: $\varepsilon_{Nd} = -5$, Indopacific $< 44°$ N: $\varepsilon_{Nd} = -7$, and remainder: $\varepsilon_{Nd} = -8$. This was revised with additional constraints, accounting for the dust plume expansions as reported by Mahowald et al. (2006), in combination with the mean Nd isotope signatures of the respective source regions as determined by the global compilation of detrital Nd isotope data by Blanchet (2019) (Fig. 3.4b).

3.2.3.2 Dissolved riverine source

To represent the Nd source from dissolved river fluxes, we used the river outflow to the ocean simulated by FAMOUS (RIVER) as our river water discharge (g m^{-2} s^{-1}) and combined this outflow with both the Nd concentration (C_{river}; μg g^{-1}) and isotopic concentration (used to calculate the flux from each Nd isotope using Eq. (3.4) and Eq. (3.5)) of river water dissolved material, as estimated by Goldstein and Jacobsen (1987, see Table 3). All river source Nd fields are shown in Fig. 3.5.

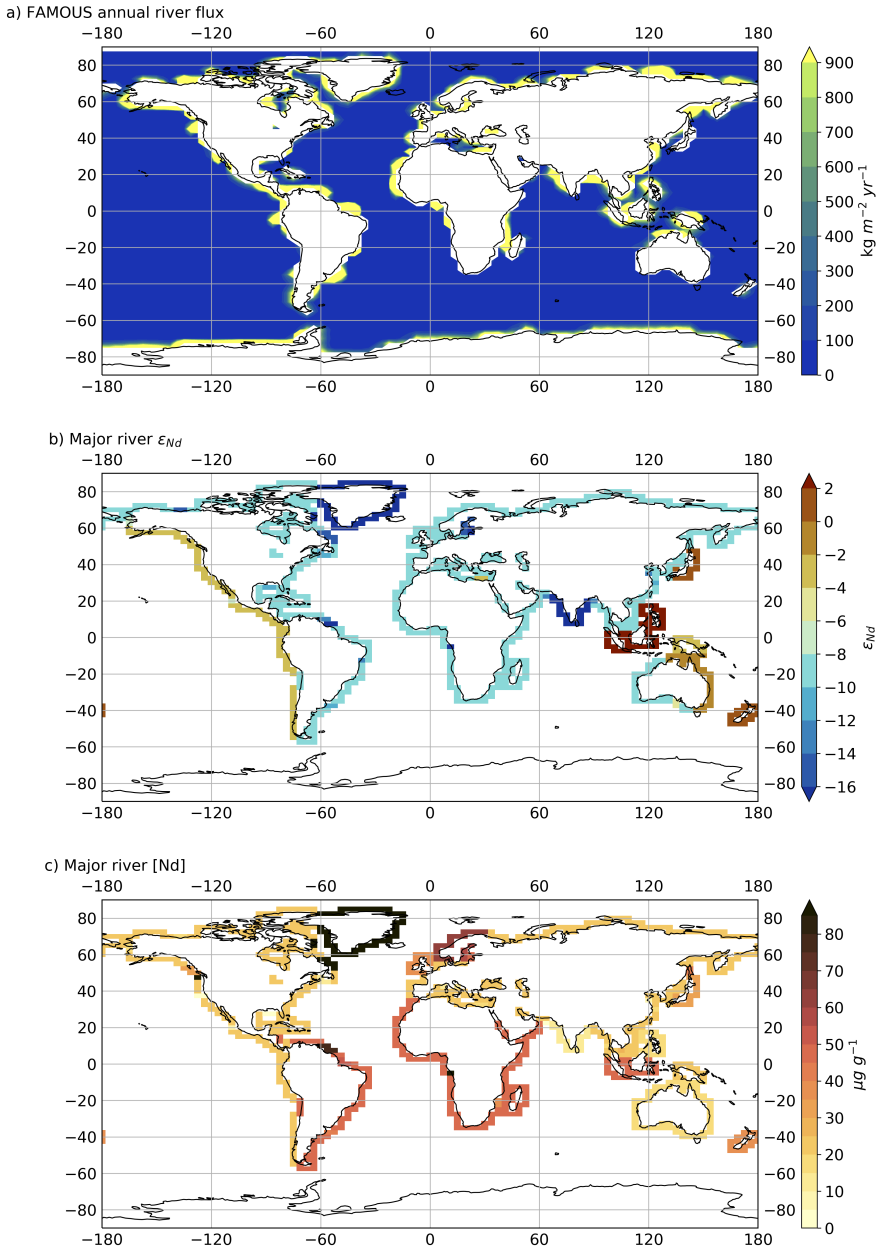

Figure 3.5: (a) Simulated river outflow (RIVER) in FAMOUS, (b) major river ε_{Nd}, and (c) major river [Nd]; (b) and (c) are prescribed following estimates by Goldstein and Jacobsen (1987).

River outflow in FAMOUS is based on a routing scheme that instantaneously delivers terrestrial runoff (precipitation - [evaporation + soil moisture]) from the location that precipitation falls to the designated coastal grid cell that the runoff would reach due to river routing (i.e., the river mouth). Relating the riverine Nd flux to the model's prognostic river discharge allows the Nd river source to respond to different climatic conditions,

making it a more dynamic and predictive tool for examining the impact of changes in the global hydrological balance, such as wetting/drying events, or shifts in the monsoons. Essentially, river outflow plumes are 'tagged' with the estimated ε_{Nd} (which is provided as an input map along the coasts; Fig. 3.5b) according to the model's projected water discharge at that location and C_{river} (also provided as an input map along the coasts; Fig. 3.5c). For palaeo or future climate applications where river routing is significantly different to today, the input maps controlling ε_{Nd} and C_{river} tagging at the coast would need to be updated to reflect Nd dissolution from the modified fluvial pathway over land, the model should predict the rest.

Estuaries are important biogeochemical reactors of rare earth elements (REEs), with sea salt driving flocculation of river-dissolved organic matter, which results in estuarine REE removal (Elderfield et al., 1990). This removal is known to be important in balancing the marine REE budgets, however the complex processes involved are still not fully constrained (Elderfield et al., 1990). Rousseau et al. (2015) summarised published observations of Nd removal (%) in estuaries from observations of estuarine dissolved Nd dynamics (Rousseau et al. 2015; their Table 1). Published values (n = 17) range from 40% in Tamar Neaps (Elderfield et al., 1990) to 97% in the Amazon (Sholkovitz, 1993), with a mean Nd removal of $71 \pm 16\%$ (s.d.). Based upon this, and parallel to previous model schemes (e.g., Rempfer et al. 2011; Gu et al. 2019; Arsouze et al. 2009), we assume that 70% of dissolved Nd from river systems are removed in estuaries (i.e., $\overline{\gamma}_{river} = 0.7$).

The dissolved riverine source per unit volume of Nd (S_{river} : g m^{-3}yr^{-1}) in the uppermost layer of the ocean is therefore calculated as:

$$S_{river}(i,k) = \frac{RIVER(i,1) \times C_{river} \times (1.0 - \overline{\gamma}_{river})}{dz(i,1)} \tag{3.7}$$

The total global flux of river sourced dissolved Nd to seawater (f_{river}) is $4.4{\times}10^8$ g(Nd) yr^{-1}. Previous Nd isotope schemes have applied either fixed annual mean continental river discharge estimates from Goldstein and Jacobsen (1987) and Dai and Trenberth (2002), as applied in the Bern3D Nd isotope scheme (Rempfer et al., 2011; Pöppelmeier et al., 2021a), or, similar to this study, using the model's own river routing and discharge schemes, as with NEMO-OPA (Arsouze et al., 2009) and CESM1 (Gu et al., 2019). Our estimated global total riverine Nd source to the oceans sits within previous model estimates ($2.6 \times 10^8 - 1.7 \times 10^9$ g(Nd) yr^{-1}; Arsouze et al. 2009; Gu et al. 2019; Pöppelmeier et al. 2020b; Rempfer et al. 2011; Tachikawa et al. 2003).

There is a larger range in estimated riverine Nd flux to the ocean relative to the estimated dust flux ranges. It should be noted that the largest simulated Nd river source amongst these studies (1.7×10^9 g(Nd) yr^{-1}; Pöppelmeier et al. 2020b) in the updated Bern3D Nd isotope scheme applied a river scaling factor, used as a tuning parameter and based on findings by Rousseau et al. (2015), who suggest a globally significant release of Nd to seawater by dissolution of river sourced lithogenic suspended sediments grounded upon observations in the Amazon estuary. Our model does not attempt to fully resolve all complex estuarine processes, and in this study we chose to represent the dissolved riverine flux as a single source to seawater. Early findings by Goldstein and Jacobsen (1987) document that the Nd isotope composition of dissolved and suspended river loads can vary by up to four epsilon units. Observations presented by Rousseau et al. (2015) showed the measured Amazon dissolved river end member value ($\varepsilon_{Nd} = -8.9$) was more radiogenic than the typical suspended river material ($\varepsilon_{Nd} = -10.6$) and as such, combining dissolved and particulate sources in river ε_{Nd} budgets is non-trivial. Furthermore, our sediment Nd source to the ocean (described Sect. 3.2.3.3), which occurs across sediment-water interfaces, utilises the continental margin and seafloor ε_{Nd} distribution maps by Robinson et al. (2021), thus using the most recent compilation of published global observations of Nd isotope compositions of river sediment samples deposited on the continental shelf and

slopes (alongside geological outcrops and marine sediment samples). It is therefore likely that this margin source encompasses at least in part the Nd isotope fingerprint from a river particle flux. Notwithstanding, our model does permit a scaling of the Nd river flux (α_{river}), which, although out of the scope of this study, could be applied in future model development to explore in more detail a particulate river source as a major Nd flux to seawater.

3.2.3.3 Continental margin and seafloor sediment source

The sediment source describes the flux of Nd into seawater entering each model grid cell adjacent to sediment, this source is not restricted to the uppermost surface layers and can be implemented across all vertical and horizonal sediment-water interfaces, as is the case for all experiments described in this study. As such, the sediment source represents (1) boundary exchange, as defined by Lacan and Jeandel (2005b), which describes the flux of Nd from particle-seawater exchange occurring predominantly across the continental margins; (2) submarine groundwater discharge, as suggested by Johannesson and Burdige (2007), which releases Nd to seawater via discharge of fresh groundwater to coastal seas and is mainly limited to the upper 200 m; and (3) a benthic flux, which specifically refers to a transfer of Nd from sediment pore water to seawater resulting from early diagenetic reactions and is not depth limited (Abbott et al., 2015b,a; Haley et al., 2017).

The total sediment Nd source per unit volume (S_{sed} : g $m^{-3}yr^{-1}$) into any given ocean grid cell is dependent on the fraction of the surface area of that cell that is in contact with sediment. Similar to previous schemes (e.g., Gu et al. 2019; Pöppelmeier et al. 2020b; Rempfer et al. 2011), the total globally integrated sediment-associated Nd source to the ocean (f_{sed} : g Nd yr^{-1}) is used as a tuning parameter.

$$S_{sed}(i,k) = f_{sed} \times \frac{A(i,k)}{A_{total}} \times \frac{1}{V(i,k)}, \tag{3.8}$$

where $A(i,k)$ is the total area of the sediment surface in contact with seawater per ocean grid cell (m^2), A_{total} is the total global area of the sediment surface where a sediment source occurs (m^2) and $V(i,k)$ is the volume of water per ocean grid cell (m^3).

There remains no true consensus on whether (and how) to apply spatial variability to sediment Nd sources, as reflected in the way previous schemes have adopted different approaches. Arsouze et al. (2009) limited the sediment flux to the upper 3,000 m of the ocean (to represent 'boundary exchange' processes), imposing a depth scaling factor, and considering estimated [Nd] distributions across the continental margins using the earlier marine margin Nd compilation by Jeandel et al. (2007). Both Rempfer et al. (2011) and Gu et al. (2019) simplified this method by applying spatially uniform sediment Nd fluxes, also limited to the upper 3,000 m. In more recent work, Pöppelmeier et al. (2020b) removed the depth limitation (as we have done), and incorporated a geographically-varying scaling factor that extrapolated modern Nd flux observations to try to capture more localised features through increased benthic fluxes (Abbott et al., 2015b; Blaser et al., 2020; Grenier et al., 2013; Lacan and Jeandel, 2005a; Rahlf et al., 2020). Pasquier et al. (2021) presented the first inverse model of global marine cycling of Nd, and in this latest scheme, the strength of the sediment Nd flux to the ocean was imposed with an exponential depth function, resembling eddy kinetic energy and particulate organic matter fluxes, which are characteristically larger near surface and coastal regions.

For our scheme, we do not assume spatial variations in the sediment source of Nd (f_{sed}). The flux per unit area is uniform with depth, latitude and longitude, essentially avoiding making explicit inferences on the nature of the sedimentary Nd source. It has been proposed that preferential mobilisation of certain components of the sediment drive spatial variations in sediment fluxes (e.g., Abbott et al. 2015a; Wilson et al. 2013; Du

et al. 2016; Abbott et al. 2019; Abbott 2019), and that both detrital and authigenic phases likely exchange Nd within pore water during early diagenesis (Du et al., 2016; Blaser et al., 2019a). However, the elusiveness of marine Nd cycling alongside our limited knowledge of the specific mechanisms controlling sediment-water Nd exchange means that determining generalisable rules for where and under what conditions (e.g., redox environments or fresh labile detrital material) preferential mobilisation may occur is unknown and challenging to resolve. Therefore, in accordance with Pöppelmeier et al. (2020a); Du et al. (2020); Gu et al. (2019) and Rempfer et al. (2011), we adopt a constant detrital sediment flux as a first-order approximation. In fact, we contend that applying this simpler method, as opposed to constructing a more complex source term that is arguably just as arbitrary (given the uncertainty in Nd cycling), allows for a more explicit quantification of differences between observed and simulated Nd distributions. As such, without overfitting our model, we allow for the clearest indication of those parts of the system that are well understood (and represented), and those which prove deficient. Under this framework, we may separate out and test the effect of many of the major Nd sources/sinks with dedicated sensitivity simulations, including the possibility, in future work, of incrementally modifying the sediment source distributions to increase the complexity of the scheme and assess the impact of our various assumptions.

The isotopic ratio of the sediment Nd flux to seawater is prescribed using the recent updated global gridded map of bulk detrital ε_{Nd} at the continental margins and seafloor (Robinson et al. 2021, Fig. 3.6a). Using Eq. (3.4) and Eq. (3.5), fluxes of each Nd isotope are calculated from this condition and bi-linearly regridded to the model's native resolution (Fig. 3.6b). Previous studies used the predecessor continental ε_{Nd} map by Jeandel et al. (2007) (e.g. Arsouze et al. 2009, 2007; Gu et al. 2019; Rempfer et al. 2011); see Fig. 5 in Robinson et al. (2021) for a comparison of the differences). Marginal ε_{Nd} distributions in our improved map are broadly more radiogenic across the Arctic Shield, Northern Eurasia, South America, north-eastern Africa and Antarctica and more unradiogenic over southern Greenland, north-eastern Europe, western and eastern Africa and parts of the Americas. Crucially, the newer map of Robinson et al. (2021) provides the first estimate of global seafloor sediment Nd isotope composition, which is necessary for considering a global (e.g., rather than depth limited) benthic flux.

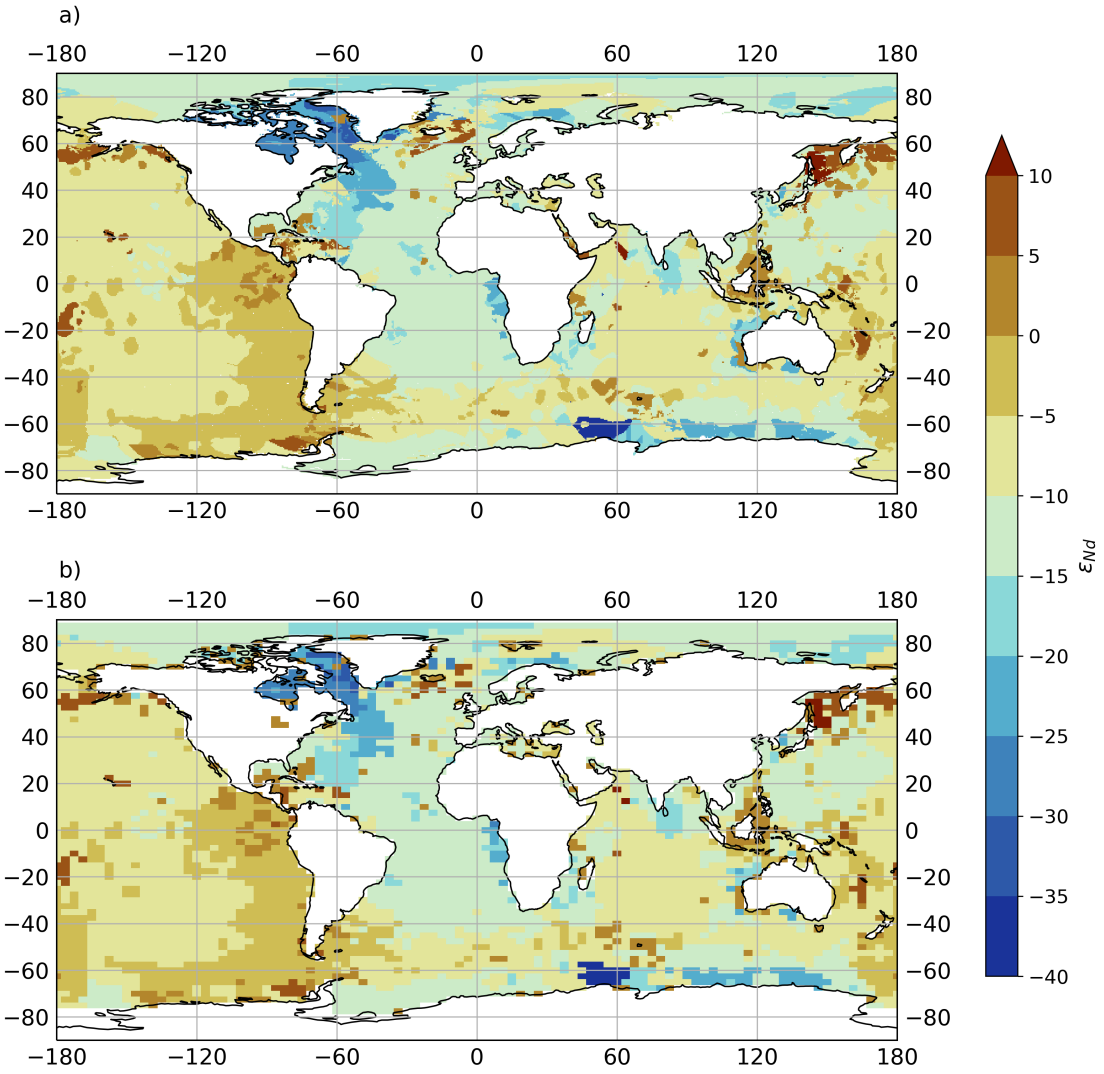

Figure 3.6: (a) Map of the global ε_{Nd} distributions at the sediment-ocean interface from Robinson et al. (2021), and (b) as used as a model input in this study (bi-linearly regridded from (a) onto the coarser FAMOUS ocean grid).

Pasquier et al. (2021) first applied the sedimentary ε_{Nd} map from Robinson et al. (2021) in their recent global marine Nd isotope scheme, imposing positive (i.e., radiogenic) modifications to the Pacific sedimentary ε_{Nd} and using a reactivity scaling factor (linked to sediment lability) that favours more extreme ε_{Nd} signals. Here, we again adopt a simpler approach, imposing the unmodified sediment ε_{Nd} distributions from Robinson et al. (2021), allowing for a presentation of our new scheme based on what we confidently know about Nd cycling without the complication of over-conditioning our model inputs. Future research may then use this work as a foundation to robustly explore different choices for model inputs (i.e., boundary conditions) to revisit these fundamental questions about Nd sediment source.

3.2.3.4 Internal cycling via reversible scavenging

Vertical cycling and removal of Nd from the water column via sinking particles ('reversible scavenging') is parameterised using the same approach as previous Nd isotope implementations (Siddall et al., 2008b; Arsouze et al., 2009; Rempfer et al., 2011; Gu et al., 2019; Pöppelmeier

et al., 2020a; Oka et al., 2021). Based on the original scheme of Bacon and Anderson (1982), the method captures the physical process of absorption/incorporation and desorption/dissolution of Nd onto particle surfaces in seawater. The scheme assumes that particle associated Nd is in dynamic equilibrium with falling particles throughout the water column, with continuous exchange between the particle and dissolved pools. This process redistributes Nd within the water column, acting as a net sink of dissolved Nd at shallower depths as they adsorb onto particle surfaces, and a net source at greater depths where dissolution of particles releases dissolved Nd back to seawater. The scavenging is the only sink of Nd in our model; Nd associated to particles (particulate organic carbon, POC; calcium carbonate, $CaCO_3$; opal; dust) reaching the seafloor is removed from the system, operating under a steady state assumption that acts to balance the three external input sources (marine sediments, dust and rivers). Previous studies (e.g., Siddall et al. 2008b; Arsouze et al. 2009; Rempfer et al. 2011; Gu et al. 2019; Wang et al. 2021) have demonstrated that reversible scavenging is an active and important component in global marine Nd cycling, and is necessary for successfully simulating both $[Nd]_d$ and ε_{Nd} distributions.

Updating the approach employed by Siddall et al. (2008b), we prescribe individual biogenic particle export fields based on satellite-derived primary production. FAMOUS does contain an optional ocean biogeochemistry module (Hadley Centre Ocean Carbon Cycle; HadOCC), which includes simplified nutrient-phytoplankton-zooplankton-detritus (NPZD) classes (Palmer and Todderdell, 2001) and could instead be used as the basis for predicting vertical particle fluxes in the ocean (which was the approach adopted by Arsouze et al. 2009; Gu et al. 2019; Rempfer et al. 2011). We favoured satellite-derived estimates in order to improve the accuracy of particle-associated cycling of Nd and reduce biases inherent to the intermediate complexity biogeochemistry model (Dentith et al., 2020; Palmer and Todderdell, 2001). This approach also optimises the computational efficiency of our scheme, since the added ecosystem and geochemistry tracer fields in HadOCC slows the model down. However, future work could modify our implementation to instead associate Nd cycling with the prognostic particle fields in HadOCC.

In our scheme, biogenic particle fields (POC, $CaCO_3$, and opal) are prescribed using gridded, global satellite-derived particle export productivity from Dunne et al. (2012, 2007). The euphotic zone (z_{eu}), is set to a globally uniform depth in FAMOUS of 81 m, the closest bottom grid box depth to match that defined in the OCMIP II protocol (75 m) (Najjar and Orr, 1998). Below z_{eu}, appropriate depth-dependent dissolution profiles, derived from assumptions of particle degradability and sinking speed (Martin et al., 1987; Laws et al., 2000; Behrenfeld and Falkowski, 1997), and widely used to model flux attenuation in ocean models (e.g. all models used in the Ocean-Carbon Cycle Model Intercomparison Project; Doney et al. 2004; Sarmiento and LeQuéré 1996), were applied to the biogenic export fluxes.

Downward fluxes of POC (F_{POC}) follow the power-law profile of Martin et al. (1987):

$$F_{POC}(z) = F_{POC}(z_{eu}) \times \left(\frac{z}{z_{eu}}\right)^{-\alpha} \text{ (for } z > z_{eu}\text{)}, \tag{3.9}$$

where z is depth (m), and α represents a dimensionless dissolution constant for POC set to 0.9 (Najjar and Orr, 1998). Although a widely used parameterisation of dissolution, it should be noted this so-called 'Martin curve' is known to underestimate the flux to the sediment in the off-equatorial tropics and subtropics and overestimates the flux in subpolar regions, indicating particles penetrate deeper than the Martin curve in the tropics and shallower in sub-polar regions (Dunne et al., 2007).

Downward fluxes of opal (F_{opal}) and $CaCO_3$ (F_{CaCO_3}) follow exponential dissolution profiles with particle-specific length scales l_{opal} (10,000 m) and $l_{calcite}$ (3,500 m) (Maier-Reimer, 1993; Henderson et al., 1999; Najjar and Orr, 1998):

$$F_{opal}(z) = F_{opal}(z_{eu}) \times \exp\left(\frac{z_{eu} - z}{l_{opal}}\right), \tag{3.10}$$

$$F_{\mathrm{CaCO_3}}(z) = F_{\mathrm{CaCO_3}}(z_{eu}) \times \exp\left(\frac{z_{eu} - z}{l_{\mathrm{CaCO_3}}}\right), \tag{3.11}$$

The sinking of dust is prescribed according to the pre-industrial annual mean dust deposition simulated by Hopcroft and Valdes (2015) (see Sect. 3.2.3.1). We assume that dust does not dissolve significantly with depth and so dust export fluxes are constant throughout the water column. In line with previous schemes (e.g. Arsouze et al. 2009; Pöppelmeier et al. 2020b; Rempfer et al. 2011; Siddall et al. 2008b), a uniform settling velocity (ω) of 1,000 m yr^{-1} is applied to all particle fields, capturing the mean particle flux to the seafloor.

Annual averaged export of biogenic fields are shown in Fig. 3.7 and the total annual export production of POC (9.6 Gt(C) yr^{-1}), $CaCO_3$ (0.45 Gt(C) yr^{-1}), and opal (90 Tmol(Si) yr^{-1}) are comparable with previous estimates, although export of $CaCO_3$ and opal are at the lower end, as highlighted in Table 3 by Dunne et al. (2007). Note, the annual export of $CaCO_3$ reflects the new optimised surface calcite parameterisation as described in Dunne et al. (2012).

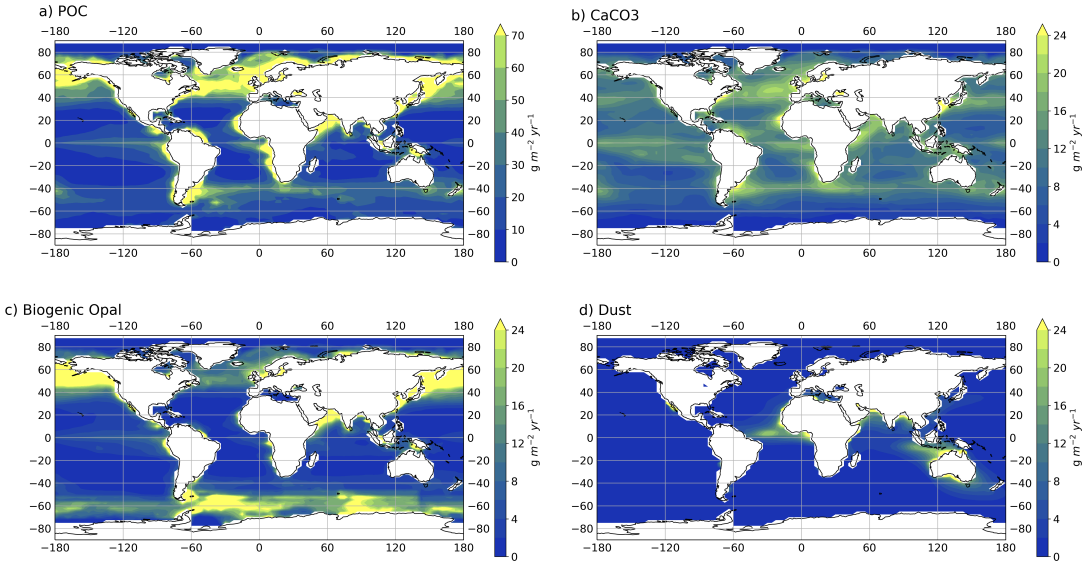

Figure 3.7: Particle export fields from the ocean surface (g m^{-2} yr^{-1}). Biogenic particle fields are prescribed using satellite-derived export productivity fields for (a) POC, (b) $CaCO_3$ and (c) opal (Dunne et al., 2007, 2012). The dust input fields (d) are annual mean dust deposition simulated for the pre-industrial by the HadGEM2-A GCM (Hopcroft and Valdes, 2015). Note the different scale used for panel (a).

Reversible scavenging (Nd_{rs}) considers total Nd for each isotope (j) as the dissolved Nd (Nd_d) and particulate Nd (Nd_p) associated with the different particle fields (χ; where χ = POC, $CaCO_3$, opal and dust).

$$[Nd]_t^j = [Nd]_d^j + [Nd]_p^j = [Nd]_d^j + \sum_{\chi}[Nd]_{p,\chi}]^j \tag{3.12}$$

Nd_p sinks in the water-column with the particles due to gravitational force. Dissolution of biogenic particles with increasing depth below the euphotic zone releases Nd incorporated/adsorbed onto particles back to seawater (i.e., the Nd is dissolved/desorbed). Thus, particles act as internal sinks for marine Nd_d in shallower depths and as sources at greater depths. This combined process for reversible scavenging (S_{rs}) in the model can be described by:

$$S_{rs}(i,k) = \frac{-\partial(\omega[Nd]_p(i,k))}{\partial z(i,k)} \tag{3.13}$$

Where $[Nd]_p$ can be determined within the model from total Nd for each isotope:

$$[Nd]_p^j(i,k) = [Nd]_t^j(i,k) \times \left(1 - \frac{1}{1 + \sum_{\chi} R_{\chi}(i,k) \times K_{\chi}^j}\right), \tag{3.14}$$

$R_{\chi}(i,k)$ describes the dimensionless ratio between particle concentration for each particle type $C_{\chi}(i,k)$ and the average density of seawater (p:1024.5 kg m^{-3}), input as fixed boundary conditions in our scheme. C_{χ} is calculated from the prescribed particle fluxes (F_{χ}; Fig. 3.7) by assuming a globally uniform settling velocity $\omega = 1,000$ m yr^{-1}, (Arsouze et al., 2009; Dutay et al., 2009; Gu et al., 2019; Kriest and Oschlies, 2008; Rempfer et al., 2011), i.e. $C_{\chi} = f_{\chi}/\omega$. The equilibrium between dissolved concentration ($[Nd]_d$)

and concentration associated to particle-type ($[Nd]_p$) can be described by the equilibrium partition coefficient (K^j_χ):

$$K^j_\chi = \frac{[Nd]^j_{p,\chi}}{[Nd]^j_d} \times \frac{1}{R_\chi}, \tag{3.15}$$

here $[Nd]_p/[Nd]_d$ represents the scavenging efficiency in the model. It is independent of particle type and is used as a tuning parameter. $\overline{R}_\chi$, however, is dependent on particle type (where $\overline{R}_\chi = \overline{C}_\chi/p$ and thus K_χ is different for different particles. Our global mean particle concentrations ($\overline{C}_\chi$; Table 3.2) are similar to those reported in previous schemes; see Supplementary Information (Sect. 3.5): Table 3.8 for a comparison.

Table 3.2: Global mean particle concentrations for each particle type used to calculate equilibrium scavenging coefficients following Eq. (3.15). In summary export fluxes of POC, $CaCO_3$ and opal are from Dunne et al. (2007, 2012) and dust fluxes are from Hopcroft and Valdes (2015).

Particle type	Acronym	Concentration (kg m^{-3})
POC	$\overline{C}_{POC}$	3.0×10^{-6}
$CaCO_3$	$\overline{C}_{CaCO_3}$	6.43×10^{-6}
Opal	$\overline{C}_{Opal}$	5.33×10^{-6}
Dust	$\overline{C}_{dust}$	1.78×10^{-6}

Isotopic fractionation during absorption/incorporation and desorption/dissolution is neglected due to similar masses of ^{143}Nd and ^{144}Nd, avoiding undue complexity arising from any assumption about preferential scavenging (Siddall et al., 2008b). Adsorption occurs everywhere that particles are present and we do not allow for preferential scavenging onto different particle types, consistent with previous models (e.g. Rempfer et al. 2011). In contrast, Siddall et al. (2008b) optimised K_χ to fit observed $[Nd]_d$ for each particle type. Their optimised solution effectively implied no scavenging of Nd by POC, this result was considered tentative due to similar dissolution profiles of $CaCO_3$ and POC, which likely biased scavenging to $CaCO_3$ that may have been more correctly attributable to POC.

Therefore, and by including advection and diffusion processes (*Transport*), it follows that the total conservation equation for each Nd isotope in the model scheme can be written as:

$$\frac{\delta[Nd]^j_t}{\delta t} = S^j_{dust} + S^j_{river} + S^j_{sed} + S^j_{rs} + Transport, \tag{3.16}$$

3.2.4 Evaluation methods & data sets

To validate the new Nd isotope scheme and to assess the model's performance, we compare the simulated $[Nd]_d$ and ε_{Nd} to modern seawater measurements, with a focus on describing the ability of the model to represent key spatial and vertical distributions across ocean basins.

As part of this assessment, a basic indication of model skill is returned by the mean absolute error (MAE):

$$MAE = \frac{1}{N}\sum_{k=1}^{N} |obs_k - sim_k|, \tag{3.17}$$

where obs_k and sim_k are measured and simulated $[Nd]_d$ or ε_{Nd} respectively, and k is an index over all observational data. For each measurement – based on its longitude,

latitude, and depth – the value predicted by the model is extracted and the mean deviation of simulated and observed $[Nd]_d$ and ε_{Nd} is presented in pmol kg^{-1} and epsilon units respectively. Here we chose specifically not to apply a grid box volume weighting to the MAE, which would act to emphasise abyssal Pacific results in our assessment of model skill, where there are few observations and relatively low variability in Nd distributions. The advantage of using an unweighted MAE is that the assessment metric better scrutinises regions with larger (spatial) gradients in both $[Nd]_d$ or ε_{Nd}; i.e., at the surface and high latitudes. The observational data used in this assessment are from the seawater REE compilation used by Osborne et al. (2017, 2015), augmented with more recent measurements including data in the GEOTRACES Intermediate Data Product 2021 (GEOTRACES Intermediate Data Product Group, 2021) from GEOTRACES cruises (GA02, GA08, GP12, GN02, GN03 and GIPY05). Combined, our observational database represents a total of 6,048 $[Nd]_d$ and 3,278 ε_{Nd} measurements, making it the largest compilation of seawater Nd data used to date to validate the performance of an Nd isotope enabled model. Notably, we omit measurements of $[Nd]_d > 100$ pmol kg^{-1} from the model data comparison because they represent very localised signals which we do not attempt to resolve. These include extreme surface concentrations present in restricted basins such as fjords, the Baltic Sea and the Gulf of Alaska (Chen et al., 2013; Haley et al., 2014), or input from hydrothermal activity (Chavagnac et al., 2018), which is not believed to govern global marine Nd distributions due to the immediate removal of hydrothermal Nd at the vent site (Goldstein and O'Nions, 1981). The location and spatial distribution of all observational records used in this study are shown in Fig. 3.8, and full details of the seawater compilation including a full list of all the references for the data sources are provided in Appendix A.

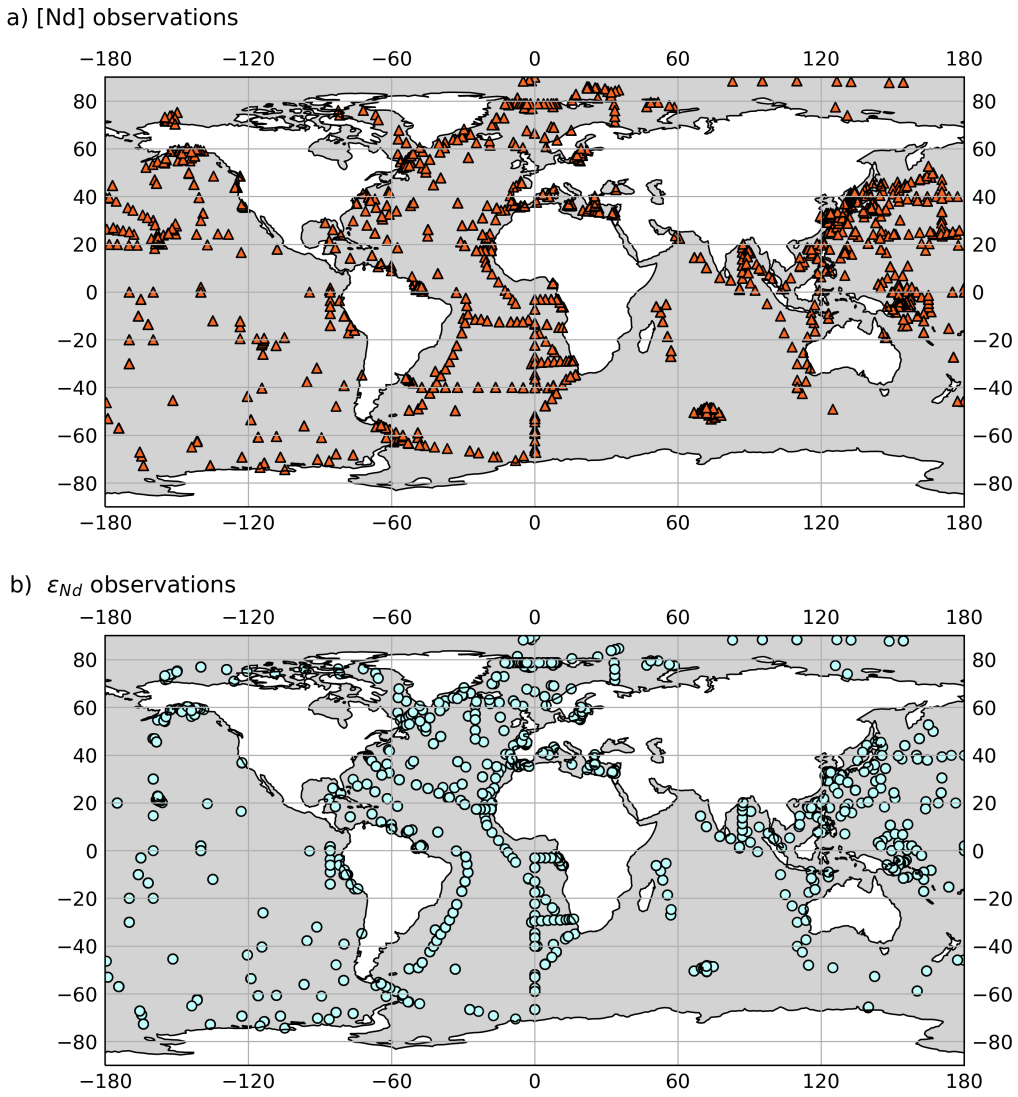

Figure 3.8: Location of marine observational records used in this study, (a) filled orange triangles show the location of dissolved Nd concentration records, and (b) filled sky-blue circles show the location of dissolved ε_{Nd} records.

Neither the horizontal nor vertical distribution of global seawater $[Nd]_d$ and ε_{Nd} observational data are even. Most $[Nd]_d$ measurements are in the Pacific Ocean followed by the Atlantic Ocean (representing 37% and 35% of measurements respectively, noting that the Pacific has more than twice the volume of the Atlantic), with far fewer measurements in the Indian Ocean (12%) and the Southern Ocean (5%). In comparison, ε_{Nd} measurements are most frequent in the Atlantic Ocean (45%), followed by Pacific Ocean (29%), and again there are fewest measurements from the Indian Ocean (8%) and Southern Ocean (7%). Both $[Nd]_d$ and ε_{Nd} observational data are biased towards shallower depths, with median depths of 496 m and 505 m, with only 10% and 11% of measurements at depths below 3,000 m respectively. It is therefore important to highlight that, as with previous studies, skew in the distribution of seawater Nd measurements will act to bias our assessment of model performance; $MAE_{[Nd]}$ towards the Pacific Ocean and Atlantic Ocean, $MAE_{\varepsilon_{Nd}}$ towards the Atlantic Ocean, and both towards shallower depths.

In some instances, near land grid cells, the location of the compared measured and modelled Nd may not match due to the coarseness of the model grid. In such cases, we

employ a nearest neighbour algorithm to extract the modelled value from the closest ocean model grid cell. Furthermore, if multiple measurements occur within one model grid cell, the arithmetic mean of the values is used for our comparison to model results, and as such, $n = 3{,}471$ and 2,136 for the calculation of both $MAE_{[Nd]}$ and $MAE_{\varepsilon_{Nd}}$ respectively.

To ensure that our evaluation is not overly reliant on the cost-function analysis alone, and hence reduce the spatial biases in our assessment from the geographically uneven spread of measured $[Nd]_d$ and ε_{Nd}, we also evaluate the capability of the model to reproduce appropriate global Nd inventories and to simulate large-scale horizontal and vertical gradients. For example, we compare $[Nd]_d$ and ε_{Nd} patterns across the global thermohaline circulation, through inter basin gradients, depth profiles and between distinct water masses, critically assessing the contributions of distinct Nd sources and cycling processes. We compare our results briefly with findings from previous modelling studies, but we highlight that the purpose of this study is to understand the behaviour of our model, and not to undertake a comprehensive calibration of its performance. Optimisation (or 'tuning') of the Nd scheme will follow this work, and this needs to be considered when comparing the cost function performance to previous schemes.

3.2.5 Sensitivity experiment design

We designed a number of sensitivity experiments (Table 3.3) to systematically vary individual model parameters describing the reversible scavenging efficiency ($[Nd]_p/[Nd]_d$) and the main Nd source (f_{sed}) in order to better understand our model's behaviour and performance. These two parameters ($[Nd]_p/[Nd]_d$ and f_{sed}) were chosen primarily as they represent important and largely unconstrained non-conservative processes that are understood to govern simulated global distributions of both seawater $[Nd]_d$ and ε_{Nd} (Rempfer et al., 2011; Pöppelmeier et al., 2020a; Gu et al., 2019; Arsouze et al., 2009; Siddall et al., 2008b). By isolating individual effects, the primary aim was to understand in detail the model's sensitivity to different forcings, identify which parameters are important for $[Nd]_d$ and/or ε_{Nd} patterns across different ocean basins and ocean depths, and to identify assumptions within the explored parameters that require further constraining (through further field campaign, laboratory analysis or model experimentation).

Firstly, $[Nd]_p/[Nd]_d$ is systematically varied in six sensitivity simulations ($[Nd]_p/[Nd]_d$ ranging 0.001-0.006), these values are based upon results from similar modelling schemes (Rempfer et al., 2011; Arsouze et al., 2009; Gu et al., 2019) and considers the few direct observations of $[Nd]_p/[Nd]_d$ (Jeandel et al., 1995; Stichel et al., 2020; Zhang et al., 2008). Here, and based upon simulations undertaken when validating the scheme, alongside estimates from previous optimised Nd isotope schemes (Arsouze et al., 2009; Rempfer et al., 2011; Gu et al., 2019; Pöppelmeier et al., 2020a), f_{sed} is fixed at 4.5×10^9 g yr^{-1} throughout.

Secondly, f_{sed} is varied in four sensitivity simulations (f_{sed} ranging $1.5 \times 10^9 - 6.0 \times 10^9$ g yr^{-1}), using values based upon previous recent estimates of a global sediment flux to seawater (3.3×10^9–5.5×10^9 g yr^{-1}; Gu et al. 2019; Pöppelmeier et al. 2020b; Rempfer et al. 2011), and encompassing a larger parameter space in order to explore the sensitivity of Nd distributions. Notably, our f_{sed} sensitivity studies alter the percentage contribution of the sediment Nd flux to the total Nd flux to seawater from 66% (where $f_{sed} = 1.5 \times 10^9$ g yr^{-1}) to 89% (where $f_{sed} = 6.0 \times 10^9$ g yr^{-1}). In all simulations $[Nd]_p/[Nd]_d$ is fixed at 0.003, based upon reasons outlined for the $[Nd]_p/[Nd]_d$ sensitivity simulations.

Table 3.3: Suite of FAMOUS simulations designed to assess the sensitivity of simulated $[Nd]_d$ and ε_{Nd} distributions to two systematically varied parameters: reversible scavenging efficiency ($[Nd]_p/[Nd]_d$) and the global rate of direct Nd transfer from sediment to ocean water (f_{sed}). Simulation name refers to the title given to each sensitivity simulation in this chapter, and the simulation identifier refers to the unique five-letter Met Office identifier (which, for example, can be used to call down full experiment details from the NERC PUMA facility: puma.nerc.ac.uk).

Simulation name	Simulation identifier	f_{sed} (g(Nd) yr^{-1})	$[Nd]_p/[Nd]_d$
Varying $[Nd]_p/[Nd]_d$			
EXPT_RS1	XPDAI	4.5×10^9	0.001
EXPT_RS2	XPDAD	4.5×10^9	0.002
EXPT_RS3	XPDAH	4.5×10^9	0.003
EXPT_RS4	XPDAE	4.5×10^9	0.004
EXPT_RS5	XPDAF	4.5×10^9	0.005
EXPT_RS6	XPDAG	4.5×10^9	0.006
Varying f_{sed}			
EXPT_SED1	XPDAL	1.5×10^9	0.003
EXPT_SED2	XPDAM	3.0×10^9	0.003
EXPT_SED3	XPDAH	4.5×10^9	0.003
EXPT_SED4	XPDAN	6.0×10^9	0.003

Dissolved seawater Nd in all simulations are initialised from zero and integrated for at least 9,000 years under constant pre-industrial boundary conditions to allow the deep ocean circulation and marine Nd cycle to reach steady state, which we define as being when the Nd inventory becomes [near] constant with time (< 0.02 % change per 100 years). All the presented results refer to or show the centennial mean from the end of the 9,000-year simulations.

3.3 Results and discussion

3.3.1 Model sensitivity to reversible scavenging efficiency ($[Nd]_p/[Nd]_d$)

The first set of sensitivity experiments test the response of simulated $[Nd]_d$ and ε_{Nd} to a systematic variation of the reversible scavenging tuning parameter ($[Nd]_p/[Nd]_d$) while all other parameters are kept constant. In the first 2,000 years, the Nd inventory increases exponentially in all simulations (Fig. 3.9). *EXPT_RS1* continues to increase rapidly until the end of the experiment, but after 2,000 years for simulations *EXPT_RS2* to *EXPT_RS6*, the rate of global Nd accumulation begins to slow as the inventories tend towards equilibrium. By year 6,000, all experiments with a global Nd inventory $< 8.0 \times 10^{12}$ g reach steady state and remain so until the end of the experiment (9,000 years). We therefore deem these simulations to have reached an acceptable equilibrium state. We explain why *EXPT_RS1* and *EXPT_RS2* do not reach equilibrium below, but otherwise, because of their unrealistic condition after 9,000 years (i.e. they reach an Nd inventory far past the target inventory of 4.2×10^{12} g; Tachikawa et al. (2003)), these two simulations are largely omitted from further discussion and analysis.

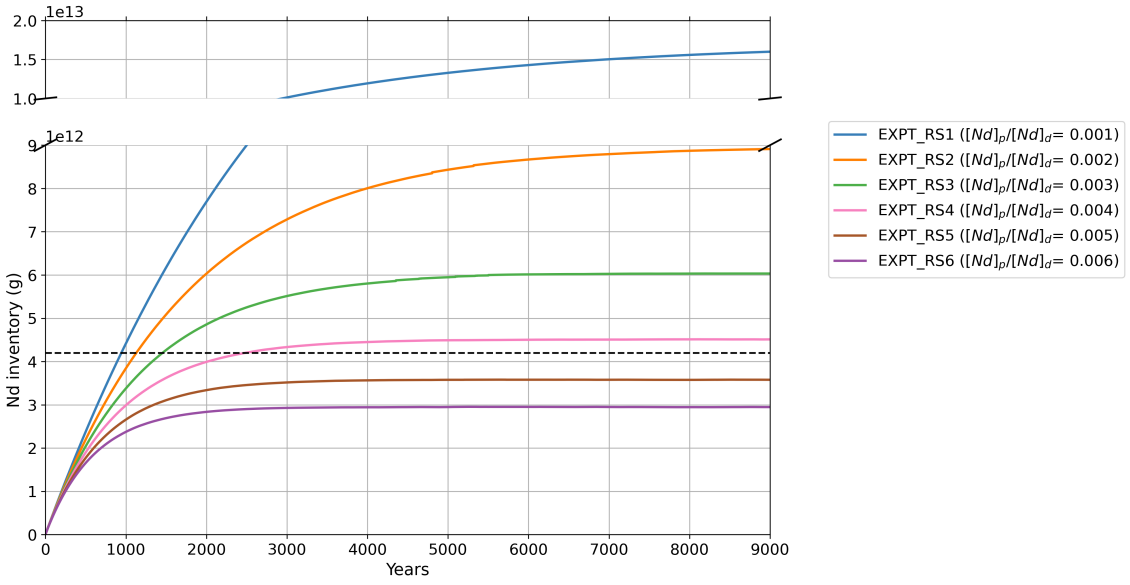

Figure 3.9: Global Nd inventory (g) simulated with different values for the reversible scavenging tuning parameter, $[Nd]_p/[Nd]_d$, as indicated. Dashed line represents the estimated global marine Nd inventory of 4.2×10^{12} g from Tachikawa et al. (2003) used as an approximate target for our simulations.

Despite total Nd flux to seawater being kept constant, varying the scavenging efficiency ($[Nd]_p/[Nd]_d$) leads to different Nd inventories and residence times (Table 3.4), consistent with previous studies (Siddall et al., 2008b; Arsouze et al., 2009; Rempfer et al., 2011; Gu et al., 2019). A higher $[Nd]_p/[Nd]_d$ increases both the Nd scavenging efficiency and removal via sedimentation by enabling a larger fraction of seawater Nd to adsorb onto particles, in turn leading to a lower Nd inventory and a lower residence time (where; residence time = Nd inventory/total Nd flux).

Table 3.4: Overview of simulations exploring model sensitivity to the reversible scavenging tuning parameter $[Nd]_p/[Nd]_d$. Displaying global mean absolute error (MAE) for $[Nd]_d$ and ε_{Nd}.

Simulation	f_{sed} ($\times 10^9$ g yr^{-1})	$[Nd]_p$ /$[Nd]_d$	Total Nd flux ($\times 10^9$ g yr^{-1})	Nd inventory ($\times 10^{12}$ g)	Residence time (years)	$MAE_{[Nd]}$ (n=3471)	% within 10 pmol kg^{-1}	$MAE_{\varepsilon_{Nd}}$ (n=2136)	% within 3 ε_{Nd} -units
EXPT_RS1	4.5	0.001	5.27	16	3036	44.46	6	3.34	48
EXPT_RS2	4.5	0.002	5.27	8.91	1691	15.96	41	3.11	53
EXPT_RS3	4.5	0.003	5.27	6.03	1145	10.13	58	2.88	57
EXPT_RS4	4.5	0.004	5.27	4.51	856	9.66	62	2.67	60
EXPT_RS5	4.5	0.005	5.27	3.58	679	10.52	56	2.46	64
EXPT_RS6	4.5	0.006	5.27	2.95	559	11.7	50	2.27	70

Neodymium in *EXPT_RS1*, which has the lowest $[Nd]_p/[Nd]_d$, has a residence time of 3,036 years. This is much larger than the global ocean overturning time of 1,500 years, resulting in an Nd inventory of 1.6×10^{13} g after 9,000 years, almost a factor of four larger than that of the estimated Nd budget in the oceans of 4.2×10^{12} g from Tachikawa et al. (2003). The $[Nd]_p/[Nd]_d$, and consequently the sink in *EXPT_RS1*, is too small to balance the input of Nd from the sources, causing such high Nd to accumulate in the simulation, which, as a result, does not reach steady state (rate of change 0.16% per 100 years at the end of the simulation; Fig. 3.9). Thus, *EXPT_RS1* returns the largest $MAE_{[Nd]}$ and $MAE_{\varepsilon_{Nd}}$ from these simulations, indicating the worst model-data fit, especially for

representing $[Nd]_d$ measurements. *EXPT_RS2*, although tending towards equilibrium at the end of the 9,000-year simulation (Fig. 3.9), just fails to reach steady state as defined above, still experiencing a rate of change of 0.022% per 100 years, highlighting that the rate of Nd removal from the ocean in this model configuration is still too low. *EXPT_RS6*, the experiment with the largest $[Nd]_p/[Nd]_d$, returns the lowest $MAE_{\varepsilon_{Nd}}$. However, reaching only 2.95×10^{12} g, the final Nd inventory is too low to be considered as capturing Nd cycling well. On balance, we surmise that *EXPT_RS4* has the most reasonable combination of prognostic skill in terms of simulated Nd inventory (4.51×10^{12} g) and residence time (856 years). This simulation, with $[Nd]_p/[Nd]_d$ of 0.004, shows balance between Nd accumulation and removal, and hence returns the lowest $MAE_{[Nd]}$ alongside a moderately well performing $MAE_{\varepsilon_{Nd}}$ that falls in the middle of the range of results.

In contrast to our model, the schemes by Rempfer et al. (2011) and Gu et al. (2019) required a lower $[Nd]_p/[Nd]_d$ of 0.001 and 0.0009 respectively for their optimised experiment with Nd inventories of $\approx 4.2 \times 10^{12}$ g. Despite having similar scavenging schemes, a direct comparison of the parameter values used in the different Nd isotope modelling studies is difficult to make. This is because the divergence in sensitivity to reversible scavenging efficiency can be attributed to a combination of the differing magnitude and spatial distributions of model biogeochemical particle fields and Nd inputs, which are also partly controlled by the different architecture and horizontal resolution of the physical models. In other words, every study has run a different experiment, and so the results are not directly comparable. We thus propose that a future modelling protocol for intercomparing different global Nd isotope schemes would be well suited to exploring these differing sensitivities comprehensively.

The different values of $MAE_{[Nd]}$ and $MAE_{\varepsilon_{Nd}}$ across our sensitivity experiments (Table 3.4) demonstrates the distinctive and uncoupled behaviour of $[Nd]_d$ and ε_{Nd} within the ocean, as broadly described by the Nd paradox, indicating that different processes govern the global distributions of each. In our results, increasing the efficiency of vertical cycling improves model-data fit for ε_{Nd} in a global sense, reducing $MAE_{\varepsilon_{Nd}}$ to a minimum of 2.27 where $[Nd]_p/[Nd]_d$ is 0.006. However, the story is more complicated for $[Nd]_d$ performance, where increasing $[Nd]_p/[Nd]_d$ from 0.001 up to 0.004 also reduces $MAE_{[Nd]}$ (to a minimum of 9.66 pmol kg^{-1}), but then subsequent increases in $[Nd]_p/[Nd]_d$ (0.005 and 0.006) worsen model-data fit for $[Nd]_d$ because the sink term becomes too strong, removing too much Nd from the ocean, as reflected in the low accumulated Nd inventories (3.58×10^{12} g and 2.95×10^{12} g respectively).

Generally, simulated $[Nd]_d$ distributions in *EXPT_RS4* match observational data well (Fig. 3.10). The lowest concentrations occur in the surface layers, and deep water $[Nd]_d$ increases along the global circulation pathway and with increasing age of water masses, with lowest $[Nd]_d$ in the North Atlantic Ocean and the highest concentrations in the deep North Pacific Ocean (Bertram and Elderfield, 1993; van de Flierdt et al., 2016; Tachikawa et al., 2017). These $[Nd]_d$ distributions are consistent with previous schemes that also take into account reversible scavenging (Arsouze et al., 2009; Gu et al., 2019; Oka et al., 2021; Rempfer et al., 2011; Siddall et al., 2008b). Thus, we may infer that the model scheme in FAMOUS does have the broad capability of representing the physical processes governing global marine $[Nd]_d$ distributions. However, the scheme does tend to simulate a too pronounced global vertical $[Nd]_d$ gradient (Fig. 3.10 and Supplementary Information: Fig. 3.24 for major ocean basin averaged depth profiles), a feature reported in previous similar model schemes (e.g. Arsouze et al. 2009; Gu et al. 2019), indicating that the representation of processes governing vertical $[Nd]_d$ does not yet fully capture all processes occurring in the ocean, leading to an underestimation of $[Nd]_d$ in the surface ocean and overestimation at abyssal depths.

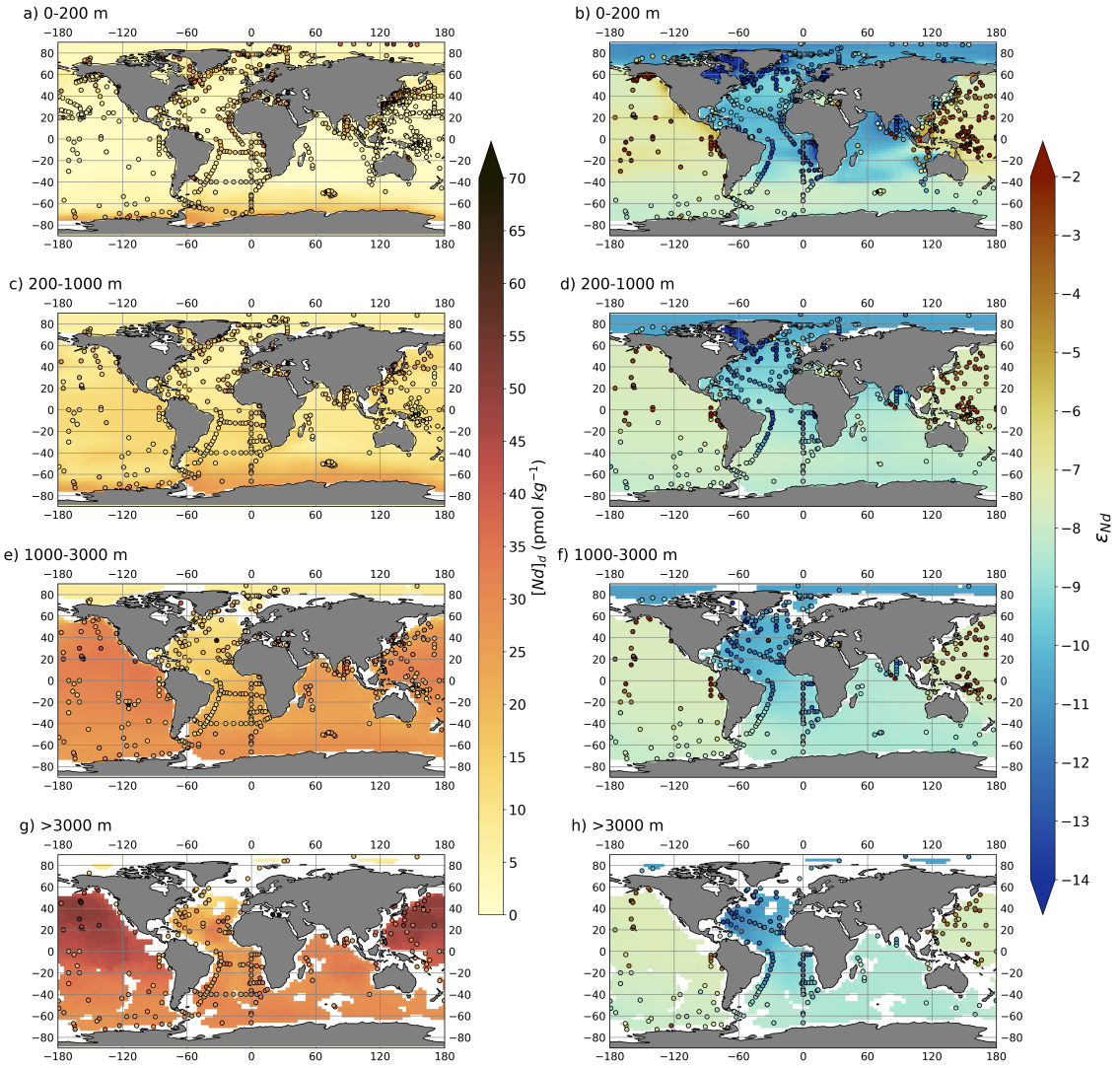

Figure 3.10: Global volume-weighted distributions of $[Nd]_d$ (left) and ε_{Nd} (right) in simulation *EXPT_RS4* split into four different depth bins, (a-b) shallow (0-200 m), (c-d) intermediate (200-1,000 m), (e-f) deep (1,000-3,000 m), and (g-h) deep abyssal ocean (>3,000 m). Water column measurements from within each depth bin (Osborne et al., 2015, 2017; GEOTRACES Intermediate Data Product Group, 2021) are superimposed as filled circles using the same colour scale.

Overestimation of the $[Nd]_d$ at depth may be caused by biases within the simulated biogenic particle fields. Direct and comprehensive global observations of sinking particle fluxes – the central driver of ocean biogeochemical cycling – remain fundamentally difficult to obtain (Dunne et al., 2007), and our particle fluxes may be inaccurate as a consequence (see Sect. 3.2.3.4 for assumptions and respective limitations). It also seems likely that the reversible scavenging parameterisations, which are simple by design due to incomplete understanding (also Sect. 3.2.3.4), restrict the model's ability to precisely capture all aspects of the measured Nd distributions. Additionally other particles such as Fe and Mn oxides and hydroxides, not considered here, may also play an important role for scavenging of Nd (e.g., Bayon et al. 2004). Further observational evidence of the processes involved and their importance for Nd cycling by combined particulate and dissolved measurements and laboratory experiments (e.g., Stichel et al. 2020; Pearce et al. 2013; Rousseau et al. 2015; Wang et al. 2021), plus experimentation within a modelling framework, may help to improve this limitation.

However, the largest model-data disparities for $[Nd]_d$ occur in the shallow ocean (above 200 m) at specific locations close to continental margins where Nd is input to the ocean through major point sources that are not well resolved by the model. This includes continental margins in the Labrador Sea (where simulated $[Nd]_d$ is 3 pmol kg^{-1} compared to measured $[Nd]_d$ of 70 pmol kg^{-1}) and the Sea of Japan (where simulated $[Nd]_d$ is 2 pmol kg^{-1} compared to measured $[Nd]_d$ of 50 pmol kg^{-1}), for example. Such low $[Nd]_d$ in the surface layers may be exacerbated by operational constraints in the scheme, such as the extensive and immediate dilution of point sourced Nd across the whole of its containing grid cell combined with the instantaneous nature of simulated reversible scavenging, which may be much faster in the model than would occur normally.

Nonetheless, consistent with compilations of water column measurements (Tachikawa et al., 2017; van de Flierdt et al., 2016), overall global distributions of simulated ε_{Nd} are broadly most unradiogenic in the North Atlantic and more radiogenic in the North Pacific (Fig. 3.10), with intermediate values in the Southern and Indian Oceans. The most unradiogenic ε_{Nd} occurs in the surface layers of the Hudson Bay and Labrador Sea regions, and they closely match measured data (ε_{Nd} = -18). However, the most radiogenic ε_{Nd}, simulated in the surface layers of marginal regions in the North and equatorial western Pacific (ε_{Nd} = -3), is significantly lower than measured (ε_{Nd} = +3), and in the central and North Pacific; particularly above 1,000 m, simulated ε_{Nd} is -7, but measurements are closer to -1 ε_{Nd}. In fact, these specific comparisons, which demonstrate a good match in the North Atlantic and weaker performance in the North Pacific, are congruent with a more general trend in the simulations. That is, at the basin scale, the magnitude of the ε_{Nd} gradient from Pacific to Atlantic is underestimated by the model, and presents a familiar bias as seen in previous Nd isotope schemes (Arsouze et al., 2009; Rempfer et al., 2011; Pöppelmeier et al., 2020a; Jones et al., 2008; Gu et al., 2019). This is mainly due to the simulated Pacific being too unradiogenic (basinal mean ε_{Nd} of -7.5) compared to measured water samples (ε_{Nd} = -4), while simulated and measured basinal mean Atlantic ε_{Nd} values are in much better agreement (ε_{Nd} = -11 and -12.5 respectively; see Supplementary Fig. 3.24).

The discrepancy in simulated and measured Pacific ε_{Nd} values may be amplified by sparse sampling that is biased towards shallow radiogenic continental regions and volcanic island areas, in which case, model performance is better than we are able to assess. In addition, and as highlighted in Sect. 3.2.4, $MAE_{\varepsilon_{Nd}}$ is biased towards the Atlantic (45% of all observational data), compared to the Pacific (29%). Consequently, due to biases in measurement density, a simulation better representing the Atlantic is more strongly favoured in the adopted cost function than one better representing the Pacific at the expense of the Atlantic. One further explanation for why our simulated Pacific ε_{Nd} is so much lower than recorded in modern water measurements is that the model boundary conditions, specifically the marine sediment source of Nd (taken directly from Robinson et al. 2021), may not be sufficiently radiogenic; a point we will return to later (Sect. 3.3.2).

Simulated $[Nd]_d$ depth profiles in all the reversible scavenging sensitivity experiments (Fig. 3.11) generally (though not always) exhibit similar depth profiles to the observational data. The closest model-data fit is seen especially within depth profiles in the Pacific and Southern Ocean, and notably more so under higher $[Nd]_p/[Nd]_d$. The largest model-data offsets across all sensitivity experiments in terms of both the magnitude and the depth gradients in $[Nd]_d$ occur in the North Atlantic Ocean. In particular, the large near-surface concentrations are not resolved, with the largest disparities occurring under higher scavenging parameterisations, where simulated $[Nd]_d < 10$ pmol kg^{-1} in the upper 1,000 m are too low compared to observed concentrations around 18-21 pmol kg^{-1}.

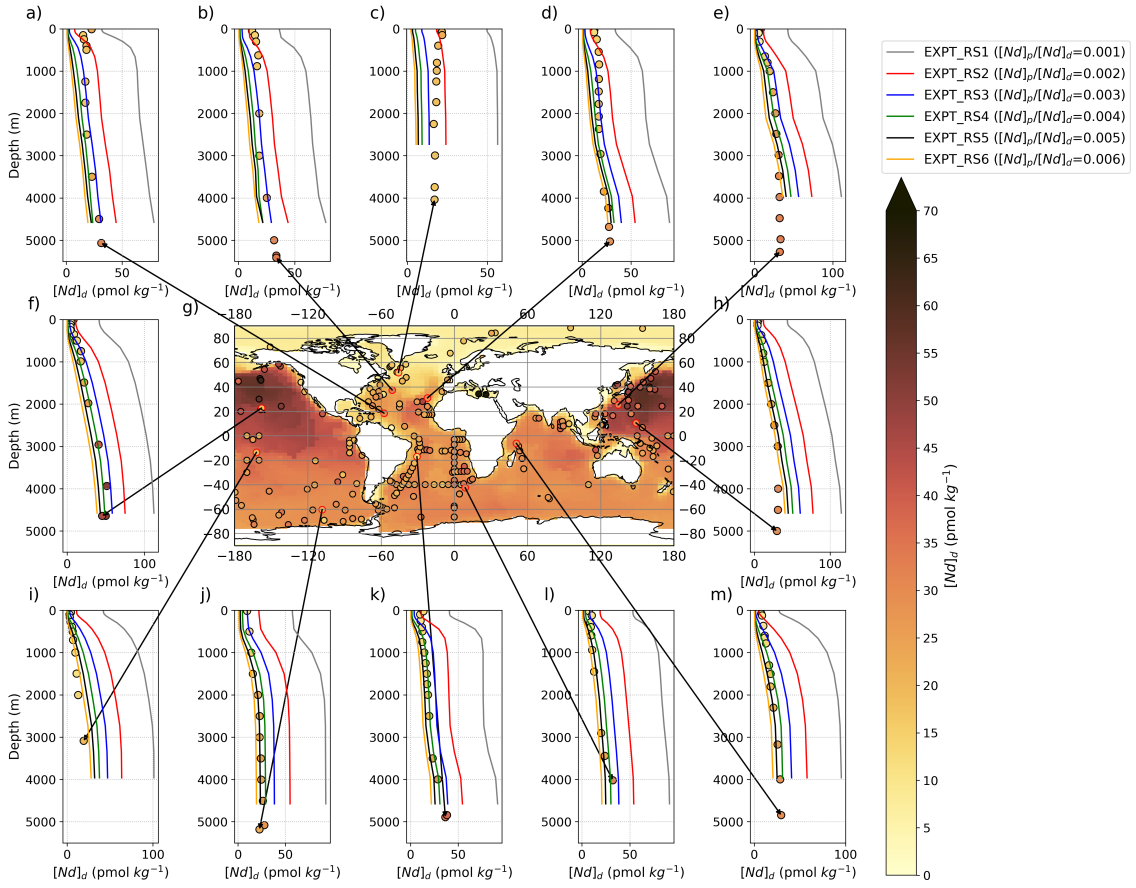

Figure 3.11: Central panel (g) displays $[Nd]_d$ at the seafloor in simulation *EXPT_RS4* (100-year mean from the end of the run), with superimposed water column measurements (Osborne et al., 2017, 2015; GEOTRACES Intermediate Data Product Group, 2021) from $\geq$ 3,000 m shown by filled coloured circles on the same colour scale. Surrounding panels (a-f) and (h-m) display depth profiles of simulated (coloured lines, one per sensitivity simulation with varied $[Nd]_p/[Nd]_d$) and measured (filled circles) $[Nd]_d$. Larger shifts in the $[Nd]_d$ between simulations highlight regions most sensitive to the efficiency of reversible scavenging.

Interestingly, we see a different sensitivity to varying $[Nd]_p/[Nd]_d$ in $[Nd]_d$ (Fig. 3.11) compared with ε_{Nd} (Fig. 3.12) within different ocean basins and depths. For $[Nd]_d$, we find that all ocean basins are sensitive to the parameterisation of reversible scavenging efficiency (i.e., wider divergence between the sensitivity for each depth profile), particularly at depths below 1,000 m, which is broadly consistent with the findings reported in previous work by Rempfer et al. (2011). However, Siddall et al. (2008b) showed a strong sensitivity of Pacific $[Nd]_d$ alongside a weak sensitivity of Atlantic $[Nd]_d$ to the reversible scavenging efficiency, the differences were attributed by the authors to the dominance of vigorous Atlantic advective lateral transport, whereas we demonstrate similar sensitivities in the Pacific, Atlantic, Indian and Southern Oceans (Fig. 3.11). The more simplified fixed surface boundary conditions applied in Siddall et al. (2008b) are not influenced by changing $[Nd]_p/[Nd]_d$, unlike the fluxes in the scheme presented here and by Rempfer et al. (2011), which may explain the contradictory response of the Atlantic basin across these studies.

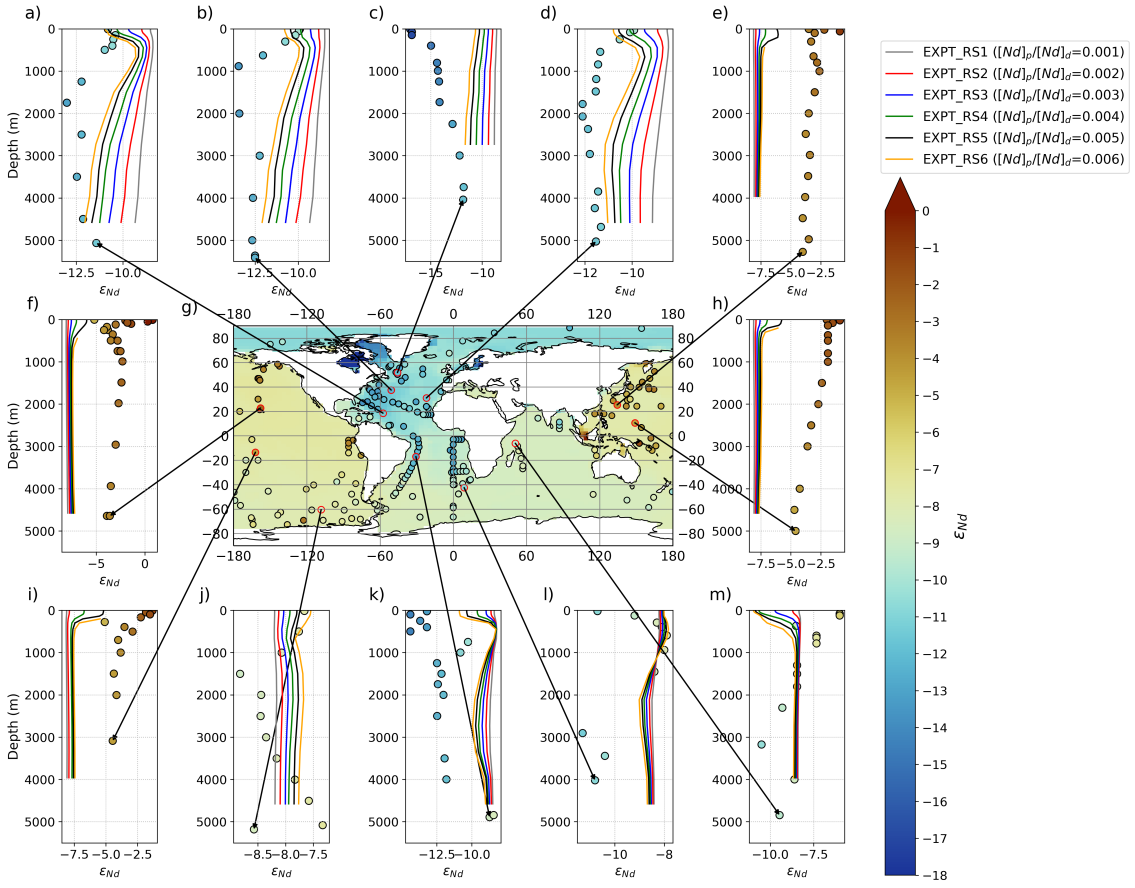

Figure 3.12: Central panel (g) displays ε_{Nd} at the seafloor in simulation *EXPT_RS4* (100-year mean from the end of the run), with superimposed water column measurements (Osborne et al., 2017, 2015; GEOTRACES Intermediate Data Product Group, 2021) from $\geq$ 3,000 m shown by filled coloured circles on the same colour scale. Surrounding panels (a-f) and (h-m) display depth profiles of simulated (coloured lines, one per sensitivity simulation with varied $[Nd]_p/[Nd]_d$) and measured (filled circles) ε_{Nd}. Larger shifts in the ε_{Nd} between simulations highlight regions most sensitive to the efficiency of reversible scavenging.

For ε_{Nd}, the response to varying scavenging efficiency has varied effects across depths and between ocean regions, indicating a more complex relationship between how reversible scavenging can delineate global ε_{Nd} distributions in comparison to $[Nd]_d$. The North Atlantic is the most sensitive basin to changes in reversible scavenging (registered by the greater ε_{Nd} profile shifts between different experiments, Fig. 3.12a-d), particularly at depths below 2,000 m, indicating that reversible scavenging is important, there, for governing the simulated ε_{Nd} signal of deep-water masses. We attribute this sensitivity to the fact that the Atlantic Ocean experiences strong convection and is surrounded by continental margins. As such, the basin is subject to substantial continental Nd inputs to the upper layers of the ocean, and the shallow ε_{Nd} signal is transferred to the ocean interior, setting the unradiogenic deep ocean signature. Thus, a stronger reversible scavenging efficiency is needed to trap regional ε_{Nd} provenance signals locally.

Typical depth profiles from measurements in the sub-tropical North Atlantic show contrasts in ε_{Nd} that co-vary with the presence of major water masses (coloured circles in Fig. 3.12a-b). Across all sensitivity experiments, there is relative consistency with depth for the profile, here (e.g., Fig. 3.12b), ranging from -10 to -12 under increasing scavenging efficiency, which acts to drive more localised unradiogenic signals. This simulated uniformity

can be partly explained by the lack of abyssal AABW, which does not extend past 20° N (Fig. 3.3). This insufficient AABW production and penetration into the Atlantic are known limitations of FAMOUS (Dentith et al., 2019; Smith, 2012), although these biases are reduced in our control compared to the previous studies (Sect. 3.2.2). Thus, the seawater basin below the surface mixed layer comprises only North Atlantic water, and in so doing, the model will not resolve the AABW signal inferred from measurements at depth in higher latitudes. Shifts in ε_{Nd} between the sensitivity studies in this region therefore relate to reversible scavenging efficiency changing the ε_{Nd} of NADW.

Higher up the water column, the more unradiogenic NADW seen in the seawater measurements is conspicuously absent (note the ε_{Nd} minima in subtropical North Atlantic measurements $\sim 1,000 - 2,000$ m deep, Fig. 3.12a-b), even though we know NADW does reside there in the model (see Fig. 3.3 for verification). We may relate this to the high latitude North Atlantic ε_{Nd} being too radiogenic to tag NADW with its characteristically unradiogenic ε_{Nd} signal, particularly around the mouth of the Labrador Sea (Fig. 3.10a-b). This could be exacerbated by a dampening of the unradiogenic NADW ε_{Nd} from a relatively radiogenic seafloor benthic flux along the water flow path (Fig. 3.6). Consequently, despite a close correlation to seawater ε_{Nd} in the subtropics and lower-NADW (where measurements of ε_{Nd} are -12.4 and simulated is -12), upper-NADW end member ε_{Nd} is not sufficiently unradiogenic, even under the highest reversible scavenging efficiency ($[Nd]_p/[Nd]_d = 0.006$) where simulated ε_{Nd} is -12 in comparison with seawater records -13.2 (Lambelet et al., 2016).

In contrast, ε_{Nd} in the Pacific Ocean is least sensitive to changes in $[Nd]_p/[Nd]_d$, particularly below 500 m (Fig. 3.12e-f, h-i). Depth variability is greatest in the equatorial Pacific, where ε_{Nd} decreases from -2.5 at the surface to -5 at depth, but, overall, simulated vertical ε_{Nd} gradients are small in the Pacific, consistent with seawater measurements. This is expected, due to the absence of major ocean convection and ventilation, meaning the Pacific contains an older, more homogenised pool of water in comparison to the Atlantic, and thus, water masses are far less distinct. This does make it possible for reversible scavenging to convey a more localised surface signal into the interior of the Pacific under a lower $[Nd]_p/[Nd]_d$ than can be achieved in the Atlantic, because the localised ε_{Nd} signal does not get dispersed via convection as rapidly.

Our less sensitive response of Pacific ε_{Nd} to reversible scavenging efficiency contrasts with results from Rempfer et al. (2011), who found a greater response of Pacific ε_{Nd} (compared to the Atlantic). We attribute this difference primarily to the spatial variation in the sediment Nd flux, which, in the study from 2011, is constrained to shallower radiogenic continental sources with no external marine Nd source below 3,000 m. In comparison, our deep seafloor wide sediment source governs simulated ε_{Nd} distributions in the intermediate-deep Pacific, due to its larger flux relative to that transported vertically via particle scavenging and dissolution, or horizontally by the sluggish convection of the Pacific.

On the whole, the relatively greater sensitivity of ε_{Nd} in the surface Pacific, compared with the deep Pacific, to the reversible scavenging efficiency produces a more radiogenic signal closer to that of the radiogenic measurements. This is likely caused by the downward transportation of radiogenic surface inputs to subsurface layers through scavenging. The stronger response in the upper ocean layers is consistent with previous modelling (e.g. Gu et al. 2019), and occurs due to the inherent presence of larger particle fluxes and therefore greater influence of reversible scavenging here compared to the deeper ocean, where particle dissolution acts to reduce particle concentrations and their associated scavenging mechanisms. One further aspect to note, is that under a high sink ($[Nd]_p/[Nd]_d = 0.006$), in some Pacific regions $[Nd]_d$ in the surface layers tends towards zero. This causes numerical instabilities in modelled Nd ratios and thus, where $[Nd]_d < 0.2$ pmol kg^{-1}, ε_{Nd} is meaningless and so is masked-out from the results shown by Fig. 3.12, to avoid

misinterpretation.

The simulated depth profile in all experiments in the Indian Ocean matches the observed intermediate ε_{Nd} signal of -8 between 500-2,000 m (Fig. 3.12m). However, the more radiogenic ε_{Nd} signal of -6 in the surface layers is not captured, nor the shift in ε_{Nd} below 2,000 m to more unradiogenic values reaching a minimum of -10.5 at 3,000 m, with all experiments simulating a relatively uniform ε_{Nd} with depth. Under higher reversible scavenging parameters for this depth profile (*EXPT_RS4-EXPT_RS6*), the surface concentrations are too low (simulated $[Nd]_d = 3$ pmol kg^{-1} and observed $[Nd]_d = 8$ pmol kg^{-1}), indicating that the model is not fully resolving either the concentration or the ε_{Nd} from a surface flux here, and scavenging may be too intense at the surface. In the deeper ocean ($\approx$ 3,000 m), these simulations show the model represents the $[Nd]_d$ profiles better, but is missing an unradiogenic exchange of ε_{Nd} at depth, where there is an insensitivity to reversible scavenging. This could point to an unradiogenic sediment source or exchange that is misrepresented by the bulk sediment boundary conditions and sediment source assumptions (e.g., our application of a global seafloor sediment source of Nd irrespective of sedimentary characteristics).

Interestingly, apart from the Indian Ocean, a model configuration with more efficient scavenging generally tends to produce results closest to the observational data (Table 3.4). In the Indian Ocean, seawater ε_{Nd} distributions are subject to monsoon systems, which facilitate the [seasonal] delivery of large riverine fluxes of Nd to seawater, for example from the Ganges and Brahmaputra Delta (Gupta and Naqvi, 1984). Large freshwater fluxes also deliver large amounts of freshly eroded and labile sediment to the continental margins, which likely contribute significantly to governing marine ε_{Nd} distributions through boundary particle-seawater exchange processes.

In the Southern Ocean, simulations with $[Nd]_p/[Nd]_d \geq 0.003$ broadly match the general measured ε_{Nd} at depths above 1,000 m (decreasing with depth from -7.8 at the surface to -8.2 at 1,000 m). Below this, and down to 3,000 m, observed diversions in ε_{Nd} are not captured in any of the sensitivity experiments. This discrepancy can be attributed to the simulation of quite homogenous AABW throughout the water column in the region, which represents a physical bias of FAMOUS (Dentith et al., 2019; Smith, 2012). Specifically, in the Pacific sector of the Southern Ocean (Fig. 3.12j), the model cannot resolve the measured unradiogenic spike at 1,500 m, which captures the distinct presence of lower Circumpolar Deep Water (CDW, $\varepsilon_{Nd} = -8.4 \pm 1.6$: Lambelet et al. 2018) formed from mixing of Atlantic, Pacific and Indian sourced waters.

The main conclusion to be made regarding model sensitivity to varying the reversible scavenging tuning parameter $[Nd]_p/[Nd]_d$, is that scavenging and removal via sedimentation is necessary to balance the simulated input sources from dust, rivers and seafloor sediment, and enables the scheme to reach equilibrium around reasonable Nd inventories. We find that reversible scavenging is an important physical process that enhances the ε_{Nd} gradient between oceans by maintaining localised basinal ε_{Nd} signals throughout the water column. The strength of this process is particularly important for maintaining the simulated unradiogenic ε_{Nd} in the well ventilated North Atlantic Ocean, but less important for the more stagnant modern Pacific Ocean.

Nonetheless, parameterising reversible scavenging efficiency alone cannot account for the correct trends and magnitude within ε_{Nd} gradients observed between basins and in depth profiles. Currently, the scheme assumes that all particles reaching the seafloor via reversible scavenging are buried in the sediment, and as such are decoupled from the seafloor sediment source. A future evolution of the scheme could explore the dissolution of authigenic sedimentary phases on the seafloor during diagenesis, to investigate how this may influence the ε_{Nd} distributions of the benthic flux. Moreover, our results demonstrate the importance of further constraining other aspects of marine Nd cycling under a holistic framework, including surface inputs from dust and river sources, sediment-seawater exchanges

and the redistribution and mixing via physical ocean circulation which also governs global $[Nd]_d$ and ε_{Nd} distributions. Furthermore, we note that the scheme described here may not be fully resolving the end member ε_{Nd} of different water masses due to an imperfect representation of the sources of Nd to seawater (i.e., the model boundary conditions and strength of the source fluxes). Thus, in some instances, the scheme carries inappropriate/dampened ε_{Nd} signals, coupled alongside particular structural model biases in the physical circulation (e.g., limited AABW intrusion in the North Atlantic), although in the case of the latter point, we note that this is not a limitation of the presented scheme, and that the implementation can be useful for identifying such physical biases.

3.3.2 Model sensitivity to Nd flux from the sediment (f_{sed})

The second tranche of sensitivity simulations tests the response of $[Nd]_d$ and ε_{Nd} to systematically varying the total Nd flux from the sediment (f_{sed}), while all other parameters were kept constant. In this experiment, Nd accumulates rapidly from the start of the simulations (Fig. 3.13) and tapers off thereafter to varying degrees depending on the rate of accumulation. For *EXPT_SED1* and *EXPT_SED2*, the rate of increase in the Nd inventory begins to reduce by 1,000 years, as these simulations, which have the smallest sediment source (f_{sed}), approach steady state. By year 2,000 the rate of Nd accumulation in *EXPT_SED3* and *EXPT_SED4* reduces, and these simulations also reach steady state, albeit above that of the target global inventory reference (4.2×10^{12} g). By year 6,000 all f_{sed} sensitivity experiments have reached steady state (< 0.02 % change per 100 years).

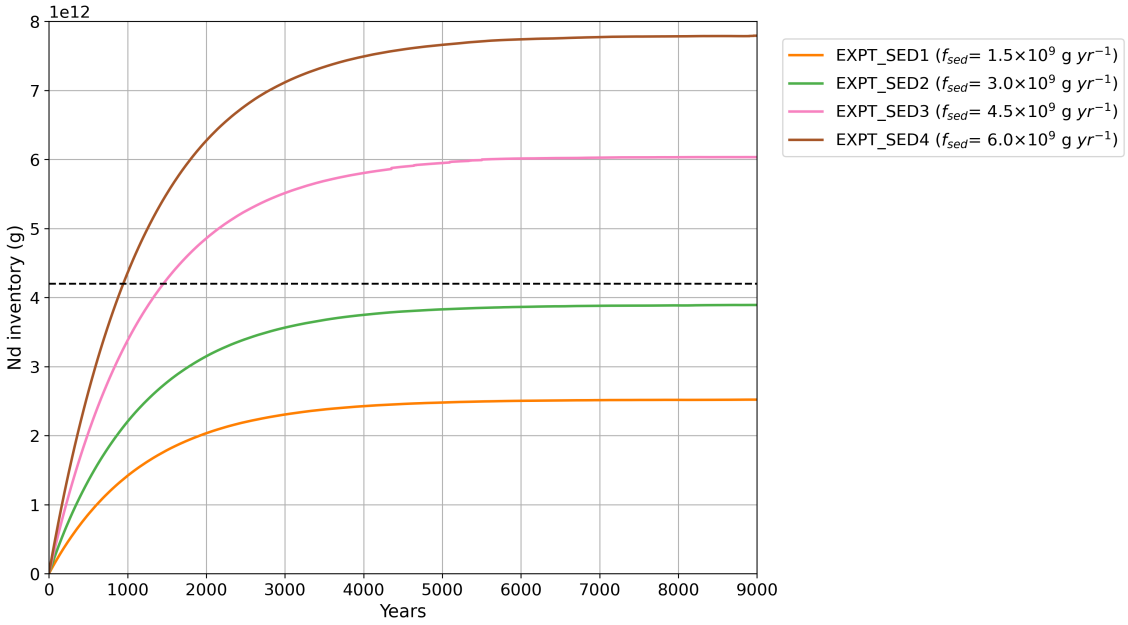

Figure 3.13: Global Nd inventory (g) simulated with different values for the total sediment flux tuning parameter (f_{sed}) as indicated. Dashed line represents the estimated global marine Nd inventory of 4.2×10^{12} g from Tachikawa et al. (2003) used as an approximate target for the simulations.

Table 3.5 summarises the final global mean marine Nd inventory and residence time of the simulations, and reports their skill according to our global cost functions, $MAE_{[Nd]}$ and $MAE_{\varepsilon_{Nd}}$. Modifying the sediment flux while keeping the sink term $[Nd]_p/[Nd]_d$ constant returns a varied equilibrium Nd inventory across the suite of simulations (Fig. 3.13). However, without changing the scavenging efficiency (i.e. Nd sink), there is a more moderate range of 40 years difference in the f_{sed} simulations' Nd residence time, consistent

with the findings of Rempfer et al. (2011). In general, the relatively low scavenging efficiency of all of the f_{sed} sensitivity simulations ($[Nd]_p/[Nd]_d = 0.003$, see Sect. 3.3.1 for context) yields long residence times greater than 1,000 years.

Table 3.5: Overview of simulations exploring model sensitivity to the total sediment Nd flux tuning parameter (f_{sed}). Displaying global mean absolute error (MAE) for $[Nd]_d$ and ε_{Nd}.

Simulation	f_{sed} ($\times 10^9$ g yr^{-1})	$[Nd]_p/[Nd]_d$	Total Nd flux ($\times 10^9$ g yr^{-1})	Nd inventory ($\times 10^{12}$ g)	Residence time (years)	$MAE_{[Nd]}$ (n=3471)	% within 10 pmol kg^{-1}	$MAE_{\varepsilon_{Nd}}$ (n=2136)	% within 3 ε_{Nd} -units
EXPT_SED1	1.5	0.003	2.27	2.5	1110	10.71	53	2.71	60
EXPT_SED2	3.0	0.003	3.77	3.89	1032	7.96	73	2.82	62
EXPT_SED3	4.5	0.003	5.27	6.03	1145	10.13	58	2.88	57
EXPT_SED4	6.0	0.003	6.77	7.79	1150	13.23	47	2.93	55

EXPT_SED1, which has the lowest f_{sed} and hence the lowest total Nd flux to the ocean, returns the smallest total Nd inventory of 2.5×10^{12} g (only half the total estimated by Tachikawa et al. 2003), but did well with ε_{Nd} distributions, returning the lowest global $MAE_{\varepsilon_{Nd}}$. Conversely, *EXPT_SED4*, which has the largest f_{sed}, results in the greatest Nd inventory (7.8×10^{12} g), producing both the worst $MAE_{[Nd]}$ and $MAE_{\varepsilon_{Nd}}$.

Compared to varying the reversible scavenging efficiency, varying f_{sed} drives relatively discrete changes in Nd distributions, as demonstrated by the minor differences in $MAE_{\varepsilon_{Nd}}$ between sensitivity experiments. This makes sense, since varying f_{sed} has no direct impact on the relative distribution of ^{143}Nd and ^{144}Nd once it is in the water, it only acts to change the fractional contribution from each specific Nd source, e.g. an enhanced f_{sed} reduces the fraction of total Nd flux coming from dust and rivers (which are inputs constrained to the surface and point sources close to the continents), concentrating the flux across the global seafloor, and vice versa. However, in all simulations, and consistent with previous studies, the sediment Nd source to seawater remains the major source, and f_{sed} would need to be reduced much more to greatly influence MAEε_{Nd}.

Overall, from the simulations in this study *EXPT_SED2* demonstrates the most appropriate skill at reaching the target Nd inventory (3.89×10^{12} g compared to the 4.2×10^{12} g target). It returns the lowest $MAE_{[Nd]}$ because it achieves the most balanced Nd source and sink terms, and although the simulation does not represent the lowest $MAE_{\varepsilon_{Nd}}$, the range across the f_{sed} experiment is small (2.71 to 2.93; Table 3.5) and it does simulate the highest percentage of simulated ε_{Nd} within 3 ε_{Nd}-units of measurements (62%).

Altogether, simulated $[Nd]_d$ in *EXPT_SED2* matches the general observational data trend of Nd concentration increasing with depth (Fig. 3.14), with good model-data fit especially in the upper 1,000 m across all ocean basins (except the North Atlantic, discussed below). However, in the deep layers of the North Pacific (below 3,000 m) simulated $[Nd]_d$ is underestimated (36 pmol kg^{-1} compared to 50 pmol kg^{-1} from seawater measurements). This underestimation of $[Nd]_d$ at depth can be explained by a combination of having a seafloor sediment source at the lower end of our range (f_{sed} is 3.0×10^9 g yr^{-1}) and slow release from reversible scavenging ($[Nd]_p/[Nd]_d$ of 0.003; our experiments suggest 0.004 may be a more suitable efficiency to use, Sect 3.3.1), highlighting the importance of both non-conservative processes in governing deep $[Nd]_d$ distributions, especially in the deep North Pacific.

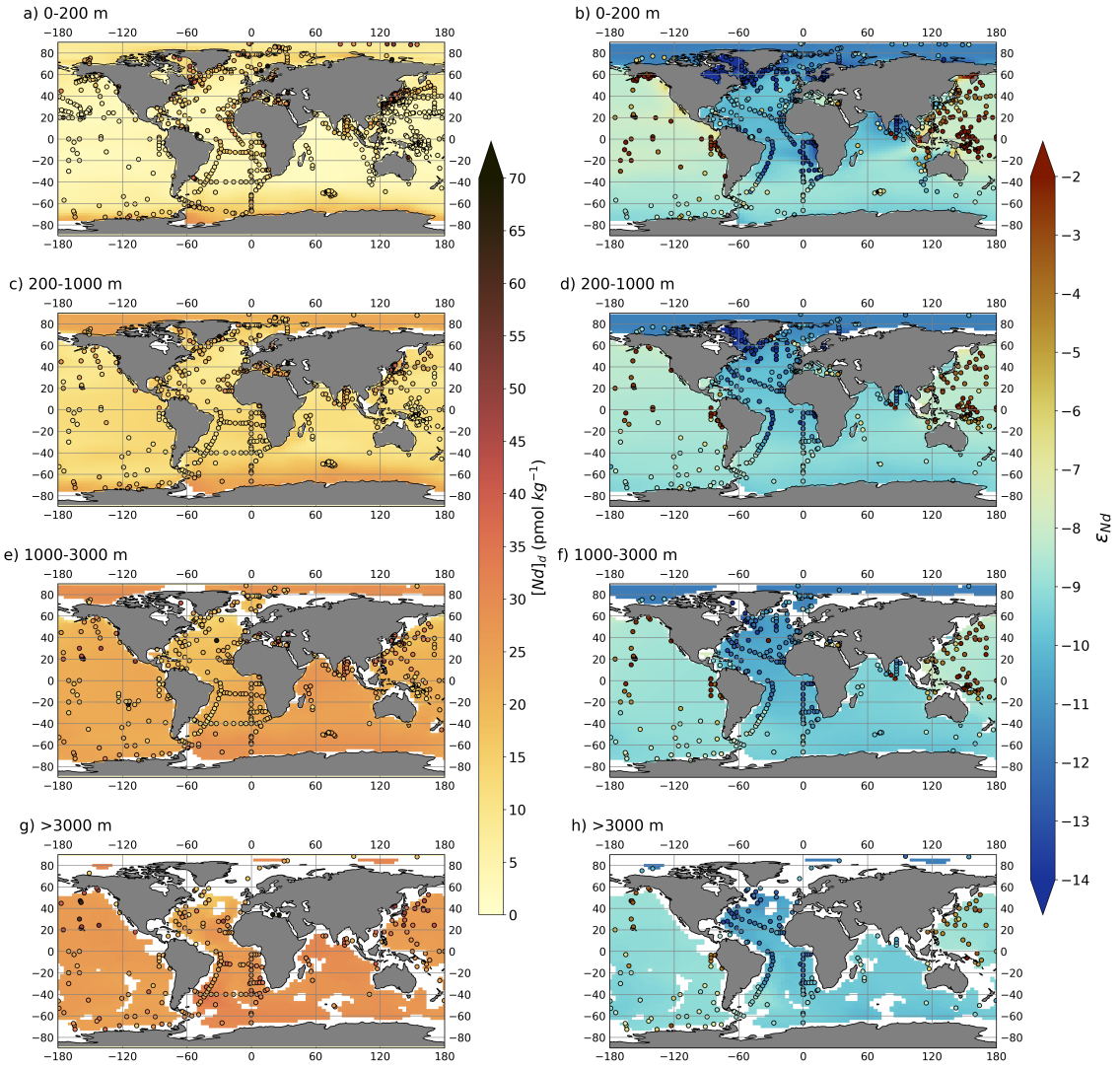

Figure 3.14: Global volume-weighted distributions of $[Nd]_d$ (left) and ε_{Nd} (right) in simulation *EXPT_SED2* split into four different depth bins, (a-b) shallow (0-200 m), (c-d) intermediate (200-1,000 m), (e-f) deep (1,000-3,000 m), and (g-h) deep abyssal ocean (>3,000 m). Water column measurements from within each depth bin (Osborne et al., 2017, 2015; GEOTRACES Intermediate Data Product Group, 2021) are superimposed as filled circles using the same colour scale.

Moreover, the longer lifetime of simulated Nd in the *EXPT_SED2* ocean (1,032 years) compared to that estimated by previous work (360-800 years; Gu et al. 2019; Rempfer et al. 2011; Siddall et al. 2008b; Tachikawa et al. 2003) means that Nd becomes well mixed in the deep ocean (below 1,000 m), homogenising the ε_{Nd} signal. This causes the observed inter-basin gradients (a critical feature in the use of Nd as an ocean circulation tracer) to become severely damped, particularly away from direct input of fresh reactive phases with distinctive ε_{Nd} (Robinson et al., 2021; Abbott et al., 2019). However, where including a reduced sediment source (e.g. compared to *EXPT_SED3* and *EXPT_SED4*) increases the relative importance of dust and river inputs, such as in the shallow Atlantic (Lambelet et al., 2016), simulated ε_{Nd} matches unradiogenic measurements with reasonable skill. Consistent with earlier studies (e.g., Arsouze et al. 2009; Jones et al. 2008), the largest model-data disparities occur in the North and equatorial Pacific, where simulated ε_{Nd} is far too unradiogenic compared to the observational data, pointing to a number of processes that may be better optimised in our Nd scheme. For example, a larger (and also

more radiogenic) sediment source (i.e., greater f_{sed}) may be needed, particularly around shallow-intermediate marginal settings; a suggestion also supported by the too low $[Nd]_d$. Additionally, increased scavenging and a lower simulated residence time would improve the representation of localised Nd isotope signatures.

Total Nd concentrations and isotopic distributions show different responses to varying f_{sed}. We find that $[Nd]_d$ is sensitive to f_{sed} across all ocean basins (i.e., a wide divergence in the depth profiles shown in Fig. 3.15), mostly at depths below 500 m where there is no direct influence from river and dust inputs and the relatively large area of the deep abyssal seafloor as an Nd interface becomes important (particularly with low reversible scavenging).

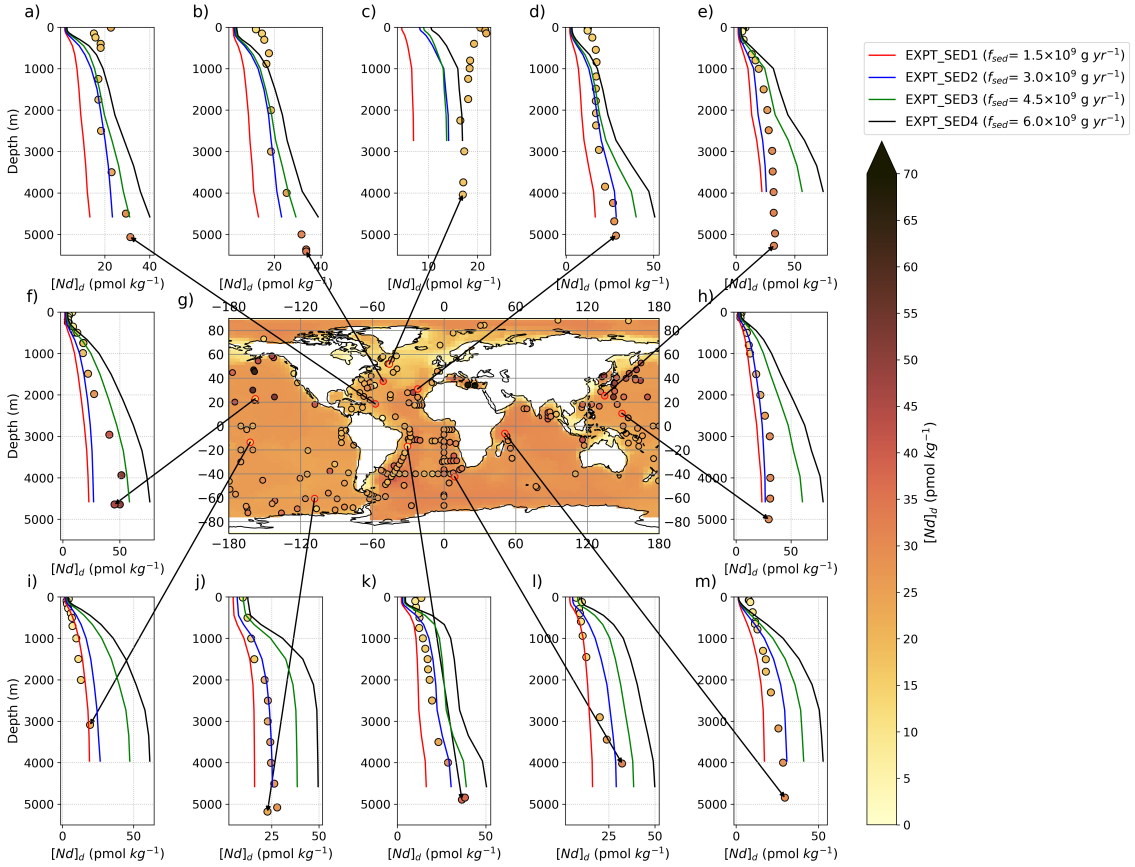

Figure 3.15: Central panel (g) displays $[Nd]_d$ at the seafloor in simulation *EXPT_SED2* (100-year mean from the end of the run), with superimposed water column measurements (Osborne et al., 2017, 2015; GEOTRACES Intermediate Data Product Group, 2021) from $\geq$ 3,000 m shown by filled coloured circles on the same colour scale. Surrounding panels (a-f) and (h-m) display depth profiles of simulated (coloured lines, one per sensitivity simulation with varied f_{sed}) and measured (filled circles) $[Nd]_d$. Larger shifts in the $[Nd]_d$ between simulations highlight regions most sensitive to the magnitude of the seafloor sediment source.

Typically, better model-data fit for $[Nd]_d$ depth-profiles is achieved under lower f_{sed} (1.5×10^9 to 3.0×10^9 g yr^{-1}), and particularly in the Pacific, Indian and Southern Ocean (Fig. 3.15). This indicates that under a relatively low reversible scavenging parameter, a corresponding smaller flux of Nd from the sediment is needed to balance the marine Nd budget, and by inference, a higher f_{sed} would be more appropriate with stronger reversible scavenging fluxes. Correspondingly, under high f_{sed} and particularly in the deeper interior of the ocean (below 3,000 m), simulated $[Nd]_d$ diverges to higher

concentrations than measured due to too much Nd being sourced to the deep ocean from the sediment. Additionally, in these high f_{sed} scenarios, the strength of the sediment source obscures horizontal seafloor $[Nd]_d$ gradients across basins (see the near-uniform seafloor $[Nd]_d$ in Fig. 3.15g), masking the influence of reversible scavenging, which is controlled by the location and dissolution of particle fields and is important for governing $[Nd]_d$ patterns (Sect. 3.3.1). Rempfer et al. (2011) found the opposite. In their study, doubling and halving f_{sed} both resulted in well pronounced nutrient-like profiles of $[Nd]_d$. This highlights the impact of having a global sediment source unrestricted in depth (our study) compared to limiting that flux to the upper 3,000 m (Rempfer et al., 2011) paired with a more efficient reversible scavenging (Rempfer et al., 2011) that allows the biogenic particle adsorption and desorption processes to dominate the deep-water distributions.

Similar to the reversible scavenging sensitivity experiment (Sec. 3.3.1), the largest simulated offsets between simulated and measured $[Nd]_d$ under all f_{sed} experiments occur in the North Atlantic and sub-tropical Atlantic at depths above $1,000$ m, where, even under the largest sediment fluxes, simulated $[Nd]_d$ is too low. The depth profile south of Greenland (Fig. 3.15c) shows the greatest sensitivity to varying f_{sed} in the upper $1,000$ m, with *EXPT_SED4*'s simulated surface concentrations of 10 pmol kg^{-1} ($f_{sed} = 6.0 \times 10^9$ g yr^{-1}) being closest to the measured concentrations of 22 pmol kg^{-1}. By implication, the accurate representation of sediment fluxes is required to reproduce upper ocean $[Nd]_d$ in this region, and an enhanced sediment flux alone cannot account fully for the observed high surface concentrations. Either, a combination of the surface and near-surface fluxes resolved here are too diluted in the model (possibly due to grid box resolution), or the model is missing a significant surface/near-surface Nd source. Previous schemes have likewise simulated too low surface $[Nd]_d$ in the North Atlantic, likely also due to difficulties in representing highly localised and variable surface features in global models (Gu et al., 2019; Rempfer et al., 2011).

Whereas $[Nd]_d$ is sensitive to f_{sed} globally, the height of ε_{Nd} sensitivity is more regional (Fig. 3.16). The Atlantic, Indian and Southern Ocean ε_{Nd} are significantly more sensitive to changes in the bulk sediment seafloor Nd flux than the Pacific Ocean. Overall, differences in f_{sed} tend to drive whole depth profile shifts of low magnitude in ε_{Nd}, this contrasts the findings of Rempfer et al. (2011), who varied a margin constrained f_{sed} and reported deep water ε_{Nd} (below 1,000 m) were affected less than in our results. If this conflicting difference in deep ocean sensitivity to f_{sed} is because of the applied spatial distributions of a sediment Nd source to seawater ($<$ 3,000 m for Rempfer et al. (2011), all depths for us), then further constraints of sediment Nd fluxes across space and time are crucial when interpreting ocean circulation from ε_{Nd}. Interestingly, there is not a linear/direct response of ε_{Nd} to changing f_{sed}. Broadly and globally, the largest f_{sed} value of 6.0×10^9 g yr^{-1} (*EXPT_SED4*) leads to more radiogenic ε_{Nd} and an intermediate f_{sed} value of 3.0×10^9 g yr^{-1} (*EXPT_SED2*) leads to the most unradiogenic ε_{Nd} shift. The largest response in ε_{Nd} to changing f_{sed} occurs with a sediment flux between 3.0×10^9 yr^{-1} and 4.5×10^9 g yr^{-1}. Increasing the flux beyond this produces a very weak response, indicating a threshold in ε_{Nd} sensitivity that results from an already dominant sediment source encompassing over 85% of the total Nd flux to seawater.

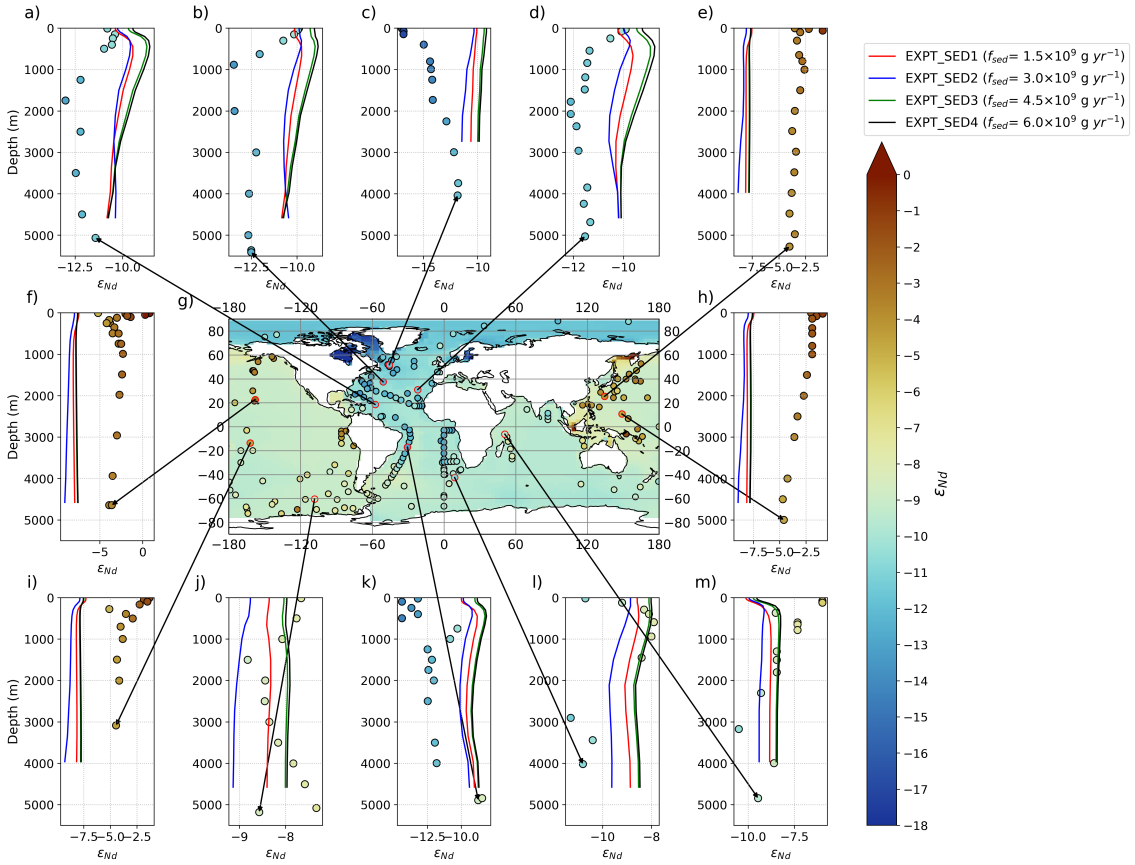

Figure 3.16: Central panel (g) displays ε_{Nd} at the seafloor in simulation *EXPT_SED2* (100-year mean from the end of the run), with superimposed water column measurements (Osborne et al., 2017, 2015; GEOTRACES Intermediate Data Product Group, 2021) from $\geq$ 3,000 m shown by filled coloured circles on the same colour scale. Surrounding panels (a-f) and (h-m) display depth profiles of simulated (coloured lines, one per sensitivity simulation with varied f_{sed}) and measured (filled circles) ε_{Nd}. Larger shifts in the ε_{Nd} between simulations highlight regions most sensitive to the magnitude of the seafloor sediment source.

Once again, the most notable ε_{Nd} model-data mismatch occurs within the depth profiles of the North Atlantic. Due to major rivers delivering a high [Nd] load to the Atlantic (Fig. 3.5c), in their vicinity, simulations with low f_{sed} are conditioned towards riverine ε_{Nd}, providing the typical unradiogenic ε_{Nd} signature of NADW and demonstrating the important balance between surface inputs and a sediment flux for simulating ε_{Nd} in the deep North Atlantic (Fig. 3.16a-d). Conversely, enhancing f_{sed} increases the fraction of Nd supplied to the ocean from the bulk seafloor sediment, which has more uniform, intermediate ε_{Nd} values in the central North Atlantic (-12.5) in contrast to the more unradiogenic ε_{Nd} signals of the continental margins and riverine source in the Labrador (-28) and West Atlantic basins (-15.6), with localised near-surface marginal sediment extreme minimums of (-34) in the northern Labrador Sea (Robinson et al., 2021). Greater f_{sed} thus acts to overprint and hence mix away the more distinct surface ε_{Nd} signal of NADW gained at their sites of deep-water formation in favour of a more general intermediate ε_{Nd} signal as it becomes exposed to Nd fluxes along its southward seafloor flow path. Model-measurement disparity at the mouth of the Labrador Sea and south of Greenland in all simulations at shallow and intermediate depths strongly suggests that a specific fraction of the bulk sediment with more unradiogenic ε_{Nd} than is captured by Robinson et al. (2021) is interacting with seawater in place of the bulk sediment ε_{Nd} signal

(Fig. 3.17). This is further supported by recent core-top particle-seawater interaction investigations of the region (Blaser et al., 2016). It therefore follows that either existing seafloor sediment measurements do not characterise this region well, or a deep ocean benthic flux, or at least, an indiscriminate whole-ocean floor flux, is neither reasonable nor necessary (in fact, it is counterproductive) for providing accurate ε_{Nd} tagging of Atlantic seawater.

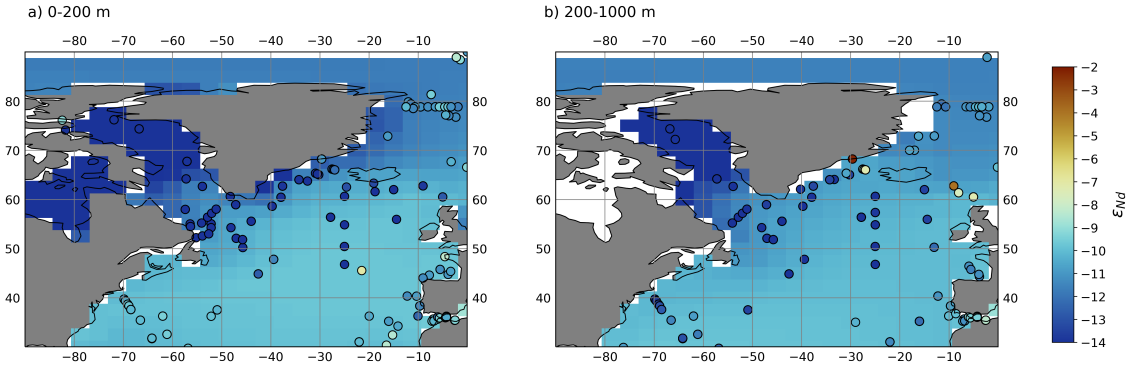

Figure 3.17: Volume-weighted distributions of ε_{Nd} in simulation *EXPT_SED2* split into two different depth bins, (a) shallow (0-200 m), and (b) intermediate (200-1,000 m) within the North Atlantic and Labrador Sea basins. Water column measurements from within each depth bin (Osborne et al., 2017, 2015; GEOTRACES Intermediate Data Product Group, 2021) are superimposed as filled circles on the same colour scale.

In contrast to the Atlantic, Pacific Ocean ε_{Nd} is the least sensitive to varying f_{sed} (Fig. 3.16e-f, h-i). Characteristically, the Pacific encompasses vast open ocean oligotrophic expanses with low biogenic particle export, in tandem with smaller relative dust and river sources, which means the seafloor sediment source already dominates the simulated Nd fluxes and distributions, even under lower sediment fluxes. Furthermore, the bulk detrital ε_{Nd} (-8) released from the seafloor sediment in the Northwest Pacific (Fig. 3.6) is the same as the signal from the dust flux off the Asian continent, which contributes significant terrigenous material to the seafloor here (Nakai et al., 1993; Han et al., 2011), which makes it hard to distinguish between these two sources. In the North Pacific, the simulations with higher f_{sed} match the observed $[Nd]_d$ better than those with lower f_{sed} (Fig. 3.15), but the ε_{Nd} signal from the bulk seafloor sediment cannot explain the radiogenic ε_{Nd} observed here (Fig. 3.16), and so the model likely is not fully capturing the correct source (or the prescribed boundary condition is not correctly representing the distribution and fraction of the sediment phase contributing to the sediment flux) of Nd to seawater. Consistent with previous literature, the greatest imbalances in the Nd isotope budget occur in the reservoirs of the vast deep Pacific (Jones et al., 2008). This could imply that a 'reactivity weighted' sedimentary flux is most important for the deep North Pacific compared with other basins, providing evidence to support the preferential dissolution of reactive Nd sediment phases in the Pacific under a model of marine Nd cycling dominated by a seafloor sediment source.

To conclude, we surmise that a sediment-seawater flux represents a key major source of $[Nd]_d$ that is particularly fundamental to the intermediate and deep ocean Nd budgets, and as such plays an important role in governing marine Nd cycling. Notably, we find that ε_{Nd} is much less sensitive than $[Nd]_d$ to changing the rate of this flux (f_{sed}), and a high f_{sed} coupled with a weak reversible scavenging cannot account for $[Nd]_d$ gradients of increasing concentration along the thermohaline circulation in the deep ocean. Indeed, a strong sediment source pushes the ocean towards a more globally uniform and too high $[Nd]_d$ than measurements from the deep ocean suggest. This could be interpreted as evidence against a 'bottom up' model (Haley et al., 2017) with constant benthic flux

across the whole seafloor in favour of the more distinct $[Nd]_d$ distributions that may be achieved under a 'top-down' driven model with greater dominance of reversible scavenging. As such, although a benthic flux can represent the depth profiles of linearly increasing $[Nd]_d$ with depth, reversible scavenging is necessary and should not be considered a secondary process in controlling the global thermohaline variations in deep water $[Nd]_d$. Nonetheless, we acknowledge that employing a more horizontally nuanced benthic flux tied to local environmental and sedimentary conditions may introduce more spatial patterning in simulated $[Nd]_d$, reducing the importance of the reversible scavenging terms.

Certainly, these sensitivity simulations demonstrate openly that the bulk ε_{Nd} of seafloor detrital sediment (Robinson et al., 2021) cannot be considered fully representative of the ε_{Nd} composition of the sediment that is interacting with seawater in all instances. They highlight the need for observational and experimental quantification of the broad mobile Nd phases globally, and their ε_{Nd} signal, as well as constraints on the spatial distribution of such a benthic flux (e.g., identifying where and under what environmental conditions a benthic flux occurs, and at what strength). The model's response to f_{sed} sets the stage for further testing of global sedimentary ε_{Nd} on marine Nd cycling, providing the foundation for resolving the inherent complex multitude of processes.

3.4 Summary and Conclusions

In this study, we describe the implementation of Nd isotopes (^{143}Nd and ^{144}Nd) into the ocean component of the FAMOUS GCM, providing a powerful tool designed for comprehensively exploring global marine Nd cycling, especially through representing explicit non-conservative processes to explore the extent of their influence on global seawater Nd distributions. We present a new reference equilibrium pre-industrial simulation (XPDAA) with appropriate basin scale physical ocean circulation performance relative to a standard version (XFHCC; Smith 2012), though we note that for this study it was not important to evaluate the performance of the surface climate. Our Nd isotope scheme starts from previous Nd isotope implementations (Rempfer et al., 2011; Gu et al., 2019; Pöppelmeier et al., 2020a; Arsouze et al., 2009; Siddall et al., 2008b), but revisits and updates Nd sources, sinks and tracer transformation in line with increased observations and recent findings relating to global marine Nd cycling. Our model represents the main features of [Nd] and ε_{Nd} well, although there is a tendency to simulate an over-pronounced vertical [Nd] gradient, and to produce a too unradiogenic ε_{Nd} signal in the Pacific.

The presented sensitivity experiments demonstrate that the Nd isotope scheme in the FAMOUS GCM is sensitive to Nd source and biogeochemical processes. Model sensitivity to reversible scavenging efficiency demonstrates its importance for determining the increase in Nd concentration with depth and along the circulation pathway. Moreover, reversible scavenging acts to homogenise ε_{Nd} vertically in the water column, enhancing regional basinal gradients in simulated ε_{Nd} by maintaining the localised provenance signal. On the other hand, a seafloor benthic flux, a term referring to a multitude of processes encompassing boundary exchange (Lacan and Jeandel, 2005a), submarine groundwater discharge (Johannesson and Burdige, 2007), and a benthic flux released from pore waters (Abbott et al., 2015a), presents a major deep ocean source of Nd, the magnitude of which governs horizonal seafloor Nd concentrations across ocean basins. The weak sensitivity of simulated ε_{Nd} in the deep North Pacific implies that with a seafloor-wide benthic flux of marine Nd, the ε_{Nd} of the sediment flux, as captured by the bulk ε_{Nd}, is not a true representation in all instances of the labile sediment phase interacting with seawater in this basin. Alternatively, it may also indicate that there is a significant missing source of radiogenic Nd to seawater, likely of volcanic origin; or possibly a combination of both explanations. Furthermore, model-data mismatch at the mouth of the Labrador Sea suggests that the labile sediment Nd phases interacting with seawater in the northern

North Atlantic are considerably more unradiogenic than captured by the bulk sediment.

Exploring in detail the behaviour of simulated $[Nd]_d$ and ε_{Nd} distributions also highlighted some of the structural limitations of the model (e.g., difficulties representing highly localised and surface features) and influential biases in the physical ocean circulation (e.g., limited northward intrusion of AABW in the North Atlantic). These results provide the groundwork for a future comprehensive optimisation of the marine Nd isotope scheme in FAMOUS. In the first instance, we suggest calibration of the key tuning parameters ($[Nd]_p/[Nd]_d$ and f_{sed}) to achieve target Nd inventories and residence times. Additionally, it would be beneficial to obtain additional observational constraints on the broad labile sediment ε_{Nd} interacting with seawater across different seafloor regions, including constraining the exchange between authigenic and detrital sediment phases during early diagenesis. This would improve the boundary conditions we can feed into the model, giving it the best chance to simulate Nd distributions accurately and making the interpretation of model performance (and thus also of the relative importance of different sources and sinks) more straightforward. Future sensitivity studies could also focus on the influence of river particulate and continental marginal sources on marine Nd in order to provide further insight to (and possibly constrain) the relative importance of these inputs, as opposed to a predominantly benthic seafloor-wide source.

Implementing Nd isotopes in a fast GCM provides a useful tool for exploring model-scheme sensitivities and uncertain marine biogeochemical processes. This framework allows for performing the long integrations necessary to spin-up ocean physics and biogeochemistry, which can be simulated for multiple time periods (e.g. in palaeo studies) in equilibrium (i.e. with fixed forcing, Haywood et al., 2016; Lunt et al., 2017) and transient (i.e. with temporally evolving forcing, e.g. Ivanovic et al. 2016; Menviel et al. 2019) scenarios. Alternatively, or in addition, large ensembles of simulations can be run for [re]calibrating (i.e., 'tuning') the model or quantifying uncertainty in the inputs (boundary conditions, parameter values etc.). In this way, it becomes possible to build on new knowledge gained by running the scheme – such as the identification of physical ocean biases – to improve the model and refine what we know about the respective sources and sinks of Nd in the ocean (e.g. the strength and isotopic composition of seafloor fluxes). Furthermore, the sophisticated, complex model physics in FAMOUS and intrinsic coupling of the ocean GCM to an atmosphere GCM and dynamic ice sheet model enables the oceanographic changes and how these may manifest in Nd distributions to be examined in conjunction with associated atmospheric and cryospheric changes, including the feedbacks between the different Earth system components.

This new model scheme can aid in the delivery of more robust applications of ε_{Nd} as a modern and palaeo-tracer. It provides a platform for dynamic modelling under different modes of marine Nd cycling (e.g., the balancing of 'top down' versus 'bottom up' fluxes) or varied climatic and oceanographic conditions, enabling current hypotheses to be tested rigorously with the aim of constraining Nd cycling under a complex, partially understood marine geochemical system.

3.5 Supplementary Information

The code detailing the advances is available via the Research Data Leeds Repository (`https://doi.org/10.5518/1136`). These files are known as code modification (i.e. 'mod') files and should be applied to the original model code, which is protected under UK Crown Copyright and can be obtained from the National Centre for Atmospheric Science (NCAS) Computational Modelling Services (CMS): `https://cms.ncas.ac.uk/`. All the files and corresponding information that need to be applied to setup the differences between the simulations are available in the same DOI (above) (note that to complete the setup of these simulations, line 4909 in each simulation's tracer.f file needs updating with the

corresponding $[Nd]_p/[Nd]_d$ value as listed in Table 3.3). Historical modification files that were used when running the simulations described in this chapter, alongside all simulation files are available in Appendix A of this thesis. The database of seawater Nd concentration and isotope measurements and references used to validate the model scheme can also be found in Appendix A.

Control candidate simulations for new FAMOUS reference

- XPDAA *control simulation* (0-5,000 years)
- XPDAB *control candidate simulation* (0-5,000 years)
- XPDAC *control candidate simulation* (0-5,000 years)
- XPDEA *control candidate simulation* (0-5,000 years)

Reversible scavenging efficiency ($[Nd]_p/[Nd]_d$) sensitivity simulations

- XPDAI $[Nd]_p/[Nd]_d = 0.001$ (0-9,000 years)
- XPDAD $[Nd]_p/[Nd]_d = 0.002$ (0-9,000 years)
- XPDAH $[Nd]_p/[Nd]_d = 0.003$ (0-9,000 years)
- XPDAE $[Nd]_p/[Nd]_d = 0.004$ (0-9,000 years)
- XPDAF $[Nd]_p/[Nd]_d = 0.005$ (0-9,000 years)
- XPDAG $[Nd]_p/[Nd]_d = 0.006$ (0-9,000 years)

Total Nd source from sediment (f_{sed}) sensitivity simulations

- XPDAL $f_{sed} = 1.5 \times 10^9\ g\ yr^{-1}$ (0-9,000 years)
- XPDAM $f_{sed} = 3.0 \times 10^9\ g\ yr^{-1}$ (0-9,000 years)
- XPDAH $f_{sed} = 4.5 \times 10^9\ g\ yr^{-1}$ (0-9,000 years)
- XPDAN $f_{sed} = 6.0 \times 10^9\ g\ yr^{-1}$ (0-9,000 years)

Text S3.1: FAMOUS pre-industrial perturbed parameter ensemble

The perturbed parameter ensemble from which we selected our control simulation for this study, forms a substantially different piece of research to the present chapter. Since the detail of the ensemble work is not required to understand the implementation described here, the calibration work (method and results) is not described in detail here. However, it is useful to have some of the information, so briefly: the pre-industrial perturbed parameter ensemble was constructed by varying 13 physical tuning parameters according to a Latin hypercube sampling design (e.g. Table 3.6), building on the work by Gregoire et al. (2011) to produce a total of 549 simulations. It stems from the XFHCC 1-sweep version of FAMOUS, with an added Rayleigh friction on the winds and was performed using the Met Office Surface Exchange Scheme (MOSES) version 1. The Hadley Ocean Carbon Cycle module (HadOCC) is not included and a salinity flux correction was applied to remove long-term drifts using the VFLUX method described by Dentith et al. (2019). The details for all simulations in the ensemble are available from `www.paleo.bris.ac.uk`. In Sect. 3.2.2 of the main text, we present and evaluate the relevant (for this study) oceanic features of a small sub-selection of ensemble members; these simulations were identified as appropriate for use in our Nd implementation based on the criteria outlined there. We did not undertake any further validation of ensemble performance.

Table 3.6: Description of parameters varied in FAMOUS pre-industrial perturbed parameter ensemble

Parameter(s)	Description
AHI1_SI, AHI2_SI, AHI3_SI	Coefficients for isopycnic diffusion, allowing it to vary with depth
CDNR	Factor of multiplication for the bulk aerodynamic coefficient for heat
CHNR	Factor of multiplication for the bulk aerodynamic coefficient for momentum
FNUB_SI	Constant used in calculating Richardson number dependent viscosity
KAPPA0_SI	Vertical diffusivity at surface
DKAPPA_DZ_SI	Vertical diffusivity rate of increase
RHcrit	The threshold of relative humidity for cloud formation (Smith, 1990)
Z0FSEA	The free convective roughness length over the sea for boundary layer processes (Smith, 1993)
Cw_Sea	The threshold value of cloud liquid water for formation of precipitation (Smith, 1990). Value of this parameter over the ocean
Cw_Land	The threshold value of cloud liquid water for formation of precipitation (Smith, 1990). Value of this parameter over the land
AlphaM	Sea ice low albedo (Crossley and Roberts, 1995)

Table 3.7: Simulation description, initial conditions, and tuned parameter values for the control candidate simulations (Sect 3.2.2 main text) from the FAMOUS pre-industrial perturbed parameter ensemble

Simulation name/ UM identifier	Owner	Spinup period (years)	Total run length (years)	CO_2 (ppmv)	CH_4 (in ppbv)	N_2O (in ppbv)	CFC11/CFC12 (in pptv)	AHI2_SI	AHI1_SI	AHI3_SI	CDNR	CHNR	FNUB_SI	KAPPA0_SI	DKAPPA_DZ_SI	RHCRIT	Z0FSEA	CW_SEA	CW_LAND	ALPHAM
xpdaa	ee14s2r	250	5000	280	760	270	0	9566.9	4.26E+03	316.12	4.78	1.23	3.08E-06	1.92E-05	6.76E-08	6.36E-01	3.90E-04	3.89E-05	7.29E-04	0.22
xpdab	ee14s2r	250	5000	280	760	270	0	2840.3	2.58E+04	611.32	3.65	1.01	1.71E-06	1.90E-05	6.52E-09	8.27E-01	4.72E-04	3.31E-04	1.04E-03	0.4
xpdac	ee14s2r	250	5000	280	760	270	0	832.28	4.20E+04	1546.1	3.07	0.97	1.10E-06	1.26E-05	1.64E-08	8.16E-01	7.76E-04	3.37E-04	6.22E-04	4.55
xpdea	ee14s2r	420	5000	280	760	270	0	310.2	1.28E+04	316.12	5.62	0.91	3.1E-06	1.07E-05	6.76E-08	6.93E-01	8.72E-04	9.78E-05	4.11E-04	0.24

Table 3.8: Global average biogenic particle concentrations

	Global average particle concentration (kg m^{-3})		
	this study	(Rempfer et al., 2011)	Gu et al. (2019)
POC	3.00×10^{-6}	3.30×10^{-6}	2.66×10^{-6}
CaCO3	6.43×10^{-6}	1.60×10^{-6}	9.53×10^{-6}
Opal	5.33×10^{-6}	5.90×10^{-6}	8.30×10^{-6}
Dust	1.78×10^{-6}	1.30×10^{-6}	1.23×10^{-6}

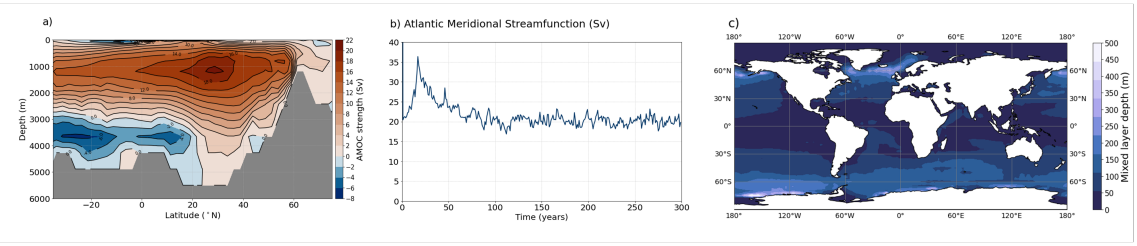

Figure 3.18: (a) Zonally integrated mean Atlantic Ocean stream function, (b) maximum annual Atlantic Meridional streamfunction, and (c) mean depth of mixed layer, all for the FAMOUS *control-candidate* reference simulation XPDAA. Climate means (a and b) are calculated from the last 10 years of the initial 300-year integration.

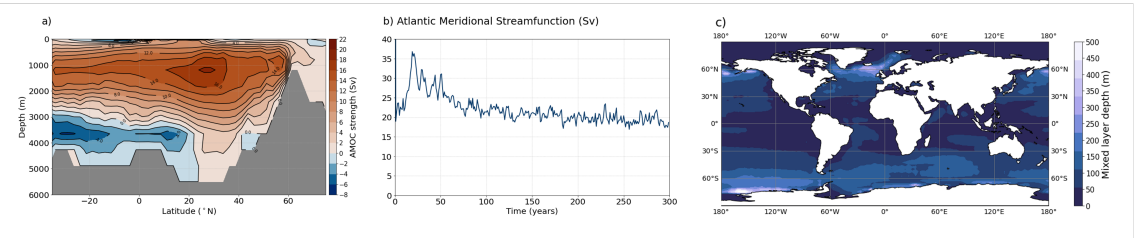

Figure 3.19: (a) Zonally integrated mean Atlantic Ocean stream function, (b) maximum annual Atlantic Meridional streamfunction, and (c) mean depth of mixed layer, all for the FAMOUS *control-candidate* reference simulation XPDAB. Climate means (a and b) are calculated from the last 10 years of the initial 300-year integration

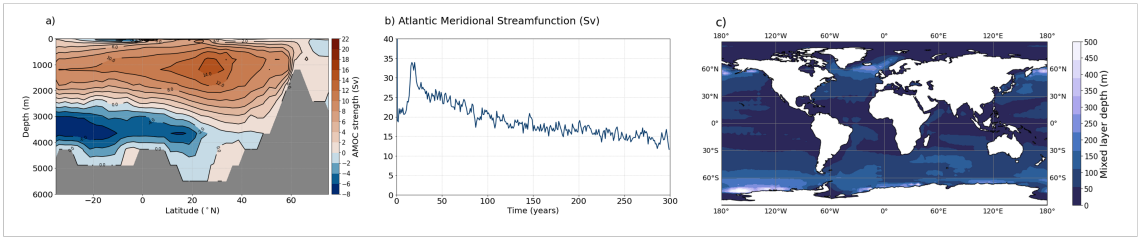

Figure 3.20: (a) Zonally integrated mean Atlantic Ocean stream function, (b) maximum annual Atlantic Meridional streamfunction, and (c) mean depth of mixed layer, all for the FAMOUS *control-candidate* reference simulation XPDAC. Climate means (a and b) are calculated from the last 10 years of the initial 300-year integration

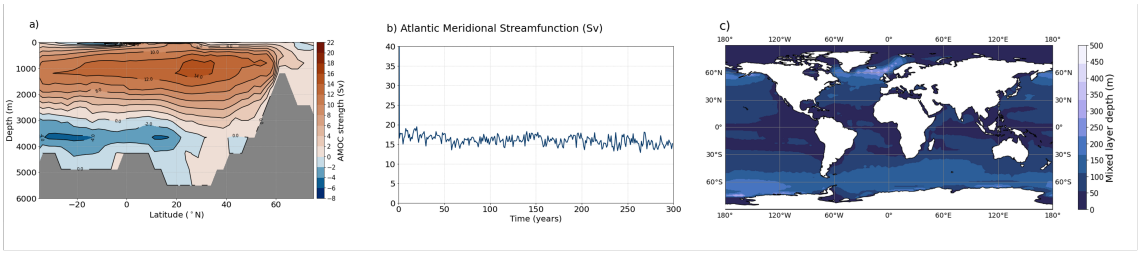

Figure 3.21: (a) Zonally integrated mean Atlantic Ocean stream function, (b) maximum annual Atlantic Meridional streamfunction, and (c) mean depth of mixed layer, all for the FAMOUS *control-candidate* reference simulation XPDEA. Climate means (a and b) are calculated from the last 10 years of the initial 300-year integration

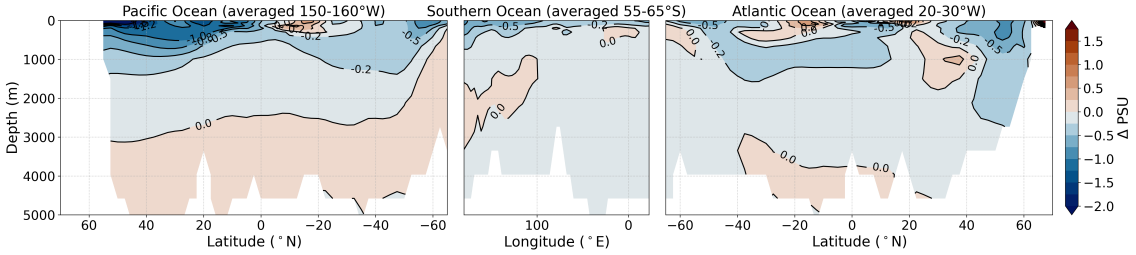

Figure 3.22: Difference in salinity (PSU) from the NOAA World Ocean Atlas database (Locarnini et al., 2018; Zweng et al., 2019) and the FAMOUS control simulation XPDAA (centennial mean from final 100 years of a 5000-year simulation) along a transect crossing the Pacific-Southern-Atlantic Ocean; NOAA *data* minus *control*.

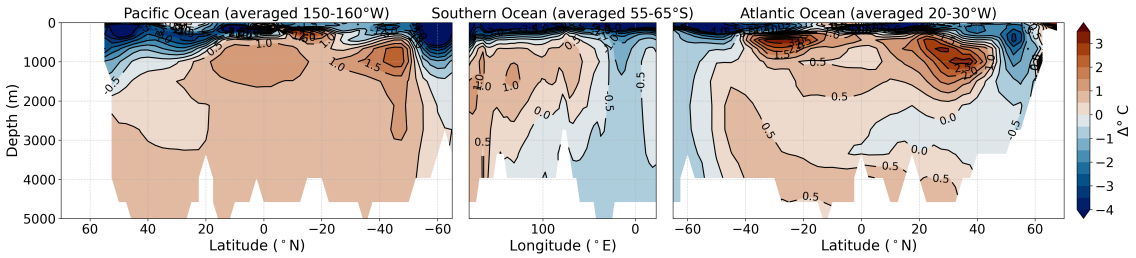

Figure 3.23: Difference in temperature (°C) from the NOAA World Ocean Atlas database (Locarnini et al., 2018; Zweng et al., 2019) and the FAMOUS control simulation XPDAA (centennial mean from final 100 years of a 5000-year simulation) along a transect crossing the Pacific-Southern-Atlantic Ocean; NOAA *data* minus *control*.

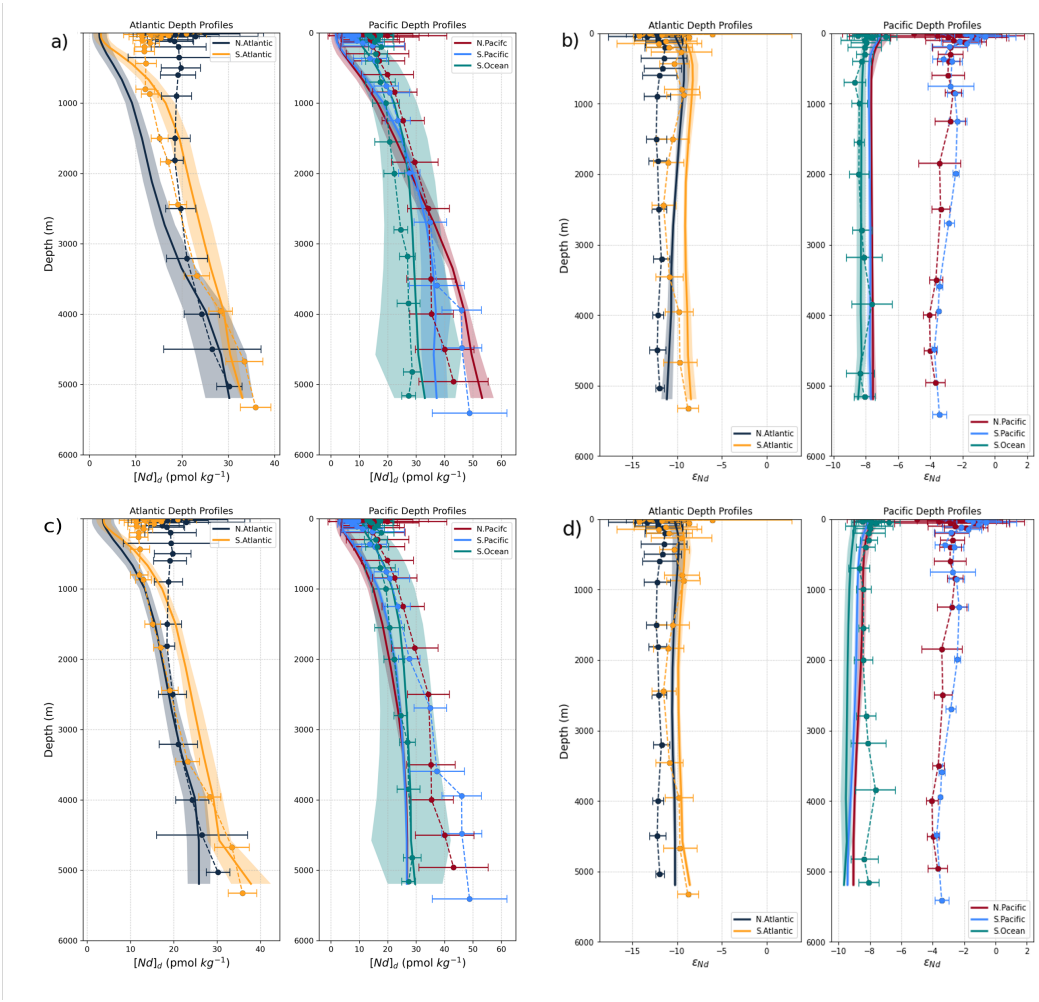

Figure 3.24: Basin averaged $[Nd]_d$ and ε_{Nd} profiles with depth in simulations (a-b) *EXPT_RS4* and (c-d) *EXPT_SED2* respectively. Ocean regions in subplots: (left panel) North and South Atlantic and (right panel) North and South Pacific and Southern Ocean. The mean and standard deviation of modern seawater measurements (Osborne et al., 2017, 2015; GEOTRACES Intermediate Data Product Group, 2021) are calculated for each vertical grid level and represented by the thinner dashed lines and error bars. The mean and standard deviation of the model are represented by the thicker solid line and lighter coloured ribbon.

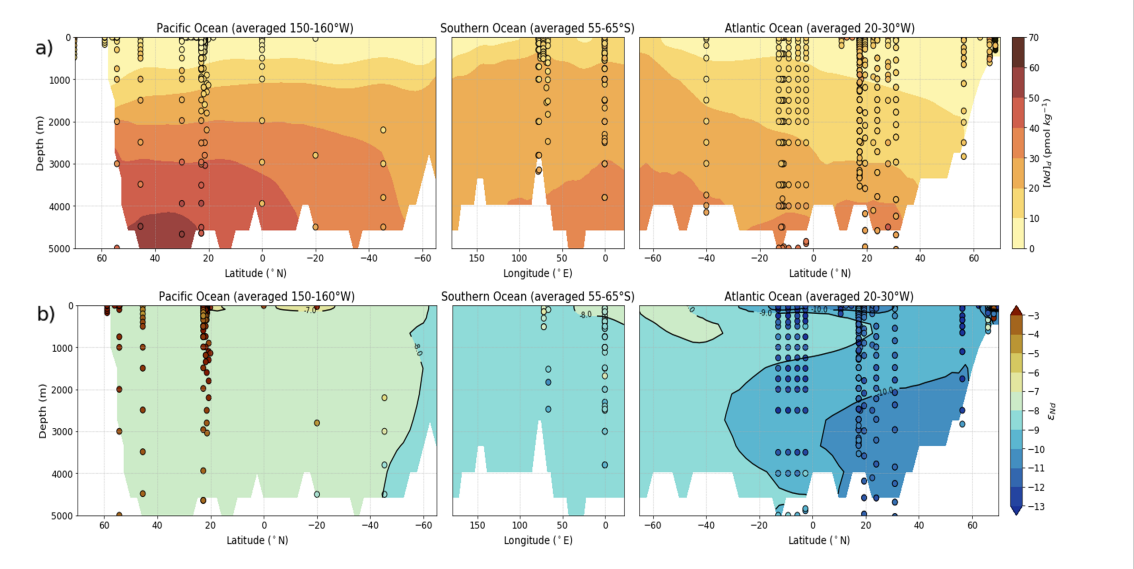

Figure 3.25: Vertical sections of simulated (a) $[Nd]_d$ and (b) ε_{Nd} in simulation *EXPT_RS4* along a transect from the Pacific to Atlantic, traversing the Southern Ocean from West to East. Water column measurements are imposed as filled circles using the same colour scale. Simulated and observed values from the Pacific are from $150 - 160°$ W, in the Southern Ocean values are from $55 - 65°$ S, and in the Atlantic values are from $20 - 30°$ W.

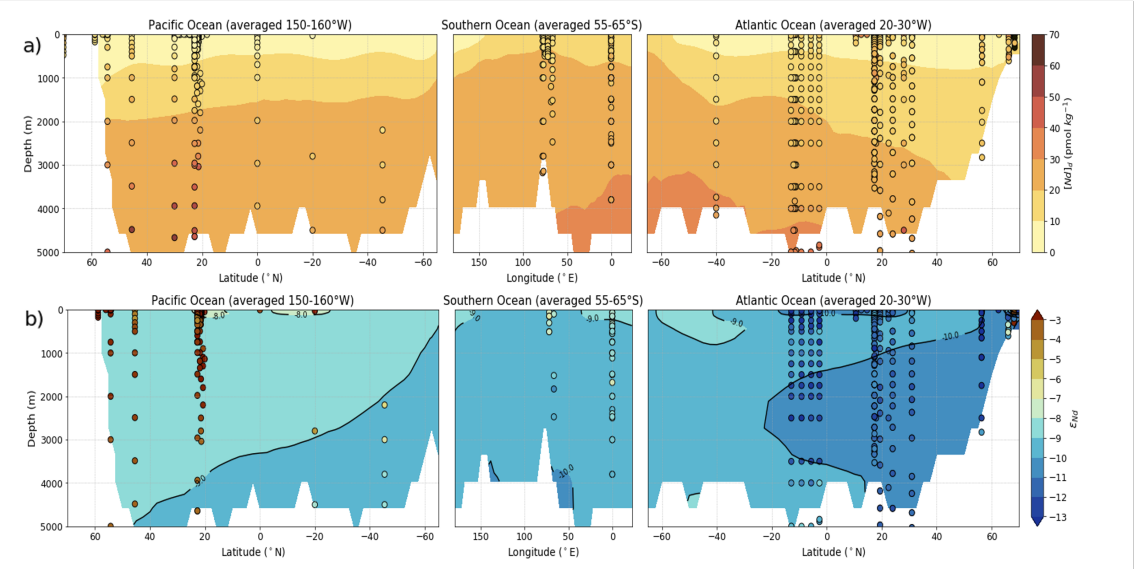

Figure 3.26: Vertical sections of simulated (a) $[Nd]_d$ and (b) ε_{Nd} in simulation *EXPT_SED2* along a transect from the Pacific to Atlantic, traversing the Southern Ocean from West to East. Water column measurements are imposed as filled circles using the same colour scale. Simulated and observed values from the Pacific are from $150 - 160°$ W, in the Southern Ocean values are from $55 - 65°$ S, and in the Atlantic values are from $20 - 30°$ W.

Chapter 4

Optimisation of the Nd isotope scheme in the ocean component of the FAMOUS general circulation model

Abstract

The neodymium (Nd) isotope composition (ε_{Nd}) of seawater can be used to trace large-scale ocean circulation features. Yet, due to the elusive nature of marine Nd cycling, particularly in discerning non-conservative particle-seawater interactions, there remains considerable uncertainty surrounding a complete description of marine Nd budgets. Here, we present an optimisation of the Nd isotope scheme within the fast coupled atmosphere-ocean general circulation model (FAMOUS), using a statistical emulator to explore the parametric uncertainty and optimal combinations of three key model inputs relating to: (1) the efficiency of reversible scavenging, (2) the magnitude of the seafloor benthic flux, and (3) a riverine source scaling, accounting for release of Nd from river sourced particulate material. Furthermore, a suite of sensitivity tests provide insight on the regional mobilisation and spatial extent (i.e., testing a margin-constrained versus a seafloor-wide benthic flux) of certain reactive sediment components. In the calibrated scheme, the global marine Nd inventory totals 4.27×10^{12} g and has a mean residence time of 727 years. Atlantic Nd isotope distributions are represented well, and the weak sensitivity of North Atlantic Deep Water to highly unradiogenic sedimentary sources implies an abyssal benthic flux is of secondary importance in determining the water mass ε_{Nd} properties under the modern vigorous circulation condition. On the other hand, Nd isotope distributions in the North Pacific are 3 to 4 ε_{Nd}-units too unradiogenic compared to water measurements, and our simulations indicate that a spatially uniform flux of bulk sediment ε_{Nd} does not sufficiently capture the mobile sediment components interacting with seawater. Our results of sensitivity tests suggest that there are distinct regional differences in how modern seawater acquires its ε_{Nd} signal, in part relating to the complex interplay of Nd addition and water advection.

4.1 Introduction

Neodymium (Nd) isotope variations in modern seawater broadly correlate with water mass provenance, geometry and mixing (Tachikawa et al., 2017; Goldstein and Hemming, 2003). This has resulted in the exploitation of Nd isotopes as a geochemical tracer of ocean circulation in the past and present (e.g. Lambelet et al. 2016; Lacan and Jeandel 2005a; Lippold et al. 2016; Piotrowski et al. 2012; van de Flierdt et al. 2010; Frank 2002;

Gutjahr et al. 2008; Piotrowski et al. 2004; Roberts et al. 2010; Howe et al. 2017; Basak et al. 2015; Dausmann et al. 2017; Hu and Piotrowski 2018; Jonkers et al. 2015; Wilson et al. 2015; Xie et al. 2014; Pöppelmeier et al. 2020b, 2022; Blaser et al. 2019b; Goldstein and Hemming 2003). With specific regard to the radiogenic properties of this rare earth element, its isotope composition is typically expressed in epsilon (ε_{Nd}) units, where $\varepsilon_{Nd} = [(^{143}Nd/^{144}Nd)_{\text{sample}}/(^{143}Nd/^{144}Nd)_{\text{CHUR}} - 1] \times 10^4$, thus describing the parts per 10,000 deviation of a sample from the chondritic uniform reservoir (CHUR) (Jacobsen and Wasserburg, 1980). Owing to somewhat poorly constrained input and output fluxes, the estimated mean ocean residence time of Nd ranges between 360-800 years (Arsouze et al., 2009; Rempfer et al., 2011; Gu et al., 2019; Pöppelmeier et al., 2020a), which is less than the global thermohaline overturning circulation time (i.e., $<$ 1,500 years). The measured Nd isotope composition of seawater is not actively involved in marine biological cycling (Blaser et al., 2019b).

Neodymium enters the ocean in dissolved and particulate phases through continental weathering via rivers and aeolian dust deposition (Frank, 2002; Goldstein and Hemming, 2003; Grousset et al., 1998; Rousseau et al., 2015; Goldstein and Jacobsen, 1987, 1988; Rahlf et al., 2020, 2021), alongside particle-seawater exchange occurring along the sediment-water boundary (Abbott et al., 2015b,a, 2019; Jeandel and Oelkers, 2015; Pearce et al., 2013; Arsouze et al., 2009; Rempfer et al., 2011; Lacan and Jeandel, 2005a; Tachikawa et al., 2003; Johannesson and Burdige, 2007; Haley et al., 2017; Grenier et al., 2013). Removal of Nd from the water column occurs via sedimentation and complexation, and incorporation into authigenic ferromanganese oxides (Bayon et al., 2004; Du et al., 2016).

Relating to the inherent spatial heterogeneity in crustal ε_{Nd}, which is broadly governed by its age and composition, seawater becomes 'tagged' with a unique ε_{Nd} signature derived from weathering of the proximal continents and hence tracks water mass provenance (Goldstein and Hemming, 2003; Robinson et al., 2021). Seawater ε_{Nd} is then redistributed throughout the ocean interior by advection and mixing, alongside particle cycling (see Tachikawa et al. 2017; van de Flierdt et al. 2016 for reviews). In the modern ocean, the ε_{Nd} signature of intermediate and abyssal waters display mostly conservative behaviour, co-varying with salinity in the Atlantic (Tachikawa et al., 2017; Goldstein and Hemming, 2003). The North Atlantic basin is surrounded by old, unradiogenic continental cratons, yielding unradiogenic ε_{Nd} values for North Atlantic Deep Water (NADW) of around -13 (Lambelet et al., 2016). In contrast, the North Pacific seawater ε_{Nd} is more radiogenic with values between -4 and -2 (Amakawa et al., 2009; Fuhr et al., 2021; Behrens et al., 2018; Fröllje et al., 2016) due to proximate mantle derived volcanic material. Antarctic circumpolar waters have intermediate ε_{Nd} values of around -8.5 (Stichel et al., 2012; Lambelet et al., 2018). These distinct water mass ε_{Nd} features form the basis for using the marine Nd cycle as a tool to explore the global circulation. Furthermore, the ε_{Nd} of bottom water can be extracted from marine archives facilitating palaeoceanographic investigations (e.g., Blaser et al. 2016; Martin and Scher 2004; Piotrowski et al. 2004; Roberts et al. 2010).

Intriguingly, in contrast to ε_{Nd} (i.e., the Nd paradox; Goldstein and Hemming 2003), which is largely governed by water mass mixing, dissolved Nd concentrations ($[Nd]_d$) deviate significantly from conservative behaviour (e.g., Zheng et al. 2016), generally increasing linearly with depth and along the circulation pathway (i.e., with ventilation age) (van de Flierdt et al., 2016). Internal vertical cycling via reversible scavenging is thought to play an important role in modulating the distribution of Nd, where adsorption/incorporation and desorption/dissolution of Nd occurs on sinking and remineralising particles throughout the water column (Siddall et al., 2008b; Bacon and Anderson, 1982; Stichel et al., 2020). Alternatively, a widespread benthic diffuse Nd flux was suggested to explain the Nd concentration and isotope decoupling (Haley et al., 2017; Abbott et al., 2015b). However, observational data to confirm both processes are rare (e.g. Abbott et al. 2019, 2015b;

Paffrath et al. 2021; Stichel et al. 2020), which limits a full quantification.

Moreover, whilst ε_{Nd} appears to trace large-scale ocean circulation features and water masses effectively, the specific geochemical processes governing its distribution remain elusive (Abbott et al., 2019). Despite over four decades of research, significant gaps in the understanding of the oceanic cycling of Nd persist, and mostly relate to quantifying the major input pathways into, and subsequent internal cycling of Nd within the ocean (e.g., Haley et al. 2017; Tachikawa et al. 2017; van de Flierdt et al. 2016; Abbott et al. 2022; Jeandel 2016). For example, we are still missing a comprehensive estimate of a particulate riverine flux as a major marine Nd source (Rousseau et al., 2015; Rahlf et al., 2021), constraints on reversible scavenging processes and its efficiency throughout the water column (Siddall et al., 2008b; Stichel et al., 2020; Paffrath et al., 2021; Haley et al., 2021), and a quantification of the diffusive benthic flux to seawater (Abbott et al., 2015a). Furthermore, the environmental conditions driving the extent and spatiotemporal variability of various elusive seafloor particle-seawater interactions remain unknown (Tachikawa et al., 2017; Abbott et al., 2015a, 2019, 2016a; Du et al., 2016; Lagarde et al., 2020; Lacan and Jeandel, 2005b; Jeandel, 2016). The last point includes the absence of an established quantification of both the spatial extent and the broad mobile sedimentary ε_{Nd} phases interacting with seawater or marine Nd archives across the seabed, and specifically across remote and abyssal ocean regions (Robinson et al., 2021).

In an attempt to address such knowledge gaps, the international GEOTRACES programme has substantially increased modern measurements of both seawater $[Nd]_d$ and ε_{Nd} (van de Flierdt et al., 2012; GEOTRACES Intermediate Data Product Group, 2021), improving our understanding of the water column processes that govern marine Nd distributions (e.g., Basak et al. 2015; Haley et al. 2021; Lambelet et al. 2018; Paffrath et al. 2021; Rahlf et al. 2020; Wang et al. 2021). However, recent investigations and results from GEOTRACES have also alluded to some inconsistencies of localised highly non-conservative behaviour, which challenge the simplified conservative assumptions of marine ε_{Nd} (Tachikawa et al., 2017; Haley et al., 2017; Abbott et al., 2015b, 2019; Wang et al., 2021). Furthermore, due to the inherent challenges of directly measuring fluxes that are both temporally and environmentally variable and globally widespread, there remain limited process-based observations, which are necessary to both compliment the seawater measurements and capture fully the marine geochemical cycling of Nd (Homoky et al., 2016).

Numerical models of the marine Nd cycle offer a unique means by which to constrain Nd budgets, providing quantitative constraints on physical processes, and can be applied to investigate specific hypotheses regarding the mechanisms driving seawater ε_{Nd} distributions (Tachikawa et al., 2003; Arsouze et al., 2009; Rempfer et al., 2011; Gu et al., 2019; Pöppelmeier et al., 2020a, 2022; Siddall et al., 2008b; Bertram and Elderfield, 1993; Arsouze et al., 2007; Rempfer et al., 2011; Oka et al., 2021). As such, these models have formed a vital tool for improving the utility and interpretative framework for ε_{Nd} as a modern and palaeoceanographic tracer.

Neodymium isotopes have been implemented into numerical models with a trend of ever increasing complexity, primarily in terms of the type of model used, with a shift from fast and 'simple-to-use' box-models (Bertram and Elderfield, 1993; Tachikawa et al., 2003) to full complexity ocean general circulation models (GCMs) (Arsouze et al. 2009; Rempfer et al. 2011; Gu et al. 2019; Pöppelmeier et al. 2020a, 2022; Robinson et al. 2022a). The latter of these model groupings has the advantage of improved spatial resolution, ability to represent more physical processes and more dynamically consistent ocean circulation fields (Flato et al., 2013), but at the cost of computational efficiency. Further complexity in numerical Nd isotope schemes has been achieved in terms of increasingly detailed descriptions of marine Nd cycling, with preliminary schemes representing ε_{Nd} in simple conservative mixing models applying crude surface boundary conditions (Bertram and Elderfield, 1993; Tachikawa et al., 2003; van de Flierdt et al., 2004). The most recent Nd

implementations in complex models simulate both ^{143}Nd and ^{144}Nd isotopes individually, allowing for simultaneous representation of both $[Nd]_d$ and ε_{Nd} and enabling a more detailed explicit representation of the major sources, sinks and cycling of marine ε_{Nd} and its sensitivity to physical ocean circulation (Arsouze et al. 2009; Rempfer et al. 2011; Gu et al. 2019; Robinson et al. 2022a). Although these represent the most up-to-date knowledge of the marine Nd cycle, such models remain confounded by inherent structural and parametric uncertainty, including uncertainty in either observation or process-based metrics, alongside errors introduced within simplified representations of fundamental physics (i.e., 'parameterisations').

Full complexity Nd isotope enabled ocean models therefore rely on adjustable parameter values to capture the dominant geochemical dynamics of a complex system, and we may optimise these inputs to find the model configuration that most appropriately captures the observed process. The demand for higher computational power necessitated by the increasing sophistication and complexity of Nd isotope schemes has meant only a handful of studies performed optimisation for their input parameters within their relevant host ocean GCM models (e.g. in the ocean components of the Bern3D model; Pöppelmeier et al. 2020b; Rempfer et al. 2011 and CESM1; Gu et al. 2019), especially since they require multi-millennial integrations to reach equilibrium. The schemes for which Nd cycling has been optimised faced a compounding problem for escalating computational demand by applying resource intensive systematic tuning (i.e., running over 100 simulations), using suboptimal space filling design methodologies that may also lead to inefficient exploration of the input space. In addition, some of these models were restricted by previous assumptions regarding the dominating processes involved in the marine Nd cycle, which limited the development of appropriate model boundary conditions – notably here, an assumption that particle-seawater interaction is constrained to shallow continental margins (called into question by studies by Abbott et al. 2015b, 2019; Haley et al. 2017).

In this study, we tackle these issues head-on, defining a new approach for efficiently refining a recent implementation of Nd isotopes in the ocean component of the Fast Met Office and UK universities Simulator (FAMOUS) GCM (Robinson et al., 2022a). The scheme revisited and updated Nd sources, sinks and transformation of the tracer in line with increased observations and current findings relating to global marine Nd cycling (Blanchet, 2019; Robinson et al., 2021; Haley et al., 2017; Siddall et al., 2008b; Arsouze et al., 2009), and has been validated against global measurements of seawater $[Nd]_d$ and ε_{Nd} (Osborne et al., 2015, 2017; GEOTRACES Intermediate Data Product Group, 2021), substantiating that the major processes influencing the global marine Nd cycle are represented in the model. Here, we first assess and reduce the uncertainty within the input space of three key unconstrained parameters detailing major non-conservative processes within the global marine Nd cycle in a Bayesian framework (Sect. 4.2). We then present an optimised reference simulation (Sect. 4.3), considered as 'suitable' from within the parameter space that satisfies physical reasoning in the context of what we know about Nd cycling, selected by minimising an objective loss function relating to model skill in reproducing modern measurements of both $[Nd]_d$ and ε_{Nd}. Subsequently, we undertake idealised sensitivity studies with this optimised reference simulation (Sect. 4.4), using a quasi-idealised experiment design to broadly investigate the preferential mobilisation of certain reactive sediment components under a seafloor-wide benthic flux model of marine Nd cycling. Finally, (Sect. 4.5), we investigate the sensitivity of marine ε_{Nd} distributions between a margin-constrained versus a seafloor-wide benthic flux.

4.2 Methods

4.2.1 Model description

Neodymium isotopes (^{143}Nd and ^{144}Nd) have been fully implemented into the ocean component of the FAMOUS coupled atmosphere-ocean GCM, representing three global sources of Nd to seawater: aeolian dust fluxes, riverine sources and dissolution of marine sediment (i.e., benthic flux), and internal cycling and sedimentation processes via reversible scavenging (Robinson et al., 2022a). The FAMOUS GCM (Smith et al., 2008; Jones et al., 2005; Smith, 2012; Jones et al., 2008) is derived from the Met Office's Hadley Centre Coupled Model V3 (HadCM3) AOGCM (Gordon et al., 2000). In brief, the atmospheric model of FAMOUS is based on quasi-hydrostatic primitive equations, has a horizontal resolution of 5° latitude by 7.5° longitude, with 11 vertical levels on a hybrid sigma-pressure coordinate system, and a 1-hour timestep. The rigid-lid ocean model has a horizontal resolution of 2.5° latitude by 3.75° longitude and 20 vertical levels, spaced unequally in thickness from 10 m at the near-surface ocean to over 600 m at deep ocean depths, and a 12-hour timestep. The atmosphere and the ocean are coupled once per day.

FAMOUS is currently capable of simulating on the order of 650 model years per wall clock day on 16 processors. As such, it is well suited to running large ensembles (Gregoire et al., 2011) and performing sensitivity studies (Gregoire et al., 2015; Smith and Gregory, 2009), alongside multi-millennial length simulations (Gregoire et al., 2012, 2015; Dentith et al., 2020), as is done here.

We use the Met Office Surface Exchange Scheme (MOSES) version 1 (Cox et al. 1999; FAMOUS-MOSES1) generation of the model. Although a more recent version of the land surface model does exist (MOSES2.2; Essery et al. 2003, 2001; Valdes et al. 2017; Williams et al. 2013), when run for multi-millennia under constant pre-industrial boundary conditions the published setup is known to produce a collapsed Atlantic Ocean convection accompanied by the formation of a strong deep Pacific meridional overturning circulation (Dentith et al., 2019). Therefore, FAMOUS-MOSES1, which simulates more realistic AMOC states over long (muti-millennia) integrations, is currently better optimised for exploring geochemical ocean tracers. However, the Nd isotope scheme can be directly transferred to other versions of the UK Met Office Unified Model (UM) version 4.5, including HadCM3/L or FAMOUS-MOSES2.2. A full description of the Nd isotope scheme in FAMOUS is provided by Robinson et al. (2022a).

Dissolved seawater Nd in all our optimisation simulations (Sect. 4.2.2) is initialised from zero and integrated for 6,000 years under the same constant pre-industrial boundary conditions as used by Robinson et al. (2022a); which, as determined in our previous study, is sufficiently long for the Nd isotope scheme to adequately reach steady state under parameters within a reasonable Nd inventory target response range (i.e., where global Nd inventory is $3.0 \times 10^{12} - 6.0 \times 10^{12}$ g), whilst avoiding unnecessary and costly additional run-time. Here, we define steady state as being when the Nd inventory becomes [near] constant with time (i.e., < 0.0025 % change per 100 years). All the presented results refer to or show the centennial mean from the end of the 6,000-year simulations.

4.2.2 Neodymium isotope scheme optimisation

To calibrate the new Nd isotope scheme, we use an approach developed within the field of Bayesian Statistics, called History Matching (Williamson et al., 2013). The framework uses a collection of tools to aid the quantification of uncertainty and rule out combinations of model parameter values that produce unrealistic outputs. In calibrating the input space, history matching does not require the assumption of probability distributions on the unknown model outputs; for this reason, it has seen widespread uptake in the climate sciences where complex non-linear simulations make realistic judgements of output

probability distributions difficult. The approach consists of running an ensemble of simulations varying key input variables simultaneously, via an efficient sampling method. The model output is then compared against observations using an implausibility metric to rule out unrealistic simulations. An emulator, a statistical regression (often a Gaussian Process: Rasmussen and Williams 2006) relating model output (or metric) to input parameters, can be used to design good input combinations for running additional waves (i.e., ensembles) of simulations to further improve model performance. In this section, we describe our implementation of this approach, starting with our choice of tuning parameters (Sect. 4.2.2.1), then introducing the Gaussian Process emulation, how we used previous sensitivity experiments to inform our new simulations, including our choice of target observations that informed the sampling of two waves of experiments (Sect. 4.2.2.2), and finally the metrics we used to identify optimised simulations (Sect. 4.2.2.3).

4.2.2.1 Tuning parameters

To calibrate the Nd isotope scheme in the FAMOUS GCM, we explore the model input uncertainty of three key input variables: (i) the reversible scavenging efficiency ($[Nd]_p/[Nd]_d$), which drives vertical cycling of marine Nd and represents the only Nd sink in the model; (ii) total sediment Nd flux (f_{sed}), which is especially important for governing Nd isotope distributions in the intermediate and deep ocean (Robinson et al., 2022a); and (iii) riverine source scaling factor (α_{river}), which is a scaling applied to the surface riverine Nd source (Table 4.1). Note that the three tuning parameters ($[Nd]_p/[Nd]_d$, f_{sed} and α_{river}) explored in this study do not vary spatially, and the total Nd sourced from aeolian dust is fixed for all the simulations. $[Nd]_p/[Nd]_d$ and f_{sed} represent the major (and largely unconstrained) processes understood to govern $[Nd]_d$ and ε_{Nd} distributions (Rempfer et al., 2011; Gu et al., 2019; Siddall et al., 2008b; Pöppelmeier et al., 2020a; Arsouze et al., 2009), and these two parameters are explored within both waves of analysis (Sect. 4.2.2.2). On the other hand, the decision to vary α_{river} in our optimisation is based on results presented by Rousseau et al. (2015), who found that in the Amazon Estuary, up to four times more Nd was supplied to the oceans via estuarine dissolution of river-sourced resuspended lithogenic material compared with dissolved sources. As such α_{river} was used to examine, to a first order, enhanced Nd sourced at river mouths, and this parameter was explored during the second wave of analysis (Sect. 4.2.2.2).

Table 4.1: Parameters chosen for the optimisation of the Nd isotope scheme in FAMOUS and their initial ranges. References are provided for the choice of initial range.

Parameter	Initial range	Unit	Description	References
$[Nd]_p/[Nd]_d$	[0.001, 0.006]	-	Reversible scavenging efficiency	(Robinson et al., 2022a)
f_{sed}	[1.5×10^9, 6.0×10^9]	g(Nd) yr^{-1}	Total seafloor sediment flux	(Robinson et al., 2022a)
α_{river}	[1.0, 4.0]	-	Riverine source scaling	(Rousseau et al., 2015)

The objective of our tuning was to statistically optimise these three key model input variables within the FAMOUS Nd isotope scheme, aiming to reduce parametric uncertainty and substantially refine the plausible parameter space to improve the model's skill at representing both modern $[Nd]_d$ and ε_{Nd} distributions. Despite FAMOUS being a fast GCM, running a simulation to equilibrium still requires 10 days on 16 processors. To make best use of computing resources, we therefore adopted an approach that uses an efficient sampling strategy; Gaussian Process emulation to 'guess' optimal parameter value combinations and multiple waves of experiments to progressively refine the model calibration.

4.2.2.2 Statistical design of multi-wave ensemble

Gaussian Process (GP) emulators are non-parametric statistical regression models that flexibly represent chosen model output or performance metrics as a function of a subset of input parameters, together with an uncertainty on that prediction (Rasmussen and Williams, 2006; Astfalck et al., 2019). We describe the model output y as a function of a vector of input parameters θ expressed as:

$$y(\theta) \sim GP(m(\theta)), k(\theta, \theta')), \tag{4.1}$$

where m represents a mean function used to provide parametric prior model beliefs, and k represents a covariance function. Our input space, θ, is defined by the uncertain Nd scheme parameters: $[Nd]_p/[Nd]_d$, f_{sed}, and α_{river} (see section above). The effects of parameters not explicitly represented in θ are handled by the random stochasticity embedded in the covariance function.

Building such a GP emulator to predict the plausible input parameter regions first requires results from multiple simulations with the Nd isotope scheme, forming a reference exploratory ensemble. Here, for efficiency, we used output of annual global Nd inventories ($Nd(I)$) and residence times (τ_{Nd}) from 11 existing single parameter perturbation simulations, which formed part of the preliminary sensitivity analysis of the new Nd isotope scheme performed by Robinson et al. (2022a); Fig.4.1 triangles, including two additional experiments run under a combined high $[Nd]_p/[Nd]_d$ and f_{sed}, with α_{river} set to 1.0 in one simulation, and set to 3.0 in the other (see Appendix A for a table with the specific combination of parameter values used in each simulation, simulation names are denoted by their unique five-letter Met Office Unified Model identifier). We refer to these simulations as the "training set".

We chose to focus the initial optimisation of the Nd isotope scheme on model outputs of annual global Nd inventories ($Nd(I)$) and residence times (τ_{Nd}) as these relatively simple and hence easy to handle terms encompass the balance of all Nd sources and sinks in the model. Further, $Nd(I)$ and τ_{Nd} determine model equilibrium and the lifetime of Nd in the ocean, the latter of which drives the distinct basinal ε_{Nd} signals that are fundamental to the water mass tracer properties of marine ε_{Nd}. Additionally, and for each wave of the multi-wave ensemble, we set a target range for $Nd(I)$ and τ_{Nd} (Table 4.2). The choice of target bounds for $Nd(I)$ (Table 4.2) reflect the widely recognised estimated global $Nd(I)$ of 4.2×10^{12} g (Tachikawa et al., 2003). Alongside these target $Nd(I)$ bounds, specific for sampling in Wave 2, we employ a maximum threshold residence time of Nd (i.e., $\tau_{Nd} < 1,000$ years). This value was chosen based on results from Robinson et al. (2022a) who demonstrated where Nd ocean residence times are over 1,000 years, close to the timescales of global overturning circulation, simulated Nd becomes well mixed in the ocean which acts to globally homogenise the ε_{Nd} signal.

Table 4.2: Design of the multi-wave FAMOUS Nd isotope scheme optimisation ensemble. Previous simulations from Robinson et al. (2022a) used as the GP 'training set' are not shown here.

	Number of simulations	Parameters explored	$Nd(I)$ target range ($\times 10^{12}$ g)	τ_{Nd} target range (years)
Wave 1	8	$[Nd]_p/[Nd]_d$, f_{sed}	[3.0, 5.0]	NA
Wave 2	15	$[Nd]_p/[Nd]_d$, f_{sed}, α_{river}	[3.7, 4.7]	[< 1,000]

The *Gaussian Process emulator* was fitted to the "training set" of simulations to emulate the predictive mean $Nd(I)$ and τ_{Nd} as a function of the uncertain parameters $[Nd]_p/[Nd]_d$, f_{sed}, and α_{river}. From these results, we predict the plausible region of the parameter space, called not-ruled-out-yet ($NROY$) space, as all the combinations of

parameter values that would likely produce $Nd(I)$ and τ_{Nd} within their target ranges (Table 4.2), given the uncertainty in the GP emulator. We successively refine this region by running two waves of ensembles. Mathematically, this can be described as follows. Using the GP emulators, at any unexplored location, θ^*, we obtain prediction of $y(\theta^*)$ described by an expectation $E(y(\theta^*))$ and variance $var[y(\theta^*)]$. Appealing to a common heuristic (here, Chebyshev's inequality) we describe the prediction interval of $y(\theta^*)$, as $P(\theta^*) = [E[y(\theta^*)] - 3\sqrt{var[y(\theta^*)]}, E[y(\theta^*)] + 3\sqrt{var[y(\theta^*)]}]$, so that $y(\theta^*) \in P(\theta^*)$ with high probability. This is a conservative rule of thumb that considers all the emulated values within 3 standard deviations of the mean (Chebyshev, 1867). For each wave we apply the set of target ranges for $Nd(I)$ and τ_{Nd} (documented in Table 4.2). We define the $NROY$ space as the collection of input parameters, θ^{NROY}, whose prediction intervals $P(\theta^{NROY})$ contain values of $Nd(I)$ and τ_{Nd} within their specified target ranges. Define the target ranges by T, mathematically we describe the $NROY$ space as:

$$NROY = \{\theta : P(\theta) \cap T \neq \{0\}\} \tag{4.2}$$

that is, the values of θ where the intersection of $P(\theta)$ and T are not the null set $\{0\}$. In plain language, this means that we define the $NROY$ space as all the parameter combinations for which the emulator predicts it is plausible that results will be within our target range.

Combinations of parameter values for each wave (Fig. 4.1) are sampled using k-extended Latin Hypercube sampling (Williamson, 2015) within the $NROY$ space so that design locations are optimally spaced with respect to the target values (Table 4.2).

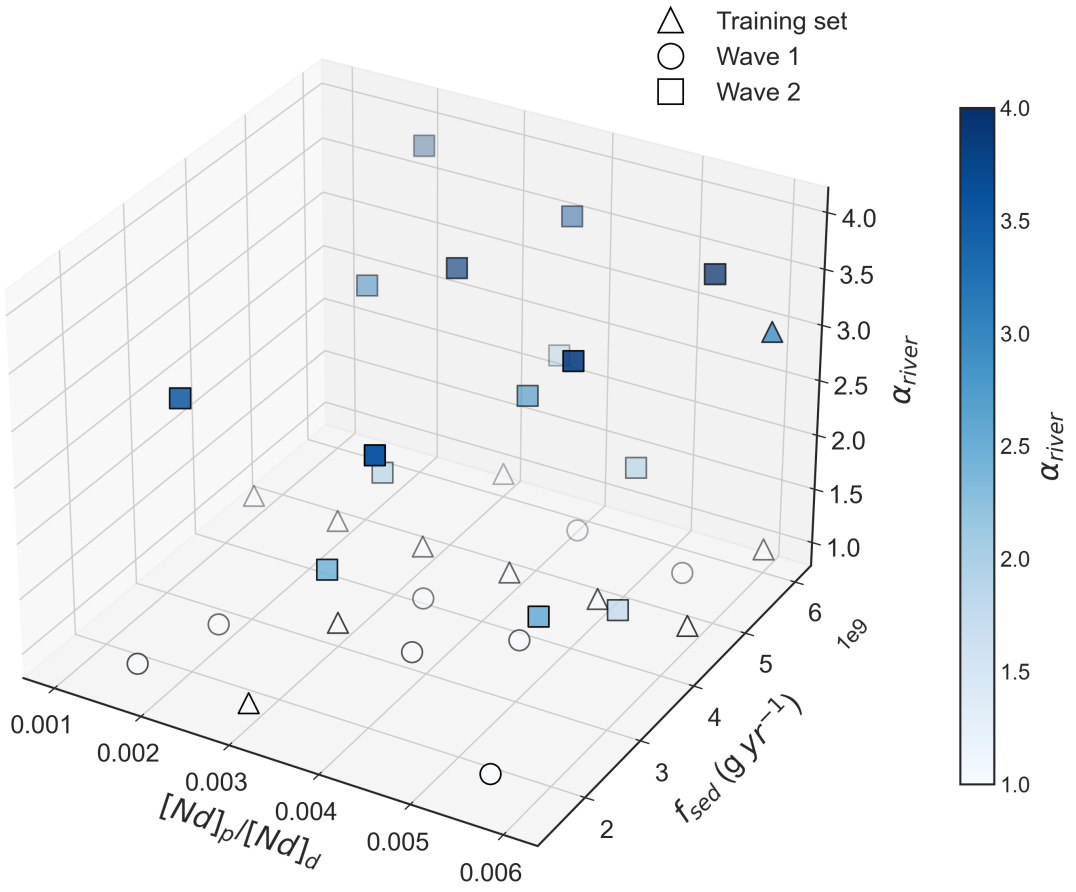

Figure 4.1: Parameter combinations of $[Nd]_p/[Nd]_d$ (x-axis), f_{sed} (y-axis) and α_{river} (z-axis and colour of filled markers) in the multi-wave FAMOUS Nd isotope scheme optimisation. Triangles indicate simulations in the training set, circles are for simulations in Wave 1, and squares are for simulations in Wave 2.

In Wave 1, we vary the two parameters detailing the major non-conservative processes believed to govern marine Nd cycling ($[Nd]_p/[Nd]_d$ and f_{sed}). Wave 2 further includes the additional third tuneable parameter (α_{river}), thus, to ensure the regions of plausible parameter space adequately capture this additional dimension, we increase the number of simulations in Wave 2 to 15 (Table 4.2).

We sample the eight simulations in Wave 1 such that GP predictive mean $Nd(I)$ is between 3.0×10^{12} g and 5.0×10^{12} g, which are intentionally wide bounds designed to better encompass the largely unexplored $NROY$ parameter space and associated uncertainty arising from the limited (11) simulations forming the exploratory ensemble. We do not yet constrain τ_{Nd}.

The GP emulator is updated for Wave 2, based on the additional results of Wave 1, to reassess the uncertainty in the remaining plausible input space. The additional information gained from Wave 1 reduces uncertainty and improves the predictive capability of the GP. This enables us to apply refined bounds on the mean $Nd(I)$ that are closer to the global $Nd(I)$ target reference of 4.2×10^{12} g ($\pm0.5\times10^{12}$ g), and to introduce the τ_{Nd} target (Table 4.2). Using the results of the Wave 2 simulations, we describe the final $NROY$ space by the Wave 2 criteria with the GP emulator trained on all resulting data from the training Wave 1 and Wave 2 simulations. After two waves of simulations, the maximum predictive standard deviations of $Nd(I)$ and τ_{Nd} within the $NROY$ space is 0.22×10^{12} g and 46 years, respectively; we deem this to be a sufficient reduction in parametric uncertainty to

end the iterative process of performing further model ensembles to inform the *GP*. More resources could have been allocated to further reduce the uncertainty, but with diminishing benefits. Thus, with only 23 new simulations (instead of the 100+ used in previous studies; Rempfer et al. 2011; Gu et al. 2019; Pöppelmeier et al. 2020a), we are in a position to optimally calibrate the Nd scheme.

4.2.2.3 Identifying a reference simulation

Following the multi-wave parameter analysis of the FAMOUS Nd isotope scheme, we apply an updated *GP* emulator to determine the parameter combinations within our remaining plausible input space to produce a statistically optimised reference simulation (named '*REF*') that most closely matches modern measurements of $[Nd]_d$ and ε_{Nd}. We first determine model skill by returning the mean absolute error (MAE):

$$MAE = \frac{1}{N}\sum_{k=1}^{N}|obs_k - sim_k|, \tag{4.3}$$

where obs_k and sim_k are measured and simulated $[Nd]_d$ or ε_{Nd} respectively, and k is an index over all observational data. For each measurement – based on its longitude, latitude, and depth – the value predicted by the simulation is extracted and the mean deviation of simulated and observed $[Nd]_d$ and ε_{Nd} is presented in pmol kg^{-1} and ε_{Nd}-units respectively. Here we chose specifically not to apply a grid box volume weighting to the MAE, which would act to emphasise abyssal Pacific results in our assessment of model skill (due to the large area of the abyssal Pacific Ocean), where there are few observations and relatively low variability in Nd distributions. The advantage of using an unweighted MAE is that the assessment metric better scrutinises regions with larger (spatial) gradients in both $[Nd]_d$ or ε_{Nd}; i.e., at the surface and high latitudes. However, we acknowledge neither the horizontal nor vertical distribution of global seawater $[Nd]_d$ or ε_{Nd} observational data are even (Robinson et al., 2022a), and some local surface features captured in the seawater measurements will not be represented in FAMOUS due to model resolution, introducing some bias into the cost function. The measurements used in this assessment are from the seawater REE compilation used by Osborne et al. (2017, 2015), augmented with more recent measurements including data from the GEOTRACES Intermediate Data Product 2021 (GEOTRACES Intermediate Data Product Group 2021; sections GA02, GA08, GP12, GN02, GN03, GIPY05). Combined, the utilised observational database represents a total of 6,048 $[Nd]_d$ and 3,278 ε_{Nd} measurements. Notably, we omit measurements of $[Nd]_d > 100$ pmol kg^{-1} from the model data comparison here because these represent very localised signals, which we do not attempt to resolve (Robinson et al., 2022a). In some instances, near land grid cells, the location of the measured and modelled Nd being compared may not match. In such cases, we employ a nearest neighbour algorithm to extract the modelled value from the closest ocean model grid cell. Furthermore, if multiple measurements occur within one model grid cell, the arithmetic mean of the values is used for our comparison to model results, and as such, $n = 3,471$ and 2,136 for the calculation of both $MAE_{[Nd]}$ and $MAE_{\varepsilon_{Nd}}$ respectively.

We then standardise the mean absolute errors ($MAE = J_i$) for both $[Nd]_d$ and ε_{Nd} (where $i = [Nd]_d$ and ε_{Nd}) as:

$$STD_{J_i} = (J_i - E(J_i))/sd(J_i), \tag{4.4}$$

where $E(.)$ and $Sd(.)$ represent the empirical mean and standard deviation. We then define our loss function (J_{loss}) as:

$$J_{loss} = STD_{J_{Nd}} + STD_{J_{\varepsilon_{Nd}}} \tag{4.5}$$

which we minimise over the $NROY$ space. The minimisation constraints applied to sample the REF parameters for $Nd(I)$ and τ_{Nd} (i.e., the bounds within which we minimise for J_{loss}) are consistent with those imposed during Wave 2 of the multi-wave parameter exploration (Table 4.2). These constraints are what we define as the capability of the model to satisfy physical reasoning within its simulation of the marine Nd cycle, alongside an additional constraint regarding an upper limit of the reversible scavenging efficiency ($[Nd]_p/[Nd]_d < 0.0045$). This maximum threshold for $[Nd]_p/[Nd]_d$ was set following results from the multi-wave analysis demonstrating that notwithstanding improved $J_{\varepsilon_{Nd}}$, above this threshold and particularly in the Pacific, numerical instabilities in simulated ε_{Nd} occur within the surface layers due to near-zero $[Nd]_d$ resulting from an over-strong particle scavenging.

Our optimisation procedure and specific choice of physical ($Nd(I)$ and τ_{Nd}; Table 4.2) and parameter ($[Nd]_p/[Nd]_d < 0.0045$) bounds are somewhat arbitrary, yet, as detailed in Sect 4.2.2.2, we approximate these from prior knowledge of marine Nd cycling and our most up-to-date capabilities in choosing appropriate constraints to solve for J_{loss} that improve model skill in representing the modern marine Nd cycle (Rempfer et al., 2011; Arsouze et al., 2009; Siddall et al., 2008b; Tachikawa et al., 2003). To test the sensitivity of simulated Nd distributions to the choice (or prioritisation) of target summary metrics (and thus what combinations of f_{sed}, $[Nd]_p/[Nd]_d$ and α_{river} are identified as optimal), we ran two additional simulations alongside REF. These use parameter value combinations that the GP emulator predicts will minimise $J_{[Nd]}$ (simulation REF_CONC1) and $J_{\varepsilon_{Nd}}$ (simulation REF_IC), removing the minimisation constraints applied for $Nd(I)$ and τ_{Nd} hence prioritising performance for $[Nd]_d$ and ε_{Nd} respectively, rather than balancing the standardised performance for both.

4.3 Optimisation results and discussion

4.3.1 Overview of multi-wave ensemble and parameter influence

The multi-wave ensemble explored the response of simulated $[Nd]_d$ and ε_{Nd} in the FAMOUS GCM to effective space-filling variations within the $NROY$ parameter space for the three tuning parameters: $[Nd]_p/[Nd]_d$, f_{sed} and α_{river}. Neodymium inventory in all experiments in the ensemble increases considerably within the first 1,000 years of simulation, and by the end of the simulations, the majority reach steady state under a range of different $Nd(I)$ (Fig. 4.2). There is less variance in the simulated $Nd(I)$ from the simulations in Wave 1. This is as expected since the first wave only explored the two-dimensional input space of $[Nd]_p/[Nd]_d$ and f_{sed}, which were the focus of the systematic exploration within our previous sensitivity analysis (Robinson et al., 2022a). As such, after Wave 1, the GP benefited from a greater exploration of the 2D parameter space, and thus from additional constraints on regions of the space that are unfeasible/unphysical, herby increasing the GP's predictive power. By adding the river scaling (α_{river}) parameter in Wave 2, we introduced an additional and widely unexplored degree of freedom into the simulations, producing a greater range of simulated $Nd(I)$ (Fig. 4.2).

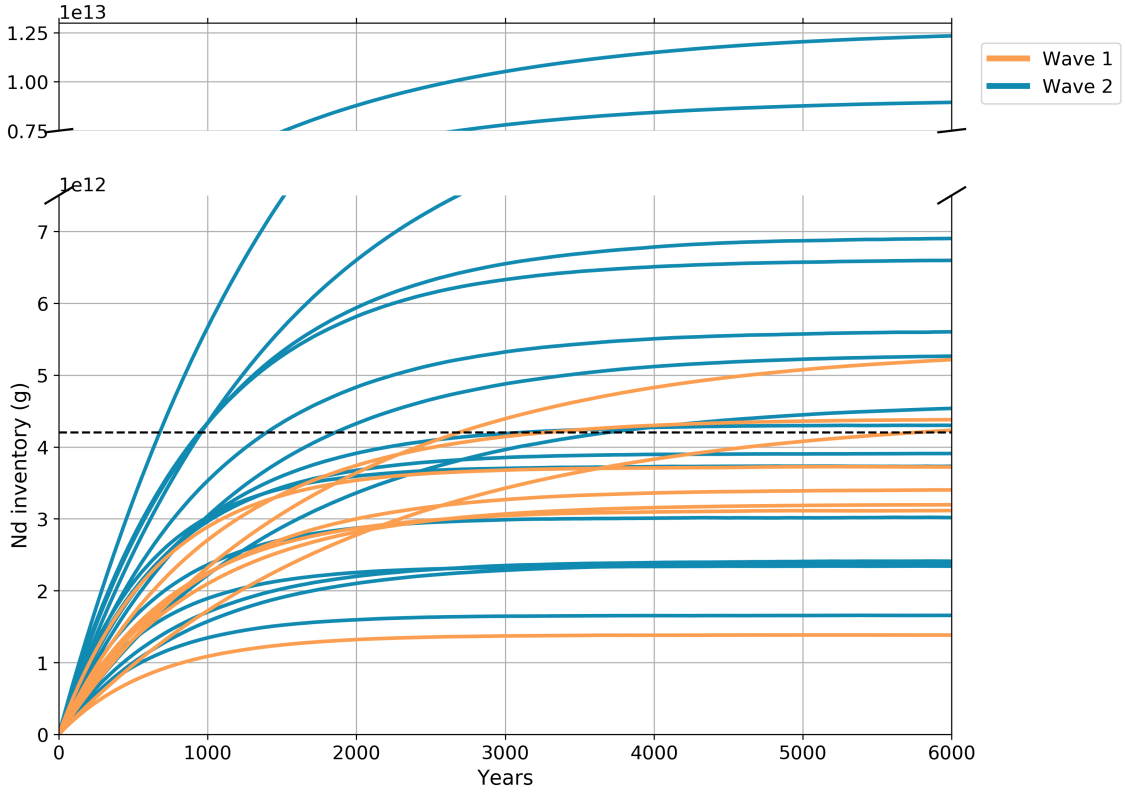

Figure 4.2: Timeseries of simulated global Nd inventory (g) from the multi-wave parameter tuning ensemble. Orange and blue lines are from simulations in Wave 1 and 2 respectively, and the dashed line represents the estimated global marine Nd inventory of 4.2×10^{12} g from Tachikawa et al. (2003).

The lowest simulated $Nd(I)$ of 1.38×10^{12} g occurs within Wave 1; this simulation (XPGTG; see Appendix A) has a strong particle scavenging efficiency ($[Nd]_p/[Nd]_d = 0.0056$) combined with a low sediment source ($f_{sed} = 1.59 \times 10^9$ g yr^{-1}), and no riverine source scaling to account for dissolution of river particulates (i.e., $\alpha_{river} = 1.0$). The low collective total Nd source (f_{total}) to the ocean of 2.36×10^9 g yr^{-1} combined with a parameterisation of strong sinking and removal in the model causes Nd to rapidly (within 3,000 years) reach equilibrium under low $Nd(I)$. In contrast, the Nd sources and sinks within two simulations from Wave 2 (XPHJH and XPHJI: see Appendix A) are especially unbalanced (i.e., Nd input outweighs Nd removal). Here the parameter combinations result in unrealistically large $Nd(I)$, ranging from 8.95×10^{12} g up to 12.3×10^{12} g, which is still increasing considerably at the end of the simulation. Importantly, though, both of these high $Nd(I)$ simulations explore similar regions of the parameter space, with combinations of low reversible scavenging efficiencies (where $[Nd]_p/[Nd]_d \leq 0.0023$) and high Nd sources ($f_{total} \geq 6.32 \times 10^9$ g yr^{-1}). A few simulations with reasonable $Nd(I)$, but which have not reached steady state, all share low reversible scavenging efficiencies relative to their total Nd source magnitudes. Here, we have learned important information from the GP, and all such simulations are determined to be within the regions of the refined parameter space that are now ruled out; based on what we deem to be an unphysical Nd residence time that is too similar to or longer than the typical timeframe of global deep ocean overturning (Sect. 4.2.2.2.).

The relationship between the three tuning parameters and their controls on determining $Nd(I)$ and τ_{Nd} demonstrate foremost that $[Nd]_p/[Nd]_d$, f_{sed} and α_{river} are almost equally important in determining the variation in $Nd(I)$, this is because each parameter governs major seawater Nd source/removal (Fig. 4.3). Alternatively, τ_{Nd} also shows a very strong

correlation between varying $[Nd]_p/[Nd]_d$, which is unsurprising considering $[Nd]_p/[Nd]_d$ drives the only sink in the model, but clearly demonstrates the important role of scavenging intensity for governing simulated Nd residence time in the ocean. In contrast, the lack of correlation between f_{sed} and α_{river} reduces direct impact of these parameters on τ_{Nd}.

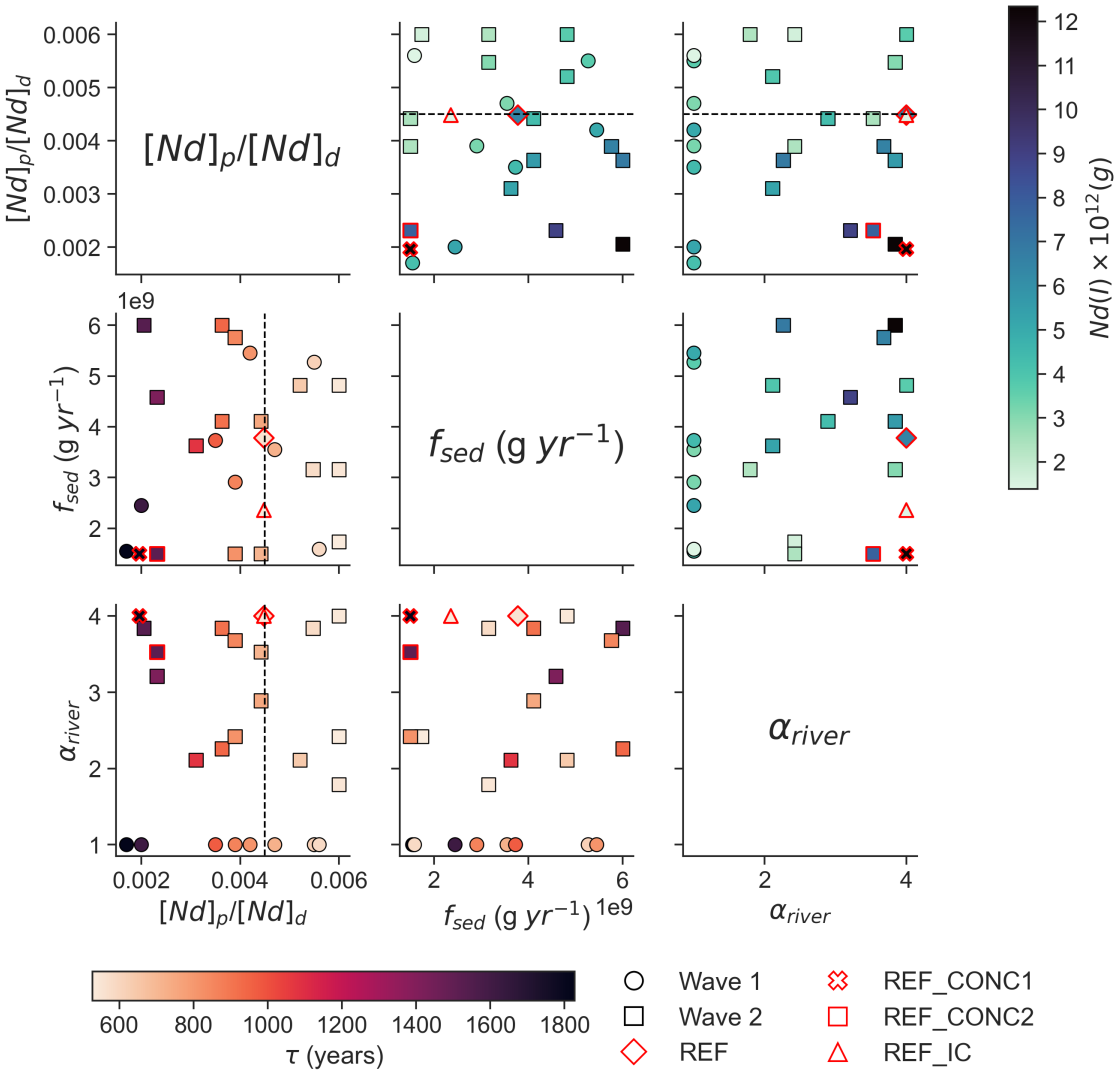

Figure 4.3: Simulated Nd inventory ($Nd(I)$) and residence time (τ_{Nd}) from *GP* predicted parameter combinations in the multi-wave FAMOUS Nd isotope ensemble and optimisation. Circles and squares represent the parameter combinations in Wave 1 and 2 respectively. Output from *REF* (red diamond), *REF_CONC1* (red cross), *REF_CONC2* (red square, see Table 4.3), and *REF_IC* (red triangle) simulations are overlain. The dashed black line indicates the upper limit of the reversible scavenging efficiency ($[Nd]_p/[Nd]_d < 0.0045$; Sect. 4.2.2.3) imposed for identifying the optimised simulations (i.e., *REF, REF_CONC1 and REF_IC*) to avoid numerical instabilities in the surface layers resulting from too strong particle scavenging.

There is a complex relationship between the three tuning parameters and their controls on model skill in simulating $[Nd]_d$ (determined by the MAE, $J_{[Nd]}$; Fig. 4.4). Broadly, best $[Nd]_d$ model-data fit occurs under balanced parameter combinations of low scavenging intensity ($[Nd]_p/[Nd]_d$) and low Nd source magnitudes (i.e., low combined f_{sed} and α_{river}) moving to high scavenging balanced by high Nd source magnitudes. Conversely, worst $[Nd]_d$ model-data fit occurs under low scavenging intensity coupled with high source

magnitudes, mostly due to imbalanced Nd budgets causing unrealistically high $[Nd]_d$ accumulation in the ocean. The largest variance in $J_{[Nd]}$ exist under different f_{sed} and α_{river} when under low particle scavenging ($[Nd]_p/[Nd]_d < 0.003$), indicating that within this region of parameter space, $[Nd]_p/[Nd]_d$ impacts are minor and the two source parameters exert a bigger influence on $[Nd]_d$ (Fig. 4.4). On the other hand, there is a much clearer relationship between the tuning parameters and $J_{\varepsilon_{Nd}}$, with minimised $J_{\varepsilon_{Nd}}$ for larger $[Nd]_p/[Nd]_d$. Reversible scavenging efficiency therefore explains most of the variance regarding model skill in simulating ε_{Nd} in our ensemble, mostly due to strong vertical cycling keeping τ_{Nd} below the global overturning time and enhancing localised basinal ε_{Nd} signals. More indistinguishable patterns for f_{sed} and α_{river} suggest these parameters are less influential for minimising $J_{\varepsilon_{Nd}}$.

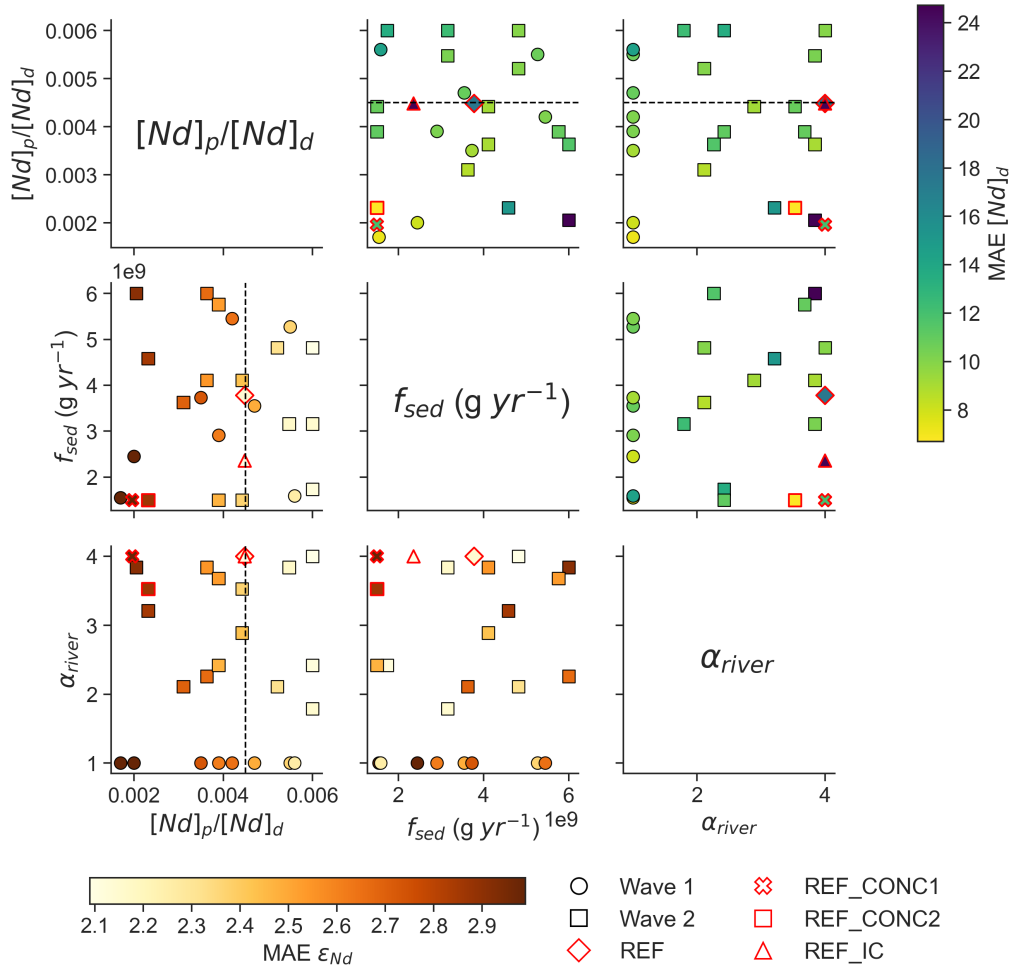

Figure 4.4: Mean absolute error (MAE_i: J_i, Eq. (4.3)) values indicating model skill in representing modern measurements of $[Nd]_d$ ($J_{[Nd]}$) and ε_{Nd} ($J_{\varepsilon_{Nd}}$) from *GP* predicted parameter combinations in the multi-wave FAMOUS Nd isotope ensemble and optimisation. Circles and squares represent the parameter combinations in Wave 1 and 2 respectively. Output from *REF* (red diamond), *REF_CONC1* (red cross), *REF_CONC2* (red square, see Table 4.3), and *REF_IC* (red triangle) are overlain. The dashed black line indicates the upper limit of the reversible scavenging efficiency ($[Nd]_p/[Nd]_d < 0.0045$; Sect. 4.2.2.3) imposed for identifying the optimised simulations (i.e., *REF, REF_CONC1 and REF_IC*) to avoid numerical instabilities in the surface layers resulting from an over strong particle scavenging.

4.3.2 Optimised reference simulation

Our statistically optimised reference simulation (*REF*) embodies an estimate of the combination of parameter values that appropriately represent the modern marine Nd cycle in FAMOUS, based upon minimising the expected loss function (J_{loss}: a standardised MAE of both $[Nd]_d$ and ε_{Nd}, from Eq. (4.5)). We highlight, here, that our estimate necessitates subjective decisions including our choice of loss function (J_{loss}), choice of tuneable parameters (Sect. 4.2.2.1), physical targets from which to minimise J_{loss} within (i.e., mean $Nd(I)$ of 4.2×10^{12} g ($\pm 0.5 \times 10^{12}$ g), $\tau_{Nd} < 1,000$ years; Sect. 4.2.2.2), and an upper limit on the reversible scavenging efficiency to prevent numerical instabilities in the surface layers (i.e., $[Nd]_p/[Nd]_d < 0.0045$; Sect. 4.2.2.3), combined with the intrinsic parametric and structural uncertainty typical within GCMs like FAMOUS. As such, it is unlikely that a single 'best' configuration exists. Rather, a subset of different parameter values within the refined parameter space (Sect. 4.3.1) could yield multiple optimal solutions, though we recognise other subsets would capture similar key characteristics of the modern marine Nd cycle as our selection of values for *REF*.

The $Nd(I)$ in *REF* is 4.27×10^{12} g and has reached steady state (where rate of change in final 100 years is 0.006%), and thus is in excellent agreement with previous Nd isotope enabled model inventories (Tachikawa et al., 2003; Rempfer et al., 2011; Gu et al., 2019; Arsouze et al., 2009). The total Nd source to the ocean (f_{total}) is 5.9×10^9 g(Nd) yr^{-1}, sitting within the range of recent estimates of 4.5×10^9 to 6.1×10^9 g(Nd) yr^{-1} (Rempfer et al., 2011; Gu et al., 2019), and Nd residence time (τ_{Nd}) is 727 years (where $\tau_{Nd} = Nd(I)/f_{total}$), which is also inside the range estimated by recent isotope enabled models (690-785 years; Rempfer et al. 2011; Gu et al. 2019; Pöppelmeier et al. 2020a). A full list of final optimised parameter values for *REF* are presented in Supplementary Table 4.5. Moreover, the optimised scheme apportions the magnitude of simulated Nd sources to seawater: the sediment source via a seafloor wide benthic flux represents the largest Nd source contributing 64% of the total Nd source, riverine sourced Nd contributes 30%, whilst dust sources make up the final 6%. Our partition of Nd sources are most comparable to recent estimates by Pöppelmeier et al. (2020a) (where sediment contributed 60%, rivers 32% and dust 9%), likely related to the river scaling applied in both studies. Moreover, the spatially uniform seafloor-wide benthic flux of 3.78×10^9 g(Nd) yr^{-1} (i.e., f_{sed}) corresponds to a sediment flux (per area) of 2.96 pmol cm^2 yr^{-1}. This value is similar to the few existing measurements of a benthic Nd flux across diverse sedimentary environments, which are mostly on the order of 10 pmol cm^2 yr^{-1} (Abbott et al., 2019, 2015a; Du et al., 2018; Haley et al., 2004). Compared with model estimates of the sediment flux, our value is close to the global benthic flux estimated by Pöppelmeier et al. (2020a) of 5.4 pmol cm^2 yr^{-1}, and lower than the value of $20 - 30$ pmol cm^2 yr^{-1} estimated by Du et al. (2020).

For comparison, we chose to run two additional simulations where the *GP* predicted parameter values to minimise for $[Nd]_d$ (i.e., $J_{[Nd]}$) or for ε_{Nd} (i.e., $J_{\varepsilon_{Nd}}$), named *REF_CONC1* and *REF_IC* respectively (Table 4.3). Interestingly, one simulation from Wave 2 of the multi-wave ensemble (XPHJF) performs better for reproducing global measurements of $[Nd]_d$ than the simulation predicted by the *GP* emulator to minimise $J_{[Nd]}$ (*REF_CONC1*). This is demonstrated by the lower MAE ($J_{[Nd]}$) of 6.69 pmol kg^{-1} compared to 7.51 pmol kg^{-1} in *REF_CONC1*; for subsequent discussion and in the figures, we name this simulation *REF_CONC2*. The reason that *REF_CONC1* performed slightly worse than *REF_CONC2* in terms of $[Nd]_d$ performance can be attributed to imprecision in the *GP*. This emulator uncertainty arises from the inability to run the simulator through every possible input configuration as a result of limited computing resources, resulting in a degree of statistical error surrounding the prediction of optimised parameters (Rasmussen and Williams, 2006; Kennedy and O'Hagan, 2001). Furthermore, uncertainties introduced into the *GP* due to inaccuracies within the observational measurements (e.g., Pahnke et al. 2012) adds an

additional degree of uncertainty to the prediction. However, the similar input values for *REF_CONC1* and *REF_CONC2* – whereby the main difference is from the smaller α_{river} of 3.53 in *REF_CONC2* compared to 4.0 in *REF_CONC1*, resulting in a smaller total Nd source to seawater (i.e., f_{total}) – demonstrates the multi-wave exploration (Sect. 4.3.1) sufficiently explored the parameter space. This illustrates that the *GP* effectively refines plausible regions of the input space for optimising model performance, albeit with an associated uncertainty in the prediction.

Table 4.3: Overview of the parameter values and general model skill for the optimised *REF* simulation, which the *GP* minimised for J_{loss} (Eq. (4.5)) compared to simulations which the *GP* minimised for $J_{[Nd]}$ (*REF_CONC1*) and $J_{\varepsilon_{Nd}}$ (*REF_IC*) separately. Due to uncertainty associated with the *GP* prediction, *REF_CONC2* describes a simulation from Wave 2 of the multi-wave parameter analysis (XPHJF) which minimised $J_{[Nd]}$.

Simulation name	UM identifier	f_{sed} ($\times 10^9$ g yr^{-1})	$[Nd]_p/[Nd]_d$	α_{river}	f_{total} ($\times 10^9$ g yr^{-1})	$Nd(I)$ ($\times 10^{12}$ g)	τ_{Nd} (yrs)	$J_{[Nd]}$ ($n = 3471$)	% within 10 (pmol kg^{-1})	$J_{\varepsilon_{Nd}}$ ($n = 2136$)	% within 3 ε_{Nd} -units
REF	*XPIAB*	3.78	0.00448	4.0	5.87	4.27	727	8.83	68	2.37	67
REF_CONC1	*XPIAD*	1.5	0.00196	4.0	3.59	5.51	1534	7.51	73	2.84	63
REF_CONC2	*XPHJF*	1.5	0.0023	3.53	3.38	4.54	1341	6.69	81	2.77	63
REF_IC	*XPIAC*	2.36	0.00448	4.0	4.45	3.16	711	9.42	63	2.34	68

The optimised parameter values vary between the three experiments that minimise J_{loss} (*REF*), $J_{[Nd]}$ (*REF_CONC2*), and $J_{\varepsilon_{Nd}}$ (*REF_IC*). Notably, *REF* has the highest sediment source (f_{sed}), and both *REF* and *REF_IC* have the highest scavenging efficiency $[Nd]_p/[Nd]_d$ of 0.00448, which lies close to the imposed upper limit on the reversible scavenging efficiency (i.e., $[Nd]_p/[Nd]_d < 0.0045$) (Table 4.3). This demonstrates that, in our ensemble, efficient reversible scavenging is key for determining ε_{Nd}. Whereas the much lower $[Nd]_p/[Nd]_d$ of 0.0023 in *REF_CONC2* facilitates a longer marine Nd residence time due to less scavenging and removal via sedimentation, which allows Nd isotopes to become better mixed throughout the ocean, improving model representation of $[Nd]_d$, but at the expense of removing distinct inter-basin water mass ε_{Nd} signals (Robinson et al., 2022a).

Riverine source scaling, to account for dissolution of river particulates, in all optimised simulations (*REF, REF_CONC2, and REF_IC*) is set to the upper bound of the scaling parameter range considered (where α_{river} is set to, or close to 4.0; Table 4.3). Here, indicating that an enhanced Nd flux from rivers considerably favours model performance for both $[Nd]_d$ and ε_{Nd}. This may suggest a particulate river source as a major global Nd flux to seawater, supporting the findings by Rousseau et al. (2015). Within the study by Rousseau et al. (2015), a simplified global extrapolation of the Amazon observation of river particle Nd release suggest that the particulate river source could even be 6-17 times larger than the dissolved, supported further by recent measurements by Rahlf et al. (2021), who reported large Nd release from river particulates in the estuary of the Congo River. Although out of the scope of this study, future work with the Nd isotope scheme in FAMOUS could explore the upper bounds of this hypothesis, which would benefit substantially from increased measurements to resolve in greater detail complex estuarine processes and account for ε_{Nd} variability between dissolved and river particulates (Goldstein and Jacobsen, 1987; Rousseau et al., 2015). That said, overall, we interpret this result with some caution, as the enhanced river flux may compensate for the model not resolving complex and highly variable surface processes where most of the observational data are biased towards (with 38% of observational data concentrated in upper 100 m compared with 11% below 3,000 m). In addition, the scaled river flux may be compensating for biases within the parameterisation of the reversible scavenging, owing to the simplified nature of the fixed globally uniform particle settling rate, which, as explored by Pöppelmeier et al. (2022) in a similar scheme parameterisation, may be too high in the upper layers

(i.e., there may be lower settling velocities in the surface mixed layer) due to enhanced turbulence (Chamecki et al., 2019; Noh et al., 2006) and complexation with organic ligands (Byrne and Kim, 1990), requiring future exploration.

Optimising our scheme for skill in simulating both $[Nd]_d$ and ε_{Nd} demonstrably produces improved results than prioritising only $[Nd]_d$ or ε_{Nd} performance, and reveals the complex behaviour in balancing model skill at simulating $[Nd]_d$ and ε_{Nd} as found previously (Rempfer et al., 2011; Gu et al., 2019; Pöppelmeier et al., 2020a). The Nd inventory in *REF* is closest to the target $Nd(I)$ of 4.2×10^{12} g, whilst *REF_IC* underestimates (3.16×10^{12} g) and *REF_CONC2* overestimates (4.54×10^{12} g) the inventory. The residence time is similar for *REF* (727 years) and *REF_IC* (711 years), which is predominantly determined by scavenging efficiency (i.e., $[Nd]_p/[Nd]_d$; Fig. 4.3), whereas for *REF_CONC2*, τ_{Nd} is 1,341 years, the latter being unphysical given the observed variations in ε_{Nd} between basins that require a lifetime less that the ocean overturning time (van de Flierdt et al., 2016). As such, our choice to weight model skill equally in both $[Nd]_d$ and ε_{Nd} favours an optimised scheme that improves constraints on the external sources to seawater and encompasses a more complete representation of the marine Nd cycle; ε_{Nd} remains key, but $[Nd]_d$ is important for governing vertical isotopic gradients (Siddall et al., 2008b; Pöppelmeier et al., 2022).

Our remaining analysis focuses on *REF*, and compares regional distributions of simulated and measured $[Nd]_d$ and ε_{Nd} values in *REF* across different ocean basins to explore model skill in representing key regional features and variance of the modern marine Nd cycle with respect to depth (Fig. 4.5). Overall, *REF* is successful in simulating the global distributions of $[Nd]_d$, closely matching measurements of increasing concentrations with depth and with a nutrient like increase along the circulation pathway (van de Flierdt et al., 2016; Goldstein and Hemming, 2003), where the highest $[Nd]_d$ (approximately 50 pmol kg^{-1}) occurs in the deep Pacific (below 5,000 m) (Fig. 4.5b). However, model-data $[Nd]_d$ mismatches occur in the upper 1,000 m across all basins. Here, mean simulated $[Nd]_d$ is underestimated, with the largest underestimations occurring within the uppermost (top 100 m) surface layers, indicating *REF* does not capture fully the measured surface $[Nd]_d$ variability, a feature common amongst previous Nd isotope implementations (Arsouze et al. 2009; Rempfer et al. 2011; Gu et al. 2019; Robinson et al. 2022a). We attribute the surface $[Nd]_d$ underestimation to a combination of the low spatial resolution of the model, which limits full representation of point surface inputs (Goldstein and Hemming, 2003), too strong particle scavenging in the surface layers, and/or the misrepresentation of elevated surface and marginal Nd sources.

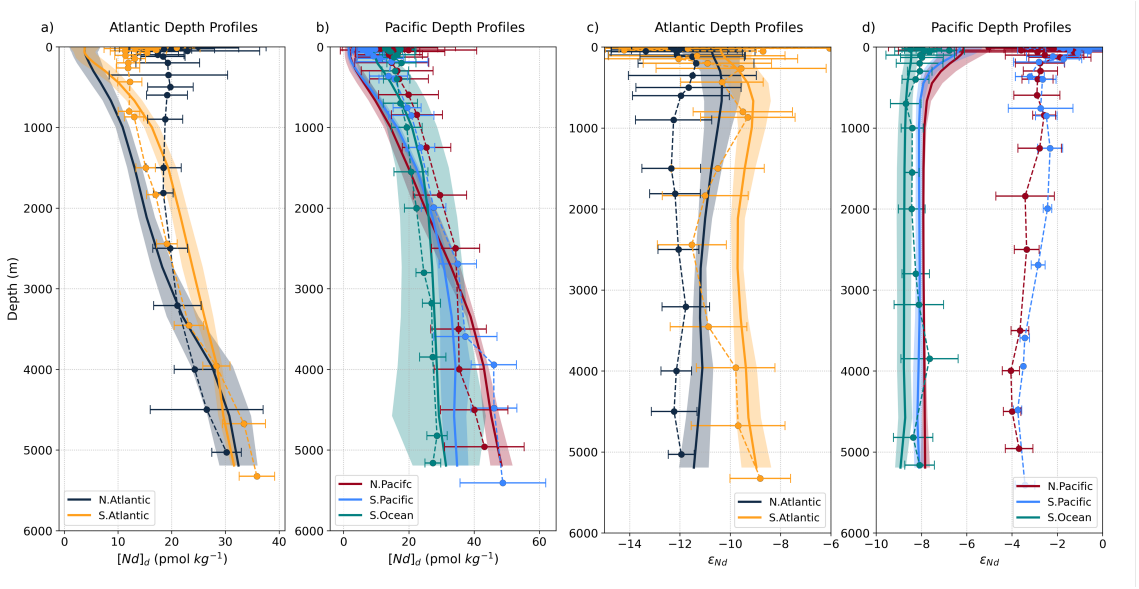

Figure 4.5: Basin averaged $[Nd]_d$ ((a); North and South Atlantic, (b); North and South Pacific and Southern Ocean) and ε_{Nd} profiles ((c); North and South Atlantic, (d); North and South Pacific and Southern Ocean) with depth in *REF*. The mean and standard deviation of modern seawater measurements (Osborne et al., 2017, 2015; GEOTRACES Intermediate Data Product Group, 2021) are calculated for each vertical grid level and represented by the thinner dashed lines and error bars. The mean and standard deviation of the model are represented by the thicker solid line and lighter coloured ribbon.

Moreover, *REF* slightly overestimates the mean vertical $[Nd]_d$ gradients compared with measurements, particularly in the North Atlantic, where measured $[Nd]_d$ is higher than simulated in the surface to intermediate layers and slightly lower than simulated at depth (Fig. 5a). Additionally, the measured profiles of $[Nd]_d$ in the upper 3,000 m are more homogenous throughout the water column than simulated. This overestimated vertical gradient implies that in the North Atlantic, high surface Nd inputs fluxes are underestimated, and in regions of deep-water convection, efficient scavenging processes are governing distributions in *REF*, which would otherwise act to homogenise $[Nd]_d$ with depth. In the South Atlantic, below about 500 m, simulated $[Nd]_d$ is a better match to observations, but remains overestimated by approximately 5 pmol kg^{-1} between 1,000 and 3,000 m, and closely matches measurements $>$ 4,000 m below the surface. In conjunction with the North Atlantic comparison, this also hints at there being too much release from reversible scavenging within the ocean's interior in the model. Thus, the rates of desorption of Nd at depth may be too strong, supporting suggestions by Haley et al. (2017) that undue emphasis is imposed on water column desorption as a primary driver of $[Nd]_d$. The inherent complexities and uncertainties regarding reversible scavenging require more detailed evaluations including a better spatial quantification of the modes and rates of scavenging, and dependence on particle type, before any full conclusions can be made (Stichel et al., 2020). The mean $[Nd]_d$ profiles are matched with better skill in the Southern Ocean, although *REF* simulates a higher variability throughout the water column compared to measurements (Fig. 4.5b). The non-conservative benthic flux sources from Antarctica's margins and seafloor coupled with an internal source via reversible scavenging notably from dissolution of biogenic opal are likely the primary drivers of this variance. *REF* captures the major basinal $[Nd]_d$ distributions in the Pacific, indicating good model skill in representing concentrations in this basin, albeit with a slight overestimation of the vertical gradient in the North Pacific.

Regarding model skill in representing regional ε_{Nd} distributions, simulated ε_{Nd} captures

the mean and bulk variance in the depth profiles of the Atlantic and the Southern Ocean, implying the boundary conditions and internal processes driving ε_{Nd} are being suitably represented here (Fig. 4.5c-d). Surface ε_{Nd} variability is not fully captured in the scheme, and a bias occurs in the North Atlantic, particularly in the Labrador Sea, whereby *REF* does not capture the distinct unradiogenic surface signal (measured ε_{Nd} is -18 compared to simulated values of -11). This potentially arises from the model underestimating the magnitude of surface Nd input, alongside the simplified prescription of ε_{Nd} from the dust and river boundary conditions, or may allude to missing processes, such as the preferential and elevated mobilisation of reactive unradiogenic sediment components driving localised marginal Nd sources. Noticeably, whilst *REF* captures the general depth profile and variance of ε_{Nd} in the Pacific, there is a distinct whole-profile offset, whereby simulated ε_{Nd} is much too unradiogenic (offset by 3 to 4 ε_{Nd}-units) compared to water column measurements, a feature common amongst sophisticated global Nd isotope enabled models (Jones et al., 2008; Arsouze et al., 2009; Rempfer et al., 2011; Gu et al., 2019; Pöppelmeier et al., 2020a). Specifically, we think that biases within the sediment boundary conditions and spatially-uniform fluxes are strong contenders for explaining a large part of the differences between measured and simulated Nd distributions, as they do not capture the regional reactive and radiogenic volcanic features present in the Pacific (Jones et al., 2008; Tachikawa et al., 2017). Future effort is therefore required to constrain such large basinal model-data mismatches if global Nd isotope models are to be used to help resolve instances of ε_{Nd} shifts in the palaeoceanographic records (e.g., Hu and Piotrowski 2018).

Distinct water mass ε_{Nd} properties are represented in *REF*, capturing important features of water mass structure in the Atlantic Ocean (as illustrated in the Atlantic stream function plot in Fig. 4.6a). For example, the vertical Atlantic ε_{Nd} cross-section at around 35° S co-varies with salinity and shows southward flowing NADW with ε_{Nd} of -11.2, underlain by northward flowing Antarctic Bottom Water (AABW) with ε_{Nd} of -10.8 (Fig. 4.6b), encompassing the canonical Atlantic zig-zag profiles of ε_{Nd} (Goldstein and Hemming, 2003). These distinct water mass tracer properties make *REF* a suitable simulation to explore the varying influences of northern and southern sourced water masses in the Atlantic, which is required to aid in palaeoceanographic reconstructions and their interpretation. However, simulated NADW is more radiogenic than indicated by water column measurements (where lower NADW ε_{Nd} is 12.4; Lambelet et al. 2016), suggesting that Nd source distributions for this water mass require further constraints. Moreover, ε_{Nd} is shifted to greater depths compared to corresponding salinity (Fig. 4.6b). This dissimilarity results from reversible scavenging processes, whereby adsorption and subsequent desorption of Nd with particle dissolution causes a non-conservative downward transport of ε_{Nd} (Rempfer et al., 2011; Pöppelmeier et al., 2022; Siddall et al., 2008b). Moreover, the benthic flux contributes a less radiogenic source to AABW along its northward bottom water flow path and causes a shift in ε_{Nd} signal towards values which are more similar to that of NADW. This vertical ε_{Nd} offset, which has also been directly observed in the modern South Atlantic (Wang et al., 2021), indicates that the rates of particle dissolution and scavenging efficiency are major vertical processes acting throughout the water column. Here, the concentration mixing dynamics (whereby vertical processes occurring in abyssal water masses with a high $[Nd]_d$ will have a weaker effect on ε_{Nd} than intermediate masses with a comparably low $[Nd]_d$) can help explain the 'Nd paradox' (Siddall et al., 2008b; Pöppelmeier et al., 2022).

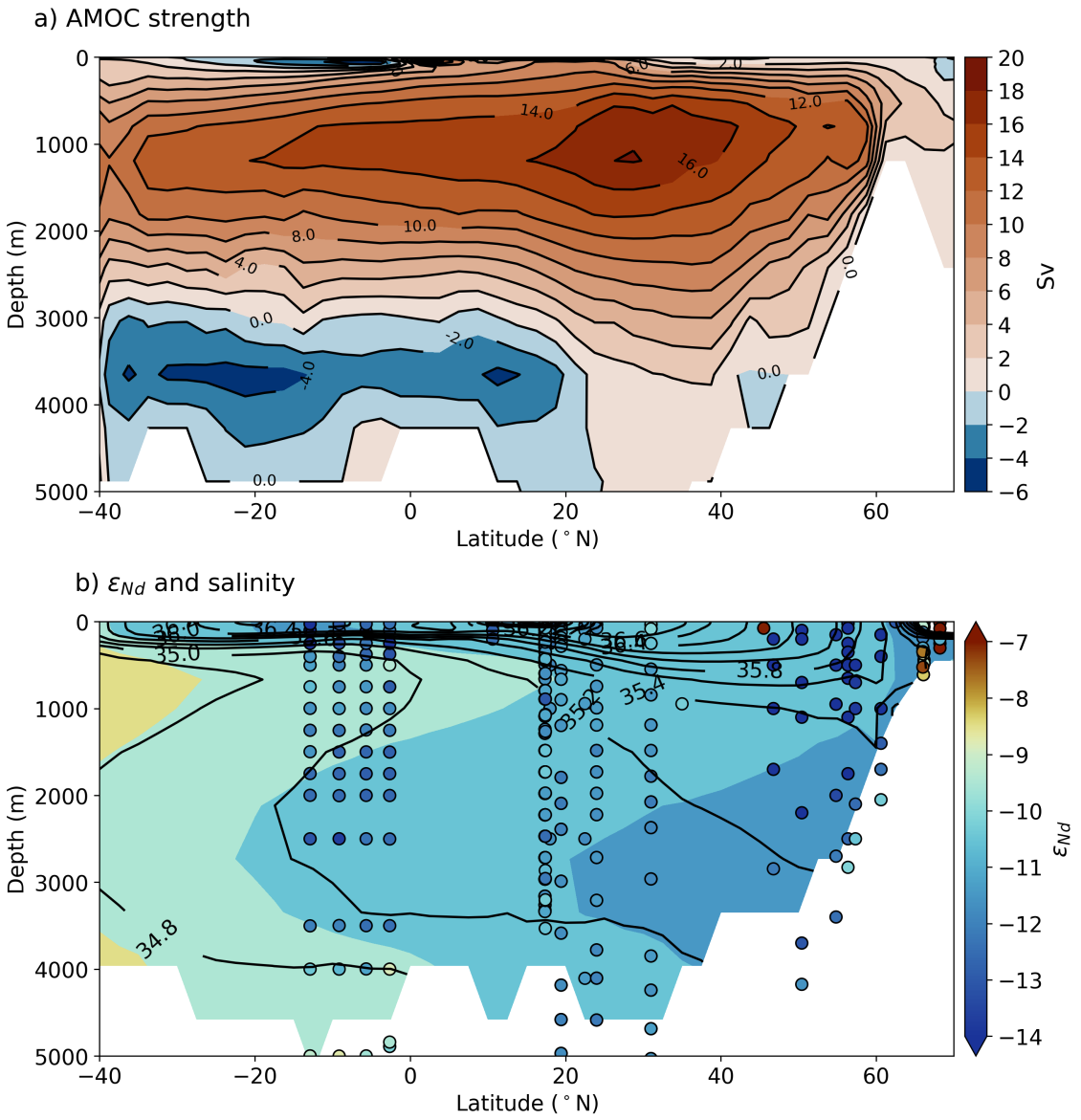

Figure 4.6: The conservative water mass tracer properties of ε_{Nd} in the optimised *REF* simulation in the Atlantic Ocean, as indicated by (a) zonally integrated Atlantic Ocean stream function (Sverdrup, Sv; where 1 Sv = $10^6 \mathrm{m}^3\ \mathrm{s}^{-1}$), (b) simulated ε_{Nd} (coloured) and salinity (contours) in a cross section of the Atlantic ($20 - 30°$ W), compared to water column measurements of ε_{Nd} (filled circles using the same colour scale).

Overall, we conclude that *REF* has skill in representing the global distributions and key features of both $[Nd]_d$ and ε_{Nd}, including the ε_{Nd} of distinct water masses in the Atlantic. Deviations in $[Nd]_d$ and ε_{Nd} from the observational data vary regionally, and can be typically attributed to the resolution of FAMOUS, alongside highlighting certain inconsistencies within the assumptions underlying the Nd inputs to seawater, which, due to the inherent elusive nature of marine Nd cycling, still remain preliminary approximations of complex sediment-seawater interactions. We suggest that future modelling and observational studies should focus on resolving upper ocean sources of Nd where the largest model-data disparity occurs, and further on improving the representation and spatial extent of labile seafloor ε_{Nd} interactions, including exploring in detail the regional differences in how seawater acquires a ε_{Nd} signal (i.e., the interplay of Nd additional versus advection time). The optimised parameters in *REF* allow for ease of future model improvements, which may include updating model ε_{Nd} source boundary conditions subject to increased

measurements and more quantitative process descriptions, alongside testing outstanding questions regarding marine Nd cycling and ocean circulation. Altogether, we argue that *REF* is a well-designed tool capable of improving the application of Nd isotopes as an ocean circulation tracer.

4.4 Sensitivity of optimised *REF* simulation to seafloor sediment ε_{Nd} distributions

To investigate the influence of varying regional reactive ε_{Nd} sources on simulated seawater Nd isotope distributions, caused by the potential preferential mobilisation of certain components of the sediment, we performed idealised sensitivity tests using our optimised *REF* simulation. We tested three different sediment maps (i.e., sediment boundary conditions shown in Fig. 4.7:a-c) in simulations *REF, REF-SED2 and REF-SED3*, representing the ε_{Nd} distributions of reactive sediment under a seafloor-wide benthic flux model of marine Nd cycling. The rationale for exploring a shift in sedimentary ε_{Nd} towards more extreme values is based upon evidence from a combination of laboratory analysis, seawater and porewater measurements, and modelling studies that demonstrate a substantial relabelling of water masses by a benthic source. These pieces of work suggest that the bulk ε_{Nd} of the sediment cannot always be assumed to represent the mobile sedimentary ε_{Nd} phase governing distributions of seawater ε_{Nd} (Abbott et al., 2015a; Wilson et al., 2013; Du et al., 2016; Lacan and Jeandel, 2005b; Jones et al., 2008; Pearce et al., 2013; Rousseau et al., 2015; Abbott et al., 2016a; Jeandel and Oelkers, 2015). Note, however, that our sensitivity analyses are designed to be quasi-idealised (i.e., simplified) end-member tests of some of the major assumptions implicit to paradigms pertaining to the mobility/exchangeability of seafloor Nd, as explained below, and are not meant to provide a redefined seafloor ε_{Nd} boundary condition for models. Like the optimisation simulations (Sect. 4.2.2), dissolved seawater Nd in all sensitivity studies is initialised from zero, and integrated for 6,000 years to enable the deep ocean and seawater Nd to reach steady state.

The first map of global ε_{Nd} distributions at the sediment-ocean interface (*REF*: Fig. 4.7a) represents the estimated bulk ε_{Nd} distributions of the continental margins and seafloor detrital material of Robinson et al. 2021 (see their Figure 4). The subsequent two maps (*REF-SED2*: Fig. 4.7b and *REF-SED3*: Fig. 4.7c) impose simplified modifications of increasing magnitude to the soluble ε_{Nd} from localised sediment regions in the Pacific (particularly across the eastern and western margins, where we cap the regional ε_{Nd} signal by imposing a minimum threshold; causing the sediment region to become more radiogenic), and in the Atlantic Ocean (particularly the Northwest Atlantic, where we cap the regional ε_{Nd} signal by imposing a maximum threshold; causing the sediment region to become less radiogenic); see Supplementary Table 4.6 and Text S4.1 for the specific definition and choice of the regional sediment ε_{Nd} thresholds. All other model parameterisations are from the optimised *REF* simulation and are the same amongst the sensitivity simulations. Thus, because the magnitude of Nd sources are fixed, $[Nd]_d$ does not vary between simulations and so here we focus our discussion on changes to seawater ε_{Nd} distributions.

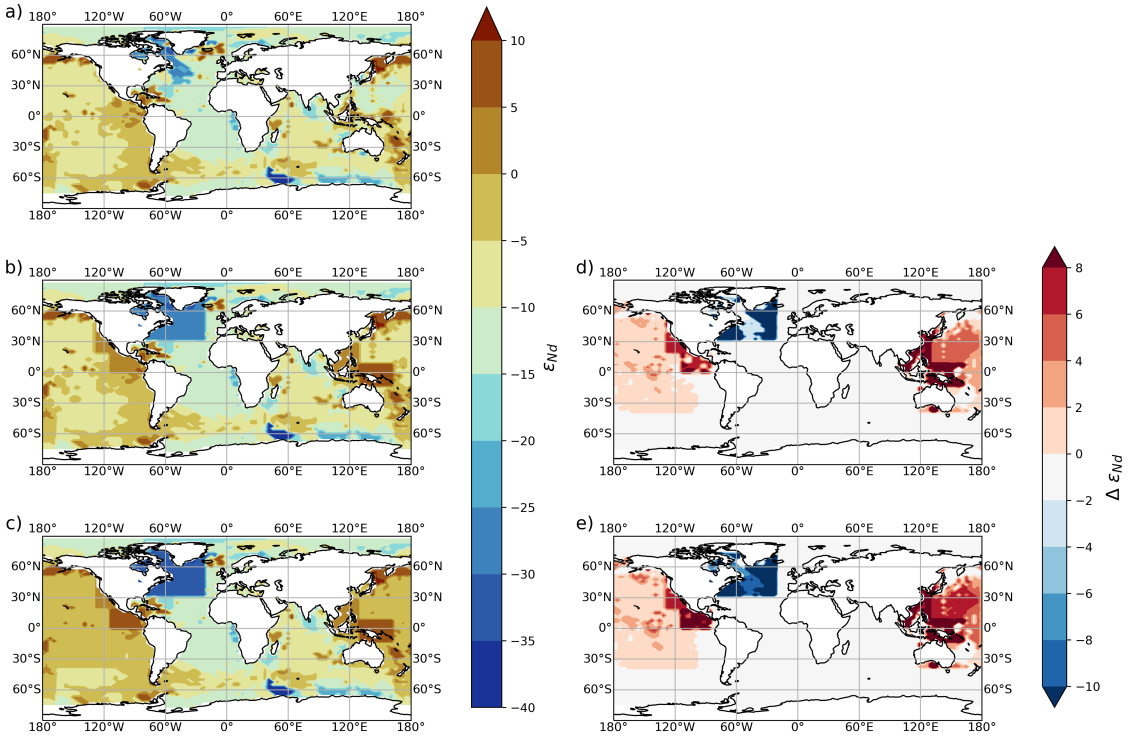

Figure 4.7: Global sediment ε_{Nd} distributions at the sediment-water interface used to represent the seafloor benthic flux under sensitivity studies testing (a; *REF*) the bulk sediment ε_{Nd} signal as presented in Figure 4; Robinson et al. (2021), and (b; *REF-SED2* and c; *REF-SED3*) representing two modified sediment ε_{Nd} maps of increasing magnitude to test the hypothesis that certain reactive sedimentary phases dominate sediment-seawater interactions. The difference between the modified ε_{Nd} maps and the bulk sediment map (a) are shown on the adjacent right-hand side plots (d-e), in ε_{Nd}-unit difference. See Fig. 4.13 for ε_{Nd} distributions on the FAMOUS GCM grid which are directly input as sediment boundary conditions in the Nd isotope scheme.

Modifying the ε_{Nd} distributions of the labile seafloor sediment influences the model's skill at representing modern measurements as indicated by the returned MAE ε_{Nd} cost functions ($J_{\varepsilon_{Nd}}$: Table 4.4), demonstrating that the heterogeneity of sediment reactivity and isotopic composition likely plays an important role in the oceanic cycling of Nd isotopes (Du et al., 2016; Wilson et al., 2013; Abbott et al., 2016a). Here, the global $J_{\varepsilon_{Nd}}$ is reduced from 2.37 ε_{Nd}-units in *REF* to 2.22 ε_{Nd}-units in *REF-SED3*. In other words, adjusting the seafloor ε_{Nd} to take account of the enhanced reactivity of particular sediment phases, which may have more extreme ε_{Nd} signatures than the bulk sediment, improves model skill; 73% of measurements in *REF-SED3* are simulated within 3 ε_{Nd}-units, compared to 67% in *REF*. As expected, varying the seafloor sediment distributions did not impact global model skill noticeably above 1,000 m, but improved skill at intermediate and deep depths below (Table 4.4). In more detail, the Pacific Ocean basin has a large $J_{\varepsilon_{Nd}}$ of 3.98 ε_{Nd}-units under bulk sediment boundary conditions (i.e., *REF*), which is improved under *REF-SED3* to 3.04 ε_{Nd}-units. In contrast, despite substantially more unradiogenic reactive sediment distributions applied in the North Atlantic compared to the bulk (with maximum ε_{Nd} values capped at -28 and -34 within the mobile sediment in *REF-SED2* and *REF-SED3* respectively, equating to localised differences of over -10 ε_{Nd}-units: Fig. 4.7d-e), model skill in representing Atlantic ε_{Nd} is relatively insensitive to these changed boundary conditions. Overall, we observe a slight decrease in Atlantic model skill, where $J_{\varepsilon_{Nd}}$ is 1.63 ε_{Nd}-units in *REF* and 1.84 ε_{Nd}-units in *REF-SED2* (Table 4.4). Furthermore, the $J_{\varepsilon_{Nd}}$ of the Southern Ocean is sensitive to changing sediment ε_{Nd} distributions in the

North Atlantic and Pacific basins, and model skill decreased under the more extreme sediment ε_{Nd} boundary conditions (where $J_{\varepsilon_{Nd}}$ is 0.52 and 1.12 ε_{Nd}-units in *REF* and *REF-SED3* respectively), whilst the Arctic and Indian Oceans are relatively insensitive. We delve into the reasons for such responses and explore spatial seawater ε_{Nd} distributions in more detail below.

Table 4.4: Overview of general model skill of the three sensitivity studies exploring labile seafloor sediment ε_{Nd} distributions. Displaying global and regional mean absolute error for ε_{Nd} (MAE:$J_{\varepsilon_{Nd}}$)

Simulation	$J_{\varepsilon_{Nd}}$ global (n=2,475)	% within 3 ε_{Nd}-units	$J_{\varepsilon_{Nd}}$ surface (0-200 m)	$J_{\varepsilon_{Nd}}$ shallow (200-1,000 m)	$J_{\varepsilon_{Nd}}$ mid-depth (1,000-3,000 m)	$J_{\varepsilon_{Nd}}$ deep (> 3,000 m)	$J_{\varepsilon_{Nd}}$ Atlantic	$J_{\varepsilon_{Nd}}$ Pacific	$J_{\varepsilon_{Nd}}$ Indian	$J_{\varepsilon_{Nd}}$ Southern Ocean	$J_{\varepsilon_{Nd}}$ Arctic
REF	2.37	67	2.68	2.26	2.32	1.68	1.63	3.98	2.88	0.52	1.82
REF-SED2	2.26	71	2.59	2.18	2.18	1.52	1.86	3.18	2.94	0.98	1.81
REF-SED3	2.22	73	2.58	2.16	2.09	1.43	1.84	3.04	2.94	1.12	1.80

What we learn from the performance of *REF-SED2 and REF-SED3* relative to *REF*, is that increasing the mobilisation of radiogenic sediment in the Pacific relative to the bulk drives Pacific seawater ε_{Nd} distributions towards more radiogenic values in slightly better agreement with measurements (Fig. 4.8). In the abyssal North Pacific, between *REF*, where seawater ε_{Nd} is -7.5, and *REF-SED3*, where seawater ε_{Nd} is -5.5, there is a change of +2 ε_{Nd}-units (see Supplementary Fig. 4.14). This is the largest shift in the magnitude of major water mass end member ε_{Nd} within all of the sensitivity simulations. The rest of the interior of the Pacific undergoes more modest changes of +1 to +2 ε_{Nd}-units, resulting from lateral and diapycnal mixing of the benthic flux signal throughout the water column. The results here broadly support the notion that preferential mobilisation of certain more reactive and more radiogenic phases (e.g., volcanic ash) within detrital sediment occurs during early diagenesis (Du et al., 2016; Abbott et al., 2015b,a, 2016a; Wilson et al., 2013). This labile Nd source, which is more radiogenic than the bulk ε_{Nd}, interacts with deep waters via a benthic flux and is necessary to explain in part the observed radiogenic change in Pacific deep water ε_{Nd} along its sluggish northward flow path in the absence of deep-water formation (Haley et al., 2017).

However, even under the considerably radiogenic Pacific sediment forcing applied in *REF-SED3* (where minimum labile seafloor sediment ε_{Nd} values are regionally capped at +8 and +10 across the western and eastern equatorial Pacific respectively; Fig. 4.7c), the general Pacific ε_{Nd} signal of -6 (Fig. 4.8c) is still too unradiogenic compared to average water column measurements of -4 ε_{Nd} in the North Pacific (Amakawa et al., 2009; Fuhr et al., 2021; Behrens et al., 2018; Fröllje et al., 2016), and especially in the upper 2,000 m (where seawater ε_{Nd} measurements are -2.5). This implies a missing or misrepresented highly radiogenic Nd source, possibly capturing strong local particle-seawater exchange occurring in the upper and intermediate ocean. This finding is supported by suggestions of highly localised non-conservative Pacific ε_{Nd} behaviour at depths between 0 and 1,500 m and within 1,000 km of coasts, including radiogenic offsets from conservative mixing in intermediate waters close to Hawaii, along the eastern coast of Japan, and margins along the eastern equatorial Pacific (Tachikawa et al., 2017). Our results imply that these marginal volcanic sediment sources, close to continental inputs with high detrital and biogenic particle concentrations (that drive strong particle-seawater interactions), may govern marine ε_{Nd} distributions in the North Pacific. As such, these shallower and marginal regions may pose a larger in magnitude and more distinct Nd source to seawater as opposed to an open-ocean abyssal benthic source; increased measurements at these locations therefore would greatly improve our understanding of this re-labelling.

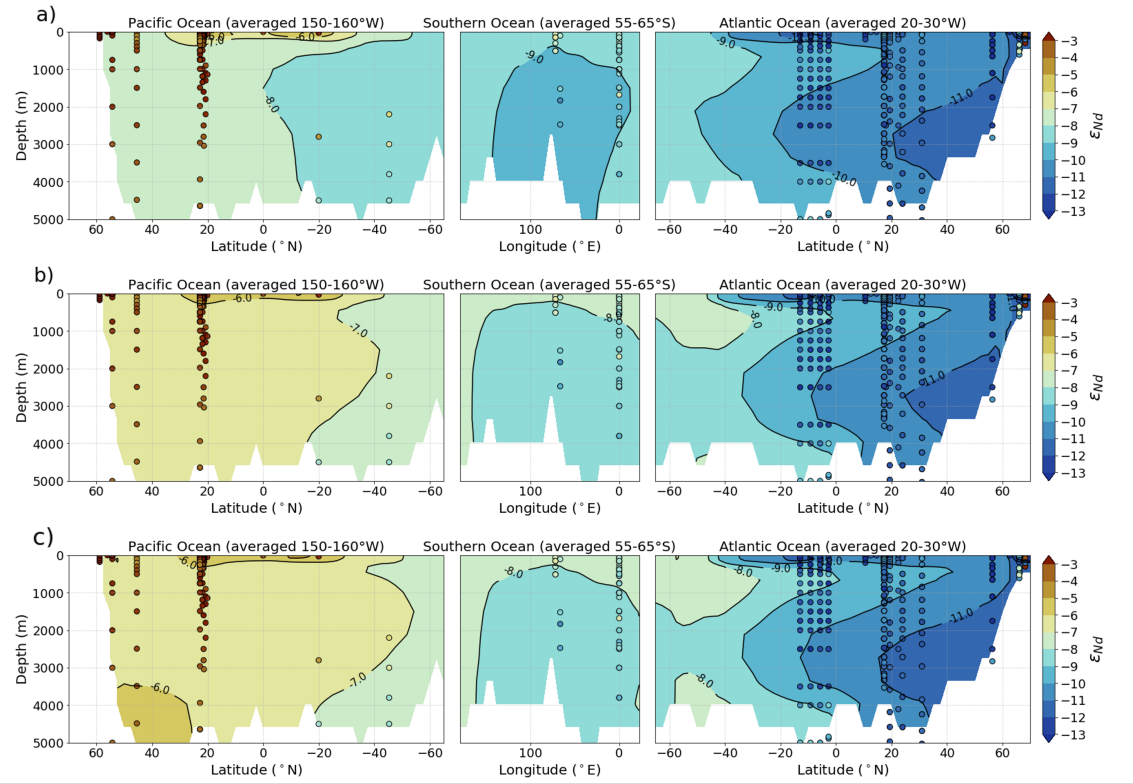

Figure 4.8: Vertical sections of simulated ε_{Nd} within three seafloor sediment ε_{Nd} sensitivity studies (a) *REF*, (b) *REF-SED2*, and (c) *REF-SED3* along a transect from the Pacific to Atlantic, traversing the Southern Ocean from West to East. Water column measurements are imposed as filled circles using the same colour scale. Simulated and measured ε_{Nd} from the Pacific are from $150 - 160°$ W, in the Southern Ocean are from $55 - 65°$ S, and in the Atlantic values are from $20 - 30°$ W.

On the other hand, the more unradiogenic reactive North Atlantic sediment ε_{Nd} distributions imposed in *REF-SED2* and *REF-SED3* (relative to the bulk sediment reconstruction used in *REF*) produces only slightly less radiogenic ε_{Nd} that are highly localised to the abyssal northern North Atlantic, with a change of -0.4 ε_{Nd}-units between *REF* and *REF-SED3* (Fig. 4.8 and Fig. 4.14). The remaining Atlantic areas bathed in NADW experience a small adjustment towards more radiogenic values, a response to the radiogenic Nd sourced in the Pacific propagating into the Atlantic. Here simulated ε_{Nd} range between -11 to -10, resulting from a shift of +0.2 to +0.8 ε_{Nd}-units in NADW in *REF-SED2* and *REF-SED3* respectively when compared with *REF*. It may be that the less radiogenic sediment ε_{Nd} forcing in the North Atlantic is required to counter the more radiogenic southern-sourced water, and without such a source, the entire Atlantic could shift to more radiogenic values; future simulations exploring the response of seawater ε_{Nd} to only the Pacific (or the Atlantic) sediment adjustments would be best suited to explore this. However, this localised and minor shift of ε_{Nd} under less radiogenic seafloor benthic fluxes in the North Atlantic (in *REF-SED2* and *REF-SED3*) implies a weak sensitivity of NADW ε_{Nd} to forcing from a localised abyssal benthic flux, where the somewhat positive response is governed by northward mixing from more radiogenic waters from the Southern Ocean. We thus find evidence that these bottom-water sediment regions are not important for governing Atlantic ε_{Nd}, likely because vigorous advection across the seafloor inhibits the exposure time of seawater to relabelling by a benthic flux. Therefore, most of the modern Atlantic ε_{Nd} signal is pre-formed. Further model experiments with sluggish Atlantic circulation could verify this, but we postulate that Atlantic seawater ε_{Nd} experiences an overriding influence from distinct and reactive unradiogenic surface and marginal Nd

inputs, around key regions of deep-water formation, such as in the Labrador Sea. This likelihood is brought to the fore by *REF-SED3*, where NADW remains too radiogenic despite a large unradiogenic forcing applied across the seafloor, indicating here the benthic flux signal does not act to relabel seawater ε_{Nd} markedly along its flow path, and so does not exert a strong control on water column ε_{Nd} distributions (Fig. 4.8c). Thus, it follows that accurate quantification of the mobile abyssal seafloor sedimentary phases may be of secondary importance in the modern North Atlantic. Instead, we suggest that future studies should be focussed on resolving upper-intermediate Atlantic Ocean Nd source isotope distributions (e.g., the magnitude and interactions from river sourced particulate material, alongside quantifying the fluxes from areas of intense boundary exchange occurring via sediment-seawater interactions with freshly eroded material near the margins). Nonetheless, the impact of a benthic flux on North Atlantic seawater ε_{Nd} distributions may be different under changed circulation regimes in the Atlantic, which thus require future explorations.

Finally, in the Southern Ocean, where the Antarctic Circumpolar Current (ACC) vigorously merges the waters from the Atlantic, Pacific and Indian Oceans, seawater ε_{Nd} experiences a shift to more radiogenic values under the modified sediment simulations (Fig. 4.8). Here, the general Southern Ocean ε_{Nd} signal increases from -9 in *REF* to -8.2 in *REF-SED2*, and to -8 in *REF-SED3*. The larger spatial extent of the labile sediment modifications in the Pacific compared to the Atlantic (Fig. 4.7), coupled with the higher-amplitude absolute response of Pacific seawater ε_{Nd} in the sensitivity simulations drives this radiogenic shift in the ε_{Nd} in the Southern Ocean. Consequently, the endmember ε_{Nd} of Antarctic Intermediate Water (AAIW) and AABW protruding into the South Atlantic (Fig. 4.8) is most radiogenic in *REF-SED3*, amplifying the distinctions between AAIW, NADW and AABW, and enhancing the South Atlantic zig-zag profiles (Goldstein and Hemming, 2003).

Overall, we consider *REF-SED3* – a simulation with optimised parameters (i.e., *REF*; Sect. 4.3.2) and an updated sedimentary boundary condition (Fig. 4.7c), which form a preliminary first-order coarse-scale representation of large scale labile sedimentary phases – to have the highest model skill within the sensitivity studies in capturing $[Nd]_d$ and ε_{Nd} distributions (Fig. 4.9). This simulation is capable of representing with good fidelity the spatial distributions of modern seawater Nd measurements and supports the preferential mobilisation of reactive radiogenic volcanic sedimentary components in the Pacific relative to the bulk ε_{Nd} under a seafloor-wide benthic-flux driven model of marine Nd cycling. Yet simulated Pacific ε_{Nd} in *REF-SED3* overall remain too unradiogenic. Future work could therefore explore the possibility of more spatially heterogeneous and isotopically unique benthic fluxes. For example, whereby volcanic material, which is more soluble than well crystalised detrital fractions, may favour elevated benthic fluxes with substantial radiogenic Nd release.

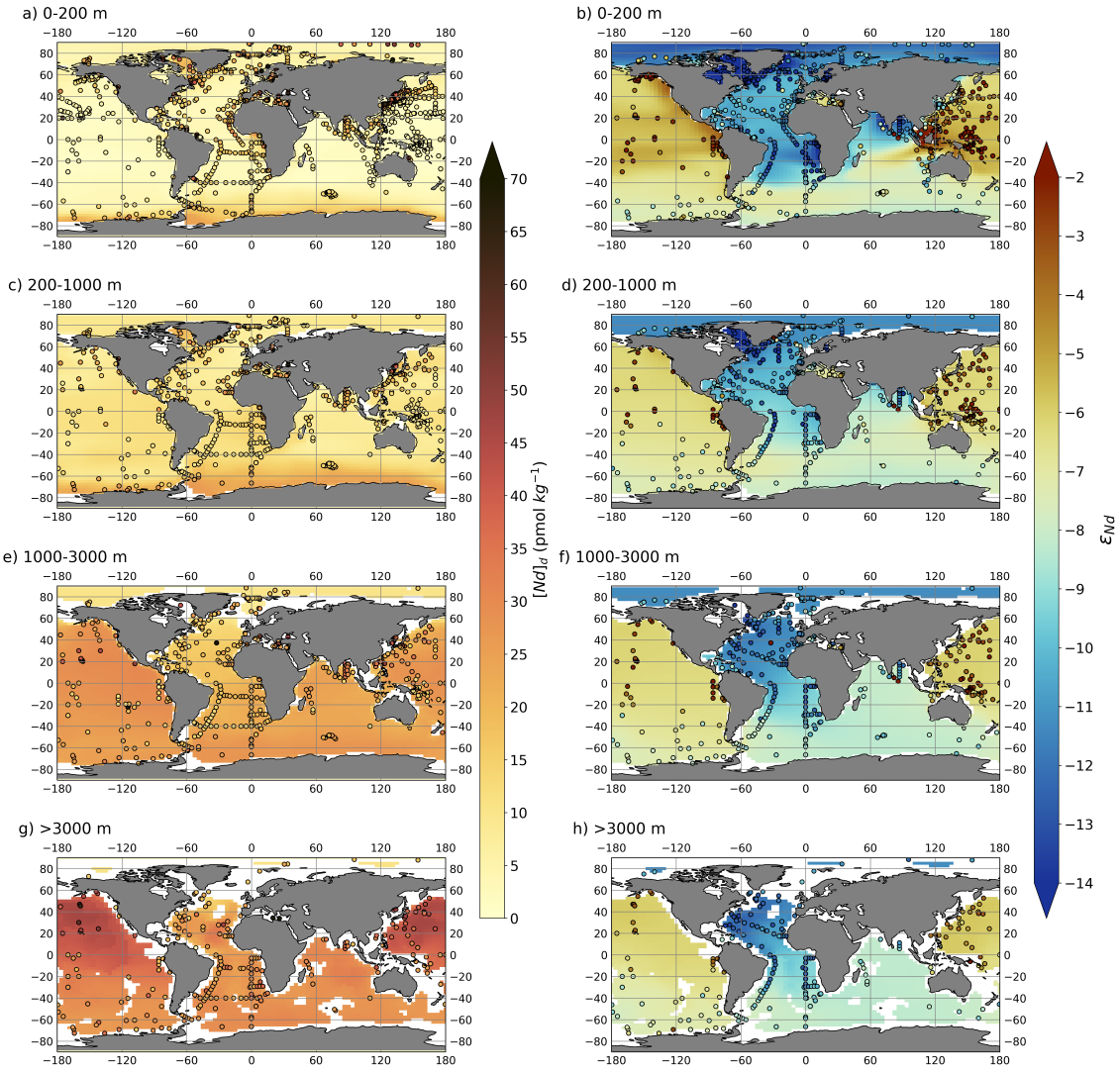

Figure 4.9: Global volume-weighted distributions of $[Nd]_d$ (left) and ε_{Nd} (right) in the optimised simulation *REF-SED3* split into four different depth bins, (a-b) shallow (0-200 m), (c-d) intermediate (200-1,000 m), (e-f) deep (1,000-3,000 m), and (g-h) deep abyssal ocean (>3,000 m). Water column measurements from within each depth bin (Osborne et al., 2017, 2015; GEOTRACES Intermediate Data Product Group, 2021) are superimposed as filled circles using the same colour scale.

4.5 Sensitivity of seawater ε_{Nd} to a margin constrained versus a seafloor-wide benthic flux

In order to further explore the sensitivity of seawater ε_{Nd} distributions to non-conservative seafloor fluxes, we investigated the difference in simulated marine Nd isotope distributions between a continental margin constrained versus a seafloor-wide benthic flux whilst all other parameters were kept constant. At present, it remains undetermined, and even disputed, whether the chemical transfer of Nd between terrestrial derived particles and seawater occurs predominantly across continental margins (proximal to large inputs of distinct and compositionally less mature lithogenic sediment, high eddy kinetic energy, and high detrital and biogenic particle concentrations promoting rapid exchange reactions: Lacan and Jeandel 2005b; Jeandel and Oelkers 2015; Tachikawa et al. 2003; Jeandel 2016; Rousseau et al. 2015), or across the abyssal seafloor (with high particle reactivities and long term benthic flux exposures of fine-grained sediment ubiquitously spread throughout

the global ocean: Abbott et al. 2015b, 2019; Du et al. 2016; Abbott et al. 2019). Hence, we performed a final simulation, using the optimised parameters and updated mobile sediment ε_{Nd} boundary conditions from *REF-SED3* (Sect. 4.4), but with the sediment source constrained specifically to the continental margins (where sediment thickness $\geq$ 1,000 m, following the continental margin definition by Robinson et al. (2021), we call this simulation *REF-SED3-MG*. See Fig. 4.17 for the gridded ε_{Nd} sedimentary distributions of the margin-only flux. In this simulation, f_{sed} is redistributed to the margins proportional to the surface area, where the constant sediment flux across the margins is 30.75 pmol cm^2 yr^{-1} (compared to a flux of 2.96 pmol cm^2 yr^{-1} when the flux is integrated across the entire ocean floor). As such, $[Nd]_d$ is generally more concentrated above 3,000 m depth and in the Atlantic and Southern Ocean compared to distributions under a seafloor-wide benthic flux (see Fig. 4.18 for the difference in $[Nd]_d$ between the simulations); note here the following discussion is focussed on exploring Nd isotope distributions and does not explore these differences to $[Nd]_d$ in further detail.

Overall, there is a marked difference in the response of seawater ε_{Nd} distributions between the Atlantic and Pacific basins under simulations with a seafloor-wide (*REF-SED3*) and a margin-only (*REF-SED3-MG*) marine sediment flux (Fig. 4.10). In the North Pacific, a benthic flux across the entire seafloor results in a more radiogenic seawater ε_{Nd} signal of -6, which sits closer to seawater measurements of -4 (Amakawa et al., 2009; Fuhr et al., 2021; Behrens et al., 2018; Fröllje et al., 2016) compared to when the sediment Nd source is only constrained to the margins (where seawater ε_{Nd} is -8.5). The largest response of seawater ε_{Nd} occurs in the abyssal North Pacific (Fig. 4.10 and Fig. 4.21), and herby reiterates the importance of a benthic flux in governing seawater ε_{Nd} within the North Pacific, characterised by long-term exposure of bottom waters, with long water residence times, to a radiogenic Nd flux from fine-grained sediment of volcanic origin (Abbott et al., 2015a,b; Du et al., 2016; Abbott et al., 2016a; Haley et al., 2017; Behrens et al., 2018). Moreover, under the margin-only simulation (*REF-SED3-MG*), the missing benthic Nd source and lack of radiogenic input into the Pacific results in the Southern Ocean ε_{Nd} signal, which is determined in part by mixing of these Pacific waters, becoming too unradiogenic (where simulated ε_{Nd} is -10: Fig. 4.10b) compared to measurements (where ε_{Nd} is -8.5: Stichel et al. (2012); Lambelet et al. (2018).

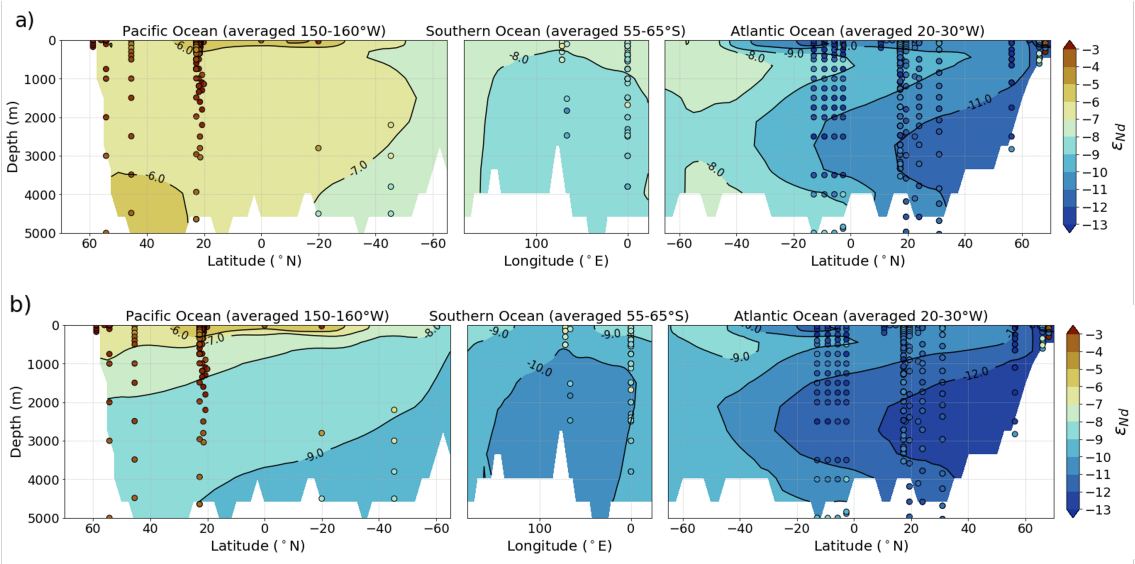

Figure 4.10: Vertical sections of simulated ε_{Nd} within sensitivity studies (a) *REF-SED3* with a seafloor-wide benthic flux and (b) *REF-SED3-MG* with a margin-only constrained benthic flux along a transect from the Pacific to Atlantic, traversing the Southern Ocean from West to East. Water column measurements are imposed as filled circles using the same colour scale. Simulated and measured ε_{Nd} from the Pacific are from $150 - 160°$ W, in the Southern Ocean are from $55 - 65°$ S, and in the Atlantic values are from $20 - 30°$ W. The continental margins are constrained following the definition by Robinson et al. (2021), where sediment thickness $\geq$ 1,000 m.

In contrast, the North Atlantic, characterised by high modern ventilation rates, displays a limited expression of non-conservative behaviour from seafloor benthic fluxes (Fig. 4.10). Here, a margin-only constrained benthic flux improves model-data fit, resulting in a more unradiogenic NADW ε_{Nd} signal of -13, which is in excellent agreement with measurements for this water mass of -13.2 (Lambelet et al., 2016), compared with -11 simulated under a seafloor-wide benthic flux. Resolving the ε_{Nd} signal of modern NADW therefore primarily resides within disentangling the highly reactive and isotopically unique surface and marginal Nd fluxes (i.e., intense localised regions of boundary exchange), especially around the locations of deep-water formation, including unradiogenic inputs originating from the Canadian Shield (where ε_{Nd} is -28), to localised radiogenic inputs from Icelandic basaltic rocks (where ε_{Nd} is +7) (Blaser et al., 2019a; Stichel et al., 2020; Morrison et al., 2019; Lacan and Jeandel, 2005a; Lambelet et al., 2016). Furthermore, mixing of the less radiogenic southern-sourced water in the Atlantic likely also contributes to the more unradiogenic signal of NADW under a margin-only constrained benthic flux.

To summarise, the ε_{Nd} signal of modern bottom waters within the Pacific Ocean are sensitive to abyssal benthic flux alterations, whilst bottom water in the North Atlantic displays a much weaker response. Our results demonstrate the importance of setting apart the interlinked roles of major sediment Nd sources (their ε_{Nd} composition, spatial extent, and reactivity), from physical ocean circulation structure (provenance of water masses and sites of convection, water ventilation rates and residence time). It would therefore be beneficial for future work to focus on further disentangling regional environmental conditions and how they may influence non-conservative marine Nd isotope behaviour (e.g., constraining pore water redox conditions, productivity, oxygenation, and pH, and how those conditions may drive benthic Nd fluxes). Moreover future work could explore the response of seawater ε_{Nd} distributions to different definitions of the continental margin extent (e.g., where sediment thickness $\geq$ 500 m; Robinson et al. (2021)).

Henceforward, the sensitivity simulations presented here provide a foundation for future work with the Nd isotope scheme in the FAMOUS GCM to further investigate and attempt to identify the environmental qualities and spatial regions of seafloor sediment that likely result in mobilised benthic fluxes within regions that dominate seawater ε_{Nd} distributions over water mass mixing in the deep ocean. This would largely benefit from increased direct measurements of pore water Nd concentration and isotopic composition alongside a greater understanding of the diagenetic Nd cycle and the role of reversible scavenging processes. Combined with such 'observations', the modelling framework presented here would allow for the crucial disentangling of non-conservative processes involved in governing distributions of marine ε_{Nd}. Based on our results, we contend that the existence of such limitations in our knowledge is perhaps overconfidently dismissed in the application of marine Nd isotopes as an ocean circulation and continental weathering tracer.

Finally, we do wish to highlight that our results in Sect. 4.4 and 4.5 only look at the influence of mobilised seafloor ε_{Nd} distributions on seawater ε_{Nd} and do not attempt to explore how varying these fluxes may overprint the signal of marine archives. Furthermore, we do not assess the sensitivity of seawater ε_{Nd} distributions to modified benthic fluxes under different circulation regimes (i.e., under a weakened AMOC or an enhanced PMOC). These constitute logical next steps in marine Nd isotope modelling.

4.6 Summary and Conclusions

In this study, we extended the implementation of Nd isotopes (^{143}Nd and ^{144}Nd) in the ocean component of the FAMOUS GCM by statistically optimising the selected combination of model parameter values to produce a tuned reference simulation for future investigative work with the scheme. Within our experimental design we found that the reversible scavenging, benthic flux magnitude and riverine source scaling all governed the variability in simulated total Nd inventory. The reversible scavenging efficiency dominated the variation in the residence time, as well as in model skill at simulating $[Nd]_d$ and ε_{Nd} consistent with water column measurements. The magnitude of the benthic flux and riverine source scaling influence model $[Nd]_d$ variability under low scavenging efficiencies.

In line with previous studies, the global Nd inventory in *REF* is 4.27×10^{12} g, owing to a global mean residence time of 727 years. Of the total Nd source to the ocean, 64% is apportioned to the seafloor benthic flux, 30% to riverine sources, and 6% to aeolian dust deposition. Our reference simulation captures the main features of the modern marine Nd cycle, although the ε_{Nd} signature of the Pacific is 3 to 4 ε_{Nd}-units too unradiogenic compared to seawater measurements, alluding to incongruent dissolution of the bulk sediment and a likely favouring of interactions from radiogenic volcanic components of the seafloor sediment that may constitute spatially elevated benthic fluxes.

Model-data inconsistencies in some instances relate to the low resolution of FAMOUS preventing full resolution of surface point sources, which are highly variable in nature. Importantly, though, these inconsistencies disclose aspects of the global marine Nd cycle to focus further detailed investigation. For example, including a better quantification of the modes and rates of scavenging, an improved understanding of Nd desorption, additional exploration of river particulates as a major global Nd source to seawater, and the need for spatial constraints on the isotopic signature and rates of a benthic flux; specifically, strong localised effects and the physical/environmental conditions driving elevated fluxes. The optimised simulation therefore forms a well-developed scheme designed to answer specific outstanding questions regarding the marine Nd cycle.

We performed idealised sensitivity studies using our optimised scheme to test three different mobile seafloor sediment ε_{Nd} distributions, investigating regions in the Atlantic and Pacific where more extreme and highly reactive sediment ε_{Nd} phases (relative to the bulk) may be preferentially contributing ε_{Nd} to the pore water and thus seawater via early

diagenetic processes. This in part attempts to broadly elucidate to a first order what the dominant labile ε_{Nd} signals of the sediment (effective sedimentary Nd release) are under a seafloor-wide benthic flux driven model of marine Nd cycling, paving the way towards a more mechanistic global model of the sedimentary Nd budget to seawater. Model skill for ε_{Nd} improved globally under a seafloor Nd source that regionally enhanced reactive sediment phases; for example, preferential mobilisation of highly radiogenic volcanic components of detrital sediment in the equatorial Pacific can partially explain the radiogenic change in Pacific deep water along its sluggish northward flow path. However, model-data offsets in intermediate layers of the Pacific demonstrate that localised marginal volcanic sediment sources likely pose a larger and more distinct Nd source, as opposed to abyssal seafloor sediment. The weak sensitivity of NADW to localised highly unradiogenic detrital sources where water mass mixing governs deep seawater ε_{Nd} distributions, suggests that an abyssal benthic flux is of secondary importance in determining the modern deep Atlantic ε_{Nd}. Seawater here is more likely influenced by the larger and more distinct reactive unradiogenic surface and marginal Nd sources in proximity to regions of direct continental weathering around key convection sites. In a final sensitivity experiment exploring the response of seawater ε_{Nd} to a continental margin constrained versus a seafloor-wide benthic flux, we demonstrate that modern bottom waters within the Pacific Ocean are sensitive to non-conservative alterations resulting from an abyssal benthic flux, whilst the North Atlantic displays a limited expression of such effects.

Fundamentally this study demonstrates that despite over a decade of increasing efforts to constrain and describe the global marine Nd cycle within complex sophisticated global models, a global framework is limited. Poor quantifications of non-conservative sediment-water interactions limits the capability of global models to fully resolve end member ε_{Nd} signals, with model-data offsets sometimes larger than the ε_{Nd} shifts observed in the palaeoceanographic records. Such errors limit the capability of global Nd isotope models to precisely resolve what climatic or oceanographic conditions may be driving such deviations in seawater ε_{Nd}, particularly in untangling complex processes during periods when global weathering regimes and/or ocean circulation convection rates are largely unconstrained. Moreover, it is becoming increasingly transparent that there are distinct regional differences in how modern seawater acquires its ε_{Nd} signal, in part relating to the interplay of Nd addition and water advection rates. Moving forwards, regional models, that can better encompass measured seawater Nd profiles, and provide more complex spatiotemporal representations of Nd source/sink distributions, may be better positioned to reconcile the marine Nd cycle and for palaeoceanographic applications.

In closing, this study illustrates that although a benthic flux is an important Nd source to seawater, and that it can describe key features of the modern marine Nd cycle, perhaps too much emphasis has recently been placed upon exclusively resolving non-conservative interactions of an abyssal deep seafloor flux to solve the Nd paradox. We recommend future studies to continue to explore marine Nd cycling in a holistic way, advancing constraints on the processes, characteristics, and spatial variability of all major sediment-water interactions. This should include a particular focus on those processes influencing seawater ε_{Nd} at intermediate depths, with the purpose of reliably predicting localised non-conservative effects and highlighting where they dominate seawater ε_{Nd} distributions in the deep ocean. Within such a framework, and under the recent ever-increasing momentum of studies seeking to resolve the marine Nd cycle, we can edge closer to unlocking the full potential of Nd isotopes as an oceanographic and climatic tracer.

4.7 Supplementary Information

The base code for FAMOUS is protected under UK Crown Copyright and can be obtained from National Centre for Atmospheric Science (NCAS) Computational Modelling Services

(CMS): `http://cms.ncas.ac.uk/wiki/UmFamous`. The code detailing the Nd isotope scheme in FAMOUS presented in Chapter 3 of this thesis is available from the Research Data Leeds Repository (`https://doi.org/10.5518/1136`). These files are known as code modification (i.e., 'mod') files and should be applied to the original base code for the model. All the additional (i.e., historical) modification files that are required on top of the base code to run the simulations described in this chapter are available in Appendix A. The files and corresponding information that need to be applied to setup the different simulations presented in this chapter are available from the Research Data Leeds Repository (`https://doi.org/10.5518/1181`).

Reference simulations from the Nd isotope scheme optimisation

- XPIAB *reference ('REF') simulation* (0-6,000 years)
- XPIAD *Nd concentration reference ('REF_CONC1') simulation* (0-6,000 years)
- XPHJF *Nd concentration reference; best performing from parameter analysis ('REF_CONC2') simulation* (0-6,000 years)
- XPIAC *Nd isotope reference ('REF_IC') simulation* (0-6,000 years)

Seafloor sediment Nd isotope distribution sensitivity simulations

- XPIAG *reference ('REF-SED2') simulation* (0-6,000 years)
- XPIAH *reference ('REF-SED3') simulation* (0-6,000 years)

Continental margin constrained benthic flux sensitivity simulation

- XPIAQ *reference ('REF-SED3-MG') simulation* (0-6,000 years)

Table 4.5: Model parameter values for *REF*, abbreviations, and units. Note that only the f_{sed}, $[Nd]_p/[Nd]_d$, and α_{river} parameter values were varied directly in the parameter space exploration and model performance optimisation ensemble (as detailed in Sect. 4.2.2, main text).

Variable	Symbol	Optimised parameter values	Unit
Total Nd concentration	$[Nd]_t$	-	pmol kg^{-1}
Dissolved Nd	$[Nd]_d$	-	pmol kg^{-1}
Particle-associated	$[Nd]_p$	-	pmol kg^{-1}
Nd source, total	f_{total}	5.9×10^9	g Nd yr^{-1}
Nd source, density	S_{total}	-	g Nd $m^{-3}yr^{-1}$
Dust source, total	f_{dust}	3.3×10^8	g Nd yr^{-1}
Dust source, density	S_{dust}	-	g Nd $m^{-3}yr^{-1}$
Flux of dust	F_{dust}	Hopcroft and Valdes (2015)	g $m^{-2}yr^{-1}$
Nd-concentration dust	C_{dust}	20	μg g^{-1}
Nd-release dust	β_{dust}	0.02	
Riverine source, total	f_{river}	1.8×10^9	g Nd yr^{-1}
Riverine source, density	S_{river}		g $m^{-2}yr^{-1}$
River discharge	RIVER	-	g $m^{-2}yr^{-1}$
Riverine scaling factor	α_{river}	4	
Nd concentration river	C_{river}	-	μg g^{-1}
Nd removal, estuaries	γ_{river}	0.7	
Sediment source, total	f_{sed}	3.8×10^9	g Nd yr^{-1}
Sediment source, density	S_{sed}	-	g Nd $m^{-3}yr^{-1}$
Total sediment surface	A_{total}	-	m^2
Gridbox sediment surface	$A(i,k)$	-	m^2
Gridbox volume	$V(i,k)$	-	m^3
Thickness of euphotic layter	z_{eu}	81	m
Penetration depth of opal	l_{opal}	10,000	m
Penetration depth of $CaCO_3$	$l_{calcite}$	3,500	m
Particle settling velocity	ω	1,000	m yr^{-1}
Ratio $[Nd]_p$ to $[Nd]_d$	$[Nd]_p/[Nd]_d$	0.00448	
Global average density of seawater	p	1,024.5	kg m^{-3}
Reversible scavenging, density	S_{rs}	-	g Nd $m^{-3}yr^{-1}$
Partition coefficient for POC	K_{POC}	1.53×10^6	
Partition coefficient for $CaCO_3$	K_{CaCO_3}	7.14×10^5	
Partition coefficient for opal	K_{opal}	8.6×10^5	
Partition coefficient for dust	K_{dust}	2.59×10^6	
Total Nd inventory after equilibrium	$Nd(I)$	4.27×10^{12}	g
Residence time	τ_{Nd}	727	years

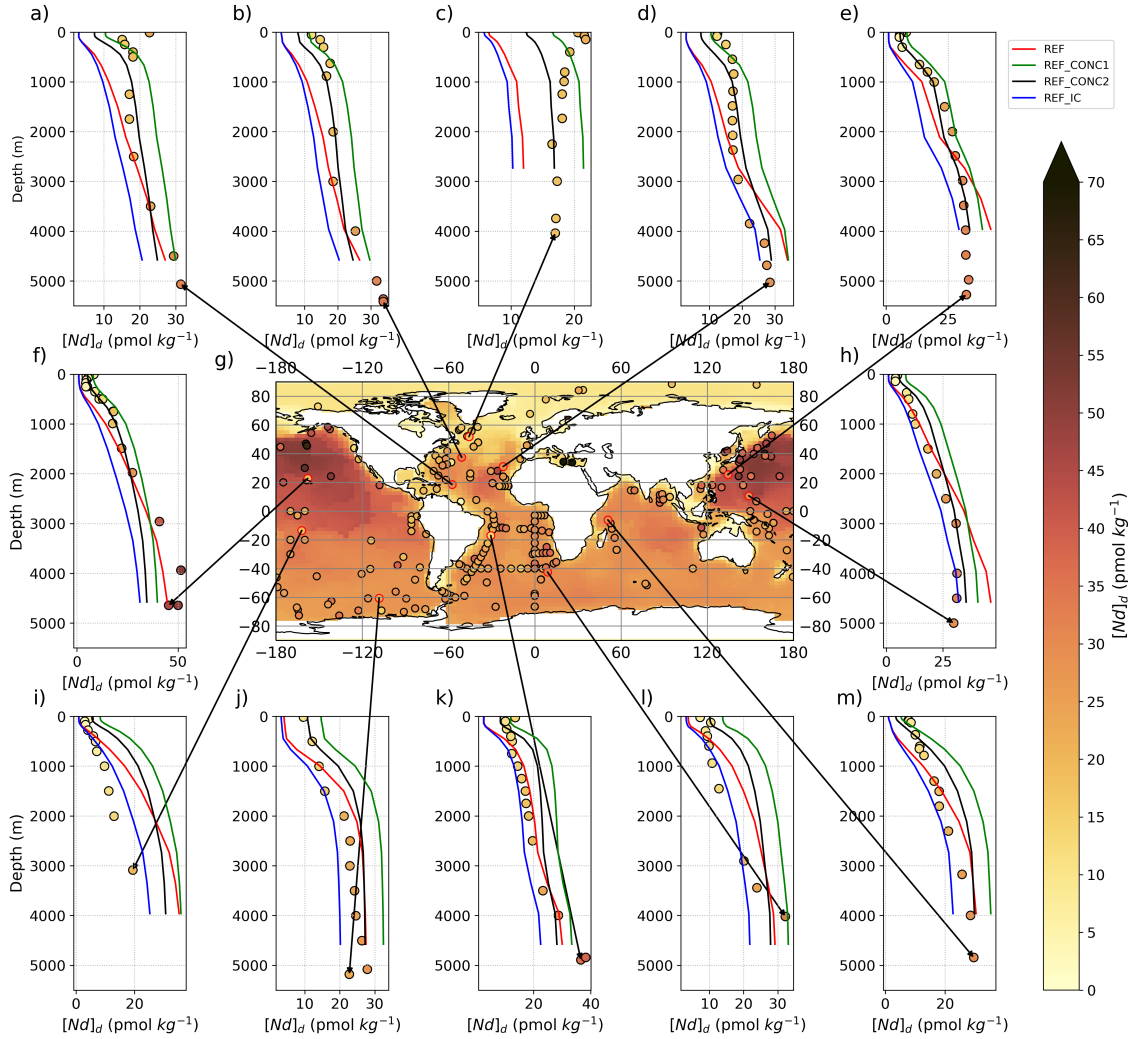

Figure 4.11: Central panel (g) displays $[Nd]_d$ at the seafloor for the final, optimised model configuration, *REF* (100-year mean from the end of the simulation), with superimposed water column measurements (Osborne et al., 2017, 2015; GEOTRACES Intermediate Data Product Group, 2021) from $\geq$ 3,000 m shown by filled coloured circles. Surrounding panels (a-f) and (h-m) display depth profiles of simulated (coloured lines: *REF* in red, *REF_CONC1* in green, *REF_CONC2* in black, and *REF_IC* in blue) and measured (filled circles) $[Nd]_d$; see Sect. 4.2.2 of the main text for a full description of the optimised model configurations. Note that simulated $[Nd]_d$ in *REF* is consistently too low in much of the shallow-intermediate Atlantic (Sect. 4.3.2, main text), alluding to the model not capturing localised surface point sources here, but otherwise there is broadly very good agreement between simulated and measured $[Nd]_d$, indicating that the model captures the major sources, sinks and internal cycling governing marine $[Nd]_d$.

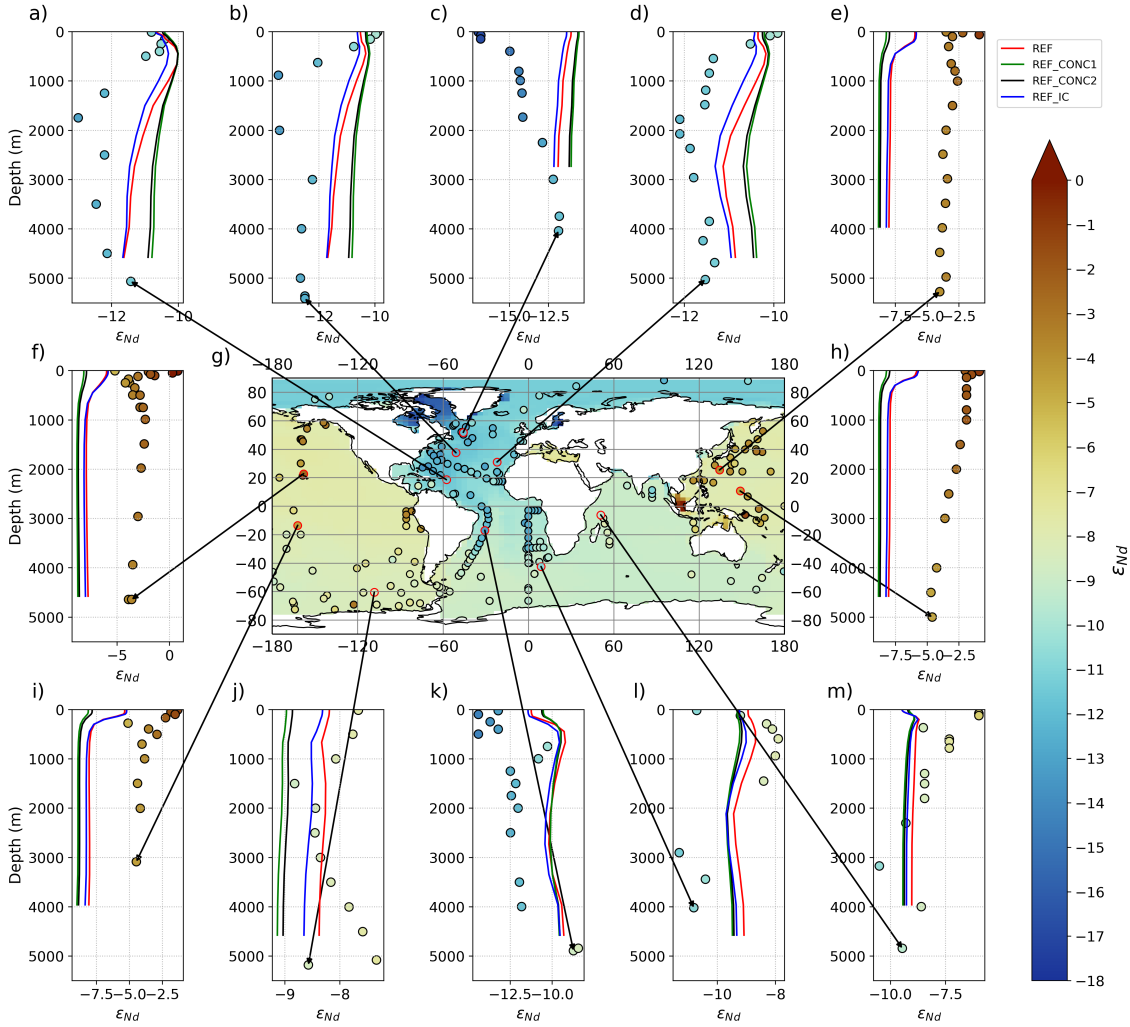

Figure 4.12: Central panel (g) displays ε_{Nd} at the seafloor for the final, optimised model configuration, *REF* (100-year mean from the end of the simulation), with superimposed water column measurements (Osborne et al., 2017, 2015; GEOTRACES Intermediate Data Product Group, 2021) from $\geq$ 3,000 m shown by filled coloured circles. Surrounding panels (a-f) and (h-m) display depth profiles of simulated (coloured lines: *REF* in red; *REF_CONC1* in green; *REF_CONC2* in black; and *REF_IC* in blue) and measured (filled circles) ε_{Nd}; see Sect. 4.2.2 of the main text for a full description of the optimised model configurations. Note that simulated ε_{Nd} in *REF* is too unradiogenic in the Pacific (Sect. 4.3.2, main text), alluding to the preferential dissolution of radiogenic volcanic components of the sediment across the seafloor, which are not effectivity captured by the bulk sediment ε_{Nd} source.

Table 4.6: Adjustments to the seafloor sediment ε_{Nd} distributions used as a boundary condition for the *REF-SED2* and *REF-SED3* simulations (gridded maps shown in Fig. 4.13) compared to the seafloor-wide distributions produced by Robinson et al. (2021) and used by to Robinson et al. (2022a) and the *REF* simulation in this study. Bounding longitude and latitude coordinates are given for the modified regions. The imposed ε_{Nd} thresholds applied to the *REF-SED2* and *REF-SED3* seafloor source are based on information in the cited texts, as explained in Text S4.1.

Region	Lat min	Lat max	Lon min	Lon max	SED2 ε_{Nd} threshold	SED3 ε_{Nd} threshold
Background Pacific	-40	70	117	260	< -5	¡-4
Western Equatorial Pacific and northwest subtropical Pacific	-5	30	100	130	$< +4$	$< +4$
Oceania	-15	10	130	165	$< +7$	$< +8$
North-eastern Pacific	20	50	230	260	$< +1$	$< +1$
Eastern Equatorial Pacific	0	20	245	275	$< +4$	$< +10$
North-west North Atlantic	30	75	270	340	> -28	> -34

Text S4.1: Choice of soluble ε_{Nd} signals applied in the *REF-SED2* and *REF-SED3* sensitivity simulations

Supplementary Table 4.6 summaries the modifications we made to the seafloor ε_{Nd} flux estimated by Robinson et al. (2022a) for the *REF-SED2* and *REF-SED3* sensitivity simulations. Here, we explain those choices.

The updated soluble ε_{Nd} signal in the Pacific for *REF-SED2* and *REF-SED3* is based upon evidence from substantial model-data imbalances in the Nd isotope budgets in the North Pacific (Tachikawa et al., 2003; Jones et al., 2008; Tachikawa et al., 2017). The evidence suggests the widespread detrital Nd across the central Pacific, which is composed of Asian continent derived lithogenic dust is inert, and implies that there is potential for preferential contributions of more radiogenic components in the sediment (Du et al., 2016; Wilson et al., 2013). Specifically, the minimum threshold ε_{Nd} chosen for the 'Background Pacific' region for *REF-SED2* of -5 follows those applied in the recent global Nd isotope scheme by Pasquier et al. (2021). This ε_{Nd} threshold is then increased moderately to -4 in *REF-SED3* to investigate the sensitivity of a more radiogenic seafloor sedimentary source from the abyssal Pacific.

Along the western Pacific margins, numerous studies have demonstrated the relabelling of water masses by a radiogenic lithogenic source, particularly by remobilised sediments from highly reactive basaltic volcanic islands, demonstrating that these are critical areas in determining the ε_{Nd} features of northward flowing Pacific equatorial water masses (Grenier et al., 2013; Lacan and Jeandel, 2005b; Fuhr et al., 2021; Tachikawa et al., 2003; Behrens et al., 2018; Molina-Kescher et al., 2018; Lacan and Jeandel, 2001). The threshold ε_{Nd} values for the 'Western Equatorial Pacific and northwest subtropical Pacific' region, is set to +4 in both *REF-SED2* and *REF-SED3*, applying the average estimated ε_{Nd} of the proximal radiogenic volcanic islands and their margins here, specifically the radiogenic ε_{Nd} signals from the Philippines and the north-eastern Japanese arc (Robinson et al., 2021). Moreover, the threshold ε_{Nd} values for the 'Oceania' region of +7 for *REF-SED2* relates to the estimated highly radiogenic Nd input signal across Papua New Guinea and its adjacent islands by Lacan and Jeandel (2005a), where remobilised sediment from these volcanic islands are believed to govern seawater ε_{Nd} distributions. This threshold was then increased to +8 in *REF-SED3* to represent a more extreme contribution from these

volcanic sediments, using the most radiogenic marginal ε_{Nd} sediment distributions around Oceania from the detrital compilation by Robinson et al. (2021).

Additionally, a dominant radiogenic contribution from the central American volcanic hotspots and island arcs around the Eastern Equatorial Pacific (EEP) and Northeast Pacific margins has been observed, including a direct radiogenic ε_{Nd} pore water flux measurement (Du et al., 2016; Abbott et al., 2015b,b; Grasse et al., 2012; Hu and Piotrowski, 2018). The threshold value applied for the 'Northeast Pacific' region of +1 in both *REF-SED2* and *REF-SED3*, follows the reference ε_{Nd} external input value to seawater predicted for the North Pacific (+0.8 to +1) (Tachikawa et al., 2003; Hu and Piotrowski, 2018), and is approximate to the pore fluid ε_{Nd} values measured across the Oregon margin, which range from -1.8 to -0.2 (Abbott et al., 2015a). Regarding the 'Eastern Equatorial Pacific' region, the threshold ε_{Nd} value of +4 applied in *REF-SED2* is based upon the dominant proximal Nd sources governing seawater distributions from the central American arcs and the Galapagos archipelago (with measurements ranging from 0 to +5) (Hu and Piotrowski, 2018). This ε_{Nd} threshold for the Eastern Equatorial Pacific' was subsequently increased to +10 to reflect more intense exchange in *REF-SED3* from dissolution of easily weatherable volcanogenic particles, imposing the most extreme radiogenic ε_{Nd} sediment distribution estimated by Robinson et al. (2021) in this region (sediment ε_{Nd} measurements of +10 located in the Galapagos archipelago).

On the other hand, the choice of the modified unradiogenic ε_{Nd} signal in the Atlantic is based upon evidence mainly from the northern Northwest Atlantic of an unradiogenic lithogenic Nd source to seawater. Areas of intense exchange of Nd between the sediment and seawater are thought to occur predominantly from highly unradiogenic Archean age Laurentide detrital sediment (with ε_{Nd} of -28 measured on reactive carbonates: Blaser et al. 2019b), thought to represent a key reactive phase contributing a substantial Nd source to surrounding deep waters (Blaser et al., 2019b, 2020; Lacan and Jeandel, 2005a). As such, the ε_{Nd} threshold value for the 'North-west North Atlantic' region in *REF-SED2* is set to -28 to encompass this intense and unradiogenic exchange. The more extreme ε_{Nd} threshold applied in *REF-SED3* of -34 represents a dominant exchange signal from the most unradiogenic detrital sediment phases in the North-west North Atlantic region, which occur in detrital measurements from Early Archean rock around southwest Greenland (Robinson et al., 2021).

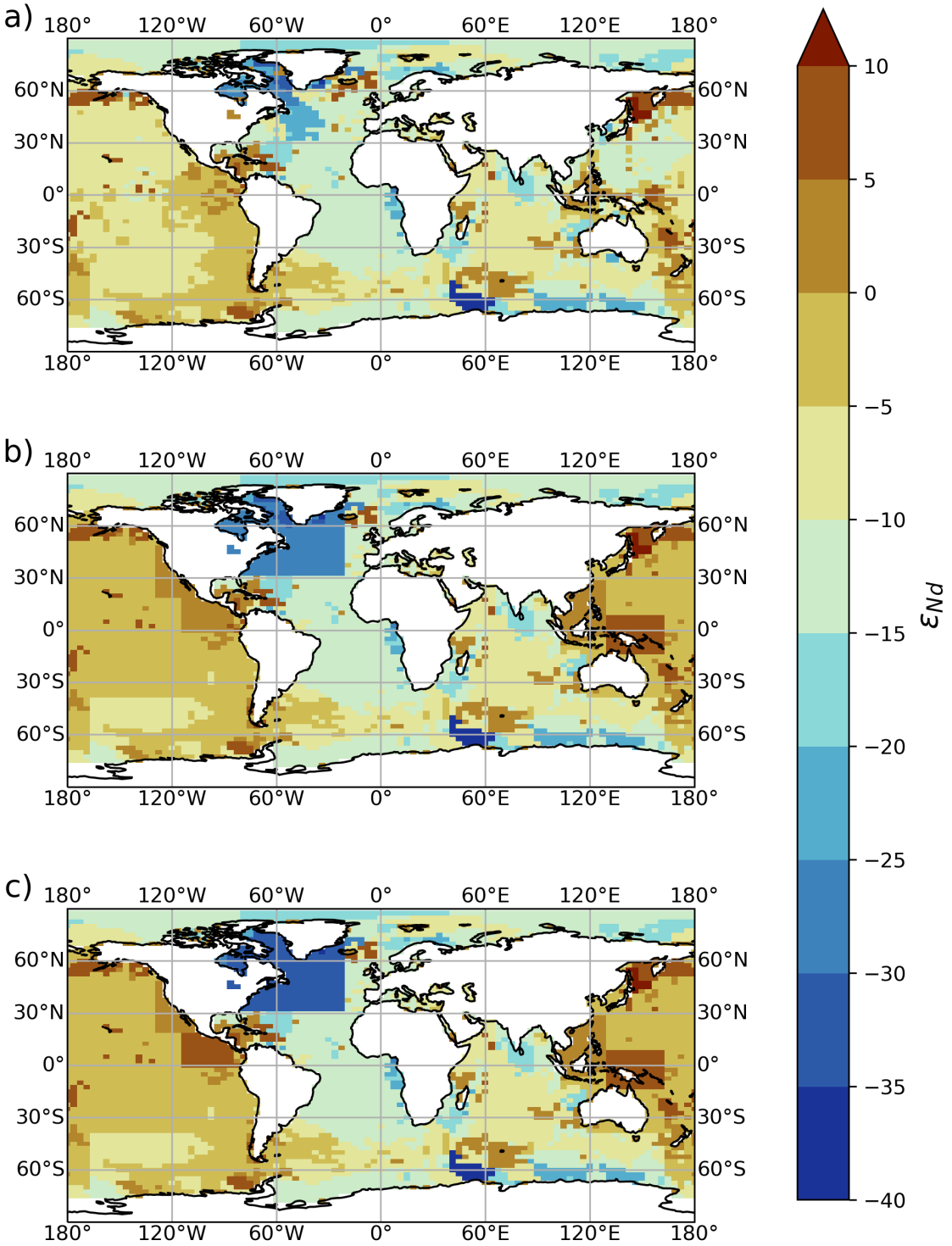

Figure 4.13: Gridded global seafloor sediment ε_{Nd} used in the sensitivity tests of the sediment-ocean boundary condition, including (a) *REF*, the bulk sediment ε_{Nd} signal as presented in Figure 4; Robinson et al. (2021); and (b) *REF-SED2* and (c) *REF-SED3*, two modified sediment ε_{Nd} maps of different extremity designed to test the hypothesis that certain reactive sedimentary phases dominate sediment-seawater interactions. See Sect. 4.4 of the main text for a full description of the experiment, and Table 4.6 and Text S4.1 for the specific definition and choice of the regional sediment ε_{Nd} thresholds.

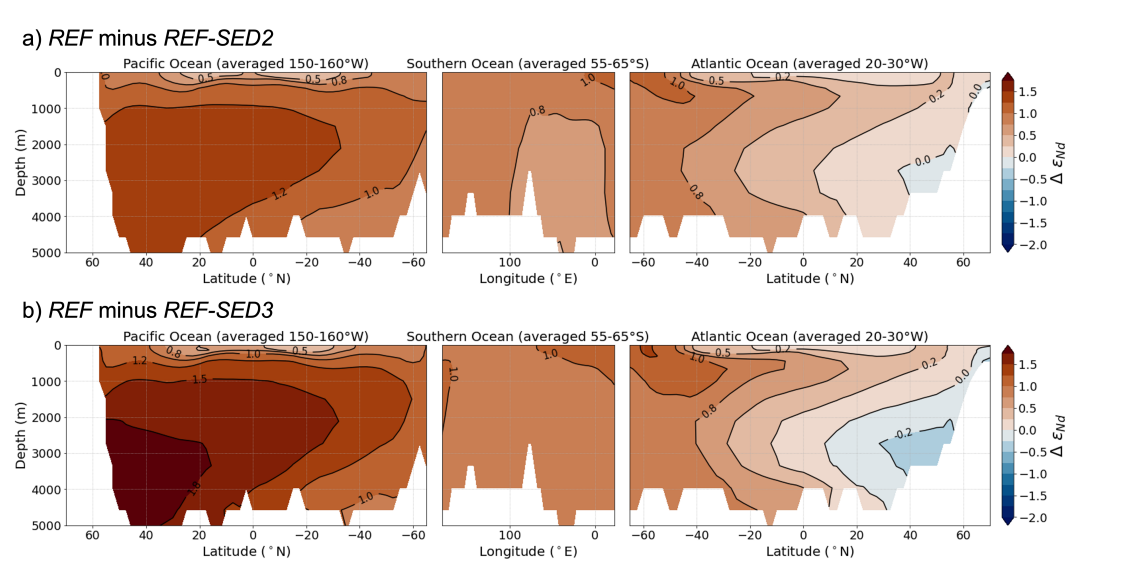

Figure 4.14: Difference between ε_{Nd} simulated in *REF* (where the seafloor sediment source is based only on bulk sediment ε_{Nd}), and (a) *REF-SED2*, and (b) *REF-SED3* following adjustments to the sediment source described in Table 4.6 and Text S4.1. $[Nd]_d$ remains the same in all simulations since there were no changes to those model inputs.

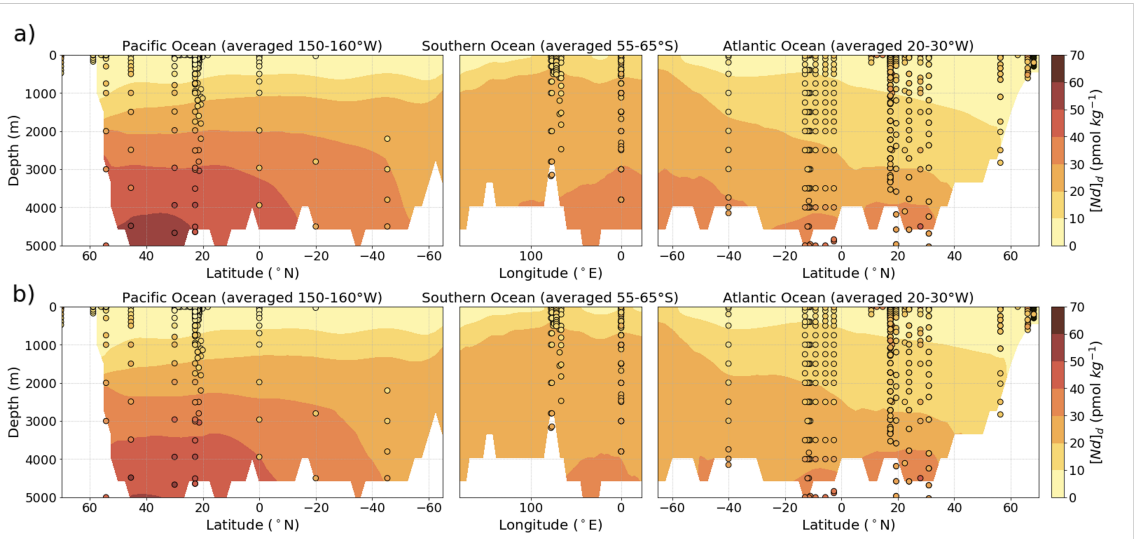

Figure 4.15: Comparison of $[Nd]_d$ in (a) *EXPT_RS4*, from Robinson et al. (2022a), (b) *REF*, the optimised simulation (Sect. 4.3.2, main text); note that *REF-SED2* and *REF-SED3* are identical to *REF* for $[Nd]_d$, since no adjustment was made to the amount of Nd entering the ocean from sediments in those simulations.

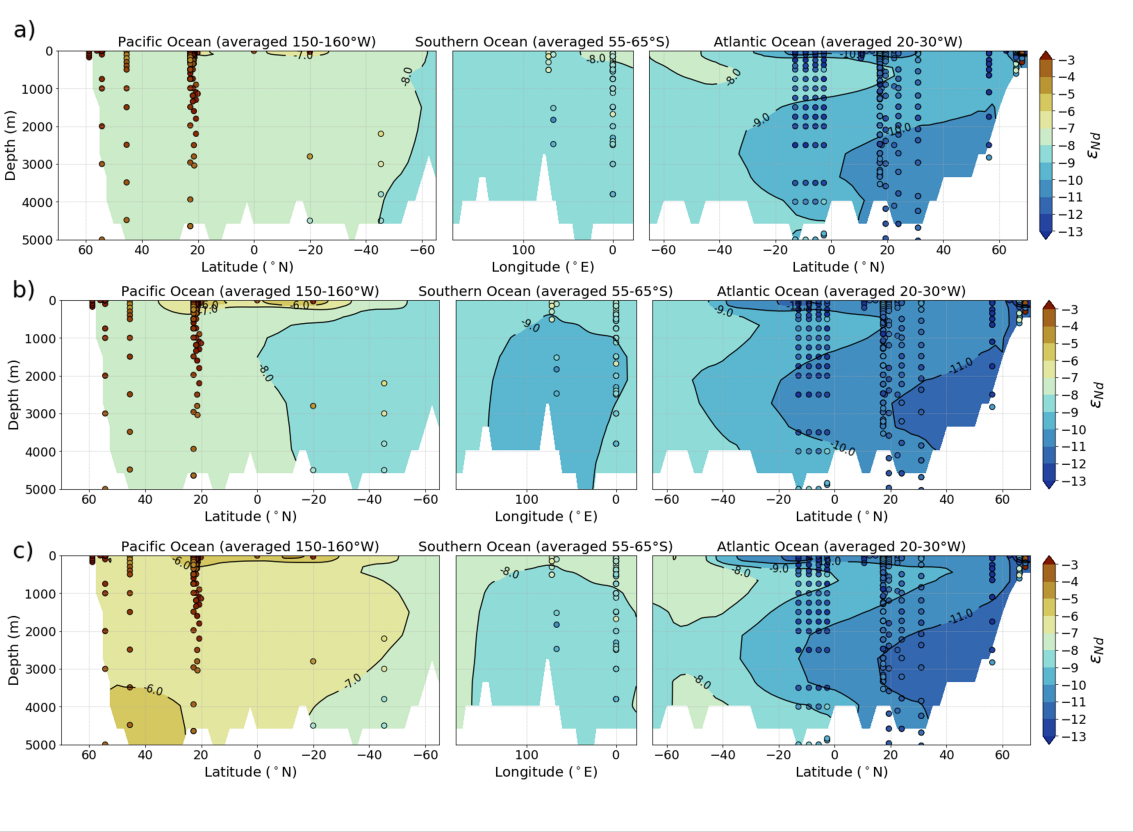

Figure 4.16: Comparison of ε_{Nd} in (a) *EXPT_RS4*, from Robinson et al. (2022a), (b) *REF*, the optimised simulation (Sect. 4.3.2, main text), and (c) *REF-SED3*, the optimised simulation with updated mobile sediment ε_{Nd} boundary conditions (Sect. 4.4, main text).

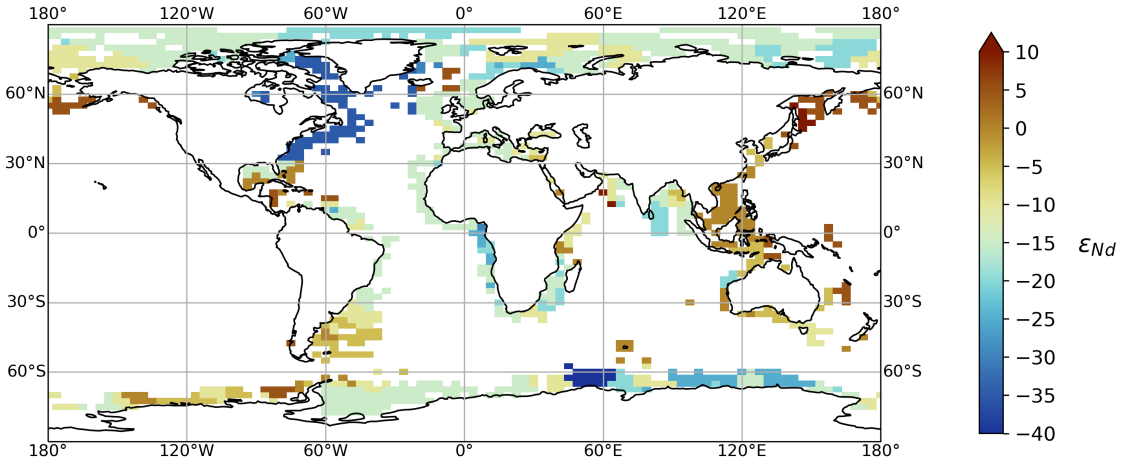

Figure 4.17: Gridded global sediment ε_{Nd} distributions at the sediment-ocean interface used as sediment source boundary conditions in the Nd isotope scheme in FAMOUS for simulation *REF-SED3-MG*, investigating the sensitivity of seawater ε_{Nd} to a margin-only constrained sediment source (Sect. 4.5, main text). The continental margins are delineated following the definition by Robinson et al. (2021), where sediment thickness $\geq$ 1,000 m.

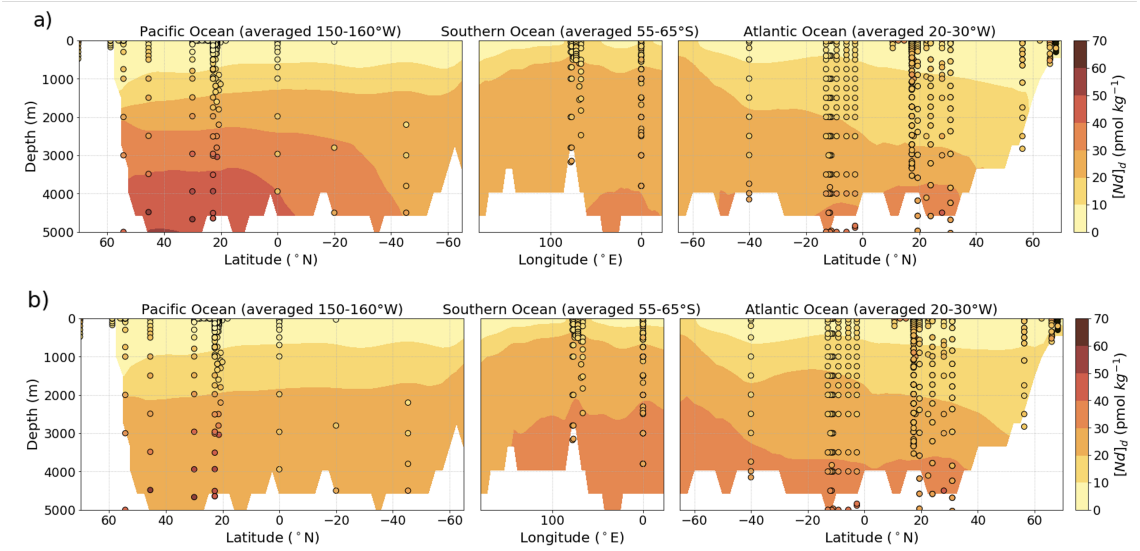

Figure 4.18: Vertical sections of simulated $[Nd]_d$ within sensitivity studies (a) *REF-SED3* with a seafloor-wide benthic flux and (b) *REF-SED3-MG* with a margin-only constrained benthic flux along a transect from the Pacific to Atlantic, traversing the Southern Ocean from West to East. Water column measurements are imposed as filled circles using the same colour scale. Simulated and measured $[Nd]_d$ from the Pacific are from $150-160°$ W, in the Southern Ocean are from $55-65°$ S, and in the Atlantic values are from $20-30°$ W. The continental margins are constrained following the definition by Robinson et al. (2021), where sediment thickness $\geq$ 1,000 m.

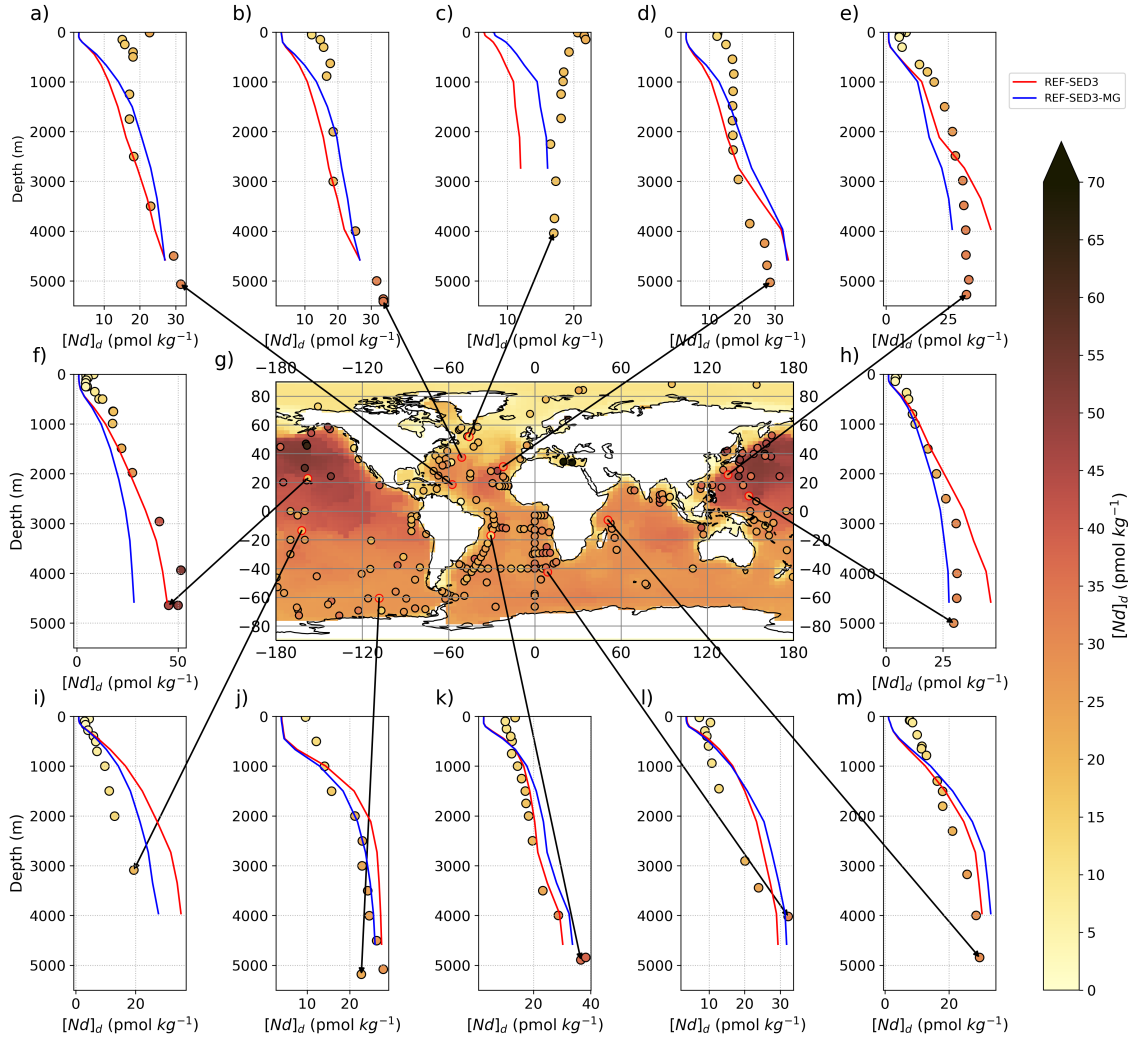

Figure 4.19: Comparison of simulated $[Nd]_d$ between a *seafloor-wide* (*REF-SED3*) and a margin-only constrained (*REF-SED3-MG*) sediment source, see Sect. 4.5 of the main text for a full experiment description. Central panel (g) displays ε_{Nd} at the seafloor for the optimised seafloor-wide benthic flux simulation with updated mobile sediment ε_{Nd} boundary conditions: *REF-SED3* (100-year mean from the end of the simulation), with superimposed water column measurements (Osborne et al., 2017, 2015; GEOTRACES Intermediate Data Product Group, 2021) from $\geq 3,000$ m shown by filled circles on the same colour scale. Surrounding panels (a-f) and (h-m) display depth profiles of simulated (coloured lines: *REF-SED3* in red, and *REF-SED3-MG* in blue) and measured (filled circles) $[Nd]_d$. Larger shifts in the $[Nd]_d$ between the two simulations highlight regions most sensitive to a margin constrained versus a seafloor wide sediment source.

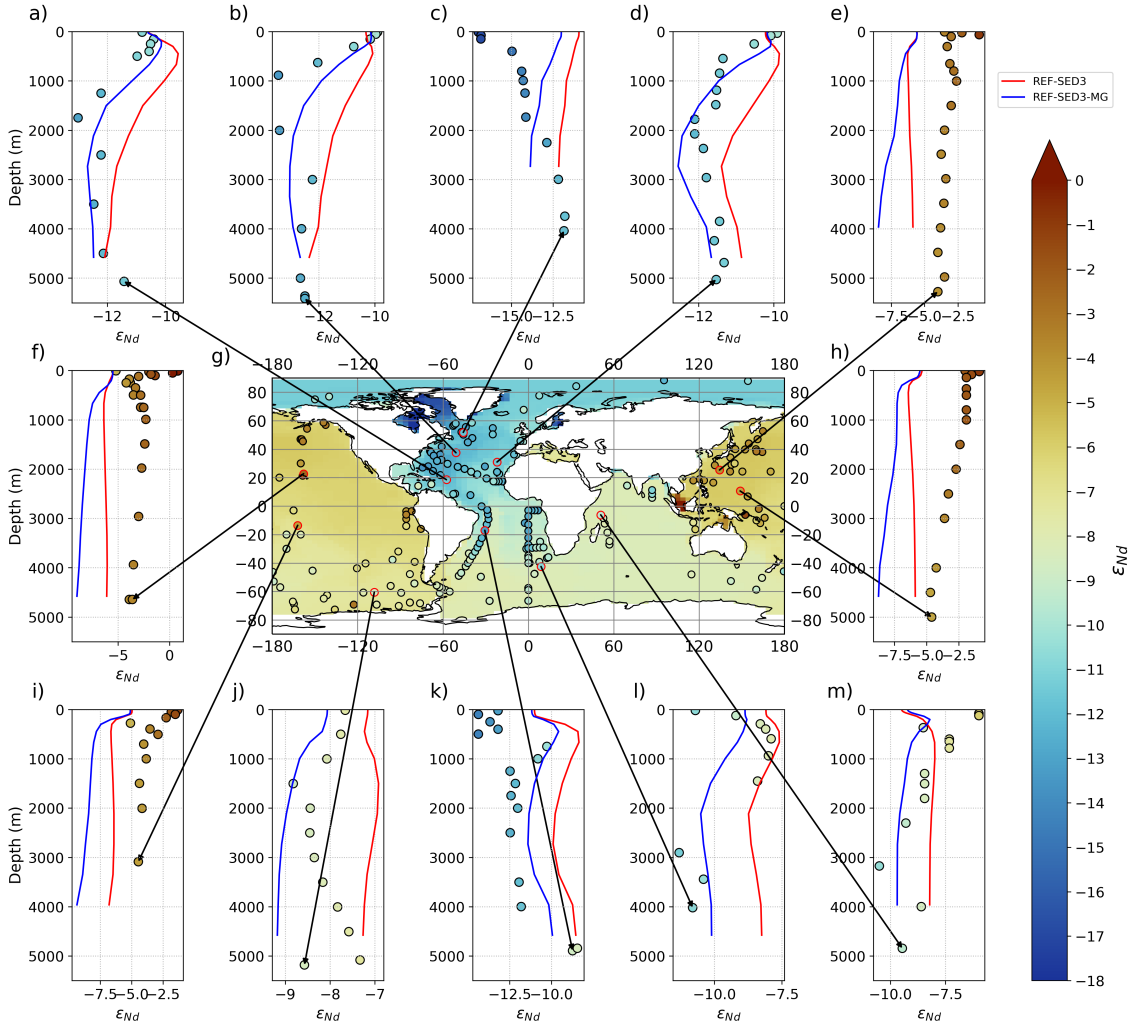

Figure 4.20: Comparison of simulated ε_{Nd} between a *seafloor-wide (REF-SED3)* and a margin-only constrained (*REF-SED3-MG*) sediment source, see Sect. 4.5 of the main text for a full experiment description. Central panel (g) displays ε_{Nd} at the seafloor for the optimised *seafloor-wide* benthic flux simulation with updated mobile sediment ε_{Nd} boundary conditions: *REF-SED3* (100-year mean from the end of the simulation), with superimposed water column measurements (Osborne et al., 2017, 2015; GEOTRACES Intermediate Data Product Group, 2021) from $\geq 3,000$ m shown by filled circles on the same colour scale. Surrounding panels (a-f) and (h-m) display depth profiles of simulated (coloured lines for simulations: *REF-SED3* in red, and *REF-SED3-MG* in blue) and measured (filled circles) ε_{Nd}. Larger shifts in the ε_{Nd} between the two simulations highlight regions most sensitive to a margin constrained versus a seafloor wide sediment source.

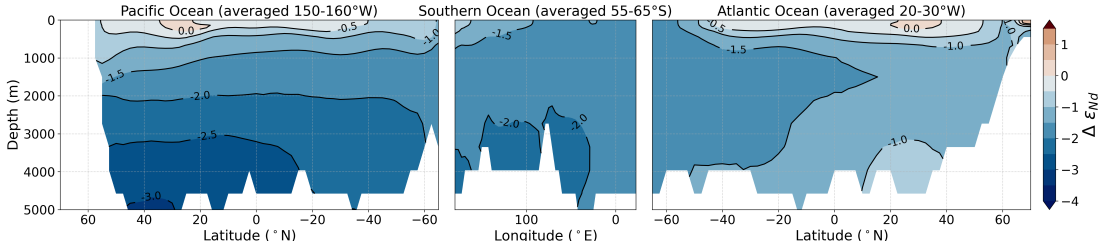

Figure 4.21: Difference between ε_{Nd} simulated in *REF-SED3* (with a *seafloor-wide* benthic flux) and *REF-SED3-MG* (with a *margin-only* constrained benthic flux) using the optimised seafloor-wide benthic flux simulation with updated mobile sediment ε_{Nd} boundary conditions (Sect. 4.5, main text): *REF-SED3* minus *REF-SED3-MG*. Note the vertical gradients for the Pacific and Southern Ocean compared to the weaker response in the Atlantic.

Chapter 5

Discussion and conclusions

5.1 Summary

The overarching aim of this thesis was:

To investigate and constrain the global marine Nd cycle within a fast, full complexity general circulation model, and apply uncertainty quantification techniques to facilitate parameter space exploration and calibration

In Chapter 1 this overarching aim was broken down into three main research questions:

RQ1) How accurately can modern Nd isotope distributions (ε_{Nd}) be simulated in a fast coupled atmosphere-ocean general circulation model?

RQ2) What are the limitations of the Nd isotope scheme, and do they challenge the general assumptions underpinning the interpretive framework of marine Nd cycling and its fundamental applications as a robust ocean circulation tracer?

RQ3) To what extent can a seafloor-wide benthic flux explain non-conservative behaviour of Nd isotopes under a global model of marine Nd cycling, and to what extent can global bulk sedimentary ε_{Nd} distributions represent a labile sedimentary flux to seawater?

The research chapters of this thesis (Chapters 2, 3 and 4) addressed these questions. This was accomplished by first developing new global maps representing the Nd isotope distributions across the continental margins, and, for the first time, across the seafloor (Chapter 2). These global seafloor ε_{Nd} maps were then applied as model boundary conditions for the development of the Nd isotope scheme in FAMOUS (Chapter 3); enabling the scheme presented in this study to represent a seafloor-wide benthic flux under a complex numerical model of the marine Nd cycle. Here substantial effort was made to revisit and revise all the key processes understood to govern marine Nd isotope distributions. The new scheme was then statistically optimised to best represent the modern marine Nd cycle (Chapter 4), providing constraints on major marine Nd budgets. The accuracy with which FAMOUS simulated modern Nd concentration ([Nd]) and isotope distributions was examined in both Chapters 3 and 4, and limitations of the scheme were contextualised under current assumptions inherent to the applications of Nd isotopes as a tracer of ocean circulation and climate. Sensitivity experiments assessing the importance of different components of Nd cycling (reversible scavenging efficiency, additional release of Nd from river sourced particulate material, and the magnitude, spatial extent, and Nd isotope distributions of a seafloor benthic flux) on seawater Nd distributions were performed in Chapters 3 and 4. These investigations then permitted an assessment in Chapter 4 of how important the benthic flux is for governing seawater Nd distributions.

In this 'Conclusions' chapter, I synthesise how the previous chapters answer the research questions and address the overarching aim of this thesis, including exploring the impacts of the research, and outline limitations and future directions of work.

5.2 Answering the research questions

5.2.1 RQ1: How accurately can modern Nd isotope distributions be simulated in a fast coupled atmosphere-ocean general circulation model?

Before a new Nd isotope scheme could be implemented into FAMOUS, and to facilitate the most accurate representation of our current knowledge of the marine Nd cycle, a considerable improvement of Nd source identification was necessary.

A decade and a half ago, the previous seminal map of the ε_{Nd} distributions at the continental margins by Jeandel et al. (2007) was developed, incorporating 246 published sedimentary ε_{Nd} measurements. Chapter 2 of this thesis synthesised an extensive and up-to-date compilation of over 5,100 published and new terrestrial and marine sedimentary ε_{Nd} measurements. This revised database was then used to construct high-resolution global gridded maps, updating the continental margin ε_{Nd} map by Jeandel et al. (2007), and, for the first time, extending this map to estimate the sedimentary ε_{Nd} distributions across the entire seafloor (Fig. 5.1). These seafloor sedimentary ε_{Nd} distributions are now a crucial model pre-requisite under the new benthic flux hypothesis (Robinson et al., 2021; Abbott et al., 2015a; Haley et al., 2017).

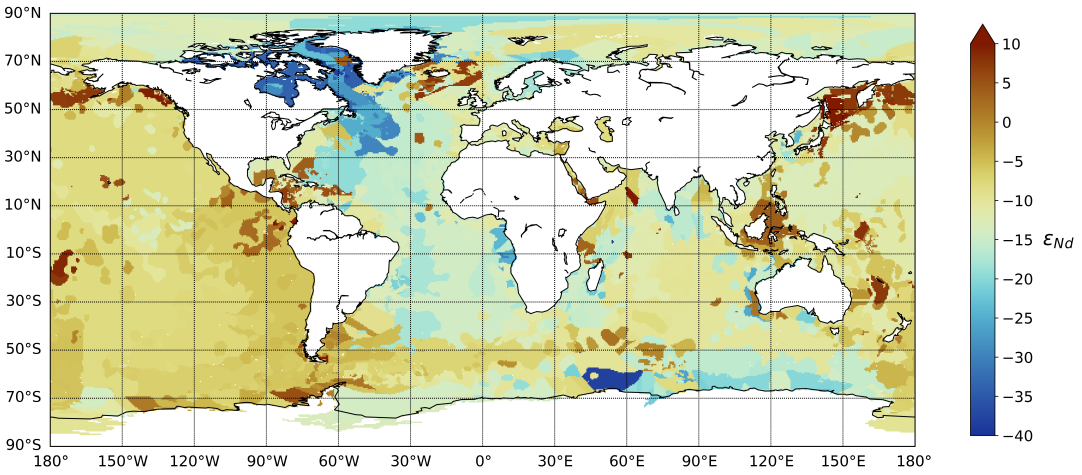

Figure 5.1: Nd isotope signature of the global sediment-water interface (Robinson et al., 2021). This final characterisation of global ε_{Nd} distributions at the sediment-ocean interface uses the continental ε_{Nd} map extrapolated to where sediment thickness $\geq 1,000$ m, and the remaining sediment regions are represented using the seafloor ε_{Nd} map. Figure reproduced from Chapter 2.

Moreover, Nd sourced from aeolian deposition was updated relative to previous schemes in Chapter 3. First, a more recent annual mean dust deposition boundary condition for the pre-industrial, as simulated by the atmosphere component of the Hadley Centre Global Environmental Model version 2 (HadGEM2-A: Collins et al. 2011) General Circulation Model (GCM) was employed. Secondly, the ε_{Nd} composition of the dust flux was revised, building upon the initial basinal estimates by Tachikawa et al. (2003). Here, additional constraints were applied to account for dust plume expansions as reported by Mahowald et al. (2006), combined with the mean ε_{Nd} of the respective source regions, as determined by the global compilation of detrital ε_{Nd} data by Blanchet (2019). The Nd sourced from rivers was updated by imposing a scaling onto the riverine source, based on recent findings suggesting a particulate river flux as a major Nd source (Rahlf et al., 2021; Rousseau et al.,

2015). This riverine scaling was used to examine enhanced Nd sourced at river mouths and explored in Chapter 4. Finally, in an effort to best represent the internal cycling of Nd via reversible scavenging, recent particle-export fields based on satellite-derived primary production were used (Dunne et al., 2007, 2012). These particle fields formed a best data-driven estimate of biogenic particle concentrations, and reduced biases that would have resulted instead from applying the highly simplified optional ocean biogeochemistry module in FAMOUS (Dentith et al., 2020; Palmer and Todderdell, 2001).

Revising all the key processes understood to govern global marine Nd isotope distributions allowed the most up-to-date model boundary conditions and model parameterisations to be created for the development of the Nd isotope scheme in FAMOUS; addressing '**OBJ1:** Estimate the bulk ε_{Nd} distributions of seafloor detrital sediment across the continental margins and seafloor', and '**OBJ2:** Implement Nd isotopes into a fast coupled atmosphere-ocean general circulation model, revisiting and updating key source and sink parameters' (Chapter 1, Sect. 1.4).

Experiments performed in Chapter 3, which first employed these updated Nd source/sink boundary conditions, revealed the new Nd isotope scheme is sensitive to Nd source and biogeochemical processes, demonstrating the success of the scheme (and its boundary conditions) in representing key features which govern distributions of Nd in seawater (e.g., Tachikawa et al. 2017; van de Flierdt et al. 2016). For example, model sensitivity to the reversible scavenging efficiency highlighted its importance for determining the characteristic increase in [Nd] with depth and along the circulation pathway. Reversible scavenging also enhanced the regional basinal gradients in simulated ε_{Nd}, in correspondence with seawater measurements (Bertram and Elderfield, 1993; Siddall et al., 2008b). Sensitivity to the magnitude of a spatially uniform seafloor-wide benthic flux in Chapter 3 illustrated it was a major intermediate and deep ocean Nd source. A benthic flux influenced marine Nd distributions at depths below 500 m, where there was no direct input from dust and river sources. Moreover, the ε_{Nd} of the sediment source set the blueprint for simulated seawater ε_{Nd} distributions. Overall, these sensitivity studies addressed '**OBJ3:** Explore the sensitivity of simulated Nd isotope distributions to different components of the marine Nd cycle' (Chapter 1, Sect. 1.4).

The Nd isotope scheme was statistically optimised in Chapter 4, using only 23 simulations (instead of the 100+ used in previous studies; Gu et al. 2019; Pöppelmeier et al. 2020b; Rempfer et al. 2011), to best represent modern measurements of seawater [Nd] and ε_{Nd}. Here, a recent seawater Nd compilation (Osborne et al., 2017, 2015) was augmented with additional measurements including data from the most recent GEOTRACES Intermediate Data Product 2021 (GEOTRACES Intermediate Data Product Group, 2021) from GEOTRACES cruises (GA02, GA08, GP12, GN02, GN03 and GIPY05), making it the largest compilation used to validate the performance of a Nd isotope enabled model to date. For example, the isotope scheme in FAMOUS was validated using a compilation of 3,278 seawater ε_{Nd} measurements, compared to 880 measurements used to validate the pioneering isotope scheme in Bern3D by Rempfer et al. (2011); that's nearly 2,400 more (or nearly a fourfold increase in the number of) measurements for the comparison. The model calibration used a Gaussian Process emulator and history matching to facilitate parameter space exploration. This method has not yet been applied to any Nd isotope model and addressed '**OBJ4:** Statistically optimise the Nd isotope scheme to best represent the modern marine Nd cycle' (Chapter 1, Sect. 1.4).

Altogether, the calibrated simulation (named '*REF*') captures the main processes of modern marine Nd cycling, with a total Nd inventory of 4.27×10^{12} g and a residence time of 727 years. Such features, alongside Nd source magnitudes and their global distributions are highly comparable with estimates from previous schemes (Rempfer et al., 2011; Gu et al., 2019; Pöppelmeier et al., 2020a; Arsouze et al., 2009).

Global mean absolute error (MAE), which explores the difference in simulated values

from the seawater measurements, for [Nd] was 8.83 pmol kg^{-1} and for ε_{Nd} was 2.37 ε_{Nd}-units in *REF*. Overall, the scheme simulates [Nd] that closely match seawater measurements (Fig. 5.2a-b), especially in the interior of the ocean (below 1,000 m), with highest [Nd] of approximately 50 pmol kg^{-1} that match measurements with high fidelity in the deep Pacific (below 5,000 m). However, the scheme consistently underestimates [Nd] in the surface and near-surface layers (with model-data disparities in the upper 1,000 m across all basins), and particularly close to continental margins; for example, where simulated [Nd] around continental margins in the Labrador Sea is 3 pmol kg^{-1} compared to measured [Nd] of 70 pmol kg^{-1}, and the Sea of Japan, where simulated [Nd] is 2 pmol kg^{-1} compared to measured [Nd] of 50 pmol kg^{-1}. Such model-data offsets, can, in part be explained by the low spatial resolution of FAMOUS which limits full representation of point surface inputs, which are highly variable in nature. Yet these underestimations also imply there is too strong particle scavenging occurring in the surface layers and/or a misrepresentation of elevated surface and marginal Nd sources.

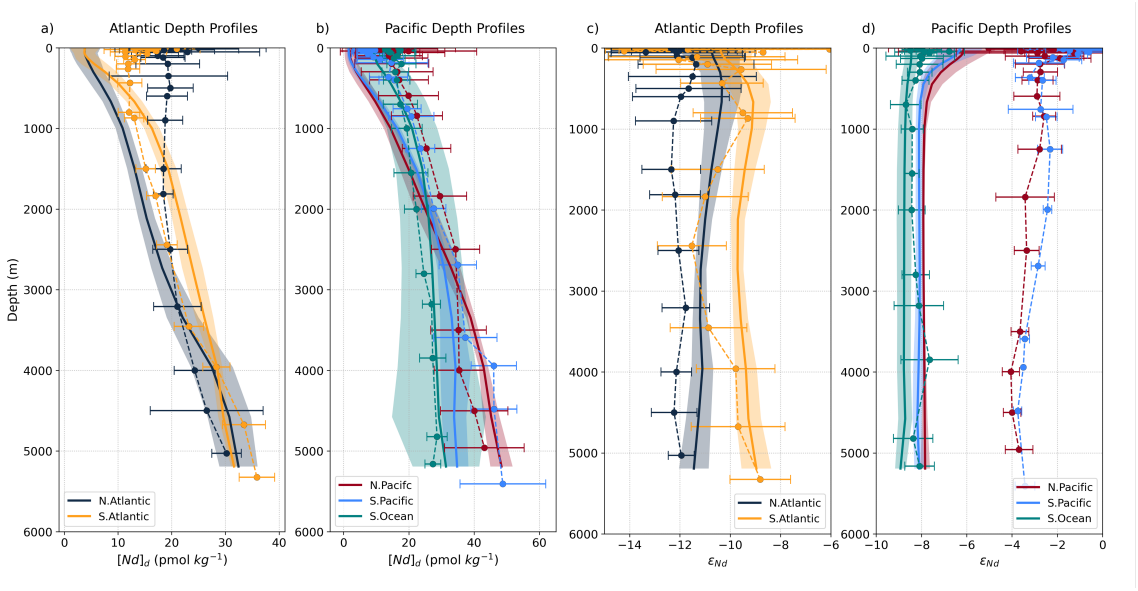

Figure 5.2: Basin averaged [Nd] ((a); North and South Atlantic, (b); North and South Pacific and Southern Ocean) and ε_{Nd} profiles ((c); North and South Atlantic, (d); North and South Pacific and Southern Ocean) with depth in *REF*. The mean and standard deviation of modern seawater measurements (Osborne et al., 2017, 2015; GEOTRACES Intermediate Data Product Group, 2021) are calculated for each vertical grid level and represented by the thinner dashed lines and error bars. The mean and standard deviation of the model are represented by the thicker solid line and lighter coloured ribbon. Figure reproduced from Chapter 4.

Regarding ε_{Nd}, the scheme represents modern ε_{Nd} measurements with moderate skill in the deep ocean interior (MAE = 1.68 at depths > 3,000 m), and in the Atlantic and Southern Ocean (MAE = 1.63 and 0.52 respectively). Alternatively, localised model-data disparity for ε_{Nd} occurs within the surface layers (MAE = 2.68 at depths $\leq$ 200 m), and likely due to similar reasons outlined above for simulating [Nd], alongside model boundary conditions not capturing the mobile and spatially elevated Nd isotope signal that is driving surface/near-surface particle-seawater interactions. The largest offset in simulated ε_{Nd} from seawater measurements occurs in sluggish waters of the North Pacific (MAE = 3.98). Here simulated Nd isotope distributions are consistently 3-4 ε_{Nd}-units too unradiogenic, a feature common amongst sophisticated global Nd isotope enabled models (Jones et al., 2008; Arsouze et al., 2009; Rempfer et al., 2011; Gu et al., 2019; Pöppelmeier

et al., 2020a). Importantly this offset demonstrates that a spatially uniform benthic flux of bulk sediment ε_{Nd} cannot sufficiently capture the mobile radiogenic sediment components interacting with seawater in the Pacific. This supports the notion of a discriminatory contribution of certain 'reactive' sediment phases (Abbott et al., 2015a; Wilson et al., 2013; Du et al., 2016; Jones et al., 2008; Pearce et al., 2013; Rousseau et al., 2015), and a likely favouring of interactions from radiogenic volcanic components of the seafloor sediment.

Distinct variations in seawater ε_{Nd} are represented in the scheme, which capture important large-scale ocean circulation features such as water mass structure within ocean regions characterised by modern high ventilation rates. This is observed particularly in the Atlantic Ocean where simulated ε_{Nd} depth profiles in the South Atlantic co-vary with salinity (Fig. 5.3), suggesting water mass advection and mixing are the primary control on deep-water ε_{Nd} distributions here, and encompassing the unique Atlantic water mass zig-zag profiles (Goldstein and Hemming, 2003). Overall, this demonstrates the Nd isotope scheme can represent ε_{Nd} features with greater accuracy in regions where large-scale ocean circulation and mixing dominate distributions, whereas larger biases occur in regions characterised by more sluggish circulation, where seawater ε_{Nd} are more influenced by highly complex and hard to resolve particle-seawater interactions.

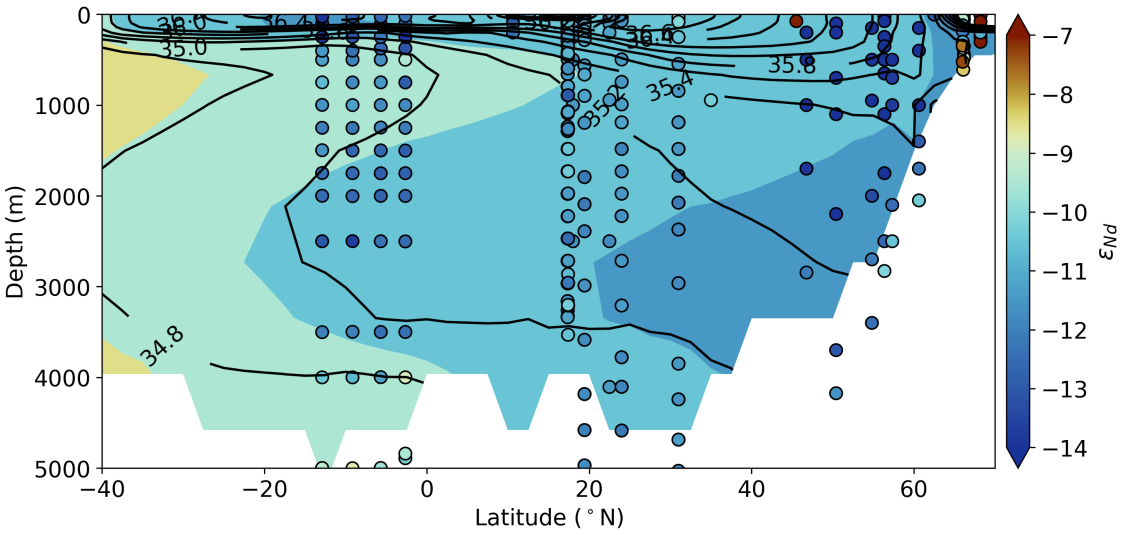

Figure 5.3: The conservative water mass tracer properties of ε_{Nd} in the optimised '*REF*' simulation in the Atlantic Ocean, as indicated by simulated ε_{Nd} (coloured) and salinity (contours) in a cross section of the Atlantic ($20 - 30°$ W), compared with water column measurements of ε_{Nd} (filled circles using the same colour scale). Figure reproduced from Chapter 4.

Thus, in answer to the original research question, the FAMOUS GCM can simulate Nd isotopes with sufficient accuracy to capture the influence of the various physical/biogeochemical processes to which Nd isotope distributions are known to be sensitive (i.e., inputs/sinks, internal cycling, large-scale ocean circulation, and water mass structure). The new scheme has provided a new tool capable of quantitively investigating the global marine Nd cycle, including exploring emerging paradigms at the forefront of our understanding of the marine Nd cycle.

However, despite efforts to revise model boundary conditions and update descriptions of the main processes believed to drive marine Nd cycling, model-data inconsistencies occur. These inaccuracies limit the ability of the model to resolve water mass end member ε_{Nd} signals with high fidelity, especially in the Pacific. However, the scheme importantly

highlights that there are key regional differences in the processes that drive seawater ε_{Nd} distributions. For example, the ε_{Nd} signal in the well-ventilated North Atlantic is predominantly governed by large-scale ocean circulation, and better represented in the scheme. Whereas, in the sluggish Pacific, ε_{Nd} are sensitive to the representation of the benthic flux, and the simulated seawater ε_{Nd} is not well resolved. Consequently, if sophisticated global Nd isotope models, such as the one presented in this study, are to be used to resolve large-scale ocean circulation properties of Nd, and help provide context to the palaeoceanographic Nd record, there needs to be improved spatiotemporal constraints on localised/regional differences in how seawater acquires its ε_{Nd} signal. Moreover, resolving the interplay of Nd addition and removal versus water mass advection time and mixing is especially important under instances where we do not know the strength of advection (e.g., during the Last Glacial Maximum; see Lynch-Stieglitz 2017, for a review), approximately 20 thousand years ago (ka).

5.2.2 RQ2: What are the limitations of the Nd isotope scheme, and do they challenge the general assumptions underpinning the interpretive framework of marine Nd cycling and its fundamental applications as a robust ocean circulation tracer?

The interpretative framework of marine Nd cycling, which forms its applications to trace both modern and past water provenance and circulation, assumes: (1) the ε_{Nd} of a water mass is geographically distinct and relates to its origin, and (2) seawater ε_{Nd} away from continental margins behaves conservatively, and corresponds to large-scale water mass mixing (Goldstein and Hemming, 2003; van de Flierdt and Frank, 2010; Tachikawa et al., 2017).

One limitation of the Nd isotope scheme in FAMOUS, was the consistently too low [Nd] simulated in the surface and near-surface layers, as detailed in Sect. 5.2.1. Such [Nd] underestimations eluded towards biases in the simplified global parameterisation of reversible scavenging that was too strong in the upper layers, alongside the misrepresentation of elevated surface and marginal sources. Moreover, the scheme also produced regional model-measurement disparities regarding resolving water mass end member ε_{Nd} signals. The greatest of these imbalances occurred in the North Pacific, whereby simulated ε_{Nd} is too unradiogenic compared to measurements (Fig. 5.2). Further disparities occurred in the northern North Atlantic, where the ε_{Nd} signal of North Atlantic Deep Water (NADW) was too radiogenic compared to measurements, particularly around the mouth of the Labrador Sea (Fig. 5.4). These limitations signify foremost that the scheme is likely not capturing strong local particle-seawater Nd exchange occurring at shallow-intermediate depths, and particularly close to margins.

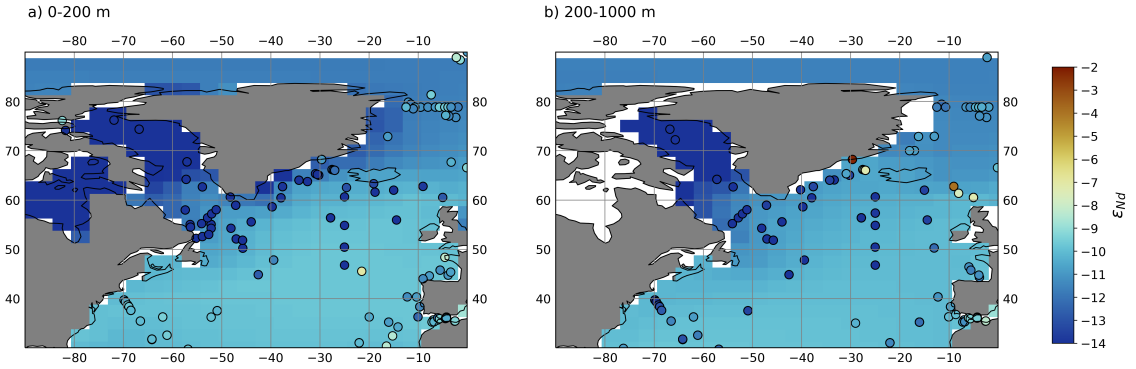

Figure 5.4: Volume-weighted distributions of ε_{Nd} in simulation *EXPT_SED2* split into two different depth bins, (a) shallow (0-200 m), and (b) intermediate (200-1,000 m) within the North Atlantic and Labrador Sea basins. Water column measurements from within each depth bin (Osborne et al., 2017, 2015; GEOTRACES Intermediate Data Product Group, 2021) are superimposed as filled circles using the same colour scale. Figure reproduced from Chapter 3.

Sensitivity studies in Chapter 4 explored how the regional heterogeneity of sediment reactivity and its isotope composition influenced seawater ε_{Nd} distributions. These studies demonstrated that in the modern oceans, the Pacific is sensitive to the influence of a benthic flux (Fig. 5.5). Such non-conservative behaviour of seawater ε_{Nd} under a widespread sedimentary Nd source demonstrates that the ε_{Nd} of a water mass can evolve due to processes (e.g., sediment dissolution) which are not reflective of large-scale circulation and mixing. However, the North Atlantic in comparison displayed minor responses towards modified benthic fluxes, implying a more conservative behaviour of modern NADW; although non-conservative effects from reversible scavenging still influence Atlantic ε_{Nd} distributions, which are shifted to greater depths in the water column compared to salinity (a conservative water mass tracer) (Fig. 5.3).

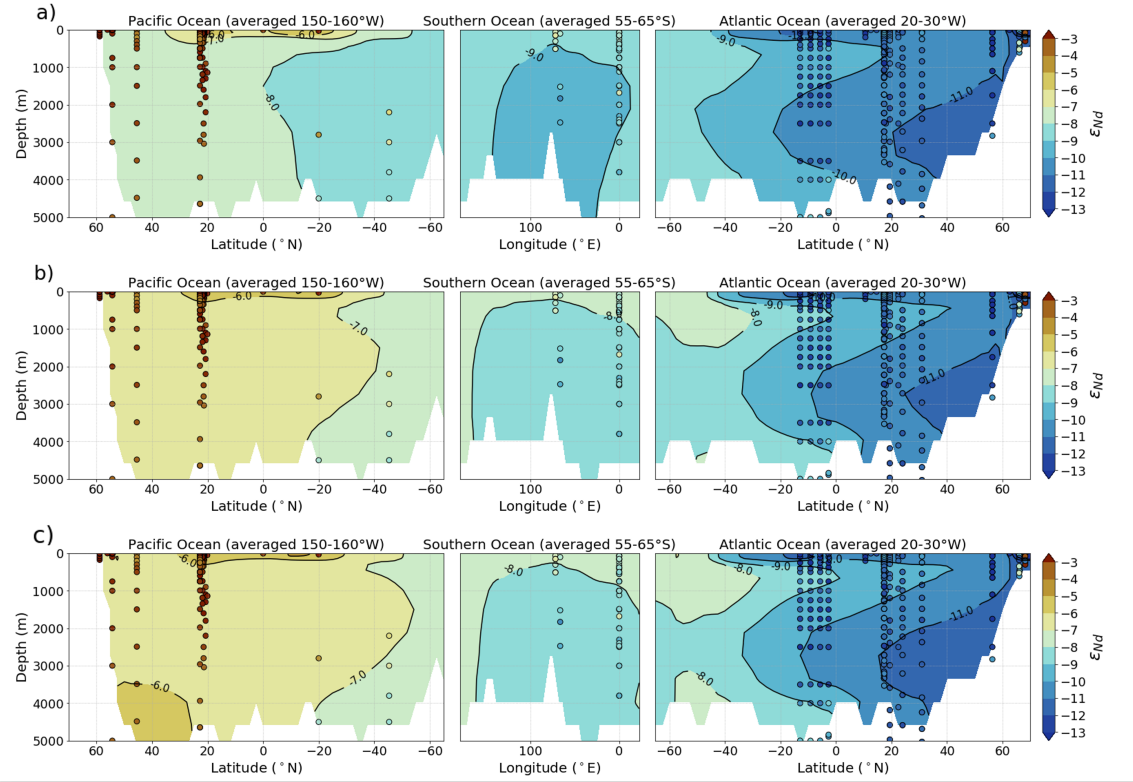

Figure 5.5: Vertical sections of simulated ε_{Nd} within three seafloor sediment ε_{Nd} sensitivity studies testing (a: *REF*) the bulk sediment ε_{Nd} signal and (b; *REF-SED2* and c; *REF-SED3*) representing two modified sediment ε_{Nd} maps of increasing magnitude to investigate the hypothesis that certain reactive sedimentary phases dominate sediment-water interactions along a transect from the Pacific to Atlantic, traversing the Southern Ocean from West to East. Water column measurements are imposed as filled circles using the same colour scale. Simulated and measured ε_{Nd} from the Pacific are from $150 - 160°$ W, in the Southern Ocean are from $55 - 65°$ S, and in the Atlantic values are from $20 - 30°$ W. Figure reproduced from Chapter 4.

Overall, the Nd isotope scheme in FAMOUS illustrates that water masses carry a distinct ε_{Nd} relating to external Nd inputs from continental weathering, alongside particle-seawater exchange. Hereby highlighting to some extent, that seawater ε_{Nd} can reflect geographically distinct water mass provenance properties, confirming general assumptions that seawater ε_{Nd} is sensitive to changes in large-scale ocean circulation. However, simulated seawater ε_{Nd} is also sensitive to multiple non-conservative forcings, consistent with recent observational and modelling investigations (e.g., Abbott et al. 2015a; Du et al. 2016; Gu et al. 2019; Haley et al. 2017; Jones et al. 2008; Lacan and Jeandel 2005a; Paffrath et al. 2021; Pöppelmeier et al. 2020b; Rahlf et al. 2021; Rempfer et al. 2011; Rousseau et al. 2015; Siddall et al. 2008b); such processes are not always limited in proximity to continental margins, and have different regional effects across depths and between basins. Although such non-conservative behaviour demonstrates the potential capability of seawater ε_{Nd} to capture climatically driven changes (e.g., changes to large-scale weathering regimes), this behaviour, which falls out of the assumed conservative tracer properties of ε_{Nd} (Goldstein and Hemming, 2003), are often overlooked in the simplified conceptual models used to interpret large-scale ocean circulation from seawater ε_{Nd} (e.g., Gutjahr et al. 2008; Jonkers et al. 2015; Piotrowski et al. 2004; Roberts et al. 2010; Rutberg et al. 2000). Moreover sediment-water interactions continue to be elusive and poorly quantified. As such, the evaluation of Nd isotope records, and how they reflect global ocean circulation regimes, needs to consider changed weathering and ocean convective regimes, biological

productivity, and environmental conditions on regional scales.

Interestingly though, and despite the role of non-conservative effects from the benthic flux (and reversible scavenging) away from continental margins, water mass ε_{Nd} required considerable forcings (where sediment regions were modified by up to 10 ε_{Nd}-units across the seafloor in the Pacific and Atlantic Oceans) to change end member ε_{Nd} signals (where the maximum response of seawater of +2 ε_{Nd}-units occurred in the abyssal North Pacific). This relative insensitivity to sediment ε_{Nd} forcings suggests, to a first order, that there may be a potential for a resilience of seawater ε_{Nd} to significant detrital inputs (resulting, for example, from changed weathering regimes). This resilience is most likely in oceanic regions with sufficient ventilation and limited benthic flux exposure times; as shown in Chapter 4 for simulated ε_{Nd} in the modern Atlantic under different benthic flux ε_{Nd} reactivities and spatial extents (i.e., seafloor-wide versus margin only benthic fluxes).

Thus, in answer to the original research question, the main limitations of the Nd isotope scheme relate to the still poor quantification of non-conservative sediment-seawater interactions, which limits fully resolving end member ε_{Nd} signals, and to biases resultant from the inherent low resolution of the model. These non-conservative processes, of which their influence on seawater ε_{Nd} signals vary on regional scales, challenge fundamental assumptions that the ε_{Nd} signal of a water mass always relates to its origin. Seawater can be overprinted with an ε_{Nd} signal resulting from a benthic flux along its deep-water flow path or modified within the water column via vertical downward transport from reversible scavenging; both these processes result in non-conservative behaviour of ε_{Nd} away from proximal margins. The results from this thesis illustrate that the applications of ε_{Nd} as a robust ocean circulation tracer require more careful interpretations to correctly disentangle the ocean circulation signal from non-conservative processes. Such interpretations need to consider the intertwined roles of varying Nd sources/sinks (e.g., changes to the sediment composition and reactivity of benthic fluxes), changed ocean circulation regimes (e.g., water mass provenance and structure), and regional environmental conditions (e.g., biological productivity and pH); all of which vary both spatially and temporally.

Nonetheless, the scheme has substantially updated, revised, and explored key critical parameters governing the marine Nd cycle, building upon the ability of the community to continue efforts to quantify the marine Nd cycle more comprehensively. With this knowledge, we can then strive towards improved capabilities to predict and resolve the non-conservative interactions that cause seawater ε_{Nd} to diverge from conservative water mass mixing, ultimately continuing the robust use of ε_{Nd} as an effective geochemical tracer.

5.2.3 RQ3: To what extent can a seafloor-wide benthic flux explain non-conservative behaviour of Nd isotopes under a global model of marine Nd cycling, and to what extent can global bulk sedimentary ε_{Nd} distributions represent a labile sedimentary flux to seawater?

Recent investigations now suggest that a seafloor-wide benthic flux is a major source of Nd to seawater; i.e., the sediment-ocean flux is not limited to shallow continental margins (Abbott, 2019; Abbott et al., 2015b; Haley et al., 2017; Du et al., 2016). Simple box models, that have been used primarily to investigate the emerging benthic flux hypothesis, suggest that this source is the primary driver of non-conservative behaviour of Nd in the ocean (Du et al., 2016, 2018, 2020; Haley et al., 2017; Pöppelmeier et al., 2020b). Yet, more constraints are essential, particularly in more complex numerical models which attempt to describe the full global marine Nd cycle, to begin establishing where and under what conditions a benthic flux exerts a strong control on seawater ε_{Nd} distributions.

High resolution Nd isotope maps of the global seafloor and continental margins, presented in Chapter 2, and constrained by over 5,100 detrital ε_{Nd} measurements formed the basis for exploring the benthic flux in this thesis. A simulated seafloor-wide benthic

flux, which utilised these bulk detrital ε_{Nd} distributions as boundary conditions, was found to be the major external source of Nd to seawater in the model. Specifically, in the optimised simulation, 64% of total Nd sourced to seawater was apportioned to a seafloor sedimentary source, and this direct deep ocean source played a key role in governing marine Nd budgets (discussed in Sect. 5.2.1).

However, the greater sensitivity of marine Nd distributions and model skill to the efficiency of reversible scavenging (another key non-conservative process acting to drive vertical downward transport of Nd in seawater) compared with the magnitude of a benthic flux in Chapter 3 demonstrated, that alone, a seafloor-wide benthic flux cannot explain all non-conservative behaviour of Nd. Specifically, although a globally uniform benthic flux could explain vertical [Nd] gradients that increase with depth, and drove, in part, the distinct labelling of water masses with unique ε_{Nd} signals, an effective system of reversible scavenging is required. Such reversible scavenging processes are necessary to govern both the global thermohaline variations in [Nd], which increase from the Atlantic to the Pacific (van de Flierdt et al., 2016). Furthermore, reversible scavenging acts to enhance the basinal gradients in simulated ε_{Nd} by maintaining the localised provenance signals through its role in vertical Nd transport and in determining the residence time of Nd in seawater (Siddall et al., 2008b; Pöppelmeier et al., 2022).

Model-data disparity in the North and equatorial Pacific strongly suggests that a specific fraction of sediment with a highly radiogenic ε_{Nd} signature relative to the bulk sediment signal is governing sediment-seawater interactions (see model-data mismatch in Fig. 5.5a). Similarly, model-data mismatch in the northern North Atlantic highlights that the bulk sediment ε_{Nd} is not capturing the Nd sources correctly here, which need to be less radiogenic (Fig. 5.4). Overall, these results uphold the notion that under a globally uniform seafloor-wide benthic flux, the bulk sediment ε_{Nd} distributions cannot be always considered fully representative of the mobile ε_{Nd} composition of the sediment interacting with seawater, eluding to the preferential mobilisation of certain 'reactive' components in the sediment (Du et al., 2016; Abbott et al., 2015b,a, 2016a; Wilson et al., 2013).

Providing insight into the regional mobilisation of 'reactive' sediment phases (Abbott et al., 2015a; Wilson et al., 2013; Du et al., 2016; Lacan and Jeandel, 2005a; Jones et al., 2008; Pearce et al., 2013; Rousseau et al., 2015; Abbott et al., 2016a; Jeandel and Oelkers, 2015), sensitivity studies were performed in Chapter 4; addressing '**OBJ5:** Investigate the spatial extent and preferential mobilisation of certain reactive sediment components from a benthic flux under a global model of the marine cycle' (Chapter 1, Sect. 1.4). These sensitivity studies demonstrated that the seawater ε_{Nd} distributions in the Pacific Ocean were sensitive to the heterogeneity of sediment reactivity and its isotope composition (Fig. 5.5).

Specifically, a more radiogenic benthic flux (relative to the bulk sediment signal) in the Pacific moderately improved model skill, as inferred by returning a global cost function (MAE). Here the Pacific MAE improved from 3.98 ε_{Nd}-units under bulk sediment boundary conditions to 3.04 ε_{Nd}-units under the more radiogenic boundary conditions. However, even under a considerable radiogenic seafloor forcing relative to the bulk sediment ε_{Nd} signal (where minimum labile seafloor sediment ε_{Nd} values were regionally capped at +8 and +10 across the western and eastern equatorial Pacific respectively), the model still simulated too unradiogenic seawater ε_{Nd} signals of -6 in the upper 2,000 m of the Pacific, compared with seawater measurements of -2.5 (Amakawa et al., 2009; Fuhr et al., 2021; Behrens et al., 2018; Fröllje et al., 2016). This model-data offset highlights a significant missing Nd source here, or missing spatial detail describing distinct regions of elevated and isotopically unique benthic fluxes.

In contrast, modern NADW showed a weak sensitivity to large unradiogenic forcings applied within localised sediment regions in the North Atlantic (where the maximum seafloor ε_{Nd} signal interacting with seawater was regionally capped at -34), with the

largest change of -0.4 ε_{Nd}-units (relative to a bulk sediment ε_{Nd} forcing) highly localised to the abyssal northern North Atlantic. This demonstrates foremost that bottom waters in the modern North Atlantic have the propensity to mask the non-conservative effects from a seafloor benthic flux. Here, we suggest that this is caused by vigorous advection in the Atlantic limiting benthic exposure time, alongside an overriding influence on seawater Nd isotope distributions from 'distinct' and 'reactive' surface and marginal inputs around key sites of convection (Abbott et al., 2019; Lambelet et al., 2016; Du et al., 2016). Although this suggests seawater ε_{Nd} characteristics in the modern Atlantic are mostly governed by large-scale ocean circulation and water mass provenance, we cannot assume this Nd cycling regime in the Atlantic holds true for palaeoceanographic applications. For example, evidence of rapid climate oscillations, during the last deglaciation (21-9 ka) (Clark et al., 2012), and large reorganisations of global ocean circulation (Jonkers et al., 2015), suggest that the Atlantic Ocean circulation may have experienced periods where convection strength was reduced (e.g., McManus et al. 2004). Reduced convection strength in the Atlantic would increase the exposure time of bottom water to a seafloor benthic flux (Abbott et al., 2015a; Haley et al., 2017). Coupling this with potentially coinciding changed weathering regimes (e.g., fluxes of poorly chemically weathered ice rafted debris during glacial melting) leads to a multitude of complex processes, all with the potential to influence seawater ε_{Nd}.

Chapter 4 of this thesis provided the first direct comparison of simulated seawater ε_{Nd} under a seafloor-wide (referred to as *'REF-SED3'*) versus a margin-only constrained benthic flux (referred to as *'REF-SED3-MG'*), and provided further evidence for the marked unique regional responses of different ocean basins to changed benthic fluxes (Fig. 5.6). Within this comparison, the ε_{Nd} of sluggish bottom waters within the Pacific Ocean were the most sensitive to non-conservative alterations resulting from an abyssal benthic flux, whilst the North Atlantic once again showed a limited expression of such effects. Here, model skill was actually improved under a margin-only constrained sediment flux, resulting in a more unradiogenic upper NADW ε_{Nd} signal of -13, which was considered to be in excellent agreement with measurements of -13.2 for this water mass (Lambelet et al., 2016), compared with -11 simulated under a seafloor-wide benthic flux.

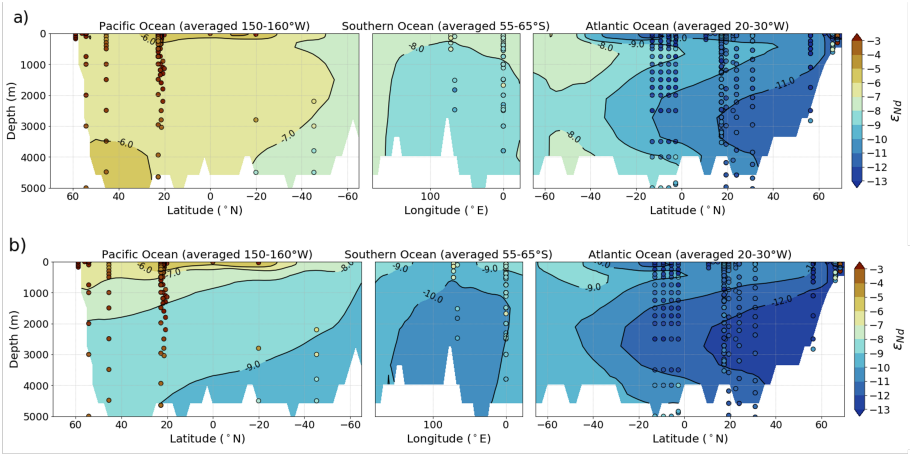

Figure 5.6: Vertical sections of simulated ε_{Nd} within sensitivity studies (a; *REF-SED3*) with a seafloor-wide benthic flux and (b; *REF-SED3-MG*) with a margin-only constrained benthic flux along a transect from the Pacific to Atlantic, traversing the Southern Ocean from West to East. Water column measurements are imposed as filled circles using the same colour scale. Simulated and measured ε_{Nd} from the Pacific are from $150 - 160°$ W, in the Southern Ocean are from $55 - 65°$ S, and in the Atlantic values are from $20 - 30°$ W. The continental margins are constrained following the definition by Robinson et al. (2021), where sediment thickness $\geq$ 1,000 m. Figure reproduced from Chapter 4.

The implications of these studies investigating large-scale non-conservative sedimentary processes demonstrates foremost that the benthic flux is capable of overprinting water mass ε_{Nd} signals. This overprinting occurs particularly in regions of sluggish convection with significant benthic fluxes that have a unique ε_{Nd} relative to that of the overlying seawater.

Thus, and in answer to the original research question, a seafloor-wide benthic flux constitutes the largest Nd source to seawater in our model and can explain non-conservative behaviour of ε_{Nd}. This behaviour is seen especially in the deeper ocean layers, and particularly in the North and equatorial Pacific, whereby a benthic flux, likely of volcanic origin, can explain in part the radiogenic overprint of sluggish deep water measured along its northward flow path (Tachikawa et al., 2017; Jones et al., 2008; Abbott et al., 2015a). Yet, the results from this thesis importantly stress the complex interplay of other key processes that also cause non-conservative deviations in seawater ε_{Nd} from water mass mixing. Notably here, the downward vertical transport of Nd via reversible scavenging, which is especially important for governing seawater ε_{Nd} distributions below 1,000 m, and in the well ventilated North Atlantic. This vertical transport in the water column illustrates that the non-conservative behaviour of marine Nd is not limited to deep abyssal sediment sources. Therefore we cannot assume the ε_{Nd} of a water mass is always resilient to non-conservative overprinting under regions with vigorous circulation and limited benthic flux exposure, supporting recent findings by Pöppelmeier et al. (2022). Lastly, and in answer to the second part of the research question, the results demonstrate clearly that global bulk sedimentary ε_{Nd} distributions cannot represent the labile sedimentary flux to seawater in all instances, supporting the notion of spatial variability and/or the preferential dissolution of mobile sediment phases driving pore water diagenesis and the benthic flux.

5.3 Limitations and future work

5.3.1 Improved spatial constraints on the magnitude and Nd isotope distributions from a benthic flux

At the time of writing this thesis, direct observational measurements of pore water ε_{Nd}, which would best represent the Nd interactions at the sediment-water interface (Du et al., 2020), were severely spatially limited to just three marginal sites in the eastern North Pacific (at depths between 500-3,000 m; Abbott et al. 2015a). As such, in Chapter 2 a pragmatic choice had to be made to also use marine detrital measurements (which are much more widespread and abundant but may not always capture the mobile sediment ε_{Nd} phases) to characterise the sedimentary ε_{Nd} distributions across the seafloor that may represent a Nd source to seawater. To better constrain the flux rates and Nd isotope distributions of a benthic flux, and how they may change under different weathering regimes and environmental conditions, future work should focus on obtaining more direct observational constraints on the broad labile sediment ε_{Nd} interacting with seawater across different seafloor regions. These measurements of the benthic flux could then feed into refining the global sediment ε_{Nd} maps presented in Chapter 2, improving the development of more accurate model boundary conditions.

Moreover, further integrated model-data assessments exploring the sediment composition reactivity of a benthic flux using numerical models, such as those presented in Chapter 4 of this study, would also improve model constraints on the benthic flux and help improve model representation of marine Nd isotope distributions. Such investigations could include assessments into how and where different environmental conditions (e.g., oxygenation, pH, authigenic contributions, organic matter fluxes) may drive more intense localised benthic fluxes. Higher resolution regional models coupled with marine sediment biogeochemical modules are likely best positioned to investigate localised benthic fluxes and the complex processes driving them, detail gained from these models could then feed back into global Nd isotope schemes.

5.3.2 Model limitations and biases

The research presented in this thesis is subject to limitations which arise from physical biases inherent to the applied climate model, and from the parameterisation and assumptions surrounding the representation of complex and elusive biogeochemical processes believed to govern the global marine Nd cycle.

Whilst the Nd isotope scheme developed in this thesis benefits from improved physics relative to intermediate complexity models, the spatial resolution of FAMOUS was shown in Chapters 3 and 4 to limit the representation of large and highly variable surface point Nd sources. Moreover, in Chapter 3 physical model biases in FAMOUS were shown to influence the distribution of simulated Nd isotopes, these biases reflected insufficient Antarctic Bottom Water (AABW) production and penetration into the Atlantic, and are known limitations of the model (Dentith et al., 2019; Smith, 2012). Future work to overcome such limitations resulting from the resolution and physical biases within FAMOUS could therefore directly transfer the Nd isotope scheme into its parent model (HadCM3) which operates at a higher spatial resolution and better represents physical ocean circulation structure, particularly in the Atlantic (Valdes et al., 2017). Transferring the Nd isotope scheme into HadCM3 would also allow for insightful investigations to be made regarding the effects of model resolution on simulated Nd isotope distributions.

Parameterisation within the Nd isotope scheme was necessary to numerically represent the global marine Nd cycle under substantial uncertainty regarding a description of the major sources and sinks of Nd to seawater, which encompasses a complex multitude of different biogeochemical processes, alongside computation constraints. In this study, the simplified global parameterisations of Nd sources and sinks have been identified as likely contributing towards model-data disparities. For example, underestimated [Nd] in the surface layers and an over pronounced vertical gradient are likely caused by the simplified representation of reversible scavenging. A future evolution of the scheme could update this parameterisation of the reversible scavenging by introducing a depth dependent particle settling velocity, this could reduce scavenging efficiency in the surface layers by better accounting for enhanced surface turbulence (Chamecki et al., 2019; Noh et al., 2006) and complexation onto organic ligands (Byrne and Kim, 1990). Although we favoured satellite-derived estimates in order to improve the accuracy of particle-associated cycling of Nd and reduce biases inherent to the intermediate complexity biogeochemistry model (Dentith et al., 2020; Palmer and Todderdell, 2001), the optional ocean biogeochemistry module in FAMOUS (Hadley Centre Ocean Carbon Cycle; HadOCC), which includes simplified nutrient-phytoplankton-zooplankton-detritus (NPZD) classes
(Palmer and Todderdell, 2001), could instead be used as the basis for predicting vertical particle fluxes in the ocean. Comparing the difference between both the satellite derived and HadOCC simulated particle fluxes would provide insights into the potential influence of biological production changes on seawater ε_{Nd} distributions.

Additionally, future efforts to build upon the parameterisation of the benthic flux, which is currently represented by a constant source to seawater across all sediment regions, could explore the response of marine Nd isotope distributions in seawater to regionally elevated benthic sources that are spatially tied to local environmental and sediment conditions.

Any future development to improve the parameterisation of the major sources/sinks and cycling of Nd in seawater would significantly benefit from increased observational measurements of Nd fluxes. Additional measurements of particle-seawater exchange of Nd, occurring both throughout the water column and across the sediment-water interface would especially help towards resolving enigmatic Nd cycling and improving its representation in models. The model calibration methods presented in this study provide an effective template for future efficient and effective parameter space exploration to re-calibrate the

Nd isotope scheme following any future updates to the scheme. Moreover, the optimisation methods could be extended in the future to explore more parameters (e.g., dust fluxes, particle scavenging coefficients, regionally scaled benthic fluxes), and further exploring different model outputs from which the statistical emulator can relate model inputs to (e.g., regional model-data cost functions).

5.3.3 Towards improved spatiotemporal constraints on the marine Nd cycle and its application as an ocean circulation tracer

The Nd isotope scheme development and optimisation used a pre-industrial simulation to best represent, constrain and explore the modern marine Nd cycle by allowing the scheme to be directly compared to modern seawater measurements. To build a greater understanding of where and under what conditions Nd isotopes reflect large-scale ocean circulation patterns, and perhaps more importantly, identify where caution needs to be taken in their interpretation due to non-conservative behaviour, future simulations with the Nd isotope scheme in FAMOUS under different physical ocean circulation states are recommended. Such experiments may include exploring how changed benthic fluxes or particle scavenging (i.e., changed weathering and biogeochemical regimes) influences the distribution of marine Nd isotopes in the Atlantic under idealised experiments with a collapsed or shallowed AMOC state. Combining this analysis of simulated ε_{Nd} with a truly conservative dye tracer and other chemical circulation tracers in FAMOUS (e.g., δ^{13}C; Dentith et al. 2020) would also allow for a more holistic assessment of large-scale ocean circulation, contributing towards better constraints on the circulation properties of Nd isotopes.

The model-data comparison of the Nd isotope scheme in this thesis was limited to modern seawater measurements, therefore a future comparison might explore the difference between simulated ε_{Nd} and extracted authigenic ε_{Nd} signals of bottom waters. Moreover, since numerous interpretations of changed water mass distributions have been inferred by millennial and glacial-interglacial scale variations in ε_{Nd} extracted from marine archives (e.g., Gutjahr et al. 2008; Piotrowski et al. 2012, 2008, 2004; Roberts et al. 2010; Rutberg et al. 2000), the scheme could be applied in reconstructions of past ocean circulation states (e.g., during the Last Glacial Maximum), or within transient reconstructions of abrupt climate changes (e.g., Heinrich and Dansgaard-Oeschger events). Such isotope-enabled palaeoceanographic reconstructions would shed light upon the characteristics of marine Nd isotopes and how sensitive they are to large-scale changed water mass structure, providing important insights into the interpretation of Nd proxy records. To better spatiotemporally constrain non-conservative effects on the archived Nd isotope signal, future idealised reconstructions representing altered Nd sources (their composition, reactivity, and fluxes) resulting from changed weathering regimes (e.g., large and recurring inputs of detrital material during glacial cycles, sea level changes resulting in different exposures of continental material to seawater, and changed atmospheric circulation; impacting direct Nd input from dust and changing biological productivity which in turn influences particle scavenging of Nd) could help explain how and where these processes may obscure the water mass ε_{Nd} signal.

In final remarks, developing a protocol for a coordinated global Nd isotope modelling intercomparison study was an early consideration on the onset of this thesis. Although such a study would provide useful insights into exploring model dependency (i.e., assessing individual model-biases), the results from this thesis suggest that the framework of a global marine Nd models is limited. Despite increased efforts to constrain global marine Nd cycling within sophisticated climate models, there remain significant (reaching offsets of 3-5 ε_{Nd}-units) model-data disparities, which transpose across multiple global isotope schemes (Jones et al., 2008; Rempfer et al., 2011; Gu et al., 2019; Pöppelmeier et al., 2020a; Pasquier et al., 2021; Arsouze et al., 2009). Such errors limit the capability of global Nd

isotope models to accurately resolve what climatic or ocean conditions may drive deviations in seawater ε_{Nd} as observed in the palaeoceanographic record. Moving forwards, the development of regional models, that can better encompass measured seawater Nd profiles, and provide more complex spatiotemporal representations of Nd source/sink distributions, may be better positioned to reconcile the marine Nd cycle and for palaeoceanographic applications.

References

Abbott, A., Löhr, S., Payne, A., Kumar, H., and Du, J. (2022). Widespread lithogenic control of marine authigenic neodymium isotope records? Implications for paleoceanographic reconstructions. *Geochimica et Cosmochimica Acta*, 319:318–336.

Abbott, A. N. (2019). A benthic flux from calcareous sediments results in non-conservative neodymium behavior during lateral transport: A study from the Tasman Sea. *Geology*, 47:363–366.

Abbott, A. N., Haley, B. A., and McManus, J. (2015a). Bottoms up: Sedimentary control of the deep North Pacific Ocean's ϵNd signature. *Geology*, 43(11):1035–1038.

Abbott, A. N., Haley, B. A., and McManus, J. (2016a). The impact of sedimentary coatings on the diagenetic Nd flux. *Earth and Planetary Science Letters*, 449:217–227.

Abbott, A. N., Haley, B. A., McManus, J., and Reimers, C. E. (2015b). The sedimentary flux of dissolved rare earth elements to the ocean. *Geochimica et Cosmochimica Acta*, 154:186–200.

Abbott, A. N., Haley, B. A., Tripati, A. K., and Frank, M. (2016b). Constraints on ocean circulation at the Paleocene-Eocene Thermal Maximum from neodymium isotopes. *Climate of the Past*, 12(4):837–847.

Abbott, A. N., Löhr, S., and Trethewy, M. (2019). Are clay minerals the primary control on the oceanic rare earth element budget? *Frontiers in Marine Science*, 6(504):1–19.

Amakawa, H., Sasaki, K., and Ebihara, M. (2009). Nd isotopic composition in the central North Pacific. *Geochimica et Cosmochimica Acta*, 73(16):4705–4719.

Anav, A., Friedlingstein, P., Kidston, M., Bopp, L., Ciais, P., Cox, P., Jones, C., Jung, M., Myneni, R., and Zhu, Z. (2013). Evaluating the land and ocean components of the global carbon cycle in the CMIP5 earth system models. *Journal of Climate*, 26(18):6801–6843.

Andersen, M. B., Vance, D., Archer, C., Anderson, R. F., Ellwood, M. J., and Allen, C. S. (2011). The Zn abundance and isotopic composition of diatom frustules, a proxy for Zn availability in ocean surface seawater. *Earth and Planetary Science Letters*, 301(1-2):137–145.

Arsouze, T., Dutay, J. C., Kageyama, M., Lacan, F., Alkama, R., Marti, O., and Jeandel, C. (2008). A modeling sensitivity study of the influence of the Atlantic meridional overturning circulation on neodymium isotopic composition at the last glacial maximum. *Climate of the Past*, 4(3):191–203.

Arsouze, T., Dutay, J. C., Lacan, F., and Jeandel, C. (2009). Reconstructing the Nd oceanic cycle using a coupled dynamical- Biogeochemical model. *Biogeosciences*, 6(12):2829–2846.

Arsouze, T., Dutay, J.-C. C., Lacan, F., and Jeandel, C. (2007). Modeling the neodymium isotopic composition with a global ocean circulation model. *Chemical Geology*, 239(1-2):165–177.

Arsouze, T., Treguier, A. M., Peronne, S., Dutay, J. C., Lacan, F., and Jeandel, C. (2010). Modeling the Nd isotopic composition in the North Atlantic basin using an eddy-permitting model. *Ocean Science*, 6(3):789–797.

Asahara, Y., Takeuchi, F., Nagashima, K., Harada, N., Yamamoto, K., Oguri, K., and Tadai, O. (2012). Provenance of terrigenous detritus of the surface sediments in the Bering and Chukchi Seas as derived from Sr and Nd isotopes: Implications for recent climate change in the Arctic regions. *Deep-Sea Research Part II: Topical Studies in Oceanography*, 61-64:155–171.

Astfalck, L. C., Cripps, E. J., Gosling, J. P., and Milne, I. A. (2019). Emulation of vessel motion simulators for computationally efficient uncertainty quantification. *Ocean Engineering*, 172(December 2018):726–736.

Ayache, M., Dutay, J. C., Arsouze, T., Révillon, S., Beuvier, J., and Jeandel, C. (2016). High-resolution neodymium characterization along the Mediterranean margins and modelling of Nd distribution in the Mediterranean basins. *Biogeosciences*, 13(18):5259–5276.

Ayache, M., Dutay, J.-c., Tachikawa, K., Arsouze, T., and Jeandel, C. (2022). Neodymium budget in the Mediterranean Sea : Evaluating the role of atmospheric dusts using a high-resolution dynamical-biogeochemical model. *Biogeosciences Discussions*, (May):1–35.

Bacon, M. P. and Anderson, R. F. (1982). Distribution of Thorium Isotopes Between Dissolved and Particulate Forms in the Deep Sea. *Journal of Geophysical Research*, 87:2045–2056.

Baede, A., Ahlonsou, E., Ding, Y., and Schimel, D. (2001). The climate system: An overview. *TAR Climate Change 2001: The Scientific Basis*, pages 51–64.

Bao, Q., Wu, G. X., Liu, Y. M., Yang, J., Wang, Z. Z., and Zhou, T. J. (2010). An introduction to the coupled model FGOALS1.1-s and its performance in East Asia. *Advances in Atmospheric Sciences*, 27(5):1131–1142.

Basak, C., Pahnke, K., Frank, M., Lamy, F., and Gersonde, R. (2015). Neodymium isotopic characterization of Ross Sea Bottom Water and its advection through the southern South Pacific. *Earth and Planetary Science Letters*, 419:211–221.

Basile, I., Grousset, F. E., Revel, M., Petit, J. R., Biscaye, P. E., and Barkov, N. I. (1997). Patagonian origin of glacial dust deposited in East Antarctica (Vostok and Dome C) during glacial stages 2, 4 and 6. *Earth and Planetary Science Letters*, 146(3-4):573–589.

Bayon, G., German, C. R., Boella, R. M., Milton, J. A., Taylor, R. N., and Nesbitt, R. W. (2002). An improved method for extracting marine sediment fractions and its application to Sr and Nd isotopic analysis. *Chemical Geology*, 187(3-4):179–199.

Bayon, G., German, C. R., Burton, K. W., Nesbitt, R. W., and Rogers, N. (2004). Sedimentary Fe-Mn oxyhydroxides as paleoceanographic archives and the role of aeolian flux in regulating oceanic dissolved REE. *Earth and Planetary Science Letters*, 224(3-4):477–492.

Bayon, G., Toucanne, S., Skonieczny, C., André, L., Bermell, S., Cheron, S., Dennielou, B., Etoubleau, J., Freslon, N., Gauchery, T., Germain, Y., Jorry, S. J., Ménot, G., Monin, L., Ponzevera, E., Rouget, M. L., Tachikawa, K., and Barrat, J. A. (2015). Rare earth elements and neodymium isotopes in world river sediments revisited. *Geochimica et Cosmochimica Acta*, 170:17–38.

Behrenfeld, M. J. and Falkowski, P. G. (1997). Photosynthetic rates derived from satellite-based chlorophyll concentration. *LIMNOLOGY AND OCEANOGRAPHY Lmnnl. Oceunogr*, 42.

Behrens, M. K., Pahnke, K., Schnetger, B., and Brumsack, H. J. (2018). Sources and processes affecting the distribution of dissolved Nd isotopes and concentrations in the West Pacific. *Geochimica et Cosmochimica Acta*, 222:508–534.

Bertram, C. J. and Elderfield, H. (1993). The geochemical balance of the rare earth elements and neodymium isotopes in the oceans. *Geochimica et Cosmochimica Acta*, 57(9):1957–1986.

Bertram, C. J., Elderfield, H., Shackleton, N. J., and MacDonald, J. A. (1995). Cadmium/calcium and carbon isotope reconstructions of the glacial northeast Atlantic Ocean. *Paleoceanography*, 10(3):563–578.

Bigg, G. R., Jickells, T. D., Liss, P. S., and Osborn, T. J. (2003). The role of the oceans in climate. *International Journal of Climatology*, 23(10):1127–1159.

Blanchet, C. L. (2019). A database of marine and terrestrial radiogenic Nd and Sr isotopes for tracing earth-surface processes. *Earth System Science Data*, 11(2):741–759.

Blaser, P., Frank, M., and van de Flierdt, T. (2019a). Revealing past ocean circulation with neodymium isotopes. *Past Global Changes Magazine*, 27(2):54–55.

Blaser, P., Gutjahr, M., Pöppelmeier, F., Frank, M., Kaboth-Bahr, S., and Lippold, J. (2020). Labrador Sea bottom water provenance and REE exchange during the past 35,000 years. *Earth and Planetary Science Letters*, 542:116299.

Blaser, P., Lippold, J., Gutjahr, M., Frank, N., Link, J. M., and Frank, M. (2016). Extracting foraminiferal seawater Nd isotope signatures from bulk deep sea sediment by chemical leaching. *Chemical Geology*, 439:189–204.

Blaser, P., Pöppelmeier, F., Schulz, H., Gutjahr, M., Frank, M., Lippold, J., Heinrich, H., Link, J. M., Hoffmann, J., Szidat, S., and Frank, N. (2019b). The resilience and sensitivity of Northeast Atlantic deep water ϵNd to overprinting by detrital fluxes over the past 30,000 years. *Geochimica et Cosmochimica Acta*, 245:79–97.

Bohm, E., Lippold, J., Gutjahr, M., Frank, M., Blaser, P., Antz, B., Fohlmeister, J., Frank, N., Andersen, M. B., and Deininger, M. (2015). Strong and deep Atlantic meridional overturning circulation during the last glacial cycle. *Nature*, 517(7532):73–76.

Boyle, E. A. and Keigwin, L. D. (1982). Deep circulation of the North Atlantic over the last 200,000 Years: Geochemical evidence. *Science*, 218(4574):784–787.

Broecker, W., Barker, S., Clark, E., Hajdas, I., Bonani, G., and Stott, L. (2004). Ventilation of the glacial deep pacific ocean. *Science*, 306(5699):1169–1172.

Broecker, W. and Peng, T.-H. (1982). *Tracers in the sea*. Palisades, NY.

Broecker, W. S. (1997). Thermohaline circulation, the achilles heel of our climate system: Will man-made CO2 upset the current balance? *Science*, 278(5343):1582–1588.

Broecker, W. S., Gerard, R., Ewing, M., and Heezen, B. C. (1960). Natural radiocarbon in the Atlantic Ocean. *Journal of Geophysical Research*, 65(9):2903–2931.

Bryan, K. (1969). A numerical method for the study of the circulation of the world ocean. *Journal of Computational Physics*, 4(3):347–376.

Bryce, J. G., DePaolo, D. J., and Lassiter, J. C. (2005). Geochemical structure of the Hawaiian plume: Sr, Nd, and Os isotopes in the 2.8 km HSDP-2 section of Mauna Kea volcano. *Geochemistry, Geophysics, Geosystems*, 6(9).

Buckley, M. W. and Marshall, J. (2016). Observations, inferences, and mechanisms of the Atlantic Meridional Overturning Circulation: A review.

Byrne, R. H. and Kim, K. H. (1990). Rare earth element scavenging in seawater. *Geochimica et Cosmochimica Acta*, 54(10):2645–2656.

Chamecki, M., Chor, T., Yang, D., and Meneveau, C. (2019). Material Transport in the Ocean Mixed Layer: Recent Developments Enabled by Large Eddy Simulations.

Chase, Z., Anderson, R. F., Fleisher, M. Q., and Kubik, P. W. (2002). The influence of particle composition and particle flux on scavenging of Th, Pa and Be in the ocean. *Earth and Planetary Science Letters*, 204(1-2):215–229.

Chavagnac, V., Saleban Ali, H., Jeandel, C., Leleu, T., Destrigneville, C., Castillo, A., Cotte, L., Waeles, M., Cathalot, C., Laes-Huon, A., Pelleter, E., Nonnotte, P., Sarradin, P. M., and Cannat, M. (2018). Sulfate minerals control dissolved rare earth element flux and Nd isotope signature of buoyant hydrothermal plume (EMSO-Azores, 37°N Mid-Atlantic Ridge). *Chemical Geology*, 499:111–125.

Chen, T. Y., Stumpf, R., Frank, M., Bełdowski, J., and Staubwasser, M. (2013). Contrasting geochemical cycling of hafnium and neodymium in the central Baltic Sea. *Geochimica et Cosmochimica Acta*, 123:166–180.

Clark, P. U., Shakun, J. D., Baker, P. A., Bartlein, P. J., Brewer, S., Brook, E., Carlson, A. E., Cheng, H., Kaufman, D. S., Liu, Z., Marchitto, T. M., Mix, A. C., Morrill, C., Otto-Bliesner, B. L., Pahnke, K., Russell, J. M., Whitlock, C., Adkins, J. F., Blois, J. L., Clark, J., Colman, S. M., Curry, W. B., Flower, B. P., He, F., Johnson, T. C., Lynch-Stieglitz, J., Markgraf, V., McManus, J., Mitrovica, J. X., Moreno, P. I., and Williams, J. W. (2012). Global climate evolution during the last deglaciation. *Proceedings of the National Academy of Sciences of the United States of America*, 109(19):E1134–E1142.

Claussen, M., Mysak, L., Weaver, A., Crucifix, M., Fichefet, T., Loutre, M. F., Weber, S., Alcamo, J., Alexeev, V., Berger, A., Calov, R., Ganopolski, A., Goosse, H., Lohmann, G., Lunkeit, F., Mokhov, I., Petoukhov, V., Stone, P., and Wang, Z. (2002). Earth system models of intermediate complexity: Closing the gap in the spectrum of climate system models. *Climate Dynamics*, 18(7):579–586.

Collins, W. J., Bellouin, N., Doutriaux-Boucher, M., Gedney, N., Halloran, P., Hinton, T., Hughes, J., Jones, C. D., Joshi, M., Liddicoat, S., Martin, G., O'Connor, F., Rae, J., Senior, C., Sitch, S., Totterdell, I., Wiltshire, A., and Woodward, S. (2011). Development and evaluation of an Earth-System model - HadGEM2. *Geoscientific Model Development*, 4(4):1051–1075.

Cook, C. P., van de Flierdt, T., Williams, T., Hemming, S. R., Iwai, M., Kobayashi, M., Jimenez-Espejo, F. J., Escutia, C., González, J. J., Khim, B. K., McKay, R. M., Passchier, S., Bohaty, S. M., Riesselman, C. R., Tauxe, L., Sugisaki, S., Galindo, A. L., Patterson, M. O., Sangiorgi, F., Pierce, E. L., Brinkhuis, H., Klaus, A., Fehr, A., Bendle, J. A., Bijl, P. K., Carr, S. A., Dunbar, R. B., Flores, J. A., Hayden, T. G., Katsuki, K., Kong, G. S., Nakai, M., Olney, M. P., Pekar, S. F., Pross, J., Röhl, U., Sakai, T., Shrivastava, P. K., Stickley, C. E., Tuo, S., Welsh, K., and Yamane, M. (2013). Dynamic behaviour of the East Antarctic ice sheet during Pliocene warmth. *Nature Geoscience*, 6(9):765–769.

Cox, M. D. (1984). *A primitive equation 3-dimensional model of the ocean.* Number 1.

Cox, P. M., Betts, R. A., Bunton, C. B., Essery, R. L., Rowntree, P. R., and Smith, J. (1999). The impact of new land surface physics on the GCM simulation of climate and climate sensitivity. *Climate Dynamics*, 15(3):183–203.

Crocket, K. C., Hill, E., Abell, R. E., Johnson, C., Gary, S. F., Brand, T., and Hathorne, E. C. (2018). Rare earth element distribution in the ne Atlantic: Evidence for benthic sources, longevity of the seawater signal, and biogeochemical cycling. *Frontiers in Marine Science*, 5(147).

Crossley, J. F. and Roberts, D. L. (1995). THE THERMODYNAMIC / DYNAMIC SEA ICE MODEL. *Unified model documentation paper No 45*, (45).

Dai, A. and Trenberth, K. E. (2002). Estimates of Freshwater Discharge from Continents : Latitudinal and Seasonal Variations. *Journal of Hydrometeorology*, 3:660–687.

Dausmann, V., Frank, M., Gutjahr, M., and Rickli, J. (2017). Glacial reduction of AMOC strength and long-term transition in weathering inputs into the Southern Ocean since the mid-Miocene: Evidence from radiogenic Nd and Hf isotopes. *Paleoceanography*, 32(3):265–283.

Dentith, J. E., Ivanovic, R., Gregoire, L., Tindall, J., Robinson, L., and Valdes, P. (2019). Simulating oceanic radiocarbon with the FAMOUS GCM: implications for its use as a proxy for ventilation and carbon uptake. *Biogeosciences Discussions*, pages 1–46.

Dentith, J. E., Ivanovic, R. F., Gregoire, L. J., Tindall, J. C., and Robinson, L. F. (2020). Simulating stable carbon isotopes in the ocean component of the FAMOUS general circulation model with MOSES1 (XOAVI). *Geoscientific Model Development*, 13(8):3529–3552.

Dixon, K. W., Delworth, T. L., Knutson, T. R., Spelman, M. J., and Stouffer, R. J. (2003). A comparison of climate change simulations produced by two GFDL coupled climate models. *Global and Planetary Change*, 37(1-2):81–102.

Doney, S. C., Lindsay, K., Caldeira, K., Campin, J. M., Drange, H., Dutay, J. C., Follows, M., Gao, Y., Gnanadesikan, A., Gruber, N., Ishida, A., Joos, F., Madec, G., Maier-Reimer, E., Marshall, J. C., Matear, R. J., Monfray, P., Mouchet, A., Najjar, R., Orr, J. C., Plattner, G. K., Sarmiento, J., Schlitzer, R., Slater, R., Totterdell, I. J., Weirig, M. F., Yamanaka, Y., and Yool, A. (2004). Evaluating global ocean carbon models: The importance of realistic physics. *Global Biogeochemical Cycles*, 18(3):3017.

Du, J., Haley, B. A., and Mix, A. C. (2016). Neodymium isotopes in authigenic phases, bottom waters and detrital sediments in the Gulf of Alaska and their implications for paleo-circulation reconstruction. *Geochimica et Cosmochimica Acta*, 193:14–35.

Du, J., Haley, B. A., and Mix, A. C. (2020). Evolution of the Global Overturning Circulation since the Last Glacial Maximum based on marine authigenic neodymium isotopes. *Quaternary Science Reviews*, 241:106396.

Du, J., Haley, B. A., Mix, A. C., Walczak, M. H., and Praetorius, S. K. (2018). Flushing of the deep Pacific Ocean and the deglacial rise of atmospheric CO2 concentrations. *Nature Geoscience*, 11(10):749–755.

Dunne, J. P., Hales, B., and Toggweiler, J. R. (2012). Global calcite cycling constrained by sediment preservation controls. *Global Biogeochemical Cycles*, 26(3):1–14.

Dunne, J. P., Sarmiento, J. L., and Gnanadesikan, A. (2007). A synthesis of global particle export from the surface ocean and cycling through the ocean interior and on the seafloor. *Global Biogeochemical Cycles*, 21(4):1–16.

Dutay, J. C., Lacan, F., Roy-Barman, M., and Bopp, L. (2009). Influence of particle size and type on 231Pa and 230Th simulation with a global coupled biogeochemical-ocean general circulation model: A first approach. *Geochemistry, Geophysics, Geosystems*, 10(1):1–26.

Dutkiewicz, A., Müller, R. D., O'Callaghan, S., and Jónasson, H. (2015). Census of seafloor sediments in the world's ocean. *Geology*, 43(9):795–798.

Ehlert, C., Frank, M., Haley, B. A., Böniger, U., De Deckker, P., and Gingele, F. X. (2011). Current transport versus continental inputs in the eastern Indian Ocean: Radiogenic isotope signatures of clay size sediments. *Geochemistry, Geophysics, Geosystems*, 12(6).

Elderfield, H., Upstill-Goddard, R., and Sholkovitz, E. R. (1990). The rare earth elements in rivers, estuaries, and coastal seas and their significance to the composition of ocean waters. *Geochimica et Cosmochimica Acta*, 54(4):971–991.

Elmore, A. C., Piotrowski, A. M., Wright, J. D., and Scrivner, A. E. (2011). Testing the extraction of past seawater Nd isotopic composition from North Atlantic deep sea sediments and foraminifera. *Geochemistry, Geophysics, Geosystems*, 12(9):9008.

England, M. H. and Maier-Reimer, E. (2001). Using Chemical Tracers to Assess Ocean Models. *Reviews of Geophysics*, 39(1):29–70.

Essery, R. L., Best, M. J., Betts, R. A., Cox, P. M., and Taylor, C. M. (2003). Explicit representation of subgrid heterogeneity in a GCM land surface scheme. *Journal of Hydrometeorology*, 4(3):530–543.

Essery, R. L. H., Best, M., and Cox, P. (2001). MOSES 2.2 technical documentation. Hadley Centre Technical Note 30.

Ferreira, D., Cessi, P., Coxall, H. K., De Boer, A., Dijkstra, H. A., Drijfhout, S. S., Eldevik, T., Harnik, N., McManus, J. F., Marshall, D. P., Nilsson, J., Roquet, F., Schneider, T., and Wills, R. C. (2018). Atlantic-Pacific Asymmetry in Deep Water Formation.

Fielding, L., Najman, Y., Millar, I., Butterworth, P., Ando, S., Padoan, M., Barfod, D., and Kneller, B. (2017). A detrital record of the Nile River and its catchment. *Journal of the Geological Society*, 174(2):301–317.

Flato, G., Marotzke, J., Abiodun, B., Braconnot, P., Sin Chan Chou, Collins, W., Cox, P., Driouech, F., Emori, S., Eyring, V., Forest, C., Gleckler, P., Guilyardi, E., Jakob, C., Kattsov, V., Reason, C., and Rummukainen, M. (2013). Evaluation of climate models. Technical report, Cambridge University Press, Cambridge, United Kingdom and New York, NY, USA.

Flato, G. M. (2011). Earth system models: An overview. *Wiley Interdisciplinary Reviews: Climate Change*, 2(6):783–800.

Frajka-Williams, E., Ansorge, I. J., Baehr, J., Bryden, H. L., Chidichimo, M. P., Cunningham, S. A., Danabasoglu, G., Dong, S., Donohue, K. A., Elipot, S., Heimbach, P., Holliday, N. P., Hummels, R., Jackson, L. C., Karstensen, J., Lankhorst, M., Le Bras, I. A., Susan Lozier, M., McDonagh, E. L., Meinen, C. S., Mercier, H., Moat, B. I., Perez, R. C., Piecuch, C. G., Rhein, M., Srokosz, M. A., Trenberth, K. E., Bacon, S., Forget, G., Goni, G., Kieke, D., Koelling, J., Lamont, T., McCarthy, G. D., Mertens, C., Send, U., Smeed, D. A., Speich, S., van den Berg, M., Volkov, D., and Wilson, C. (2019). Atlantic meridional overturning circulation: Observed transport and variability.

Frank, M. (2002). Radiogenic isotopes: Tracers of past ocean circulation and erosional input. *Reviews of Geophysics*, 40(1):1001.

Frierson, D. M., Hwang, Y. T., Fučkar, N. S., Seager, R., Kang, S. M., Donohoe, A., Maroon, E. A., Liu, X., and Battisti, D. S. (2013). Contribution of ocean overturning circulation to tropical rainfall peak in the Northern Hemisphere. *Nature Geoscience*, 6(11):940–944.

Fröllje, H., Pahnke, K., Schnetger, B., Brumsack, H. J., Dulai, H., and Fitzsimmons, J. N. (2016). Hawaiian imprint on dissolved Nd and Ra isotopes and rare earth elements in the central North Pacific: Local survey and seasonal variability. *Geochimica et Cosmochimica Acta*, 189:110–131.

Fuhr, M., Laukert, G., Yu, Y., Nürnberg, D., and Frank, M. (2021). Tracing Water Mass Mixing From the Equatorial to the North Pacific Ocean With Dissolved Neodymium Isotopes and Concentrations. *Frontiers in Marine Science*, 7:1261.

Ganachaud, A. and Wunsch, C. (2000). Improved estimates of global ocean circulation, heat transport and mixing from hydrographic data. *Nature*, 408(6811):453–457.

Ganopolski, A. and Rahmstorf, S. (2001). Rapid changes of glacial climate simulated in a coupled climate model. *Nature*, 409(6817):153–158.

GEOTRACES Intermediate Data Product Group (2021). The GEOTRACES Intermediate Data Product 2021 (IDP2021).

Gherardi, J. M., Labeyrie, L., McManus, J. F., Francois, R., Skinner, L. C., and Cortijo, E. (2005). Evidence from the Northeastern Atlantic basin for variability in the rate of the meridional overturning circulation through the last deglaciation. *Earth and Planetary Science Letters*, 240(3-4):710–723.

Gischler, E. (2006). Sedimentation on Rasdhoo and Ari Atolls, Maldives, Indian ocean. *Facies*, 52(3):341–360.

Godwin, H. (1962). Half-life of Radiocarbon. *Nature*, 195:984.

Goldberg, E. L., Phedorin, M. A., Chebykin, E. P., Khlystov, O. M., and Zhuchenko, N. A. (2008). The decade-resolved record of the response of East Siberia to abrupt climatic changes in the North Atlantic over the last glacial-interglacial cycle. *Doklady Earth Sciences*, 421(2):961–964.

Goldstein, S. and Hemming, S. (2003). Long-lived Isotopic Tracers in Oceanography, Paleoceanography, and Ice-Sheet Dynamics. *Treatise on Geochemistry*, pages 453–483.

Goldstein, S. J. and Jacobsen, S. B. (1987). The Nd and Sr isotopic systematics of river-water dissolved material: Implications for the sources of Nd and Sr in seawater. Technical report.

Goldstein, S. J. and Jacobsen, S. B. (1988). Rare earth elements in river waters. *Earth and Planetary Science Letters*, 89(1):35–47.

Goldstein, S. L., Arndt, N. T., and Stallard, R. F. (1997). The history of a continent from U-Pb ages of zircons from Orinoco River sand and Sm-Nd isotopes in Orinoco basin river sediments. *Chemical Geology*, 139(1-4):271–286.

Goldstein, S. L. and O'Nions, R. K. (1981). Nd and Sr isotopic relationships in pelagic clays and gerromanganese deposits. *Nature*, 292:324–327.

Goldstein, S. L., O'Nions, R. K., and Hamilton, P. J. (1984). A Sm-Nd isotopic study of atmospheric dusts and particulates from major river systems. *Earth and Planetary Science Letters*, 70(2):221–236.

Goosse, H., Brovkin, V., Fichefet, T., Haarsma, R., Huybrechts, P., Jongma, J., Mouchet, A., Selten, F., Barriat, P. Y., Campin, J. M., Deleersnijder, E., Driesschaert, E., Goelzer, H., Janssens, I., Loutre, M. F., Morales Maqueda, M. A., Opsteegh, T., Mathieu, P. P., Munhoven, G., Pettersson, E. J., Renssen, H., Roche, D. M., Schaeffer, M., Tartinville, B., Timmermann, A., and Weber, S. L. (2010). Description of the Earth system model of intermediate complexity LOVECLIM version 1.2. *Geoscientific Model Development*, 3(2):603–633.

Gordon, C., Cooper, C., Senior, C. A., Banks, H., Gregory, J. M., Johns, T. C., Mitchell, J. F., and Wood, R. A. (2000). The simulation of SST, sea ice extents and ocean heat transports in a version of the Hadley Centre coupled model without flux adjustments. *Climate Dynamics*, 16(2-3):147–168.

Gorsline, D. S. (1984). A review of fine-grained sediment origins, characteristics, transport and deposition. *Geological Society Special Publication*, 15:17–34.

Grasse, P., Stichel, T., Stumpf, R., Stramma, L., and Frank, M. (2012). The distribution of neodymium isotopes and concentrations in the Eastern Equatorial Pacific: Water mass advection versus particle exchange. *Earth and Planetary Science Letters*, 353-354:198–207.

Greaves, M. J., Statham, P. J., and Elderfield, H. (1994). Rare earth element mobilization from marine atmospheric dust into seawater. *Marine Chemistry*, 46(3):255–260.

Gregoire, L. J., Otto-Bliesner, B., Valdes, P. J., and Ivanovic, R. (2016). Abrupt Bølling warming and ice saddle collapse contributions to the Meltwater Pulse 1a rapid sea level rise. *Geophysical Research Letters*, 43(17):9130–9137.

Gregoire, L. J., Payne, A. J., and Valdes, P. J. (2012). Deglacial rapid sea level rises caused by ice-sheet saddle collapses. *Nature*, 487(7406):219–222.

Gregoire, L. J., Valdes, P. J., and Payne, A. J. (2015). The relative contribution of orbital forcing and greenhouse gases to the North American deglaciation. *Geophysical Research Letters*, 42(22):9970–9979.

Gregoire, L. J., Valdes, P. J., Payne, A. J., and Kahana, R. (2011). Optimal tuning of a GCM using modern and glacial constraints. *Climate Dynamics*, 37(3):705–719.

Gregory, J. M., Browne, O. J., Payne, A. J., Ridley, J. K., and Rutt, I. C. (2012). Modelling large-scale ice-sheet-climate interactions following glacial inception. *Climate of the Past*, 8(5):1565–1580.

Grenier, M., Jeandel, C., Lacan, F., Vance, D., Venchiarutti, C., Cros, A., and Cravatte, S. (2013). From the subtropics to the central equatorial Pacific Ocean: Neodymium isotopic composition and rare earth element concentration variations. *Journal of Geophysical Research: Oceans*, 118(2):592–618.

Grousset, F. E., Biscaye, P. E., Revel, M., Petit, J. R., Pye, K., Joussaume, S., and Jouzel, J. (1992). Antarctic (Dome C) ice-core dust at 18 k.y. B.P.: Isotopic constraints on origins. *Earth and Planetary Science Letters*, 111(1):175–182.

Grousset, F. E., Biscaye, P. E., Zindler, A., Prospero, J., and Chester, R. (1988). Neodymium isotopes as tracers in marine sediments and aerosols: North Atlantic. *Earth and Planetary Science Letters*, 87(4):367–378.

Grousset, F. E., Parra, M., Bory, A., Martinez, P., Bertrand, P., Shimmield-M, G., and Ellamn, R. M. (1998). Saharan Wind Regimes Traced by the Sr-Nd Isotopic Composition of Subtropical Atlantic Sediments: Last Glacial Maximum vs Today. Technical report.

Gu, S., Liu, Z., Jahn, A., Rempfer, J., Zhang, J., and Joos, F. (2019). Modeling Neodymium Isotopes in the Ocean Component of the Community Earth System Model (CESM1). *Journal of Advances in Modeling Earth Systems*, 11(3):624–640.

Gupta, R. S. and Naqvi, S. W. (1984). Chemical oceanography of the Indian Ocean, north of the equator. *Deep Sea Research Part A, Oceanographic Research Papers*, 31(6-8):671–706.

Gutjahr, M., Frank, M., Stirling, C. H., Keigwin, L. D., and Halliday, A. N. (2008). Tracing the Nd isotope evolution of North Atlantic Deep and Intermediate Waters in the western North Atlantic since the Last Glacial Maximum from Blake Ridge sediments. *Earth and Planetary Science Letters*, 266(1-2):61–77.

Gutjahr, M., Frank, M., Stirling, C. H., Klemm, V., van de Flierdt, T., and Halliday, A. N. (2007). Reliable extraction of a deepwater trace metal isotope signal from Fe-Mn oxyhydroxide coatings of marine sediments. *Chemical Geology*, 242(3-4):351–370.

Hague, A. M., Thomas, D. J., Huber, M., Korty, R., Woodard, S. C., and Jones, L. B. (2012). Convection of North Pacific deep water during the early Cenozoic. *Geology*, 40(6):527–530.

Haley, B. A., Du, J., Abbott, A. N., and McManus, J. (2017). The Impact of Benthic Processes on Rare Earth Element and Neodymium Isotope Distributions in the Oceans. *Frontiers in Marine Science*, 4:426.

Haley, B. A., Frank, M., Hathorne, E., and Pisias, N. (2014). Biogeochemical implications from dissolved rare earth element and Nd isotope distributions in the Gulf of Alaska. *Geochimica et Cosmochimica Acta*, 126:455–474.

Haley, B. A., Klinkhammer, G. P., and McManus, J. (2004). Rare earth elements in pore waters of marine sediments. *Geochimica et Cosmochimica Acta*, 68(6):1265–1279.

Haley, B. A. and Polyak, L. (2013). Pre-modern Arctic Ocean circulation from surface sediment neodymium isotopes. *Geophysical Research Letters*, 40(5):893–897.

Haley, B. A., Wu, Y., Muratli, J. M., Basak, C., Pena, L. D., and Goldstein, S. L. (2021). Rare earth element and neodymium isotopes of the eastern US GEOTRACES Equatorial Pacific Zonal Transect (GP16). *Earth and Planetary Science Letters*, 576:117233.

Hall, R. (2002). Cenozoic geological and plate tectonic evolution of SE Asia and the SW Pacific: Computer-based reconstructions, model and animations. *Journal of Asian Earth Sciences*, 20(4):353–431.

Hammond, J. O., Kendall, J. M., Collier, J. S., and Rümpker, G. (2013). The extent of continental crust beneath the Seychelles. *Earth and Planetary Science Letters*, 381:166–176.

Han, Y., Zhao, T., Song, L., Fang, X., Yin, Y., Deng, Z., Wang, S., and Fan, S. (2011). A linkage between Asian dust, dissolved iron and marine export production in the deep ocean. *Atmospheric Environment*, 45(25):4291–4298.

Hawkins, E., Smith, R. S., Gregory, J. M., and Stainforth, D. A. (2016). Irreducible uncertainty in near-term climate projections. *Climate Dynamics*, 46(11-12):3807–3819.

Hemming, S. R., Van De Flierdt, T., Goldstein, S. L., Franzese, A. M., Roy, M., Gastineau, G., and Landrot, G. (2007). Strontium isotope tracing of terrigenous sediment dispersal in the Antarctic circumpolar current: Implications for constraining frontal positions. *Geochemistry, Geophysics, Geosystems*, 8(6).

Henderson, G. M., Heinze, C., Anderson, R. F., and Winguth, A. M. (1999). Global distribution of the 230Th flux to ocean sediments constrained by GCM modelling. *Deep-Sea Research Part I: Oceanographic Research Papers*, 46(11):1861–1893.

Henry, L. G., McManus, J. F., Curry, W. B., Roberts, N. L., Piotrowski, A. M., and Keigwin, L. D. (2016). North Atlantic ocean circulation and abrupt climate change during the last glaciation. *Science*, 353(6298):470–474.

Homoky, W. B., Weber, T., Berelson, W. M., Conway, T. M., Henderson, G. M., Van Hulten, M., Jeandel, C., Severmann, S., and Tagliabue, A. (2016). Quantifying trace element and isotope fluxes at the ocean-sediment boundary: A review. *Philosophical Transactions of the Royal Society A*, 374(20160246).

Hopcroft, P. O. and Valdes, P. J. (2015). Last glacial maximum constraints on the Earth System model HadGEM2-ES. *Climate Dynamics*, 45(5-6):1657–1672.

Horikawa, K., Asahara, Y., Yamamoto, K., and Okazaki, Y. (2010). Intermediate water formation in the Bering Sea during glacial periods: Evidence from neodymium isotope ratios. *Geology*, 38(5):435–438.

Howe, J. N., Piotrowski, A. M., Hu, R., and Bory, A. (2017). Reconstruction of east–west deep water exchange in the low latitude Atlantic Ocean over the past 25,000 years. *Earth and Planetary Science Letters*, 458:327–336.

Howe, J. N., Piotrowski, A. M., Noble, T. L., Mulitza, S., Chiessi, C. M., and Bayon, G. (2016). North Atlantic Deep Water Production during the Last Glacial Maximum. *Nature Communications*, 7.

Hu, R. and Piotrowski, A. M. (2018). Neodymium isotope evidence for glacial-interglacial variability of deepwater transit time in the Pacific Ocean. *Nature Communications*, 9(1):1–12.

Hu, R., Piotrowski, A. M., Bostock, H. C., Crowhurst, S., and Rennie, V. (2016). Variability of neodymium isotopes associated with planktonic foraminifera in the Pacific Ocean during the Holocene and Last Glacial Maximum. *Earth and Planetary Science Letters*, 447:130–138.

Huck, C. E., Van De Flierdt, T., Jiménez-Espejo, F. J., Bohaty, S. M., Röhl, U., and Hammond, S. J. (2016). Robustness of fossil fish teeth for seawater neodymium isotope reconstructions under variable redox conditions in an ancient shallow marine setting. *Geochemistry, Geophysics, Geosystems*, 17(3):679–698.

Huybrechts, P., Goelzer, H., Janssens, I., Driesschaert, E., Fichefet, T., Goosse, H., and Loutre, M. F. (2011). Response of the Greenland and Antarctic Ice Sheets to Multi-Millennial Greenhouse Warming in the Earth System Model of Intermediate Complexity LOVECLIM. *Surveys in Geophysics*, 32(4-5):397–416.

Innocent, C., Fagel, N., Stevenson, R. K., and Hillaire-Marcel, C. (1997). Sm-Nd signature of modern and late Quaternary sediments from the northwest North Atlantic: Implications for deep current changes since the Last Glacial Maximum. *Earth and Planetary Science Letters*, 146(3-4):607–625.

Ivanovic, R. F., Gregoire, L. J., Kageyama, M., Roche, D. M., Valdes, P. J., Burke, A., Drummond, R., Peltier, W. R., and Tarasov, L. (2016). Transient climate simulations of the deglaciation 21-9 thousand years before present (version 1) - PMIP4 Core experiment design and boundary conditions. *Geoscientific Model Development*, 9(7):2563–2587.

Jacobsen, S. B. and Wasserburg, G. J. (1980). Sm-Nd evolution of chondrites. *Earth and Planetary Science Letters*, 50:139–155.

Jahnke, R. A., Emerson, S. R., Reimers, C. E., Schuffert, J., Ruttenberg, K., and Archer, D. (1989). Benthic recycling of biogenic debris in the eastern tropical Atlantic Ocean. *Geochimica et Cosmochimica Acta*, 53(11):2947–2960.

Jeandel, C. (1993). Concentration and isotopic composition of Nd in the South Atlantic Ocean. *Earth and Planetary Science Letters*, 117(3-4):581–591.

Jeandel, C. (2016). Overview of the mechanisms that could explain the 'Boundary Exchange' at the land-ocean contact.

Jeandel, C., Arsouze, T., Lacan, F., Téchiné, P., and Dutay, J. C. (2007). Isotopic Nd compositions and concentrations of the lithogenic inputs into the ocean: A compilation, with an emphasis on the margins. *Chemical Geology*, 239(1-2):156–164.

Jeandel, C., Bishop, J. K., and Zindler, A. (1995). Exchange of neodymium and its isotopes between seawater and small and large particles in the Sargasso Sea. *Geochimica et Cosmochimica Acta*, 59(3):535–547.

Jeandel, C., Delattre, H., Grenier, M., Pradoux, C., and Lacan, F. (2013). Rare earth element concentrations and Nd isotopes in the Southeast Pacific Ocean. *Geochemistry, Geophysics, Geosystems*, 14(2):328–341.

Jeandel, C. and Oelkers, E. H. (2015). The influence of terrigenous particulate material dissolution on ocean chemistry and global element cycles.

Johannesson, K. H. and Burdige, D. J. (2007). Balancing the global oceanic neodymium budget: Evaluating the role of groundwater. *Earth and Planetary Science Letters*, 253(1-2):129–142.

Johns, W. E., Baringer, M. O., Beal, L. M., Cunningham, S. A., Kanzow, T., Bryden, H. L., Hirschi, J. J., Marotzke, J., Meinen, C. S., Shaw, B., and Curry, R. (2011). Continuous, array-based estimates of atlantic ocean heat transport at 26.5°N. *Journal of Climate*, 24(10):2429–2449.

Jones, C. (2003). A fast ocean GCM without flux adjustments. *Journal of Atmospheric and Oceanic Technology*, 20(12):1857–1868.

Jones, C., Gregory, J., Thorpe, R., Cox, P., Murphy, J., Sexton, D., and Valdes, P. (2005). Systematic optimisation and climate simulation of FAMOUS, a fast version of HadCM3. *Climate Dynamics*, 25(2-3):189–204.

Jones, C. E., Halliday, A. N., Rea, D. K., and Owen, R. M. (1994). Neodymium isotopic variations in North Pacific modern silicate sediment and the insignificance of detrital REE contributions to seawater. *Earth and Planetary Science Letters*, 127(1-4):55–66.

Jones, K. M., Khatiwala, S. P., Goldstein, S. L., Hemming, S. R., and van de Flierdt, T. (2008). Modeling the distribution of Nd isotopes in the oceans using an ocean general circulation model. *Earth and Planetary Science Letters*, 272:610–619.

Jonkers, L., Zahn, R., Thomas, A., Henderson, G., Abouchami, W., François, R., Masque, P., Hall, I. R., and Bickert, T. (2015). Deep circulation changes in the central South Atlantic during the past 145 kyrs reflected in a combined231Pa/230Th, Neodymium isotope and benthic δC13 record. *Earth and Planetary Science Letters*, 419:14–21.

Joshi, M., von Glasow, R., Smith, R. S., Paxton, C. G., Maycock, A. C., Lunt, D. J., Loptson, C., and Markwick, P. (2017). Global warming and ocean stratification: A potential result of large extraterrestrial impacts. *Geophysical Research Letters*, 44(8):3841–3848.

Kamenov, G. D. (2008). High-precision Pb isotopic measurements of teeth and environmental samples from Sofia (Bulgaria): Insights for regional lead sources and possible pathways to the human body. *Environmental Geology*, 55(3):669–680.

Kennedy, M. C. and O'Hagan, A. (2001). Bayesian calibration of computer models. *Journal of the Royal Statistical Society. Series B: Statistical Methodology*, 63(3):425–464.

Khélifi, N., Sarnthein, M., Frank, M., Andersen, N., and Garbe-Schönberg, D. (2014). Late Pliocene variations of the Mediterranean outflow. *Marine Geology*, 357:182–194.

Kriest, I. and Oschlies, A. (2008). On the treatment of particulate organic matter sinking in large-scale models of marine biogeochemical cycles. *Biogeosciences*, 5(1):55–72.

Kuhlbrodt, T., Griesel, A., Montoya, M., Levermann, A., Hofmann, M., and Rahmstorf, S. (2007). On the driving processes of the Atlantic meridional overturning circulation. *Reviews of Geophysics*, 45(2):2001.

Lacan, F. and Jeandel, C. (2001). Tracing Papua New Guinea imprint on the central Equatorial Pacific Ocean using neodymium isotopic compositions and rare earth element patterns. *Earth and Planetary Science Letters*, 186(3-4):497–512.

Lacan, F. and Jeandel, C. (2005a). Acquisition of the neodymium isotopic composition of the North Atlantic Deep Water. *Geochemistry, Geophysics, Geosystems*, 6(12).

Lacan, F. and Jeandel, C. (2005b). Neodymium isotopes as a new tool for quantifying exchange fluxes at the continent-ocean interface. *Earth and Planetary Science Letters*, 232(3-4):245–257.

Lacan, F., Tachikawa, K., and Jeandel, C. (2012). Neodymium isotopic composition of the oceans: A compilation of seawater data. *Chemical Geology*, 300-301:177–184.

Lagarde, M., Lemaitre, N., Planquette, H., Grenier, M., Belhadj, M., Lherminier, P., and Jeandel, C. (2020). Particulate Rare Earth Element behavior in the North Atlantic (GEOVIDE cruise). *Biogeosciences Discussions*, pages 1–32.

Lambelet, M., van de Flierdt, T., Butler, E. C., Bowie, A. R., Rintoul, S. R., Watson, R. J., Remenyi, T., Lannuzel, D., Warner, M., Robinson, L. F., Bostock, H. C., and Bradtmiller, L. I. (2018). The Neodymium Isotope Fingerprint of Adélie Coast Bottom Water. *Geophysical Research Letters*, 45(20):11,247–11,256.

Lambelet, M., van de Flierdt, T., Crocket, K., Rehkämper, M., Kreissig, K., Coles, B., Rijkenberg, M. J., Gerringa, L. J., de Baar, H. J., and Steinfeldt, R. (2016). Neodymium isotopic composition and concentration in the western North Atlantic Ocean: Results from the GEOTRACES GA02 section. *Geochimica et Cosmochimica Acta*, 177:1–29.

Laws, E. A., Falkowski, P. G., Smith, W. O., Ducklow, H., and McCarthy, J. J. (2000). Temperature effects on export production in the open ocean. *Global Biogeochemical Cycles*, 14(4):1231–1246.

Lippold, J., Grützner, J., Winter, D., Lahaye, Y., Mangini, A., and Christi, M. (2009). Does sedimentary 231Pa/230Th from the Bermuda Rise monitor past Atlantic Meridional Overturning Circulation? *Geophysical Research Letters*, 36(12).

Lippold, J., Gutjahr, M., Blaser, P., Christner, E., de Carvalho Ferreira, M. L., Mulitza, S., Christl, M., Wombacher, F., Böhm, E., Antz, B., Cartapanis, O., Vogel, H., and Jaccard, S. L. (2016). Deep water provenance and dynamics of the (de)glacial Atlantic meridional overturning circulation. *Earth and Planetary Science Letters*, 445:68–78.

Locarnini, R., Mishonov, A., Baranova, O., Boyer, T., Zweng, M., Garcia, H., Reagan, J., Seidov, D., Weathers, K., Paver, C., I.V., S., Boyer, T., Locarnini, R., Garcia, H., Mishonov, A., Baranova, . O., Weathers, K., Paver, C., Smolyar, I., Baranova, O., Boyer, T., Zweng, M., Garcia, H., Reagan, J., Seidov, D., Weathers, K., Paver, C., I.V., S., Boyer, T., Locarnini, R., Garcia, H., Mishonov, A., Baranova, . O., Weathers, K., Paver, C., and Smolyar, I. (2018). World Ocean Atlas 2018.

Luo, Y., Tjiputra, J., Guo, C., Zhang, Z., and Lippold, J. (2018). Atlantic deep water circulation during the last interglacial. *Scientific Reports*, 8(1).

Lupker, M., France-Lanord, C., Galy, V., Lavé, J. Ô., and Kudrass, H. (2013). Increasing chemical weathering in the Himalayan system since the Last Glacial Maximum. *Earth and Planetary Science Letters*, 365:243–252.

Lynch-Stieglitz, J. (2003). Tracers of Past Ocean Circulation. In *Treatise on Geochemistry*, volume 6-9, pages 433–451. Pergamon.

Lynch-Stieglitz, J. (2017). The Atlantic Meridional Overturning Circulation and Abrupt Climate Change.

Lynch-Stieglitz, J., Curry, W. B., and Slowey, N. (1999a). A geostrophic transport estimate for the Florida Current from the oxygen isotope composition of benthic foraminifera. *Paleoceanography*, 14(3):360–373.

Lynch-Stieglitz, J., Curry, W. B., and Slowey, N. (1999b). Weaker Gulf Stream in the Florida straits during the Last Glacial Maximum. *Nature*, 402(6762):644–648.

Lynch-Stieglitz, J. and Marchitto, T. M. (2003). Tracers of Past Ocean Circulation. In *Treatise on Geochemistry: Second Edition*, volume 8, pages 435–452.

Maccali, J., Hillaire-Marcel, C., Carignan, J., and Reisberg, L. C. (2013). Geochemical signatures of sediments documenting Arctic sea-ice and water mass export through Fram Strait since the Last Glacial Maximum. *Quaternary Science Reviews*, 64:136–151.

Macdonald, A. M. and Wunsch, C. (1996). An estimate of global ocean circulation and heat fluxes. *Nature*, 382(6590):436–439.

Mahowald, N. M., Muhs, D. R., Levis, S., Rasch, P. J., Yoshioka, M., Zender, C. S., and Luo, C. (2006). Change in atmospheric mineral aerosols in response to climate: Last glacial period, preindustrial, modern, and doubled carbon dioxide climates. *Journal of Geophysical Research Atmospheres*, 111(10).

Maier-Reimer, E. (1993). Geochemical cycles in an ocean general circulation model. Preindustrial tracer distributions. *Global Biogeochemical Cycles*, 7(3):645–677.

Marshall, J., Donohoe, A., Ferreira, D., and McGee, D. (2014). The ocean's role in setting the mean position of the Inter-Tropical Convergence Zone. *Climate Dynamics*, 42(7-8):1967–1979.

Martin, E. E. and Scher, H. (2006). A Nd isotopic study of southern sourced waters and indonesian throughflow at intermediate depths in the Cenozoic Indian Ocean. *Geochemistry, Geophysics, Geosystems*, 7(9).

Martin, E. E. and Scher, H. D. (2004). Preservation of seawater Sr and Nd isotopes in fossil fish teeth: Bad news and good news. *Earth and Planetary Science Letters*, 220(1-2):25–39.

Martin, J. H., Knauer, G. A., Karl, D. M., and Broenkow, W. W. (1987). VERTEX: carbon cycling in the northeast Pacific. *Deep Sea Research Part A, Oceanographic Research Papers*, 34(2):267–285.

McCarthy, G. D., Smeed, D. A., Johns, W. E., Frajka-Williams, E., Moat, B. I., Rayner, D., Baringer, M. O., Meinen, C. S., Collins, J., and Bryden, H. L. (2015). Measuring the Atlantic Meridional Overturning Circulation at 26°N. *Progress in Oceanography*, 130:91–111.

McCulloch, M. T. and Perfit, M. R. (1981). 143Nd/144Nd, 87Sr/86Sr and trace element constraints on the petrogenesis of Aleutian island arc magmas. *Earth and Planetary Science Letters*, 56:167–179.

McLennan, S. M., Taylor, S. R., McCulloch, M. T., and Maynard, J. B. (1990). Geochemical and Nd-Sr isotopic composition of deep-sea turbidites: Crustal evolution and plate tectonic associations. *Geochimica et Cosmochimica Acta*, 54(7):2015–2050.

McManus, J. F., Francois, R., Gherardl, J. M., Kelgwin, L., and Drown-Leger, S. (2004). Collapse and rapid resumption of Atlantic meridional circulation linked to deglacial climate changes. *Nature*, 428(6985):834–837.

Measures, C., Henderson, G., Anderson, R., Adkins, J., Andersson, P., Boyle, E., Cutter, G., de Baar, H., Eisenhauer, A., Frank, M., Francois, R., Orians, K., Gamo, T., German, C., Jenkins, W., Moffett, J., Jeandel, C., Jickells, T., Krishnaswami, S., Mackey, D., Masque, P., Moore, J., Oschlies, A., van der Loeff, M., Sharma, M., von Damm, K., Zhan, J., and SCOR Working Group (2007). GEOTRACES – An international study of the global marine biogeochemical cycles of trace elements and their isotopes. *Chemie der Erde geochemistry*, 64(2):85–131.

Menviel, L., Capron, E., Govin, A., Dutton, A., Tarasov, L., Abe-Ouchi, A., Drysdale, R. N., Gibbard, P. L., Gregoire, L., He, F., Ivanovic, R. F., Kageyama, M., Kawamura, K., Landais, A., Otto-Bliesner, B. L., Oyabu, I., Tzedakis, P. C., Wolff, E., and Zhang, X. (2019). The penultimate deglaciation: Protocol for Paleoclimate Modelling Intercomparison Project (PMIP) phase 4 transient numerical simulations between 140 and 127 ka, version 1.0. *Geoscientific Model Development*, 12(8):3649–3685.

Menviel, L., Yu, J., Joos, F., Mouchet, A., Meissner, K. J., and England, M. H. (2017). Poorly ventilated deep ocean at the Last Glacial Maximum inferred from carbon isotopes: A data-model comparison study. *Paleoceanography*, 32(1):2–17.

Mikhalsky, E. V., Laiba, A. A., and Beliatsky, B. V. (2006). Tectonic Subdivision of the Prince Charles Mountains: A Review of Geologic and Isotopic Data. *Antarctica*, (i):69–81.

Mikhalsky, E. V., Sheraton, J. W., Kudriavtsev, I. V., Sergeev, S. A., Kovach, V. P., Kamenev, I. A., and Laiba, A. A. (2013). The mesoproterozoic Rayner Province in the Lambert Glacier area: Its age, origin, isotopic structure and implications for Australia-Antarctica correlations. *Geological Society Special Publication*, 383(1):35–57.

Molina-Kescher, M., Hathorne, E. C., Osborne, A. H., Behrens, M. K., Kölling, M., Pahnke, K., and Frank, M. (2018). The influence of basaltic islands on the oceanic REE distribution: A case study from the Tropical South Pacific. *Frontiers in Marine Science*, 5:50.

Morrison, R., Waldner, A., Hathorne, E. C., Rahlf, P., Zieringer, M., Montagna, P., Colin, C., Frank, N., and Frank, M. (2019). Limited influence of basalt weathering inputs on the seawater neodymium isotope composition of the northern Iceland Basin. *Chemical Geology*, 511(February 2018):358–370.

Najjar, R. G. and Orr, J. C. (1998). Design of OCMIP-2 simulations of chlorofluorocarbons, the solubility pump and common biogeochemistry. *Internal OCMIP Report*, page 25.

Nakai, S., Halliday, A. N., and Rea, D. K. (1993). Provenance of dust in the Pacific Ocean. *Earth and Planetary Science Letters*, 119(1-2):143–157.

Newkirk, D. R. and Martin, E. E. (2009). Circulation through the Central American Seaway during the Miocene carbonate crash. *Geology*, 37(1):87–90.

Noh, Y., Kang, I. S., Herold, M., and Raasch, S. (2006). Large eddy simulation of particle settling in the ocean mixed layer. *Physics of Fluids*, 18(8):85109.

Oka, A., Hasumi, H., Obata, H., Gamo, T., and Yamanaka, Y. (2009). Study on vertical profiles of rare earth elements by using an ocean general circulation model. *Global Biogeochemical Cycles*, 23(4).

Oka, A., Tazoe, H., and Obata, H. (2021). Simulation of global distribution of rare earth elements in the ocean using an ocean general circulation model. *Journal of Oceanography*, 1:3.

Oliver, K. I., Hoogakker, B. A., Crowhurst, S., Henderson, G. M., Rickaby, R. E., Edwards, N. R., and Elderfield, H. (2010). A synthesis of marine sediment core δ13C data over the last 150 000 years. *Climate of the Past*, 6(5):645–673.

Orsi, A. H., Johnson, G. C., and Bullister, J. L. (1999). Circulation, mixing, and production of Antarctic Bottom Water. *Progress in Oceanography*, 43(1):55–109.

Osborne, A. H., Haley, B. A., Hathorne, E. C., Plancherel, Y., and Frank, M. (2015). Rare earth element distribution in Caribbean seawater: Continental inputs versus lateral transport of distinct REE compositions in subsurface water masses. *Marine Chemistry*, 177:172–183.

Osborne, A. H., Hathorne, E. C., Schijf., J., Plancherel, Y., Boning, P., and Frank, M. (2017). The potential of sedimentary foraminiferal rare earth element patterns to trace water masses in the past. *Geochemistry Geophysics Geosystems*, 18:1–26.

Paffrath, R., Pahnke, K., Böning, P., Rutgers van der Loeff, M., Valk, O., Gdaniec, S., and Planquette, H. (2021). Seawater-Particle Interactions of Rare Earth Elements and Neodymium Isotopes in the Deep Central Arctic Ocean. *Journal of Geophysical Research: Oceans*, 126(8):e2021JC017423.

Pahnke, K., van de Flierdt, T., Jones, K. M., Lambelet, M., Hemming, S. R., and Goldstein, S. L. (2012). GEOTRACES intercalibration of neodymium isotopes and rare earth element concentrations in seawater and suspended particles. Part 2: Systematic tests and baseline profiles. *Limnology and Oceanography: Methods*, 10:252–269.

Palmer, J. R. and Todderdell, I. J. (2001). Production and export in a global ocean ecosystem model. *Deep-sea research Part 1*, 48:1169–1198.

Pasquier, B., Hines, S. K. V., Liang, H., Wu, Y., and John, S. G. (2021). GNOM v1 . 0 : An optimized steady-state model of the modern marine neodymium cycle. *Geoscientific Model Development*, 147.

Pearce, C. R., Jones, M. T., Oelkers, E. H., Pradoux, C., and Jeandel, C. (2013). The effect of particulate dissolution on the neodymium (Nd) isotope and Rare Earth Element (REE) composition of seawater. *Earth and Planetary Science Letters*, 369-370:138–147.

Pérez, F. F., Mercier, H., Vázquez-Rodríguez, M., Lherminier, P., Velo, A., Pardo, P. C., Rosón, G., and Ríos, A. F. (2013). Atlantic Ocean CO2 uptake reduced by weakening of the meridional overturning circulation. *Nature Geoscience*, 6(2):146–152.

Peucker-Ehrenbrink, B., Miller, M. W., Arsouze, T., and Jeandel, C. (2010). Continental bedrock and riverine fluxes of strontium and neodymium isotopes to the oceans. *Geochemistry, Geophysics, Geosystems*, 11(3).

Phedorin, M. A., Bobrov, V. A., Goldberg, E. L., Navez, J., Zolotaryov, K. V., and Grachev, M. A. (2000). SR-XFA as a method of choice in the search of signals of changing palaeoclimates in the sediments of Lake Baikal, compared to INAA and ICP-MS. *Nuclear Instruments and Methods in Physics Research, Section A: Accelerators, Spectrometers, Detectors and Associated Equipment*, 448(1):394–399.

Phipps, S. J., Rotstayn, L. D., Gordon, H. B., Roberts, J. L., Hirst, A. C., and Budd, W. F. (2011). The CSIRO Mk3L climate system model version 1.0 - Part 1: Description and evaluation. *Geoscientific Model Development*, 4(2):483–509.

Piepgras, D. J. and Wasserburg, G. J. (1980). Neodymium isotopic variations in seawater. *Earth and Planetary Science Letters*, 50(1):128–138.

Piepgras, D. J., Wasserburg, G. J., and Dasch, E. J. (1979). The isotopic composition of Nd in different ocean masses. *Earth and Planetary Science Letters*, 45(2):223–236.

Pierce, E. L., Williams, T., van de Flierdt, T., Hemming, S. R., Goldstein, S. L., and Brachfeld, S. A. (2011). Characterizing the sediment provenance of East Antarctica's weak underbelly: The Aurora and Wilkes sub-glacial basins. *Paleoceanography*, 26(4).

Pin, C. and Santos Zalduegui, J. F. (1997). Sequential separation of light rare-earth elements, thorium and uranium by miniaturized extraction chromatography: Application to isotopic analyses of silicate rocks. *Analytica Chimica Acta*, 339(1-2):79–89.

Piotrowski, A. M., Galy, A., Nicholl, J. A. L., Roberts, N., Wilson, D. J., Clegg, J. A., and Yu, J. (2012). Reconstructing deglacial North and South Atlantic deep water sourcing using foraminiferal Nd isotopes. *Earth and Planetary Science Letters*, 357-358:289–297.

Piotrowski, A. M., Goldstein, S. L., Hemming, S. R., and Fairbanks, R. G. (2004). Intensification and variability of ocean thermohaline circulation through the last deglaciation. *Earth and Planetary Science Letters*, 225(1-2):205–220.

Piotrowski, A. M., Goldstein, S. L., Hemming, Sidney, R., Fairbanks, R. G., and Zylberberg, D. R. (2008). Oscillating glacial northern and southern deep water formation from combined neodymium and carbon isotopes. *Earth and Planetary Science Letters*, 272(1-2):394–405.

Plank, T. and Langmuir, C. H. (1998). The chemical composition of subducting sediment and its consequences for the crust and mantle. *Chemical Geology*, 145(3-4):325–394.

Pope, V. D., Gallani, M. L., Rowntree, P. R., and Stratton, R. A. (2000). The impact of new physical parametrizations in the Hadley Centre climate model: HadAM3. *Climate Dynamics*, 16(2-3):123–146.

Pöppelmeier, F., Blaser, P., Gutjahr, M., Jaccard, S., Frank, M., Max, L., and Lippold, J. (2020a). Northern Sourced Water dominated the Atlantic Ocean during the Last Glacial Maximum. *Geology*, 48.

Pöppelmeier, F., Blaser, P., Gutjahr, M., Süfke, F., Thornalley, D. J., Grützner, J., Jakob, K. A., Link, J. M., Szidat, S., and Lippold, J. (2019). Influence of Ocean Circulation and Benthic Exchange on Deep Northwest Atlantic Nd Isotope Records During the Past 30,000 Years. *Geochemistry, Geophysics, Geosystems*, 20(9):4457–4469.

Pöppelmeier, F., Janssen, D. J., Jaccard, S. L., and Stocker, T. F. (2021a). Modeling the marine chromium cycle: new constraints on global-scale processes. *Biogeosciences*, 18(19):5447–5463.

Pöppelmeier, F., Lippold, J., Blaser, P., Gutjahr, M., Frank, M., and Stocker, T. F. (2022). Neodymium isotopes as a paleo-water mass tracer: A model-data reassessment. *Quaternary Science Reviews*, 279:107404.

Pöppelmeier, F., Scheen, J., Blaser, P., Lippold, J., Gutjahr, M., and Stocker, T. F. (2020b). Influence of Elevated Nd Fluxes on the Northern Nd Isotope End Member of the Atlantic During the Early Holocene. *Paleoceanography and Paleoclimatology*, 35(11):e2020PA003973.

Pöppelmeier, F., Scheen, J., Jeltsch-Thömmes, A., and F. Stocker, T. (2021b). Simulated stability of the Atlantic Meridional Overturning Circulation during the Last Glacial Maximum. *Climate of the Past*, 17(2):615–632.

Porcelli, D., Andersson, P. S., Baskaran, M., Frank, M., Björk, G., and Semiletov, I. (2009). The distribution of neodymium isotopes in Arctic Ocean basins. *Geochimica et Cosmochimica Acta*, 73(9):2645–2659.

Rae, J. W., Sarnthein, M., Foster, G. L., Ridgwell, A., Grootes, P. M., and Elliott, T. (2014). Deep water formation in the North Pacific and deglacial CO2 rise. *Paleoceanography*, 29(6):645–667.

Rahlf, P., Hathorne, E., Laukert, G., Gutjahr, M., Weldeab, S., and Frank, M. (2020). Tracing water mass mixing and continental inputs in the southeastern Atlantic Ocean with dissolved neodymium isotopes. *Earth and Planetary Science Letters*, 530:115944.

Rahlf, P., Laukert, G., Hathorne, E. C., Vieira, L. H., and Frank, M. (2021). Dissolved neodymium and hafnium isotopes and rare earth elements in the Congo River Plume: Tracing and quantifying continental inputs into the southeast Atlantic. *Geochimica et Cosmochimica Acta*, 294:192–214.

Rahmstorf, S. (2002). Ocean circulation and climate during the past 120,000 years.

Rasmussen, C. E. and Williams, C. K. I. (2006). Gaussian processes for machine learning.

Reimer, P. J., Baillie, M. G., Bard, E., Bayliss, A., Beck, J. W., Blackwell, P. G., Ramsey, C. B., Buck, C. E., Burr, G. S., Edwards, R. L., Friedrich, M., Grootes, P. M., Guilderson, T. P., Hajdas, I., Heaton, T. J., Hogg, A. G., Hughen, K. A., Kaiser, K. F., Kromer, B., McCormac, F. G., Manning, S. W., Reimer, R. W., Richards, D. A., Southon, J. R., Talamo, S., Turney, C. S., van der Plicht, J., and Weyhenmeyer, C. E. (2009). IntCal09 and Marine09 radiocarbon age calibration curves, 0-50,000 years CAL BP. *Radiocarbon*, 51(4):1111–1150.

Rempfer, J., Stocker, T. F., Joos, F., and Dutay, J. C. (2012). On the relationship between Nd isotopic composition and ocean overturning circulation in idealized freshwater discharge events. *Paleoceanography*, 27(3):PA3211.

Rempfer, J., Stocker, T. F., Joos, F., Dutay, J.-C., and Siddall, M. (2011). Modelling Nd-isotopes with a coarse resolution ocean circulation model: Sensitivities to model parameters and source/sink distributions. *Geochimica et Cosmochimica Acta*, 75:5927–5950.

Revel, M., Cremer, M., Grousset, F. E., and Labeyrie, L. (1996). Grain-size and Sr-Nd isotopes as tracer of paleo-bottom current strength, Northeast Atlantic Ocean. Technical report.

Ridgwell, A., Hargreaves, J. C., Edwards, N. R., Annan, J. D., Lenton, T. M., Marsh, R., Yool, A., and Watson, A. (2007). Marine geochemical data assimilation in an efficient Earth system model of global biogeochemical cycling. *Biogeosciences*, 4(1):87–104.

Roberts, N. L. and Piotrowski, A. (2015). Radiogenic Nd isotope labeling of the northern NE Atlantic during MIS 2. *Earth and Planetary Science Letters*, 423:125–133.

Roberts, N. L., Piotrowski, A. M., McManus, J. F., and Keigwin, L. D. (2010). Synchronous deglacial overturning and water mass source changes. *Science*, 327(5961):75–78.

Robinson, S., Ivanovic, R., Gregoire, L., Tindall, J., van de Flierdt, T., Pöppelmeier, F., Tachikawa, K., and Valdes, P. (2022a). Simulating marine neodymium isotope distributions using ND v1.0 coupled to the ocean component of the FAMOUS-MOSES1 climate model: sensitivities to reversible scavenging efficiency and benthic source distributions. *Geoscientific Model Development [in review]*.

Robinson, S., Ivanovic, R., van de Flierdt, T., Blanchet, C. L., Tachikawa, K., Martin, E. E., Cook, C. P., Williams, T., Gregoire, L., Plancherel, Y., Jeandel, C., and Arsouze, T. (2021). Global continental and marine detrital ϵNd: An updated compilation for use in understanding marine Nd cycling. *Chemical Geology*, 567:120119.

Robinson, S., Ivanovic, R. F., Gregoire, L. J., Astfalck, L., van de Flierdt, T., Plancherel, Y., Pöppelmeier, F., and Tachikawa, K. (2022b). Optimisation of the Nd isotope scheme in the ocean component of the FAMOUS general circulation model. *Biogeosciences [submitted]*.

Rosenthal, Y., Boyle, E. A., and Labeyrie, L. (1997). Last glacial maximum paleochemistry and deepwater circulation in the Southern ocean: Evidence from foraminiferal cadmium. *Paleoceanography*, 12(6):787–796.

Rousseau, T. C., Sonke, J. E., Chmeleff, J., Van Beek, P., Souhaut, M., Boaventura, G., Seyler, P., and Jeandel, C. (2015). Rapid neodymium release to marine waters from lithogenic sediments in the Amazon estuary. *Nature Communications*, 6.

Roy, M., van de Flierdt, T., Hemming, S. R., and Goldstein, S. L. (2007). 40Ar/39Ar ages of hornblende grains and bulk Sm/Nd isotopes of circum-Antarctic glacio-marine sediments: Implications for sediment provenance in the southern ocean. *Chemical Geology*, 244(3-4):507–519.

Rutberg, R. L., Hemming, S. R., and Goldstein, S. L. (2000). Reduced North Atlantic Deep Water flux to the glacial Southern Ocean inferred from neodymium isotope ratios. *Nature*, 405(6789):935–938.

Sagoo, N., Valdes, P., Flecker, R., and Gregoire, L. J. (2013). The early eocene equable climate problem: Can perturbations of climate model parameters identify possible solutions? *Philosophical Transactions of the Royal Society A: Mathematical, Physical and Engineering Sciences*, 371(2001).

Sarmiento, J. L. and LeQuéré, C. (1996). Oceanic carbon dioxide uptake in a model of century-scale global warming. *Science*, 274(5291):1346–1350.

Scher, H. D. and Martin, E. E. (2006). Timing and climatic consequences of the opening of drake passage. *Science*, 312(5772):428–430.

Scheuvens, D., Schütz, L., Kandler, K., Ebert, M., and Weinbruch, S. (2013). Bulk composition of northern African dust and its source sediments - A compilation.

Schmittner, A., Chiang, J. C., and Hemming, S. R. (2013). *Ocean Circulation: Mechanisms and Impacts - Past and Future Changes of Meridional Overturning*. American Geophysical Union.

Sepulchre, P., Arsouze, T., Donnadieu, Y., Dutay, J. C., Jaramillo, C., Le Bras, J., Martin, E., Montes, C., and Waite, A. J. (2014). Consequences of shoaling of the Central American Seaway determined from modeling Nd isotopes. *Paleoceanography*, 29(3):176–189.

Shi, Y., Gong, W., Duan, Q., Charles, J., Xiao, C., and Wang, H. (2019). How parameter specification of an Earth system model of intermediate complexity influences its climate simulations. *Progress in Earth and Planetary Science*, 6(1):1–18.

Sholkovitz, E. R. (1993). The geochemistry of rare earth elements in the Amazon River estuary. *Geochimica et Cosmochimica Acta*, 57(10):2181–2190.

Siddall, M., Anderson, R. F., Winckler, G., Henderson, G. M., Bradtmiller, L. I., McGee, D., Franzese, A., Stocker, T. F., and Müller, S. A. (2008a). Modeling the particle flux effect on distribution of 230Th in the equatorial pacific. *Paleoceanography*, 23(2):PA2208.

Siddall, M., Henderson, G. M., Edwards, N. R., Frank, M., Müller, S. A., Stocker, T. F., and Joos, F. (2005). 231Pa/230Th fractionation by ocean transport, biogenic particle flux and particle type. *Earth and Planetary Science Letters*, 237(1-2):135–155.

Siddall, M., Khatiwala, S., van de Flierdt, T., Jones, K., Goldstein, S. L., Hemming, S., and Anderson, R. F. (2008b). Towards explaining the Nd paradox using reversible scavenging in an ocean general circulation model. *Earth and Planetary Science Letters*, 274(3-4):448–461.

Siddall, M., Stocker, T. F., Henderson, G. M., Joos, F., Frank, M., Edwards, N. R., Ritz, S. P., and Müller, S. A. (2007). Modeling the relationship between 231Pa/230Th distribution in North Atlantic sediment and Atlantic meridional overturning circulation. *Paleoceanography*, 22(2).

Sigman, D. M., Jaccard, S. L., and Haug, G. H. (2004). Polar ocean stratification in a cold climate. *Nature*, 428(6978):59–63.

Simões Pereira, P., van de Flierdt, T., Hemming, S. R., Hammond, S. J., Kuhn, G., Brachfeld, S., Doherty, C., and Hillenbrand, C. D. (2018). Geochemical fingerprints of glacially eroded bedrock from West Antarctica: Detrital thermochronology, radiogenic isotope systematics and trace element geochemistry in Late Holocene glacial-marine sediments. *Earth-Science Reviews*, 182:204–232.

Sinha, B., Smeed, D. A., McCarthy, G., Moat, B. I., Josey, S. A., Hirschi, J. J., Frajka-Williams, E., Blaker, A. T., Rayner, D., and Madec, G. (2018). The accuracy of estimates of the overturning circulation from basin-wide mooring arrays. *Progress in Oceanography*, 160:101–123.

Smeed, D. A., McCarthy, G. D., Cunningham, S. A., Frajka-Williams, E., Rayner, D., Johns, W. E., Meinen, C. S., Baringer, M. O., Moat, B. I., Duchez, A., and Bryden, H. L. (2014). Observed decline of the Atlantic meridional overturning circulation 2004-2012.

Smith, R. N. (1990). A scheme for predicting layer clouds and their water content in a general circulation model. *Quarterly Journal of the Royal Meteorological Society*, 116(492):435–460.

Smith, R. N. B. (1993). Subsurface, surface and boundary layer processes. *Unified model documentation paper No 24*, (24).

Smith, R. S. (2012). The FAMOUS climate model (versions XFXWB and XFHCC): Description update to version XDBUA. *Geoscientific Model Development*, 5(1):269–276.

Smith, R. S., George, S., and Gregory, J. M. (2021). FAMOUS version xotzt (FAMOUS-ice): A general circulation model (GCM) capable of energy- And water-conserving coupling to an ice sheet model. *Geoscientific Model Development*, 14(9):5769–5787.

Smith, R. S. and Gregory, J. (2012). The last glacial cycle: Transient simulations with an AOGCM. *Climate Dynamics*, 38(7-8):1545–1559.

Smith, R. S. and Gregory, J. M. (2009). A study of the sensitivity of ocean overturning circulation and climate to freshwater input in different regions of the North Atlantic. *Geophysical Research Letters*, 36(15):L15701.

Smith, R. S., Gregory, J. M., and Osprey, A. (2008). A description of the FAMOUS (version XDBUA) climate model and control run. *Geoscientific Model Development*, 1(1):53–68.

Stephens, B. B. and Keeling, R. F. (2000). The influence of antarctic sea ice on glacial-interglacial CO2 variations. *Nature*, 404(6774):171–174.

Stichel, T., Frank, M., Rickli, J., and Haley, B. A. (2012). The hafnium and neodymium isotope composition of seawater in the Atlantic sector of the Southern Ocean. *Earth and Planetary Science Letters*, 317-318:282–294.

Stichel, T., Kretschmer, S., Geibert, W., Lambelet, M., Plancherel, Y., Rutgers van der Loeff, M., and van de Flierdt, T. (2020). Particle–Seawater Interaction of Neodymium in the North Atlantic. *ACS Earth and Space Chemistry*.

Stocker, T., Qin, D., Plattner, G.-K., Tignor, M., Allen, S., Boschung, J., Nauels, A., Xia, Y., Bex, V., and Midgley, P. (2013). Intergovernmental Panel on Climate Change Climate change 2013: The physical science basis. Contribution of Working Group I to the Fifth Assessment Report of the Intergovernmental Panel on Climate Change. Technical report, Cambridge, United Kingdom and New York, NY: Cambridge University Press.

Straume, E. O., Gaina, C., Medvedev, S., Hochmuth, K., Gohl, K., Whittaker, J. M., Abdul Fattah, R., Doornenbal, J. C., and Hopper, J. R. (2019). GlobSed: Updated Total Sediment Thickness in the World's Oceans. *Geochemistry, Geophysics, Geosystems*, 20(4):1756–1772.

Stumpf, R., Frank, M., Schönfeld, J., and Haley, B. A. (2010). Late Quaternary variability of Mediterranean Outflow Water from radiogenic Nd and Pb isotopes. *Quaternary Science Reviews*, 29(19-20):2462–2472.

Stumpf, R., Kraft, S., Frank, M., Haley, B., Holbourn, A., and Kuhnt, W. (2015). Persistently strong Indonesian Throughflow during marine isotope stage 3: Evidence from radiogenic isotopes. *Quaternary Science Reviews*, 112:197–206.

Sweeney, C., Gloor, E., Jacobson, A. R., Key, R. M., McKinley, G., Sarmiento, J. L., and Wanninkhof, R. (2007). Constraining global air-sea gas exchange for CO2 with recent bomb 14C measurements. *Global Biogeochemical Cycles*, 21(2).

Tachikawa, K., Arsouze, T., Bayon, G., Bory, A., Colin, C., Dutay, J. C., Frank, N., Giraud, X., Gourlan, A. T., Jeandel, C., Lacan, F., Meynadier, L., Montagna, P., Piotrowski, A. M., Plancherel, Y., Pucéat, E., Roy-Barman, M., and Waelbroeck, C. (2017). The large-scale evolution of neodymium isotopic composition in the global modern and Holocene ocean revealed from seawater and archive data. *Chemical Geology*, 457:131–148.

Tachikawa, K., Athias, V., and Jeandel, C. (2003). Neodymium budget in the modern ocean and paleo-oceanographic implications. *Journal of Geophysical Research*, 108(C8):3254.

Tachikawa, K., Jeandel, C., Vangriesheim, A., and Dupré, B. (1999). Distribution of rare earth elements and neodymium isotopes in suspended particles of the tropical Atlantic Ocean (EUMELI site). *Deep-sea research Part 1*, 46(5):733–755.

Tachikawa, K., Rapuc, W., Dubois-Dauphin, Q., Guihou, A., and Skonieczny, C. (2020). Reconstruction of ocean circulation based on neodymium isotopic composition: Potential limitations and application to the mid-pleistocene transition. *Oceanography*, 33(2):80–87.

Tachikawa, K., Roy-Barman, M., Michard, A., Thouron, D., Yeghicheyan, D., and Jeandel, C. (2004). Neodymium isotopes in the Mediterranean Sea: Comparison between seawater and sediment signals. *Geochimica et Cosmochimica Acta*, 68(14):3095–3106.

Takahashi, T., Sutherland, S. C., Wanninkhof, R., Sweeney, C., Feely, R. A., Chipman, D. W., Hales, B., Friederich, G., Chavez, F., Sabine, C., Watson, A., Bakker, D. C., Schuster, U., Metzl, N., Yoshikawa-Inoue, H., Ishii, M., Midorikawa, T., Nojiri, Y., Körtzinger, A., Steinhoff, T., Hoppema, M., Olafsson, J., Arnarson, T. S., Tilbrook, B., Johannessen, T., Olsen, A., Bellerby, R., Wong, C. S., Delille, B., Bates, N. R., and de Baar, H. J. (2009). Climatological mean and decadal change in surface ocean pCO2, and net sea-air CO2 flux over the global oceans. *Deep-Sea Research Part II: Topical Studies in Oceanography*, 56(8-10):554–577.

Talley, L. (2013). Closure of the Global Overturning Circulation Through the Indian, Pacific, and Southern Oceans: Schematics and Transports. *Oceanography*, 26(1):80–97.

Talley, L. D., Pickard, G. L., Emery, W. J., and Swift, J. H. (2011). *Descriptive physical oceanography: An introduction: Sixth edition.* Academic Press.

Tanaka, T., Togashi, S., Kamioka, H., Amakawa, H., Kagami, H., Hamamoto, T., Yuhara, M., Orihashi, Y., Yoneda, S., Shimizu, H., Kunimaru, T., Takahashi, K., Yanagi, T., Nakano, T., Fujimaki, H., Shinjo, R., Asahara, Y., Tanimizu, M., and Dragusanu, C. (2000). JNdi-1: A neodymium isotopic reference in consistency with LaJolla neodymium. *Chemical Geology*, 168(3-4):279–281.

Taylor, S. R., McLennan, S. M., and McCulloch, M. T. (1983). Geochemistry of loess, continental crustal composition and crustal model ages. *Geochimica et Cosmochimica Acta*, 47(11):1897–1905.

Toggweiler, J. R., Russell, J. L., and Carson, S. R. (2006). Midlatitude westerlies, atmospheric CO2, and climate change during the ice ages. *Paleoceanography*, 21(2).

Toucanne, S., Soulet, G., Freslon, N., Silva Jacinto, R., Dennielou, B., Zaragosi, S., Eynaud, F., Bourillet, J. F., and Bayon, G. (2015). Millennial-scale fluctuations of the European Ice Sheet at the end of the last glacial, and their potential impact on global climate. *Quaternary Science Reviews*, 123:113–133.

Valdes, P. J., Armstrong, E., Badger, M. P., Bradshaw, C. D., Bragg, F., Crucifix, M., Davies-Barnard, T., Day, J., Farnsworth, A., Gordon, C., Hopcroft, P. O., Kennedy, A. T., Lord, N. S., Lunt, D. J., Marzocchi, A., Parry, L. M., Pope, V., Roberts, W. H., Stone, E. J., Tourte, G. J., and Williams, J. H. (2017). The BRIDGE HadCM3 family of climate models: HadCM3@Bristol v1.0. *Geoscientific Model Development*, 10(10):3715–3743.

van de Flierdt, T. and Frank, M. (2010). Neodymium isotopes in paleoceanography. *Quaternary Science Reviews*, 29(19-20):2439–2441.

van de Flierdt, T., Frank, M., Lee, D. C., Halliday, A. N., Reynolds, B. C., and Hein, J. R. (2004). New constraints on the sources and behavior of neodymium and hafnium in seawater from Pacific Ocean ferromanganese crusts. *Geochimica et Cosmochimica Acta*, 68(19):3827–3843.

van de Flierdt, T., Grifths, A. M., Lambelet, M., Little, S. H., Stichel, T., and Wilson, D. J. (2016). Neodymium in the oceans: A global database, a regional comparison and implications for palaeoceanographic research.

van de Flierdt, T., Hemming, S. R., Goldstein, S. L., Gehrels, G. E., and Cox, S. E. (2008). Evidence against a young volcanic origin of the Gamburtsev Subglacial Mountains, Antarctica. *Geophysical Research Letters*, 35(21):L21303.

van de Flierdt, T., Pahnke, K., Amakawa, H., Andersson, P., Basak, C., Coles, B., Colin, C., Crocket, K., Frank, M., Frank, N., Goldstein, S. L., Goswami, V., Haley, B. A., Hathorne, E. C., Hemming, S. R., Henderson, G. M., Jeandel, C., Jones, K., Kreissig, K., Lacan, F., Lambelet, M., Martin, E. E., Newkirk, D. R., Obata, H., Pena, L., Piotrowski, A. M., Pradoux, C., Scher, H. D., Schöberg, H., Singh, S. K., Stiche, T., Tazoe, H., Vance, D., and Yang, J. (2012). GEOTRACES intercalibration of neodymium isotopes and rare earth element concentrations in seawater and suspended particles. Part 1: Reproducibility of results for the international intercomparison. *Limnology and Oceanography: Methods*, 10:234–251.

van de Flierdt, T., Robinson, L. F., and Adkins, J. F. (2010). Deep-sea coral aragonite as a recorder for the neodymium isotopic composition of seawater. *Geochimica et Cosmochimica Acta*, 74(21):6014–6032.

Vellinga, M. and Wood, R. A. (2002). Global climatic impacts of a collapse of the atlantic thermohaline circulation. *Climatic Change*, 54(3):251–267.

Voelker, A. H., Lebreiro, S. M., Schönfeld, J., Cacho, I., Erlenkeuser, H., and Abrantes, F. (2006). Mediterranean outflow strengthening during northern hemisphere coolings: A salt source for the glacial Atlantic? *Earth and Planetary Science Letters*, 245(1-2):39–55.

Vogt-Vincent, N., Lippold, J., Kaboth-Bahr, S., and Blaser, P. (2020). Ice-rafted debris as a source of non-conservative behaviour for the ϵNd palaeotracer: insights from a simple model. *Geo-Marine Letters*.

von Blanckenburg, F. (1999). Tracing past ocean circulation? *Science*, 286(5446):1862b–1863.

von Blanckenburg, F. (2001). Long-term Tracer Changes. In *Encyclopedia of Ocean Sciences*, pages 1492–1503. Academic Press.

Walter, H. J., Hegner, E., Diekmann, B., Kuhn, G., and Rutgers Van Der Loeff, M. M. (2000). Provenance and transport of terrigenous sediment in the South Atlantic Ocean and their relations to glacial and interglacial cycles: Nd and Sr isotopic evidence. *Geochimica et Cosmochimica Acta*, 64(22):3813–3827.

Wang, R., Clegg, J. A., Scott, P. M., Larkin, C. S., Deng, F., Thomas, A. L., Zheng, X. Y., and Piotrowski, A. M. (2021). Reversible scavenging and advection – Resolving the neodymium paradox in the South Atlantic. *Geochimica et Cosmochimica Acta*, 314:121–139.

Weldeab, S., Frank, M., Stichel, T., Haley, B., and Sangen, M. (2011). Spatio - temporal evolution of the West African monsoon during the last deglaciation. *Geophysical Research Letters*, 38(13):L13703.

Williams, J. H. T., Smith, R. S., Valdes, P. J., Booth, B. B. B., and Osprey, A. (2013). Optimising the FAMOUS climate model: inclusion of global carbon cycling. *Geoscientific Model Development*, 6(1):141–160.

Williamson, D. (2015). Exploratory ensemble designs for environmental models using k-extended Latin Hypercubes. *Environmetrics*, 26(4):268–283.

Williamson, D., Goldstein, M., Allison, L., Blaker, A., Challenor, P., Jackson, L., and Yamazaki, K. (2013). History matching for exploring and reducing climate model parameter space using observations and a large perturbed physics ensemble. *Climate Dynamics*, 41(7-8):1703–1729.

Wilson, D. J., Crocket, K. C., van de Flierdt, T., Robinson, L. F., and Adkins, J. F. (2015). Dynamic intermediate ocean circulation in the North Atlantic during Heinrich Stadial 1: A radiocarbon and neodymium isotope perspective. *Paleoceanography*, 29(11):1072–1093.

Wilson, D. J., Piotrowski, A. M., Galy, A., and Clegg, J. A. (2013). Reactivity of neodymium carriers in deep sea sediments: Implications for boundary exchange and paleoceanography. *Geochimica et Cosmochimica Acta*, 109:197–221.

Wilson, J. D., Barker, S., and Ridgwell, A. (2012). Assessment of the spatial variability in particulate organic matter and mineral sinking fluxes in the ocean interior: Implications for the ballast hypothesis. *Global Biogeochemical Cycles*, 26(4):GB4011.

Woodward, S. (2011). Hadley Centre Technical Note 87: Mineral Dust in HadGEM2. *MetOffice*.

Xie, R. C., Marcantonio, F., and Schmidt, M. W. (2014). Reconstruction of intermediate water circulation in the tropical North Atlantic during the past 22,000 years. *Geochimica et Cosmochimica Acta*, 140:455–467.

Yeager, S. G., Shields, C. A., Large, W. G., and Hack, J. J. (2006). The Low-Resolution CCSM3. *Journal of Climate*, 19:2545–2566.

Yu, E. F., Francois, R., and Bacon, M. P. (1996). Similar rates of modern and last-glacial ocean thermohaline circulation inferred from radiochemical data. *Nature*, 379(6567):689–694.

Zhang, Y., Lacan, F., and Jeandel, C. (2008). Dissolved rare earth elements tracing lithogenic inputs over the Kerguelen Plateau (Southern Ocean). *Deep-Sea Research Part II: Topical Studies in Oceanography*, 55(5-7):638–652.

Zhang, Z., Jiang, F., Li, T., Yang, D., Zhou, X., Xiong, Z., Qiu, X., Jia, Q., Yan, Y., and Feng, X. (2020). Sea-level changes controlled detrital sediment inputs to the Bicol Shelf in the western Philippine Sea since 150 ka. *Journal of Oceanology and Limnology*, 38(4):1153–1168.

Zheng, X. Y., Plancherel, Y., Saito, M. A., Scott, P. M., and Henderson, G. M. (2016). Rare earth elements (REEs) in the tropical South Atlantic and quantitative deconvolution of their non-conservative behavior. *Geochimica et Cosmochimica Acta*, 177:217–237.

Zweng, M., Reagan, J., Seidov, D., Boyer, T., Locarnini, R., Garcia, H., Mishonov, A., Baranova, . O., Weathers, K., Paver, C., and Smolyar, I. (2019). World Ocean Atlas 2018.

Appendices

Appendix A

Code and data availability

Note that the database of sedimentary and marine $\varepsilon_{\mathrm{Nd}}$ measurements, along with the global gridded datasets and all input files for reproducing the sedimentary $\varepsilon_{\mathrm{Nd}}$ distribution maps of the continental margins and seafloor are in the relevant supplementary information of Chapter 2 (Sect. 2.6). For an easy point of reference, they are available via the Research Data Leeds Repository (Robinson et al. 2021; `https://doi.org/10.5518/928`).

The main repository for the Met Office Unified Model (UM) version 4.5, as presented in this thesis, can be found at:
`https://cms.ncas.ac.uk/unified-model/`

The base code for FAMOUS is protected under UK Crown Copyright and can be obtained from National Centre for Atmospheric Science (NCAS) Computational Modelling Services (CMS): `https://cms.ncas.ac.uk/miscellaneous/um-famous/`.

The UM simulation files for the simulations described in Chapters 3 and 4, as denoted by their unique five-letter Met Office UM identifiers (outlined in Table A.1), can be accessed via the Providing Unified Model Access (PUMA) service: `https://cms.ncas.ac.uk/puma/`

Table A1: Overview of the simulations described in this thesis, as denoted by their unique five letter Met Office UM identifiers and the notation used within this thesis.

Identifier	Simulation	Duration
Control candidate simulations for new FAMOUS reference		
XPDAA	*control*	0-5,000 years
XPDAB	*control candidate*	0-5,000 years
XPDAC	*control candidate*	0-5,000 years
XPDEA	*control candidate*	0-5,000 years
Reversible scavenging efficiency ($[\mathrm{Nd}]_p/[\mathrm{Nd}]_d$) sensitivity simulations		
XPDAI	*EXPT_RS1*	0-9,000 years
XPDAD	*EXPT_RS2*	0-9,000 years
XPDAH	*EXPT_RS3*	0-9,000 years
XPDAE	*EXPT_RS4*	0-9,000 years
XPDAF	*EXPT_RS5*	0-9,000 years
XPDAG	*EXPT_RS6*	0-9,000 years
Total Nd source from sediment (f_{sed}) sensitivity simulations		
XPDAL	*EXPT_SED1*	0-9,000 years
XPDAM	*EXPT_SED2*	0-9,000 years
XPDAH	*EXPT_SED3*	0-9,000 years
XPDAN	*EXPT_SED4*	0-9,000 years

Additional simulations for Nd isotope scheme optimisation training set		
XPDAU	*TRAINING_SET1*	0-9,000 years
XPDAV	*TRAINING_SET2*	0-9,000 years
Simulations from Wave 1 of multi-wave ensemble		
XPGTA	*WAVE1_1*	0-6,000 years
XPGTB	*WAVE1_2*	0-6,000 years
XPGTC	*WAVE1_3*	0-6,000 years
XPGTD	*WAVE1_4*	0-6,000 years
XPGTE	*WAVE1_5*	0-6,000 years
XPGTF	*WAVE1_6*	0-6,000 years
XPGTG	*WAVE1_7*	0-6,000 years
XPGTH	*WAVE1_8*	0-6,000 years
Simulations from Wave 2 of multi-wave ensemble		
XPHJA	*WAVE2_1*	0-6,000 years
XPHJB	*WAVE2_2*	0-6,000 years
XPHJC	*WAVE2_3*	0-6,000 years
XPHJD	*WAVE2_4*	0-6,000 years
XPHJE	*WAVE2_5*	0-6,000 years
XPHJF	*WAVE2_6/REF_CONC2*	0-6,000 years
XPHJG	*WAVE2_7*	0-6,000 years
XPHJH	*WAVE2_8*	0-6,000 years
XPHJI	*WAVE2_9*	0-6,000 years
XPHJJ	*WAVE2_10*	0-6,000 years
XPHJK	*WAVE2_11*	0-6,000 years
XPHJL	*WAVE2_12*	0-6,000 years
XPHJM	*WAVE2_13*	0-6,000 years
XPHJN	*WAVE2_14*	0-6,000 years
XPHJO	*WAVE2_15*	0-6,000 years
Optimised reference simulations		
XPIAB	*REF*	0-6,000 years
XPIAC	*REF_IC*	0-6,000 years
XPIAD	*REF_CONC1*	0-6,000 years
Seafloor sediment Nd isotope distribution sensitivity simulations		
XPIAG	*REF-SED2*	0-6,000 years
XPIAH	*REF-SED3*	0-6,000 years
Margin-only constrained benthic flux sensitivity stimulation		
XPIAQ	*REF-SED3-MG*	0-6,000 years

Note that all the code, input files, post-processing scripts, and pre-stash files for implementing Neodymium isotopes (^{143}Nd and ^{144}Nd) in the ocean component of the UM4.5, as presented in in the supplement of the relevant research chapters (Chapter 3; Sect. 3.5 and Chapter 4; Sect. 4.7).

For completeness, and an easy point of reference, the relevant model code and output presented in the implementation of Nd isotopes in FAMOUS GCM as presented in Chapter 3, can be accessed via the Research Data Leeds Repository (Robinson et al. 2022a; https://doi.org/10.5518/1136).

Additionally, all the relevant model code and output presented for the optimisation of the Nd isotope scheme and sensitivity studies exploring the isotope composition and spatial extent of a benthic flux presented in Chapter 4 can be accessed via the Research Data Leeds Repository (Robinson et al. 2022b; https://doi.org/10.5518/1181).

Lastly, data tables containing: (1) the seawater rare earth element (REE) compilation

used in Chapters 3 and 4 to validate the Nd isotope scheme, and (2) all parameter values for the simulations forming the optimisation of the Nd isotope scheme, alongside all additional (i.e., historical) modification files (that are required on top of the FAMOUS base code to run the simulations described in this thesis), simulation files (Table A1), and scripts for the scheme optimisation can be accessed via the Research Data Leeds Repository (Robinson, 2022; `https://doi.org/10.5518/1182`).